Thèse n° 10 469

# Topological photonic transport in disordered scattering networks

Présentée le 24 mai 2024

Faculté des sciences et techniques de l’ingénieur
Laboratoire d’ingénierie des ondes
Programme doctoral en photonique

pour l’obtention du grade de Docteur ès Sciences

par

**Zhe ZHANG**

Acceptée sur proposition du jury

Prof. E. D. N. Matioli, président du jury
Prof. R. C. R. Fleury, directeur de thèse
Prof. A. Szameit, rapporteur
Prof. S. Rotter, rapporteur
Prof. J.-Ph. Brantut, rapporteur

École
polytechnique
fédérale
de Lausanne

2024

In pursuit of knowledge,something is acquired.
In pursuit of the highest wisdom, something is dropped.
— Laozi

To the world.

# Acknowledgements

This thesis and my doctoral research could not have been accomplished without the support and help of numerous individuals, to whom I am deeply grateful. I am also indebted to many who have helped me grow into the person I am today.

First and foremost, I express my sincere and deepest gratitude to my advisor, Prof. Romain Fleury, for his encouragement, understanding, guidance, and unwavering support throughout my time at EPFL. Working with him and having him as my advisor has been one of the best experiences of my life. His insightful comments and inspiring ideas were invaluable in broadening my view of the world, refining my thinking, and enhancing the quality of my work. I have gained not only great inspiration in physics from him but also learned from his broad perspectives on scientific and life wise disciplines. Four years ago, I was a Master student with no knowledge of topological insulators, disordered systems, and condensed matter physics. Romain transformed me into a versatile researcher in these fields, deeply engaged in theory, numerical analysis, experiments, and practical applications, and aspiring to conduct top-tier research in academia. There are countless moments with Romain that will forever be etched in my memory, continually motivating me to be curious, to think broadly in research, to dream big, to discover novel phenomena and validate them through various experimental platforms, to disseminate our findings widely, to stay at the forefront of research, and to aspire to be a professor like him. I could not have wished for a better advisor; he has truly become a role model for me.

I would also like to extend my wholehearted thanks to Prof. Pierre Delplace, whose influence has significantly shaped my approach to theoretical physics and my research interest. His lecture at EPFL in 2022 and every discussion we've had have guided me to a deeper understanding of topological physics and invariants. I consistently find new intriguing points in his papers, even after multiple readings. I am also grateful for Pierre's hospitality, for welcoming me several times at ENS de Lyon, and for introducing me to a wide network of researchers.

I also would like to thank my thesis committee, Prof. Matioli, Prof. Szameit, Prof. Rotter, Prof. Delplace, and Prof. Brantut, for carefully reading this manuscript and for our interesting scientific discussion during my private defence.

My next round of thanks goes to the members of LWE, starting with my PhD companions, Aleksi and Rongrong. They, like water – "The highest goodness is like water," as Laozi says – have taught me how to live peacefully. Discussions with Aleksi could reach incredible depths, with many concepts in my work refined and motivated by his sharp inquiries and sincere suggestions. From him, I learned how pure curiosity can spur and motivate significant research. Rongrong has been like an elder sister to me, helping me smoothly adapt to life overseas in Switzerland and manage life's pressures. She demonstrated how to persistently pursue a project year after year until finally observing the phenomena. Our senior colleagues, Farzad and Theodoros, guided us in our initial steps and shared their wisdom on PhD life and how to live happily – advice I have gladly followed, for which I am very thankful. Our junior colleagues, Junda, Tim, Haoye, and Ali, represent the future and immense potential of our lab, generating impressive ideas and research.

In addition, I wish to express my gratitude to our postdocs, including Matthieu (M. M.), Benjamin, Janez, Amir, Guillaume, and Maliheh. I have received numerous excellent suggestions regarding my academic career, research topics, presentations, projects, and even lifestyle. Matthieu (M. M.) taught me how to be an exemplary group member and cooperate with others through his always welcoming attitude and the many efforts and time he devoted to organizing various activities. Benjamin made a lasting impression on me with his clear, engaging, and inspiring talks, always showing me how to grasp the essence of complex backgrounds.

I extend my thanks to many LWEer for shorter research projects and visiting scholars, including Bingkun, Qiaolu, Zhechen, Robin, and Tinggui, for their helps and collaborations. My work with Qiaolu and Zhechen, in particular, showcased their brilliant and careful minds in addressing every question in both theory and experiments, contributing to the perfection of our projects. Not least, I want to thank Eva for making the lab feel like home, for helping many students, including me, to integrate smoothly into the lab environment, for protecting us from complex administrative tasks, and for assisting me with several challenging issues in my life.

The ELB0 corridor has been the source of many happy hours and celebrations. I am grateful to all its members for our "Launch time" and "Beer time": Maxime, Matthieu (M. P.), Xinxin, Stas, Behzad, Vincent, Qin, Hervé, Anja, Denys, Ismael, Martin, and many others.

I would like to thank many friends, including Jianqi, Chen, Zelin, Xiaoxin, Yifei, Yinghua, Xinyu, Yi, Shanci, Shiling, Kaiyue, Da, Darong, and many others. I would also like to extend my thanks to Prof. Shiwen Yang and Prof. Jin Pan for shaping my knowledge of electromagnetism regarding theory, computations, and engineering.

I am thankful to Benjamin, and Matthieu (M. M.) for proofreading the thesis manuscript. I have learned a lot from your revisions and suggestions!

Last, but certainly not least, I would like to thank my parents and young sister for everything they have done for me, as well as my wife's parents for all their support. Most especially, I am deeply grateful to my wife, Yuqi Song, for her continuous and unparalleled support and unconditional love. My world becomes colorful and meaningful because of you. This accomplishment is as much yours as it is mine.

*Lausanne, 1 May 2024* **Z. Z.**

# Abstract

Scattering network models play a crucial role in both photonics and condensed matter, where they are used to describe the transport of photons and electrons in arbitrary potential landscapes and guided wave circuits. Among the important physical phenomena occurring in 2D networks, topological transport has raised considerable interest as it enables back-scattering immune point-to-point routing along topological interfaces, which is an appealing new possibility in planar electronics and integrated photonics. This Ph.D. thesis unveils the unique topological phenomena occurring in such networks, focusing on the intricate interplay between their Floquet topology, the presence of disorder, and their unitary scattering at microscopic and macroscopic scales. Using theoretical, numerical, and experimental explorations, it uncovers: 1) the robustness of topological phases under various forms of disorder, 2) the physical distinctions between the two possible topologically non-trivial phases in networks, namely the anomalous Floquet insulator (AFI) and the Chern insulator (CI), and 3) a renormalization group method on unitary scattering systems to explain the microscopic origin of robust macroscopic chiral transport.

We start by categorizing the Floquet topological bands, identified in honeycomb lattice scattering networks with broken time-reversal symmetry (TRS), into three distinct phases: AFI, CI, and trivial phases. The evolution of topological features when tuning the degree of disorder is evaluated by various means, including scattering at external ports, band structures, eigenstates of closed networks, and topological invariants.

Based on theoretical and numerical modelling, we uncover the superior robustness of chiral edge transport in the AFI in the presence of strong distributed disorder, imparted either on the network phase-delay links, on its structure, or on the scattering properties of the nodes. This remarkable robustness, connected to the physics of anomalous Floquet Anderson insulators (AFAI), positions AFI as a promising platform for genuine unidirectional topological edge transports robust to disorder or on-purpose reconfiguration.

A significant proportion of the work is dedicated to experimental validations performed on photonic scattering networks at microwave frequencies, confirming the theoretical predictions. These experiments demonstrate the robust nature of topological edge states amid a wide array of disorder, showcasing the practical potential of AFI in real-world scenarios. Moreover, we introduce innovative methods for measuring topological invariants within finite disordered networks. A specific device is designed to implement twisted boundary conditions, enabling the direct observation and measurement of topological properties.

Finally, a unified framework is proposed to capture the topological properties of scattering networks even in the strong disordered regime: a real-space renormalization group (RG) theory, driven by block-scattering transformations of unitary systems, which, unlike traditional approaches, does not rely on the renormalization of Hamiltonians or wave functions. The resulting RG flows, RG phase diagrams, scaling analysis, and critical behavior studies, prove and explain why chiral topological edge states exist even under the strongest available disorder levels, providing useful guidelines for constructing robust topological photonic systems that never localize.

In conclusion, this work establishes bridges between different concepts in condensed matter physics and photonics, from topology to renormalization group, uncovering the unitary topological physics of scattering networks and the important role of disorder. We envision new opportunities for applications of these physical effects in reconfigurable electromagnetic systems for future communication technologies.

**Key words:**

- Scattering network
- Topological insulator
- Anomalous Floquet topology
- Disorder
- Topological robustness
- Renormalization group
- Localization
- Photonic and condensed matter systems

# Résumé

Les modèles de réseaux de diffusion jouent un rôle crucial tant en photonique qu'en matière condensée, où ils servent à décrire le transport de photons et d'électrons dans des paysages potentiels arbitraires et des circuits d'ondes guidées. Parmi les phénomènes physiques importants se produisant dans les réseaux 2D, le transport topologique a suscité un intérêt considérable car il permet un routage de point à point immunisé contre la rétro-diffusion le long des interfaces topologiques, ce qui représente une nouvelle possibilité séduisante en électronique planaire et en photonique intégrée. Cette thèse de doctorat dévoile les phénomènes topologiques uniques se produisant dans de tels réseaux, en se concentrant sur l'interaction complexe entre leur topologie de Floquet, la présence de désordre, et leur diffusion unitaire à des échelles microscopiques et macroscopiques. À travers des explorations théoriques, numériques et expérimentales, elle révèle : 1) la robustesse des phases topologiques sous diverses formes de désordre, 2) les distinctions physiques entre les deux phases topologiquement non triviales possibles dans les réseaux, à savoir l'isolant de Floquet anormal (AFI) et l'isolant de Chern (CI), et 3) une méthode de groupe de renormalisation sur les systèmes de diffusion unitaire pour expliquer l'origine microscopique du transport chiral macroscopique robuste.

Nous commençons par catégoriser les bandes topologiques de Floquet, identifiées dans les réseaux de diffusion en treillis de miel avec symétrie de renversement du temps (TRS) brisée, en trois phases distinctes : AFI, CI et phases triviales. L'évolution des caractéristiques topologiques lors du réglage du degré de désordre est évaluée par divers moyens, y compris la diffusion aux ports externes, les structures de bandes, les états propres des réseaux fermés et les invariants topologiques.

Sur la base de modélisation théorique et numérique, nous découvrons la robustesse supérieure du transport de bord chiral dans l'AFI en présence de désordre distribué fort, impartie soit sur les liens de retard de phase du réseau, sur sa structure, ou sur les propriétés de diffusion des nœuds. Cette robustesse remarquable, liée à la physique des isolants d'Anderson de Floquet anormaux (AFAI), positionne l'AFI comme une plateforme prometteuse pour des transports de bord topologiques unidirectionnels authentiques robustes au désordre ou à la reconfiguration à dessein.

Une proportion significative du travail est dédiée aux validations expérimentales effectuées sur des réseaux de diffusion photoniques à des fréquences micro-ondes, confirmant les prédictions théoriques. Ces expériences démontrent la nature robuste des états de bord topologiques au milieu d'un large éventail de désordres, mettant en évidence le potentiel pratique de l'AFI dans des scénarios réels. De plus, nous introduisons des méthodes innovantes pour mesurer les invariants topologiques au sein de réseaux désordonnés finis. Un dispositif spécifique est conçu pour mettre en œuvre des conditions aux limites tordues, permettant l'observation directe et la mesure des propriétés topologiques.

Enfin, un cadre unifié est proposé pour capturer les propriétés topologiques des réseaux de diffusion même dans le régime fortement désordonné : une théorie du groupe de renormalisation (RG) en espace réel, entraînée par des transformations de diffusion en blocs de systèmes unitaires, qui, contrairement aux approches traditionnelles, ne repose pas sur la renormalisation des Hamiltoniens ou des fonctions d'onde. Les flux RG résultants, les diagrammes de phase RG, l'analyse d'échelle et les études de comportement critique, prouvent et expliquent pourquoi les états de bord chiraux topologiques existent même sous les niveaux de désordre les plus forts disponibles, fournissant des lignes directrices utiles pour la construction de systèmes photoniques topologiques robustes qui ne se localisent jamais.

En conclusion, ce travail établit des ponts entre différents concepts en physique de la matière condensée et en photonique, de la topologie au groupe de renormalisation, en découvrant la physique topologique des réseaux de diffusion et le rôle important du désordre. Nous envisageons de nouvelles opportunités pour les applications de ces effets physiques dans des systèmes électromagnétiques reconfigurables pour les technologies de communication futures.

**Mots clefs :**

- Réseau de diffusion
- Isolant topologique
- Topologie de Floquet anormale
- Désordre
- Robustesse topologique
- Groupe de renormalisation
- Localisation
- Systèmes photoniques et de matière condensée

# Contents

**Acknowledgements** **i**

**Abstract (English/Français)** **iii**

**List of figures** **xi**

**List of tables** **xv**

**1 Introduction** **1**

- 1.1 Topological insulator and topological robustness against disorder . . . . . . . . 2
  - 1.1.1 Topology concept and topological insulator . . . . . . . . . . . . . . . . . 2
  - 1.1.2 Topological robustness against disorder . . . . . . . . . . . . . . . . . . . 5
- 1.2 The role of disorder in topological systems . . . . . . . . . . . . . . . . . . . . . 5
  - 1.2.1 Why should we care about disorder in topological systems? . . . . . . . . 5
  - 1.2.2 Models for describing disordered topological systems . . . . . . . . . . . 6
- 1.3 Floquet topological insulator . . . . . . . . . . . . . . . . . . . . . . . . . . . . 9
  - 1.3.1 Floquet analysis framework . . . . . . . . . . . . . . . . . . . . . . . . . . 10
  - 1.3.2 Floquet topological phases . . . . . . . . . . . . . . . . . . . . . . . . . . 12
  - 1.3.3 Anomalous Floquet topological phase and its platforms . . . . . . . . . . 14
  - 1.3.4 Disordered Floquet topological systems . . . . . . . . . . . . . . . . . . . 15
- 1.4 Floquet topological physics in network models . . . . . . . . . . . . . . . . . . . 16
- 1.5 Motivation and structure of the thesis . . . . . . . . . . . . . . . . . . . . . . . . 20

**2 Theory and analysis framework of disordered unitary scattering networks** **23**

- 2.1 Basics of scattering networks . . . . . . . . . . . . . . . . . . . . . . . . . . . . 25
  - 2.1.1 Honeycomb non-reciprocal network configuration and Floquet band structure . . . . . . . . . . . . . . . . . . . . . . . . . . . . . . . . . . . . 26
  - 2.1.2 Intrinsic symmetries in photonic systems . . . . . . . . . . . . . . . . . . 29
  - 2.1.3 Parameterization of scattering nodes . . . . . . . . . . . . . . . . . . . . . 31
  - 2.1.4 Disorder in scattering networks . . . . . . . . . . . . . . . . . . . . . . . . 36
  - 2.1.5 Mapping between three-port scattering networks with bidirectional phase links and scattering networks with oriented phase links . . . . . . . . . . 40
- 2.2 Momentum-space analysis for networks: Phase-delay band structures and topological invariants . . . . . . . . . . . . . . . . . . . . . . . . . . . . . . . . . . 42

2.2.1 Clean-limit case . . . . . . . . . . . . . . . . . . . . . . . . . . . . . . . . . . . 44
2.2.2 Disordered case . . . . . . . . . . . . . . . . . . . . . . . . . . . . . . . . . . . 47
2.3 Real space analysis of scattering networks: observables in finite networks . . . 50
2.3.1 Transport with external ports . . . . . . . . . . . . . . . . . . . . . . . . . . 50
2.3.2 Cavity without external ports . . . . . . . . . . . . . . . . . . . . . . . . . . 52
2.3.3 Mutually consistent observables in analysis . . . . . . . . . . . . . . . . . 53
2.4 Localization length calculations and scaling analysis . . . . . . . . . . . . . . . . 55
2.5 Topological scattering invariant in disordered scattering networks. . . . . . . . . 57
2.5.1 Topological invariants in disordered systems . . . . . . . . . . . . . . . . . 57
2.5.2 Topological scattering invariant . . . . . . . . . . . . . . . . . . . . . . . . . 58
2.5.3 Relation with Wigner- Smith operator . . . . . . . . . . . . . . . . . . . . . 60

**3 Topological scattering networks in honeycomb lattice 63**
3.1 Introduction . . . . . . . . . . . . . . . . . . . . . . . . . . . . . . . . . . . . . . . 64
3.2 Anomalous topological phase and topological phase diagram . . . . . . . . . . . 64
3.3 Transport distinctions in anomalous and Chern topological scattering networks 68
3.3.1 Transport distinctions of AFI and CI in the clean-limit network . . . . . . 68
3.3.2 Experimental realizations for AFI and CI . . . . . . . . . . . . . . . . . . . 69
3.3.3 Experimental setups . . . . . . . . . . . . . . . . . . . . . . . . . . . . . . . 72
3.3.4 Robust anomalous edge states against an abrupt phase-delay jump . . . 73
3.4 Conclusions . . . . . . . . . . . . . . . . . . . . . . . . . . . . . . . . . . . . . . . 78

**4 Superior robustness of anomalous topological transport 79**
4.1 Introduction . . . . . . . . . . . . . . . . . . . . . . . . . . . . . . . . . . . . . . . 80
4.2 Superior robustness of AFI against random phase-delay disorder . . . . . . . . . 80
4.3 Superior robustness of AFI against distributed disorder on scattering nodes . . 85
4.4 Experiments . . . . . . . . . . . . . . . . . . . . . . . . . . . . . . . . . . . . . . . 88
4.5 Robustness comparisons with other Chern phases . . . . . . . . . . . . . . . . . 91
4.6 Conclusion . . . . . . . . . . . . . . . . . . . . . . . . . . . . . . . . . . . . . . . . 94

**5 Anomalous topological waves in strongly amorphous scattering networks 95**
5.1 Introduction . . . . . . . . . . . . . . . . . . . . . . . . . . . . . . . . . . . . . . . 96
5.2 Amorphous non-reciprocal networks . . . . . . . . . . . . . . . . . . . . . . . . . 97
5.3 Exceptional resilience of anomalous edge states to strong amorphism . . . . . . 99
5.3.1 Transport comparison . . . . . . . . . . . . . . . . . . . . . . . . . . . . . . 99
5.3.2 Design of Chern network . . . . . . . . . . . . . . . . . . . . . . . . . . . . . 99
5.4 Amorphism-enhanced anomalous topological phase: AFAI . . . . . . . . . . . . 102
5.4.1 Transports through amorphous networks . . . . . . . . . . . . . . . . . . . 102
5.4.2 Spectra of closed amorphous networks . . . . . . . . . . . . . . . . . . . . 107
5.4.3 Supercell band structures of amorphous networks . . . . . . . . . . . . . 109
5.4.4 Topological scattering invariant for amorphous networks . . . . . . . . . 114
5.5 Measurement of topological scattering invariant in the strongly amorphous regime116
5.5.1 Measurement methods and bulk ports . . . . . . . . . . . . . . . . . . . . 116

5.5.2 Experimental realization of twisted boundary conditions . . . . . . . . . 116
5.5.3 Experimental observation of Anderson localization in trivial scattering networks induced by the strong amorphism . . . . . . . . . . . . . . . . . 119
5.5.4 Direct measurement of topological indices for anomalous topological networks in the strongly amorphous regime. . . . . . . . . . . . . . . . . . 119
5.6 Conclusion . . . . . . . . . . . . . . . . . . . . . . . . . . . . . . . . . . . . . . . 123

**6 Real-space renormalization group scheme 125**
6.1 Introduction of renormalization group . . . . . . . . . . . . . . . . . . . . . . . 126
6.2 Two examples of disordered scattering networks: from microscopic to macroscopic scale . . . . . . . . . . . . . . . . . . . . . . . . . . . . . . . . . . . 129
6.3 RG on scattering networks with phase-link disorder . . . . . . . . . . . . . . . . 132
6.3.1 Iterative block-scattering transformations . . . . . . . . . . . . . . . . . . 132
6.3.2 Replica scheme . . . . . . . . . . . . . . . . . . . . . . . . . . . . . . . . . 135
6.3.3 Results for random phase-link disorder . . . . . . . . . . . . . . . . . . . . 137
6.4 Scaling analysis of the localization length . . . . . . . . . . . . . . . . . . . . . 141
6.4.1 Localization length and critical exponents . . . . . . . . . . . . . . . . . . 142
6.4.2 Topological phase diagrams comparisons and two critical exponent values 144
6.5 Experiments . . . . . . . . . . . . . . . . . . . . . . . . . . . . . . . . . . . . . . 146
6.6 RG on scattering networks with structural disorder . . . . . . . . . . . . . . . . 147
6.7 Conclusion . . . . . . . . . . . . . . . . . . . . . . . . . . . . . . . . . . . . . . . 148

**7 Conclusion and outlook 151**
7.1 Conclusions . . . . . . . . . . . . . . . . . . . . . . . . . . . . . . . . . . . . . . 151
7.1.1 Theoretical contributions . . . . . . . . . . . . . . . . . . . . . . . . . . . . 152
7.1.2 Experimental realizations and implications . . . . . . . . . . . . . . . . . 152
7.2 Future directions . . . . . . . . . . . . . . . . . . . . . . . . . . . . . . . . . . . . 153
7.2.1 Applications: robust and versatile topological photonic manipulations . 153
7.2.2 Further explorations on network models . . . . . . . . . . . . . . . . . . . 155
7.2.3 Disorder effects on topological phases for non-interaction electron and time-driven systems . . . . . . . . . . . . . . . . . . . . . . . . . . . . . . 155
7.2.4 Potentials for scattering RG theory . . . . . . . . . . . . . . . . . . . . . . 156
7.3 Conclusion . . . . . . . . . . . . . . . . . . . . . . . . . . . . . . . . . . . . . . . 156

**A Density of states and skin distance definitions 159**

**B Distinction between frequency and phase-delay (Floquet) band structures 161**

**C Unitarity of $S_{probe}$ upon invertible $C_{net} - S_{net}$ 165**

**D Recovery of one $S' \in U(3)$ from 3 by 3 non-negative matrix $E_S$ 167**

**Bibliography 196**

**Curriculum Vitae 197**

# List of Figures

1.1 Topology concept and topological insulators . . . . . . . . . . . . . . . . . . . . . . 3
1.2 Interplay of disorder and topological systems. . . . . . . . . . . . . . . . . . . . . . 7
1.3 Topological phases in Floquet systems . . . . . . . . . . . . . . . . . . . . . . . . . 12
1.4 Mapping between discrete-time dependent tight-binding (TB) models and scattering networks. . . . . . . . . . . . . . . . . . . . . . . . . . . . . . . . . . . . . 17

2.1 Topological non-reciprocal wave network in honeycomb lattice. . . . . . . . . . 26
2.2 Photonic honeycomb network and associated signal labelling convention in the unit cell. . . . . . . . . . . . . . . . . . . . . . . . . . . . . . . . . . . . . . . . . 27
2.3 Scattering properties of $S_0$ in $(\xi,\eta)$ parameter space. . . . . . . . . . . . . . . . . 35
2.4 Disordered scattering networks, from the microscopic to the macroscopic scale. 37
2.5 Amorphous scattering networks generated from a weighted Voronoi tessellation. 39
2.6 Three amorphous stages revealed by the evolution of network statistics with $\alpha$ . 40
2.7 Mapping between a non-reciprocal scattering network in honeycomb lattice and an oriented Eulerian graph in Kagome lattice. . . . . . . . . . . . . . . . . . 41
2.8 Implementation of an oriented Eulerian graph as a non-reciprocal 3-port circulators network. . . . . . . . . . . . . . . . . . . . . . . . . . . . . . . . . . . . . . . 43
2.9 Systematic mapping between non-reciprocal networks and oriented Eulerian graphs. . . . . . . . . . . . . . . . . . . . . . . . . . . . . . . . . . . . . . . . . . . 43
2.10 Examples of bulk and ribbon band structures in the periodic honeycomb networks 45
2.11 Ribbon band structures colored with eigenstate positions. . . . . . . . . . . . . . 46
2.12 Twisted boundary condition in scattering networks. . . . . . . . . . . . . . . . . 48
2.13 Connections between momentum-space observables and real-space observables. 54
2.14 Topological phase transitions by scaling analysis of the localization length. . . . 57
2.15 Topological invariant in scattering networks. . . . . . . . . . . . . . . . . . . . . . 61

3.1 Gap closing and reopening in phase-delay band structure at $|R| = 1/3$. . . . . . . 65
3.2 Anomalous and Chern topological phases in non-reciprocal scattering networks. 66
3.3 Phase-delay band structures at two special points of the topological phase diagram. 67
3.4 Band gap map of the network . . . . . . . . . . . . . . . . . . . . . . . . . . . . . 68
3.5 Finite honeycomb scattering network with circulators $S_0(\xi,\eta)$ with three external ports. . . . . . . . . . . . . . . . . . . . . . . . . . . . . . . . . . . . . . . . . . . 69

3.6 Comparison between boundary-port transport properties and the ribbon band structures of anomalous and Chern phases. . . . . . . . . . . . . . . . . . . . . . 70
3.7 Experimental validation of the model assumptions. . . . . . . . . . . . . . . . . . 71
3.8 Experimental setups for scattering parameter and field distribution measurements. 73
3.9 Robustness of anomalous non-reciprocal topological edge transmission against abrupt phase-delay jump. . . . . . . . . . . . . . . . . . . . . . . . . . . . . . . . . 74
3.10 Numerical and experimental field maps for excitation at port 2. . . . . . . . . . 75
3.11 Numerical and experimental field maps for excitation at port 3. . . . . . . . . . 76
3.12 Experimental network design and measured scattering parameters in bands of Chern and anomalous phases. . . . . . . . . . . . . . . . . . . . . . . . . . . . . 77

4.1 Superior robustness of anomalous non-reciprocal topological edge transmission against phase-delay disorder. . . . . . . . . . . . . . . . . . . . . . . . . . . . . 81
4.2 Field maps anomalous and Chern edge mode transmissions at several phase-delay disorder levels. . . . . . . . . . . . . . . . . . . . . . . . . . . . . . . . . 82
4.3 Superior robustness of anomalous edge transport regardless of the center of disordered $\varphi$ . . . . . . . . . . . . . . . . . . . . . . . . . . . . . . . . . . . . 83
4.4 Average transmission in the fully disordered phase-link case for all possible networks in the parameter space. . . . . . . . . . . . . . . . . . . . . . . . . . 84
4.5 Effect of scattering matrix disorder on the Chern edge mode transmission. . . . 86
4.6 Effect of scattering matrix disorder on the anomalous edge mode transmission. 87
4.7 Superior robustness of the AFI phase to scattering disorder. . . . . . . . . . . . 88
4.8 Experiments on irregularly shaped and disordered networks. . . . . . . . . . . 88
4.9 Experimental validation of anomalous phase disorder robustness in four other prototypes with distinct disorder realizations. . . . . . . . . . . . . . . . . . . . 90
4.10 Measured transports averaged over five prototypes in anomalous and Chern frequency bands. . . . . . . . . . . . . . . . . . . . . . . . . . . . . . . . . . . 90
4.11 Effect of the number of trivial band gaps (noted $M$) on the robustness of the edge mode transmission to phase link disorder. . . . . . . . . . . . . . . . . . . 92
4.12 Effect of the number of Chern edge modes on the transmission robustness. . . 93

5.1 Anomalous edge states can survive any level of amorphism. . . . . . . . . . . . 98
5.2 Exceptional resilience of anomalous edge states to strong amorphism. . . . . . 100
5.3 Design of a Chern network by adding reciprocal scatterers in the middle of the phase delay lines of an anomalous network. . . . . . . . . . . . . . . . . . . . . 101
5.4 Amorphism-enhanced edge transmission and bulk insulation of the anomalous phase. . . . . . . . . . . . . . . . . . . . . . . . . . . . . . . . . . . . . . . . . 104
5.5 Chern networks become trivial when networks are strongly amorphous. . . . . 105
5.6 Trivial insulating networks under amorphism. . . . . . . . . . . . . . . . . . . . 106
5.7 Amorphism localizes the states and populates them in the entire phase delay spectrum. . . . . . . . . . . . . . . . . . . . . . . . . . . . . . . . . . . . . . . 107
5.8 Unique transition in anomalous networks driven by strong amorphism. . . . . 108
5.9 Strong amorphism creates new edge states in anomalous networks. . . . . . . . 109

5.10 Band structures of networks in clean limit and in fully amorphous regime in the cylinder geometry. . . . . . . . . . . . . . . . . . . . . . . . . . . . . . . . . . . . . . . . 111
5.11 Strong amorphism enhanced anomalous topology: AFAI. . . . . . . . . . . . . . 112
5.12 Trivialization and localization in Chern networks induced by a strong amorphous disorder. . . . . . . . . . . . . . . . . . . . . . . . . . . . . . . . . . . . . . . . . . 113
5.13 Localization in trivial networks in the fully amorphous regime. . . . . . . . . . . 114
5.14 Emergence of anomalous Floquet Anderson insulating phase (AFAI) in anomalous scattering networks when inducing strong amorphism. . . . . . . . . . . . 115
5.15 Measurement method and bulk port design. . . . . . . . . . . . . . . . . . . . . . 117
5.16 Design and measurement of our reconfigurable non-reciprocal phase shifter (twisted boundary condition). . . . . . . . . . . . . . . . . . . . . . . . . . . . 118
5.17 Measured field maps of trivial networks. . . . . . . . . . . . . . . . . . . . . . . . 119
5.18 Direct measurement of topological indices in the strongly amorphous regime. . 120
5.19 Experimental validation of the chiral edge state in the amorphous anomalous network. . . . . . . . . . . . . . . . . . . . . . . . . . . . . . . . . . . . . . . . . . 121
5.20 Measured topological invariant in the operating band for honeycomb and fully amorphous networks. . . . . . . . . . . . . . . . . . . . . . . . . . . . . . . . . 122

6.1 Block scattering transformations for a renormalization group of unitary scattering networks. . . . . . . . . . . . . . . . . . . . . . . . . . . . . . . . . . . . . . . 127
6.2 Trivial and topological systems and their scattering attractors. . . . . . . . . . . 128
6.3 Examples leading to trivial and topological macroscopic properties, under phase-link disorder and structural disorder (amorphism). . . . . . . . . . . . . . . . . 130
6.4 Topological phases and observables. . . . . . . . . . . . . . . . . . . . . . . . . . . 131
6.5 Renormalization group of a unitary scattering network with phase-link disorder. 132
6.6 Numerical RG scheme of disordered scattering networks. . . . . . . . . . . . . 136
6.7 Two examples of RG on scattering networks with random phase-link disorder. . 138
6.8 RG phase diagram. . . . . . . . . . . . . . . . . . . . . . . . . . . . . . . . . . . . . 139
6.9 RG flow diagram. . . . . . . . . . . . . . . . . . . . . . . . . . . . . . . . . . . . . . 140
6.10 Critical scattering properties. . . . . . . . . . . . . . . . . . . . . . . . . . . . . . . 141
6.11 Topological phase transitions and critical behaviors by a scaling analysis of the localization length. . . . . . . . . . . . . . . . . . . . . . . . . . . . . . . . . . . . 143
6.12 Scaling of $\Lambda(L_y)$ under y-periodic boundary conditions in the vicinity of the critical point $\xi_c \approx 0.93$ on the line of $\xi = -\eta$. . . . . . . . . . . . . . . . . . . . . . 144
6.13 Comparisons of the topological phase diagrams and critical behaviors obtained from RG and LL analysis. . . . . . . . . . . . . . . . . . . . . . . . . . . . . . . . 145
6.14 Scaling analysis in the vicinity of another type critical point: $\xi_c \approx 0.0947$ on the line of $\xi = -\eta$. . . . . . . . . . . . . . . . . . . . . . . . . . . . . . . . . . . . . 146
6.15 Experimental validation of renormalization group flow. . . . . . . . . . . . . . 147
6.16 Renormalization group of a unitary scattering network with structural disorder. 148
6.17 RG topological phase diagram and flow diagram for networks under the strongest structural disorder. . . . . . . . . . . . . . . . . . . . . . . . . . . . . . . . . 149

7.1 Wave routing with superior topological protection. . . . . . . . . . . . . . . . . . . 153
7.2 Topological filters and multiplexers. . . . . . . . . . . . . . . . . . . . . . . . . . . . . 154

A.1 Definition of the skin distance. . . . . . . . . . . . . . . . . . . . . . . . . . . . . . . . . 160

B.1 Frequency band structures of our networks in the clean limit. . . . . . . . . . . . . 162
B.2 Field maps of wave transmissions in the clean limit ($\alpha = 0$) and fully amorphous regime ($\alpha = 8$) for $|R| = 0.24$ and $|R| = 0.51$ at $f = f_0$. . . . . . . . . . . . . . . . . . . 163
B.3 Phase-delay spectra for $|R| = 0.24$ and $|R| = 0.51$ at $f = f_0$. . . . . . . . . . . . . . . . 164

# List of Tables

2.1 Symmetries of the five examples of Eq. (2.6). . . . . . . . . . . . . . . . . . . . . . . 29
2.2 Symmetries in photonic systems described by Hamiltonians in Eq. (2.8). . . . . . 30

# 1 Introduction

Exploring new phases of matter occupies a prominent place in modern physics. Traditional paradigms have extensively categorized these phases through the lens of symmetry breaking, a concept that underlies the structural and magnetic ordering observed in materials such as crystals and magnets. Quintessential examples include translational symmetry breaking, observed in the crystallization of water into ice, and rotational symmetry breaking, manifested in the magnetic ordering of spins. These examples provide foundational insights into the emergence of matter from the collective interactions among constituents—ions, magnetic moments, or electrons. However, the observation of the Berezinskii-Kosterlitz–Thouless phase transition [1] marked a decisive turning point in our understanding of matter, as we discovered another type of phase transition, which is completely free of any symmetry breaking. This discovery led to the climax of topological matter, beyond the symmetry-breaking paradigm, propelled by the integer [2] and fractional quantum Hall effects [3] found in the 1980s: a two-dimensional electron gas, subject to an external static perpendicular magnetic field, causes the electrons to circulate in quantized orbits. In the quantum Hall effect, the electron is prohibited from moving in the bulk but circulates along its edge in a single direction that depends on the orientation of the external magnetic field. One of the most important breakthroughs in the past decades is that similar topological phases can be found in crystals, systems that remain invariant under spatially discrete translations. Band theory is conventionally applied to classify crystals into insulators, semi-metals, or metals. These systems have been named topological insulators, as they are insulators in the bulk but exhibit unavoidable metallic states at their boundaries, which is a consequence of the non-trivial topology of their eigenstate structure in momentum space [4–7].

In this chapter, we begin by introducing the concepts of topological insulators and the Chern number in Sec. 1.1, highlighting the robustness of topological edge states against impurities or defects. We stress on the particular reliability of the Chern insulating phase, as its existence does not require any prerequisite on system symmetries. Next, Sec. 1.2 delves into the impact of distributed disorder on topological systems and presents physical models for disordered topological systems, concluding with the reason why this thesis focuses on scattering networks.

In Sec. 1.3, starting from the state-of-the-art, we outline the basis of time-Floquet systems and define the various Floquet topological phases, including the anomalous Floquet insulator (AFI), which has no counterpart in Hamiltonian (Hermitian) topology, and only exist in Unitary topology. We also introduce a recently-found topological phase occurring in disordered Floquet systems- the anomalous Floquet Anderson insulating phase (AFAI). Sec. 1.4 establishes a connection between scattering networks, which are static, and time-Floquet systems, which are periodically-driven, demonstrating their potential as platforms for exploring further the physical differences between the various topological phases, and the effects of distributed disorder. Throughout these discussions, we weave in the motivations driving the research presented in this thesis. We consolidate these motivations in Sec. 1.5, which outlines the structure of the thesis and overarching questions. We use a third person narrative style, which is more inclusive for the reader, however all results correspond to the individual work of the author.

## 1.1 Topological insulator and topological robustness against disorder

### 1.1.1 Topology concept and topological insulator

When we think of two objects with distinct topology, the differences in the geometries of the objects come first in mind, e.g. a rubber band and a Möbius strip as depicted in Fig. 1.1. Generally speaking, the concept of topology is based on a branch of mathematics focused on properties of objects that remain unchanged under smooth transformations, quantitatively described by discrete values known as topological invariants. In our examples, for instance, we cannot continuously deform a rubber band into a Möbius strip unless we cut the band at one point (which is no longer a smooth transformation) and twist one side by 180 degrees before gluing the two sides of the cut back together. One way to quantitatively describe this non-continuous transformation is to rotate a vector around the band and strip. For the rubber band (Fig. 1.1a), if one rotates a vector by 360 degrees around the band following the dashed white line, the vector ends up with its original orientation, as opposed to the case of the Möbius strip, in which one observes a 180-degree angle difference. The number of half turns accumulated during this process can therefore serve as a topological invariant to distinguish two topologically distinct ribbons. Once an observable is written as a topological invariant, it only changes discretely, and only through discontinuous transformations. If we deform the rubber band without cutting it, we cannot change this invariant.

Similarly, in a topological insulator, the topology emerges from the quantized collective behaviour of eigenstates defined on dispersion bands in reciprocal (momentum) space [I]. Traditionally, band theory merely focuses on the energy spectrum with eigenstates ignored. Following the seminal work on quantum Hall conductance in periodic potentials described

---

[I] In topological insulators, eigenstates and dispersion bands replace vectors and bases (rubber band and Möbius strip) in the examples of panel a and b, respectively.

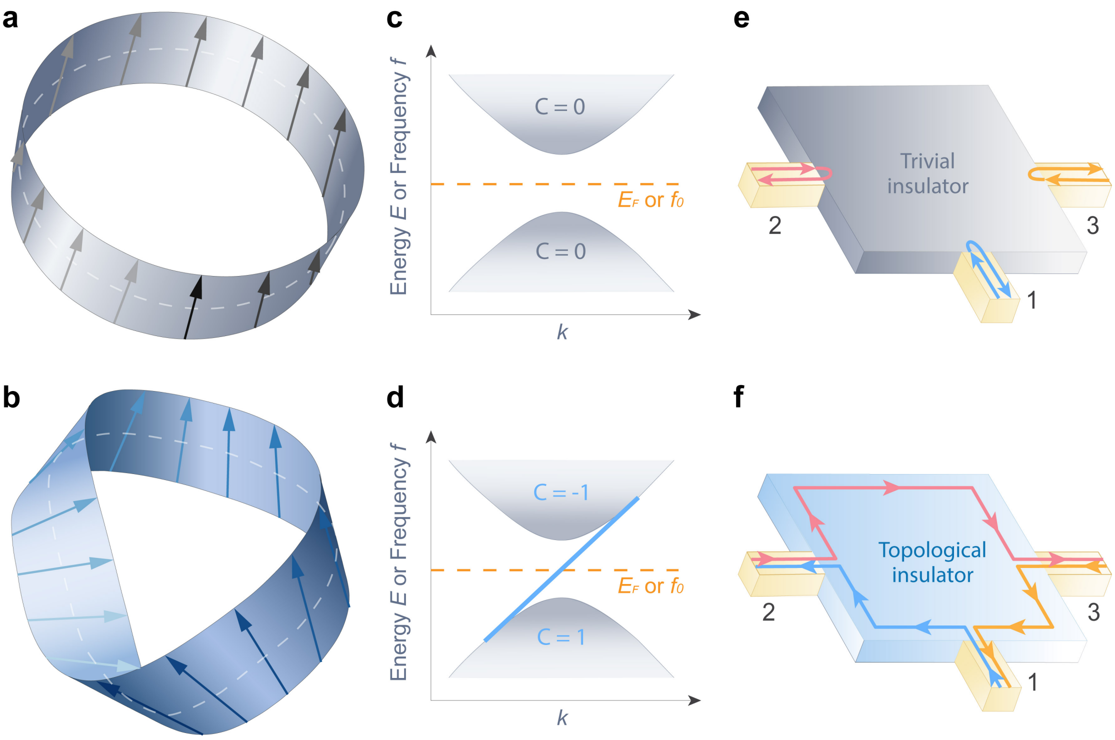

Figure 1.1: **Topology concept and topological insulators**. **a,** In the rubber band example: if we rotate a vector around the rubber band, it returns to its original direction. The gray color gradient in the figure shows the movement path. **b,** Möbius strip example: when a vector rotates 360 degrees along a Möbius strip, it surprisingly points in the opposite direction upon completing the loop. This unique behavior of the vector encircling the Möbius strip illustrates its non-trivial topology, distinguishing it from a rubber band, which cannot be transformed into a Möbius strip without cutting and rejoining. **c, d,** Trivial (c) and non-trivial (d) topological band structures. Similarly, band structures reveal topological concepts defined by Chern numbers, which remain invariant unless altered by a topological phase transition involving the closing and reopening of the band gap. **e, f,** A non-vanishing Chern number signifies a band's non-trivial topology, causing conducting states within the band gap ($E_F$ or $f_0$) that circulate unidirectionally along the edge, as shown in panel (f). Conversely, a trivial topology, indicated by a Chern number of zero, results in complete insulation within the band gap, as depicted in panel (e). Such effect is measurable and robust due to the nature of topology.

by Thouless, Kohmoto, Nightingale, and Nijs (TKNN) [8], the well-known quantized Hall conductance can be determined by topological invariants of bands. The topological invariant of an isolated band, namely Chern number $C$, is defined over the Brillouin zone (BZ), a base space which is a torus of the momentum. Chern number can be expressed as

$$C = -\frac{1}{2\pi}\int_{BZ} F(\mathbf{k})\,d\mathbf{k} = -\frac{1}{2\pi}\int_{BZ} \nabla\times A(\mathbf{k})\,d\mathbf{k} = -\frac{i}{2\pi}\int_{BZ} d\mathbf{k}\left[\partial_{k_x}\langle\psi|\partial_{k_y}|\psi\rangle - \partial_{k_y}\langle\psi|\partial_{k_x}|\psi\rangle\right], \quad (1.1)$$

where $F(\mathbf{k})$ is the Berry curvature, defined by Berry connection $A(\mathbf{k})$ as $F(\mathbf{k}) = \nabla\times A(\mathbf{k})$. $|\psi\rangle$ is the Bloch state on the band. The odd symmetry of $A(\mathbf{k})$ in relation to the time reversal operator indicates that Chern numbers vanish in time reversal symmetric (TRS) systems. However, static magnetic fields can break TRS and induce non-zero Chern numbers of bands [8–10].

Moreover, the "cut and glue" operation on the rubber band discussed previously is now replaced in the topological insulator case, by the closing and reopening of band gaps, in line with the topological band theory. Figs. 1.1 (c, d) aim to illustrate the difference between a trivial (zero Chern number) and a non-trivial (non-zero Chern number) topological insulators respectively. The systems with non-trivial topological bands are therefore in the Chern insulating phase. The closing and reopening of the band gap trigger a topological phase transition between trivial and Chern insulating phases, characterized by a change in Chern numbers. Although the concept of Chern number is not intuitively obvious, this number just counts algebraically the number of chiral edge states that enter or leave a given bulk band. Non-trivial Chern numbers typically lead to the existence of gapless chiral edge states in the band gap, whose number depend on the difference of the Chern numbers of the surrounding bands, a property known as the bulk-edge correspondence. These remarkable gapless states exhibit a topological edge current that circulates unidirectionally around the system, exemplified by the famous quantum Hall current [9, 11], which is measurable in experiments (Fig. 1.1 (f)).

Although topologically non-trivial bands were first discovered in electronic systems, topological band theory fundamentally relies on the geometric phase effects of eigenstates within the compact base space (Brillouin torus), but not on the system's spatial scale or physical nature. This crucial point was first highlighted by the seminal work of Haldane [10] and Raghu [12], who demonstrated that photonic Chern insulators could be realized with electromagnetic waves in spatially periodic structures with a broken TRS obtained from magnetically biased magneto-optical elements. This then sparked explorations of topological phases in classical platforms using a wide variety of waves, including photonic [6, 7, 13–22], phononic [23–26], water wave [27], and even in geophysical and astrophysical waves [28, 29].

Topological phases are nevertheless not restricted to systems with broken time-reversal symmetry. Recently, topological phases were shown in systems with intrinsic symmetries (time reversal, chiral, and particle-hole symmetries) or spatial symmetries (for example, rotational and reflection symmetry), as indicated by the tenfold classifications [30–32] and the periodic tables of topological crystalline insulators [33–35]. These extensions of topological band theories have simultaneously stimulated the study of their photonic and phononic analogues [14, 36, 37]. Note that the tenfold classification assumes a system described by a Hermitian eigenproblem. Other systems, for example the ones based on Unitary eigenproblems used in this thesis, possess their own classification table [38–40]. In particular, because the space of unitary operators is not simply connected, they exhibit additional topological phases, including the anomalous Floquet insulator mentioned throughout this thesis, which is distinct from a Chern insulator, although it leads to similar chiral edge states. We will come back to this in details in the following sections.

### 1.1.2 Topological robustness against disorder

One of the most distinguishing features of 2D topological insulators is the presence of edge states, guaranteed even if the system is subject to disorder and defects, as long as the bulk invariant does not change. This is a consequence of the resilience of the invariant against continuous deformations of the system. These topological protected edge states lead to quantized currents in electronic systems [8, 9, 11, 41], enabling the high accuracy determination of physical constants [2], and also promise robust photonic and phononic wave manipulations against fabrication flaws or imperfections [6, 7]. Compared to their electronic counterparts, classical topological systems offer considerable freedom for practical control of spatial and temporal properties, thanks to recent advances in microwave, optical and acoustic components and devices. As a result, they represent a particularly relevant platform for detecting and harnessing topological effects that are difficult to implement in condensed matter systems.

Among all topological phases, Chern insulators in A class are to date the most reliable designs [10, 12, 13, 17–22, 36, 42–48], as no intrinsic nor spatial symmetries are prerequisites. As a by-product of time-reversal symmetry breaking, their edge states are unidirectional, and break reciprocity. They are called chiral edge states, a concept that should not be mixed with the one of chiral media in continuous electrodynamics [49], which is a class of reciprocal magneto-electric media that unfortunately bears the same name. Chiral edge states provide waveguides with genuine backscattering immunity to obstacles placed on the edge [50, 51]. They are attractive due to their compact planar geometries compatible with the fabrication technologies used in modern electronics and photonics. They were reported in non-reciprocal artificial wave media, such as externally-biased magneto-photonic crystals [17–22, 48, 52] or mechanical systems [51, 53] with moving media or time-varying elements [23, 36, 43, 44]. Although protected from *local* disorder and defects by their non-trivial topology, Chern edge modes cannot withstand *distributed* bulk disorder of sufficiently strong magnitude, especially when the average fluctuation amplitude is greater than the band gap size. This behaviour inherently limits the topological protection of Chern phases to small distributed disorder levels. Better understanding this limitation is ***the first motivation*** for this thesis.

As we wish to study topological edge states in disordered scattering networks, we will now examine the state-of-the art in understanding the role of disorder in topological insulators, and how networks emerge as a cornerstone model for quantitatively describing disorder effects.

## 1.2 The role of disorder in topological systems

### 1.2.1 Why should we care about disorder in topological systems?

The interplay between disorder and topological systems is complex and challenging to analyze, yet it remains a fascinating and widespread topic. On the one hand, disorder typically disrupts spatial translational symmetry, rendering topological band theories ineffective due to the absence of a well-defined momentum space. As a result, in disordered systems, it becomes necessary to carefully redefine topological invariants and observables to accurately identify topological edge states. On the other hand, compared to crystalline systems, disordered systems offer a more general framework and are inevitable in experiments and practical applications. The concept of topology is not fundamentally limited to systems with spatial translation symmetry, as suggested by the first observations of the quantum Hall effect in disordered samples [54], and theoretical predictions in non-commutative geometry [55–57]. Disorder gives birth to tremendous counter-intuitive phenomena, including Anderson localization [58, 59] and unity transport through highly turbid media [60, 61]. A notable example of the interplay between disorder and topological systems is the emergence of the topological Anderson insulator, where moderate disorder turns a topologically trivial system into a topologically non-trivial phase, although stronger disorder eventually leads to the trivialization of the system [62–66]. Consequently, a thorough understanding of the role of disorder in topological systems is crucial to address three key aspects of topological physics. These aspects raise challenging questions that have rarely been explored in depth:

1. Topological robustness: How robust are topological systems, when subject to distributed disorder? How do they react to different kinds of disorder, and to what level of perturbations can we still define and use topological effects?
2. Interplay with disorder: How does microscopic disorder affect macroscopic observables, e.g. topological edge states and edge transport?
3. Harnessing disorder: Can we utilize disorder to sustain, induce, or perhaps enhance topological effects?

These considerations lead to ***the second motivation*** of this thesis.

### 1.2.2 Models for describing disordered topological systems

Interest in the effects of disorder on topological systems dates back to the early studies of the quantum Hall effect on the theory of plateau transitions. The plateaus of the applied static magnetic field, which exhibit quantized Hall conductance attributed to topological chiral transports, can be stabilized due to the presence of disorder [8, 11, 67–69], as illustrated by chiral edge states (blue lines) in Fig. 1.2a. In the absence of disorder, one expects the reappearance of classical Hall conductance in pristine samples, as bulk transports overwhelm the contributions of topological chiral edge transport. At a moderate level of disorder, the topological edge states persist, which are responsible for transverse conductance $G_{xy} = \nu G_0$ ($G_0 = \frac{e^2}{h}$) with $e$ the electron charge and $h$ Planck's constant, whereas the longitudinal conductance $G_{xx}$ disappears because disorder induces localization in bulk transports. The localization of bulk transport makes the topological edge states obvious in the conductance and eventually leads to quantized plateaus. However, at sufficiently high levels of disorder, the quantum Hall sample undergoes Anderson localization, shown in Fig. 1.2b. This Anderson transition, induced by strong disorder, occurs in Chern insulators within both photonic and phononic

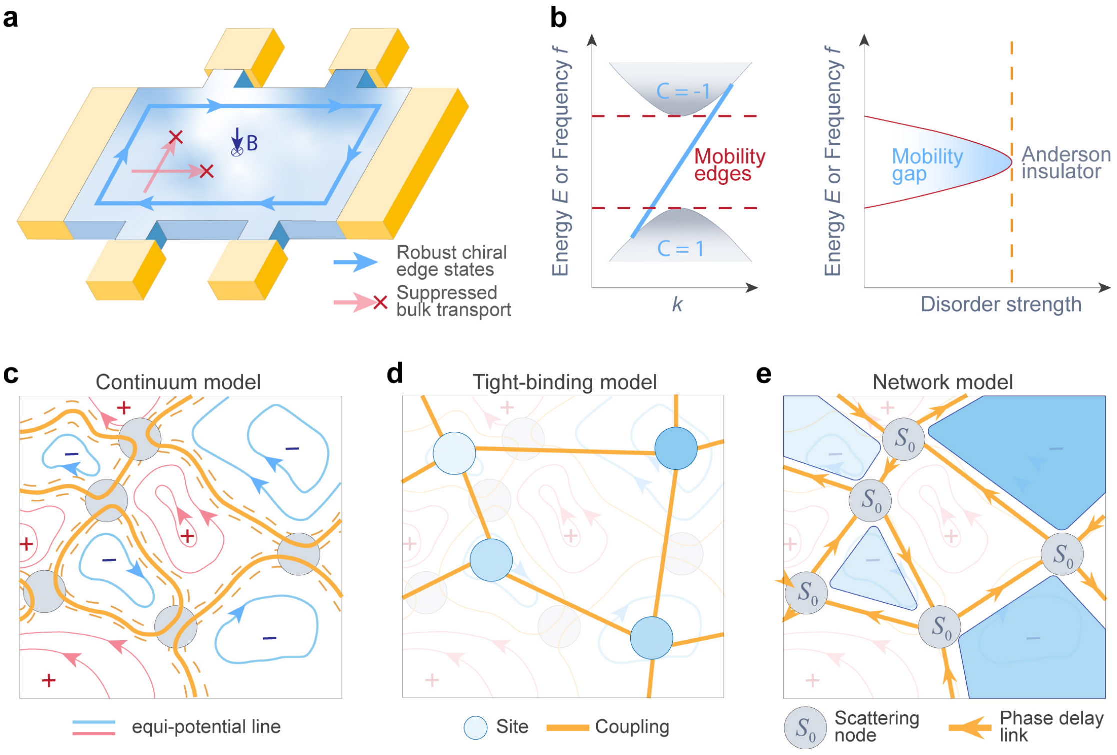
a
B
Robust chiral edge states
Suppressed bulk transport
b
Energy $E$ or Frequency $f$
C = -1
Mobility edges
C = 1
$k$
Energy $E$ or Frequency $f$
Mobility gap
Anderson insulator
Disorder strength
c
Continuum model
+
−
equi-potential line
d
Tight-binding model
Site
Coupling
e
Network model
$S_0$
Scattering node
Phase delay link

Figure 1.2: **Interplay of disorder and topological systems. a,** Quantum Hall sample under disorder. Disorder plays a crucial role in stabilizing the plateaus of quantized Hall conductance. It suppresses the bulk transports (pink lines) but keeps topological chiral edge states (blue lines), therefore broadening the Landau levels into wider bands and localizes the bulk eigenstates at the bands' boundaries. **b,** Anderson transition of Chern insulators in the strong disorder. Disorder leads to the formation of mobility bands and gaps. They are separated by mobility edges (red dashed lines). When increasing disorder strength, the mobility edges approach each other. At a critical threshold, the mobility gap closes, transitioning the system into an Anderson localized state. **c- e**, Various models for describing disorder in topological systems: continuum model (c), tight-binding model (d), and network model (e).

systems. Specifically, disorder turns the definitions of band and band gap in the clean limit into the concepts of mobility bands and gaps[II] [70]. The transition points between mobility bands and gaps are known as mobility edges (Fig. 1.2b). As the strength of disorder increases, topological edge states are eliminated when the mobility gap closes, a process which is called pair levitation and annihilation [67, 71]. In this process, the extended states with opposite Chern numbers move to each other and finally annihilate, leaving behind a fully localized system characterized by completely flat bands and trivial gaps.

Several models have been developed to quantitatively model disorder in topological systems. Among others, the continuum model, tight-binding model, and network model are the most

---

[II] In disordered systems, non-localized states form mobility bands, and a mobility edge is defined as the energy/frequency separating localized and non-localized states in the conduction or valence bands.

commonly used and are illustrated on quantum Hall systems in Figs. 1.2(c-e) as examples. The continuum description of disorder in Fig. 1.2c, which is the starting point for analytical analysis, lies on the disordered potential [72–76]. The continuum model characterizes non-interacting two-dimensional (2D) Dirac fermions in a static magnetic field, navigating through a disordered potential $V(\boldsymbol{r})$ within the system. Dynamics of these fermions are governed by Schrödinger equation which reads

$$H|\psi\rangle = [H_0 + V(\boldsymbol{r})]|\psi\rangle = E|\psi\rangle, \tag{1.2}$$

where $H_0$ is the clean-limit Hamiltonian (the Landau model) formulated as

$$H_0 := \frac{1}{2m}\Big(\frac{h}{\mathrm{i}}\nabla + e\mathbf{A}\Big)^2. \tag{1.3}$$

Here, $A$ is the vector potential, with $B = \nabla \times A$ representing the magnetic field. The electron trajectory is dictated by the random potential's contour, navigating along equipotential lines identified at the Fermi energy $E_F$, illustrated as yellow lines. At crossings of equi-potential lines (saddle points), quantum tunneling can happen.

Yet, although the continuum model provides a detailed description of disordered systems, analytically solving the Schrödinger equations with disordered potentials is rarely feasible [77, 78], especially for the analysis of critical properties at phase transitions. The tight-binding (TB) model was thus introduced [79] to obtain a computable theory of phase transitions and to identify topological phases in the integer quantum Hall effect, by featuring electron hopping between discrete sites as shown in Fig. 1.2d. Sites can trap electrons and are located at the minima of the potential function, while the hopping term is extracted from the tunnelling strength at the saddle points of the potential. TB Hamiltonian can then be expressed as

$$H = -\sum_{\langle ij\rangle}(tc_i^\dagger c_j + \text{h.c.}) + \sum_i \epsilon_i c_i^\dagger c_i, \tag{1.4}$$

where $\epsilon_i$ is the onsite energy and $t$ is the hopping term between nearest neighbor sites. The static magnetic field induces a complex phase in the hopping terms through Peierls substitution. Consequently, the TB model manifests disorder through variations in onsite energies, hopping terms, or spatial structure, encapsulating different facets of disorder within the system [63, 65, 80–83].

Finally, network models, pioneered by Chalker and Coddington [84], represent a crucial framework for analyzing phase transitions in systems with disorder. The Chalker-Coddington (CC) network model assumes the disorder potential to be smooth at the scale of the magnetic length. As a result, the electron's motion can be treated within the semi-classical approximation [85]. The saddle points of the potential is transformed into scattering nodes, whose scattering process is described by a unitary scattering matrix $S_0$. The parameterization of $S_0$ depends on the unitary matrix group governed by the system's symmetries [III]. Scattering nodes within this

---

[III] One can simply classify them by time-reversal symmetry, unitarity, and reciprocity, see details in Sec. 2.1.2.

model are interconnected by phase-delay links, illustrating how electrons drift along equipotential lines of disordered potentials, thereby acquiring a random phase. The random phase originates from the randomness of the length of the lines, induced by disordered potentials. In addition, network model can be mapped back to continuum and tight-binding Hamiltonians. For example, the CC network model is proved to be the discretization of nonlinear $\sigma$ model [73, 77]. The equivalent TB Hamiltonian $\tilde{H}$ can be written by $U = e^{-\mathrm{i}\tilde{H}}$, where $U$ is a unitary operator written from the network scattering process [77, 86–88]. $\tilde{H}$ symbolizes a Dirac Hamiltonian, reflecting the effects of randomness in mass, scalar potential, and vector potential[IV].

Chalker-Coddington (CC) networks, with their easy access to the conductance, have achieved great success in quantitative descriptions of plateau transitions in QHE by providing an accurate critical exponent, which is close to the experimental result [54, 84, 88–98]. Subsequently, despite appearing specialized and limited initially, the network model has demonstrated its ability to elucidate a broad spectrum of phenomena in a much wider class of systems, including various disorder-induced topological phase transitions [95, 99–108]. Network models have provided useful theoretical insights and have even been tractable analytically around a critical point, for example the quantum critical point separating $\mathbb{Z}2$ quantum spin-Hall state from a metallic state [100]. Although in the literature, randomness is mostly introduced through a $U(1)$ random phase along the phase-delay links, generally speaking, network disorder can also take the form of structural disorder [20, 109, 110], which makes the network amorphous, as well as the randomness on the scattering properties of scattering nodes [19, 100].

Moving forward, we delve into the connection between network models and time-Floquet topological insulators in the next two sections, discussing the various topological phase available, which surpassing those of insulators based on Hermitian eigenproblems. These Floquet systems can exhibit unique and peculiar properties of their own, such as the coexistence of topologically protected edge states and vanishing Chern numbers of all bands that could normally be considered as "topologically trivial" in conventional topological band theory. Finally, we discuss disorder effects in Floquet topological physics.

## 1.3 Floquet topological insulator

Even after the intensive research carried out on topological insulators over the last few decades, topological physics still yields new surprises. Among the most astonishing developments, certain crystals, initially deemed topologically trivial, have been shown to manifest topological properties when subjected to periodic driving, surpassing traditional topological physics expectations [40, 111]. Floquet theory provides a powerful framework for the analysis of such periodic systems. Note that the terms "periodically-driven systems" and "time-Floquet systems" can be used interchangeably. Hence, we simply designate these crystals, which acquire non-trivial topological phases under periodic driving, as Floquet topological insulators.

---

[IV] This mapping and its further understanding will be elucidated in Sec.1.4.

### 1.3.1 Floquet analysis framework

For a system described by a Hermitian Hamiltonian $H$, subject to temporal periodic driving with a period $T = 2\pi/\Omega$ (where $\Omega$ is the driving frequency), the corresponding eigenequation is

$$\mathrm{i}\hbar\frac{d}{dt}|\psi(t)\rangle = H(t)|\psi(t)\rangle, H(t+T) = H(t). \tag{1.5}$$

In the following, for simplicity, we set $\hbar = 1$. Particularly, one can also describe the state's evolution using the unitary time evolution operator $U(t)$, expressed as [40]

$$U(t) = \mathscr{P}e^{-\mathrm{i}\int_0^T H(t)dt}, \tag{1.6}$$

where $\mathscr{P}$ denotes time ordering.

According to Floquet's theorem, the temporal evolution of these systems can be captured in a complete basis of orthogonal Floquet states $\{|\psi_n(t)\rangle\}$, where $n$ is the index for the basis. These Floquet states are the states that return to themselves after one period of time, with an additional phase accumulation ${\epsilon_n}^{\mathrm{V}}$, satisfying

$$|\psi_n(t+T)\rangle = e^{-\mathrm{i}\epsilon_n T}|\psi_n(t)\rangle. \tag{1.7}$$

The state $|\psi_n(t)\rangle$ can be decomposed into a product of a plane wave $e^{-\mathrm{i}\epsilon_n t}$ along temporal dimension and a temporally periodic function $|\Phi_n(t)\rangle$, namely

$$|\psi_n(t)\rangle = e^{-\mathrm{i}\epsilon_n t}|\Phi_n(t)\rangle, |\Phi_n(t+T)\rangle = |\Phi_n(t)\rangle, \tag{1.8}$$

$|\Phi_n(t)\rangle$ can then be developed in the harmonic basis of the driving frequency $\Omega$, expressed as

$$|\Phi_n(t)\rangle = \sum_m e^{-\mathrm{i}m\Omega\cdot t}|\phi_n^{(m)}\rangle, \tag{1.9}$$

where $|\phi_n^{(m)}\rangle$ is $m_{\mathrm{th}}$ Fourier component of the Floquet state.

To solve the eigenequation Eq. (1.5), one then needs to apply the Fourier expansion for Hamiltonian due to its periodicity:

$$H(t) = \sum_m e^{-\mathrm{i}m\Omega\cdot t}H^{(m)}, \tag{1.10}$$

where $H^{(m)} = 1/T\int_0^T H(t)e^{\mathrm{i}m\Omega\cdot t}dt$.

Equation (1.5) can therefore be reshaped into a form in Fourier harmonic space:

$$(\epsilon_n + m\Omega)|\phi_n^{(m)}\rangle = H^{(m)} * |\phi_n^{(m)}\rangle, \tag{1.11}$$

---

[V] This can also be an amplification in parametric oscillations when there is an external driven field.

where $*$ represents the convolution operation. Solving Eq. (1.11) then leads to the determination of $\epsilon_n$ and the corresponding Floquet states. The set of $\epsilon_n$ determines the Floquet spectrum.

Alternatively, rather than focusing solely on Hamiltonians, one can determine the Floquet spectrum and states by utilizing the time evolution operator. In fact, as revealed by Eq. (1.7), these Floquet states are the eigenstates of the unitary evolution operator over one period $U(T)$:

$$U(T)|\psi_n(t)\rangle = e^{-\mathrm{i}\epsilon_n T}|\psi_n(t)\rangle, \tag{1.12}$$

where $\epsilon_n$ represents the eigenphase of $U(T)$, termed as *quasienergy*. It plays a role analogous to the energy in a Hamiltonian eigenstate of a non-driven system. Similar to the Brillouin zone that emerges from discrete translational invariance in space, the system's temporal periodicity forms a "temporal Brillouin zone" for quasienergy $\epsilon_n$, defined as

$$-\frac{\pi}{T} \leq \epsilon_n < \frac{\pi}{T}. \tag{1.13}$$

The periodicity in the quasienergy dimension is also evident from the eigenvalue property of $U(T)$: $e^{-\mathrm{i}(\epsilon_n+\cdot p\Omega)T} = e^{-\mathrm{i}\epsilon_n T}$.

In crystals, a spatial version of Floquet's theorem, the Bloch's theorem, is used in the analysis, describing the Hamiltonian, the time-evolution operator, the Floquet state and the quasienergy by $H(t,\boldsymbol{k})$, $U(t,\boldsymbol{k})$, $|\psi_n(t,\boldsymbol{k})\rangle$, and $\epsilon_n(\boldsymbol{k})$ in the Brillouin zone.

Therefore, the Floquet spectrum is organized into bands, established on a compact Floquet-Brillouin zone. The goal of Floquet topological band engineering is to dynamically manipulate the system parameters to induce non-trivial topological phases, for example, by controlling the driving frequency, the coupling strength, or the onsite energy.

In some cases, a stroboscopic dynamics point of view can also be helpful. One can imagine that the time evolution over a period $T$ of a periodically driven system comes from an effective time-invariant Hamiltonian $H_{eff}$ [VI], that reads as

$$H_{eff}(\boldsymbol{k}) = \frac{\mathrm{i}}{T}\ln(U(T,\boldsymbol{k})). \tag{1.14}$$

Initial attempts to describe the topology of Floquet systems based on the Hermitian classification classes applied to $H_{eff}$ showed that such stroboscopic picture is not enough to predict the existence of topological edge states, which also depends on sub-period dynamics. As we explain in the following section, an anomalous Floquet topological phase can emerge, although the Chern numbers of all bands of $H_{eff}(\boldsymbol{k})$ are zero.

---

[VI] It should be emphasized that logarithm operation of $U(T,\boldsymbol{k})$ makes $H_{eff}(\boldsymbol{k})$ not unique[112].

### 1.3.2 Floquet topological phases

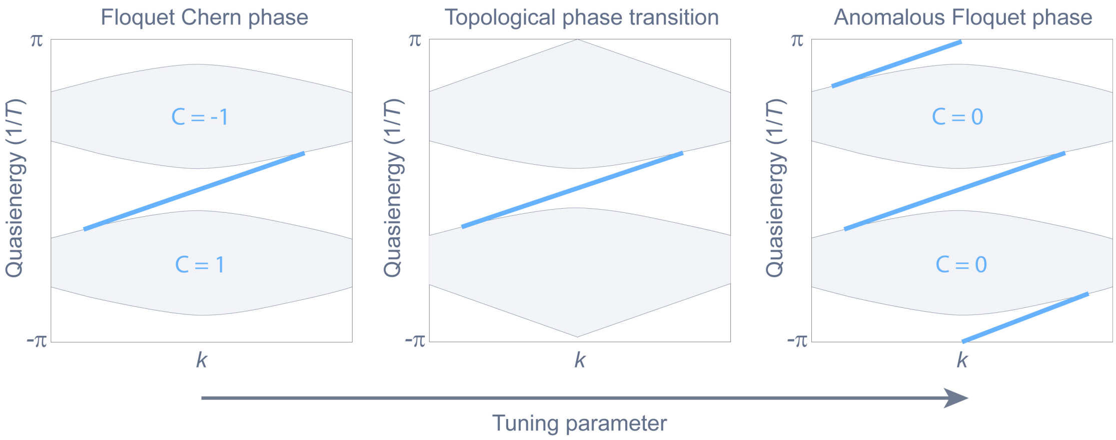

Figure 1.3: **Topological phases in Floquet systems.** Unlike the energy/frequency spectrum of the Hamiltonian, which is defined along the real axis in an open domain as illustrated in panel d of Fig. 1.1, the Floquet spectrum resides within a compact, periodic Floquet-Brillouin zone. This quasienergy dimension's periodicity uniquely allows for phase transitions through the closing and reopening of the gap at either $\pi/T$ or $-\pi/T$, a phenomenon without counterparts in static and non-driven systems. Beginning with a Floquet Chern phase, a phase transition occurring at the $\pi/T$ band gap causes the Chern numbers of the top and bottom bands to cancel out. Given that the topological edge state in the 0 gap remains intact, a corresponding topological edge state in the $-\pi/T$ gap must also exist to maintain bulk-edge correspondence. This new topological phase is characterized by bands with zero Chern numbers—typically considered topologically trivial according to conventional band theory. However, it defies expectations by exhibiting topological edge states within every band gap. Consequently, this phase is termed the anomalous Floquet phase. Its topological invariant is characterized by the non-trivial winding around the Floquet- Brillouin zone, which is an integer number.

Initially, periodic driving served to induce a topological phase transition from a trivial configuration ($C = 0$) in a non-driven system to a non-trivial state for the system's Floquet bands under driving ($C \neq 0$). Systems with non-zero Chern numbers for their Floquet bands are therefore in Floquet Chern phase (Fig. 1.3), which is fully captured by $U(T)$ or $H_{eff}$ defined on the BZ torus. A typical example is the graphene irradiated by the circularly polarized light, which can exhibit the same non-trivial topology as QHE [113–119]. Specifically, the circularly polarized light naturally breaks time-reversal symmetry, which can replace the external static magnetic field, leading to the quantum Hall states. Such external time-periodic field control on quantum matter can induce topological polariton [120] by implementing interaction between light and matter, which are, if taken separately, topologically trivial. In photonic platforms, lattices of photonic resonators periodically driven by electro-optic modulators can realize Floquet Chern insulator thanks to the time-driving induced synthetic magnetic field [121].

The exploration of Floquet topological physics continues to yield intriguing discoveries. What quickly ignites the field of Floquet topological physics and makes it very active, was the discovery of a unique topological phase in Floquet systems, the anomalous Floquet topological phase, which cannot be understood in the scope of topological band theory of Hamiltonians [122, 123]. The anomalous Floquet phase is characterized by zero Chern numbers of bands, yet it has topological edge states in every band gap. Its emergence is due to the periodicity of the quasienergy, which belongs to a compact space, effectively providing an additional gap at quasienergy $\pm\frac{\pi}{T}$ between the highest band and the lowest band. Since Chern numbers count the net number of chiral edge states leaving and entering a given band, this additional gap allows a new type of topological phase (anomalous) where all Chern numbers are zero, and the same amount of edge states is present in each gap (including the new one). This leads to a new type of topological transition, markedly different from the only possible one in static system (the Trivial-Chern phase transition). In static systems with finely tuned parameters, a topological phase transition between trivial and Chern insulating phases can happen by closing and reopening the band gap around $E_F$ or $f_0$ as shown in Fig. 1.1. In a Floquet system, the anomalous Floquet phase can be realized starting from a Chern phase with a gap centered at 0 quasienergy, if one manages to close the trivial gap at $\pi/T$ or $-\pi/T$, and reopen it as topological, as shown in Fig. 1.3.

Since the conventional topology characterization breaks down when applied to the anomalous Floquet phase, a new topological invariant $W_\tau[U]$ for Floquet systems was proposed as the winding number (or degree) of a "periodized evolution operator" $V_\tau(t,\boldsymbol{k})$ defined for each spectral gap $\tau$ of $U(T,\boldsymbol{k})$ [39, 123–132]. To be more specific, unitary time evolution operator $U(t,\boldsymbol{k})$ defines a smooth mapping from $[0,T]\times BZ \to U(N)$, where $N$ is the finite internal degrees of freedom. However, the homotopy topological invariant, which depicts the topological features of the mapping between the two manifolds, is trivial. The situation can be different if the mapping of a unitary operator $V_\tau(t,\boldsymbol{k})$ is 3-torus $S^1\times BZ \to U(N)$, whose homotopy topological invariant is the one of the group $\pi_3(U(N)) = \mathbb{Z}$. To achieve this, $V_\tau(t,\boldsymbol{k})$ should be periodic and constructed from the unitary time evolution operator $U(t,\boldsymbol{k})$. To construct $V_\tau(t,\boldsymbol{k})$, a method called "relative construction" was suggested [112, 123, 125, 129, 132]. The construction begins with $H^\tau_{eff}(\boldsymbol{k})$ by the branch cut $\tau$ in a spectral gap of $U(T,\boldsymbol{k})$:

$$H^\tau_{eff}(\boldsymbol{k}) = \frac{\mathrm{i}}{T}\ln_{-\tau}[U(T,\boldsymbol{k})]. \tag{1.15}$$

The operation of the branch cut $\tau$ with the complex logarithm is defined as

$$\ln_{-\tau}(e^{\mathrm{i}\epsilon T}) = \mathrm{i}\epsilon T \text{ for } -\tau-2\pi \le \epsilon T < -\tau. \tag{1.16}$$

The periodized unitary time evolution operator $V_\tau(t,\boldsymbol{k})$, is then defined as

$$V_\tau(t,\boldsymbol{k}) = U(t,\boldsymbol{k})e^{\mathrm{i}tH^\tau_{eff}(\boldsymbol{k})}, \tag{1.17}$$

and the homotopy topological invariant [112, 123, 132] as

$$W_\tau[U] = \frac{1}{24\pi^2}\int_{[0,T]\times BZ} \mathrm{tr}\big[(V_\tau^{-1}\mathrm{d}V_\tau)^3\big] \equiv \deg(V_\tau(t,\boldsymbol{k})) \in \mathbb{Z}, \tag{1.18}$$

where $\mathrm{d}V_\tau$ stands for $\frac{\partial V_\tau}{\partial k_x} dk_x + \frac{\partial V_\tau}{\partial k_y} dk_y + \frac{\partial V_\tau}{\partial t} dt$. The power 3 must be understood in the language of differential forms, and the integral runs over a 3-torus. The invariant $W_\tau[U]$ is actually a gap invariant which is well defined until the spectral gap closes. In contrast, the Chern numbers are band invariants inferred from the eigenstates of $H^\tau_{eff}(\boldsymbol{k})$, and thus cannot capture the anomalous Floquet topology in unitary operators of the Floquet system, owing to the non-consideration of the temporal micromotion $U(t, \boldsymbol{k})$. Although Chern numbers cannot provide the full picture for Floquet topology, the Chern number of the bands are still significant and related with $W_\tau[U]$. For a band sandwiched in between top gap $\tau_1$ and bottom gap $\tau_2$, the difference of the gap invariants $W_{\tau_1}[U]$ and $W_{\tau_2}[U]$ is exactly the Chern number $C$ of the band

$$C = W_{\tau_1}[U] - W_{\tau_2}[U]. \tag{1.19}$$

We note that, before the work carried in this thesis, both Chern and anomalous phase seemed to lead to the same physics, namely the existence of Chiral edge states. Their distinction seems to be merely theoretical. We will show in subsequent chapters that this is not the case, and the two phases do not behave similarly when disorder is imparted.

### 1.3.3 Anomalous Floquet topological phase and its platforms

Recent research into anomalous Floquet topological insulators (AFI) has spurred numerous experimental studies in condensed matter platforms [117, 133] and ultra-cold atoms [134–137]. Yet, realizing and experimentally characterizing AFI faces two significant challenges. First, while a periodic driving may lead to a non-trivial topology in Floquet band structure for platforms of electrons or cold atoms, it is not sufficient to guarantee that one observe the desired physical properties in the system. Finding the conditions, in which a stable stationary state with anomalous Floquet topological characteristics emerges in a periodically driven system, is therefore one of the central challenges in the field [111]. Therefore, platforms and driving mechanisms, which are convenient for implementations and observations, are desired. Second, to date, observations of unidirectional edge states in Floquet systems can be attributed to either Chern or anomalous phases, and they can only be distinguishable when one can access the entire Floquet band structure. For example, one needs to determine all band gaps and check whether there is a topological edge state in every gap, or measures the Chern numbers and gap invariants. However, accessing the entire Floquet band structure is very difficult [138]. This leads to ***the third motivation*** for this thesis. Is there another observable, apart from topological invariants of $W_\tau[U]$ and $C$, capable of distinguishing and detecting easily AFI from Chern phase (CI) and not require determining all information about all band eigenstates?

To circumvent the implementation of continuous temporal driving, discrete-time dynamics can be considered, which is both theoretically convenient and also experimentally appealing. In fact, discrete-time dependent systems were the first models that demonstrated AFI, and they were later experimentally confirmed in photonic devices [139–144], as well as cold atom platforms [145], where the discrete mechanism is often referred to as discrete-time quantum walk [139, 146]. The discrete time manipulation mechanism can also be the building blocks for the approximation of arbitrary continuous time driving, paving the way for the ultimate Floquet topological control.

Moreover, since the topological properties of Floquet systems stem from the unitarity of time-evolution operators, they are naturally applicable for any kind of platforms whose eigenstates are described by a unitary Bloch eigenproblem [112, 147–149], including the scattering networks models of interest in this thesis. As a result, we will use interchangeably the terms "Floquet topology" and "Unitary topology" in the following, despite our preference would lean towards the use of the term "Unitary topology" for all these systems. Unitary operators could be propagators of particles or waves along a propagation coordinate which serves as the analogue of time [147, 150–155], or scattering matrices describing the scattering process among multiple scatterers in scattering networks [112, 148, 149]. These unitary operators provide new platforms and mechanisms for Floquet topology and especially AFI, beyond the topological phases defined in Hermitian operators. Several artificial systems have been proposed to exhibit and probe anomalous Floquet phases, such as photonic and acoustic scattering networks [112, 148, 149, 156–160], as well as in evanescently coupled helical waveguide lattices [144, 147, 150, 152–155, 161, 162], with the advantage of not having to deal with temporal modulations.

### 1.3.4 Disordered Floquet topological systems

Shifting our focus to disordered systems, the quasienergy dimension's periodicity can be leveraged to explore unique avenues in Floquet topology- the existence of an anomalous topological phase in disordered systems when the quasienergy spectrum is completely filled by both mobility gaps accommodating topological edge states and Anderson localized bulk states. Such a case cannot be found for a disordered Chern phase (topological Anderson insulators), where the delocalized bulk states at some energies are necessary for the existence of chiral edge states [11, 112]. These phenomena[VII], known as anomalous Floquet Anderson insulators (AFAI) [131, 132, 163–170], have been proposed based on time-dependent disorder applied to on-site potentials [163, 164, 167, 168].

Although most proposed AFAI models tend to be trivialized via Floquet Anderson transition [152, 171] under large parameter fluctuations, recent theories predict the possible existence of AFAI in strongly disordered regimes [71, 132, 149, 169, 170], for example by fully randomizing the quasienergy through a time-dependent kicking on phase factors, implying that the unique topological observable of AFI might be related to robustness against disorder. Yet, experimental platforms for realizing disorder in Floquet systems are very scarce. Disorder type

---

[VII] Under strong disordered cases, the Floquet topological invariant $W$ should be generalized to a branch cut in the mobility gap [131, 132], and transport properties can also be applied for topological characterization [163].

adopted in theoretical models may not be directly related with the disorder already existing in experiments or practically applied, and the effect of disorder on topological systems might be dependent on the type of disorder [65]. Therefore, our understanding of disorder's role in Floquet topological phases and exploration of anomalous Floquet topological phases in strong disorder are still in their infancy.

Next, we will demonstrate how scattering networks offer promising avenues, for exploring and advancing in Floquet topological physics and disorder effects on them.

## 1.4 Floquet topological physics in network models

As introduced in Sec. 1.2, from the original context, network models were proposed to describe a disordered system with a static Hamiltonian— a non-interacting electron gas in a magnetic field and disorder potential. Crucially, following the spirit of Sec. 1.3, the equivalence of Floquet topology and unitary operators' topology enables the definition of a unitary scattering matrix $U$ in the network models that behaves as a discrete time evolution operator [77, 86–88, 172].

Delplace and his colleagues further elucidated this Floquet mapping in scattering networks, showing how $U$ acts as a discrete-time evolution operator in scattering networks [112, 149]. To evidence it, we present two examples: discrete-time dependent tight-binding models in the square [123] and honeycomb [122] lattices. Both lattices can exhibit anomalous Floquet insulating phases and are widely implemented in quantum walk platforms [139–144]. For the Floquet TB model in square lattice shown in Fig. 1.4a, the hopping term $J_i$ represents the coupling between nearest neighbor sites, and are cyclically switched on and off around each plateau. The temporal switching status of $J_i$ in a period $t \in [0, T)$ is shown in the bottom panel, which is only turned on for a $\tau_i$ time slot while off for the other time during $[0, T)$. Therefore, the discrete-time dependent Hamiltonian $H(t, \boldsymbol{k})$ is temporally piecewise, and can be expressed as

$$H(t, \boldsymbol{k}) = \begin{cases} J_1 h_1(\boldsymbol{k}) & 0 \le t < \tau_1 \\ J_2 h_2(\boldsymbol{k}) & \tau_1 \le t < \tau_2 \\ J_3 h_3(\boldsymbol{k}) & \tau_2 \le t < \tau_3 \\ J_4 h_4(\boldsymbol{k}) & \tau_3 \le t < T \end{cases}, \tag{1.20}$$

where $\boldsymbol{k}$ is the momentum.

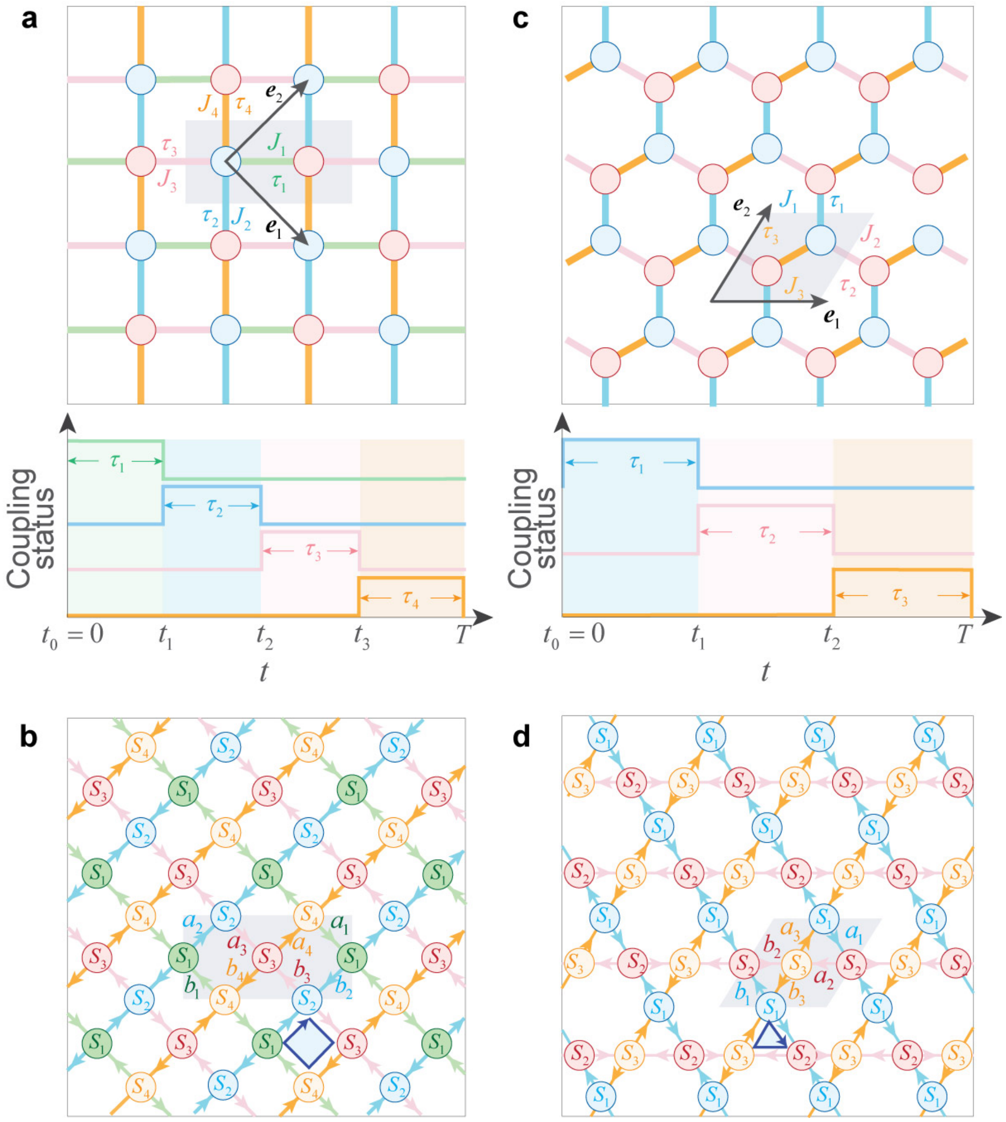

Figure 1.4: **Mapping between discrete-time dependent tight-binding (TB) models and scattering networks [149]. a, c,** Discrete-time dependent TB models in a square lattice (a) and a honeycomb lattice (c). Hamiltonians are temporally periodic with periodicity $T$, employing time-sequential couplings $J_i$ persisting for a time $\tau_i$. The unit cells, shown in grey, are defined by lattice vectors $\boldsymbol{e}_1$ and $\boldsymbol{e}_2$. There are two sublattice freedoms (two sites) for TB models of both square and honeycomb lattices. **b, d,** Scattering networks on $L$ lattice (b) and Kagome (d) lattice, mapped from discrete-time dependent TB models in the square lattice (a) and honeycomb (c) lattice, respectively. Such correspondences between Floquet TB models and scattering networks are actually dual-graph transformations. In a transformation, Hermitian hopping involving $N_0$ sites in TB models during a time step is substituted with a scattering node (marked as the same color) with $N_0$ incoming links and $N_0$ outgoing links, whose scattering process is described by a unitary $N_0 \times N_0$ matrix. For the $L$ (b) and Kagome (d) lattices, the unit cells, marked in grey, incorporate 8 and 6 sublattice sites, respectively.

With the lattice vectors $\boldsymbol{e}_1$ and $\boldsymbol{e}_2$, we can define $h_i(\boldsymbol{k})$ for $i = 1, 2, 3, 4$ as

$$\begin{aligned} h_1(\boldsymbol{k}) &= \begin{bmatrix} 0 & e^{-\mathrm{i}k_+} \\ e^{\mathrm{i}k_+} & 0 \end{bmatrix}, \qquad h_2(\boldsymbol{k}) = \begin{bmatrix} 0 & e^{-\mathrm{i}k_-} \\ e^{\mathrm{i}k_-} & 0 \end{bmatrix}, \\ h_3(\boldsymbol{k}) &= \begin{bmatrix} 0 & e^{\mathrm{i}k_+} \\ e^{-\mathrm{i}k_+} & 0 \end{bmatrix}, \qquad h_4(\boldsymbol{k}) = \begin{bmatrix} 0 & e^{\mathrm{i}k_-} \\ e^{-\mathrm{i}k_-} & 0 \end{bmatrix}, \end{aligned} \tag{1.21}$$

where $k_\pm = \boldsymbol{k} \cdot \frac{\boldsymbol{e}_1 + \boldsymbol{e}_2}{2}$.

The time evolution operator $U_i(\boldsymbol{k})$ in the time slot $i$ can be written as

$$U_i(\boldsymbol{k}) = e^{-\mathrm{i}\theta_i h_i(\boldsymbol{k})} = B_i S_i B_i^\dagger, \tag{1.22}$$

where $\theta_i \equiv J_i \tau_i$ and the second equality is obtained by unitary decomposition for $h_i(\boldsymbol{k})$. $B_i$ expressed as $B_i = B(x)|_{x=-\frac{1}{2}\ln[h_i(\boldsymbol{k})|_{(2,1)}]}$ with

$$B(x) = \begin{bmatrix} 0 & e^{x} \\ e^{-x} & 0 \end{bmatrix}, \tag{1.23}$$

which is unitary while $S_i$ is defined by

$$S_i = \begin{bmatrix} \cos\theta_i & \mathrm{i}\sin\theta_i \\ \mathrm{i}\sin\theta_i & \cos\theta_i \end{bmatrix}. \tag{1.24}$$

Therefore, with Eq. (1.6), one can write the time evolution operator $U(T)$ in a whole period $t \in [0, T)$ as

$$U(T, \boldsymbol{k}) = U_4(\boldsymbol{k}) U_3(\boldsymbol{k}) U_2(\boldsymbol{k}) U_1(\boldsymbol{k}), \tag{1.25}$$

whose detailed expression is

$$U(T, \boldsymbol{k}) = B(-\frac{k_-}{2}) S_4 T_{\boldsymbol{e}_1} S_3 T_{-\boldsymbol{e}_2} S_2 T_{-\boldsymbol{e}_1} S_1 B^\dagger(\frac{k_+}{2}). \tag{1.26}$$

$T_{\boldsymbol{e}_i}$ is a unitary translation operator imparting phase terms along the vectors $\pm e_i/2$ and read as

$$T_{\boldsymbol{e}_i} = \begin{bmatrix} e^{\mathrm{i}\frac{\boldsymbol{k}\cdot\boldsymbol{e}_i}{2}} & 0 \\ 0 & e^{-\mathrm{i}\frac{\boldsymbol{k}\cdot\boldsymbol{e}_i}{2}} \end{bmatrix}. \tag{1.27}$$

In fact, as a change in the origin of time for $U(T)$ should not alter its topological properties, cyclic permutation in the time-ordered multiples in Eq. (1.26) is allowed. Therefore, one can equivalently describes the Floquet dynamics by the unitary operator

$$\tilde{U}(T, \boldsymbol{k}) = S_4 T_{\boldsymbol{e}_1} S_3 T_{-\boldsymbol{e}_2} S_2 T_{-\boldsymbol{e}_1} S_1 T_{\boldsymbol{e}_2}, \tag{1.28}$$

where $T_{\boldsymbol{e}_2} = B^\dagger(\frac{k_+}{2})B(-\frac{k_-}{2})$. The above expression shows that each time after a free propagation along $\pm\boldsymbol{e}_1$ or $\pm\boldsymbol{e}_2$, particles or waves encounter a scatterer represented by $S_i$. This scattering phenomenon happens cyclically and can be clearly interpreted as a successive local scattering process arranged in real space, resulting in a scattering network in $L$ lattice shown in Fig. 1.4b. In this transformation from the Floquet TB model (Fig. 1.4a) to scattering network (Fig. 1.4b), the hopping $J_i$, which involves 2 sites in TB model and persists for a time step $\tau_i$, is equivalent to a scattering node with 2 incoming links and 2 outgoing links. Its scattering process is described by a unitary $2 \times 2$ matrix $S_i$ with $\theta_i = J_i\tau_i$.

Generally speaking, Hermitian hopping involving $N_0$ sites in the Floquet TB model leads to a unitary scattering node with $N_0$ outgoing/incoming links, described by a $N_0 \times N_0$ unitary matrix. The scattering nodes are then unidirectionally connected via oriented links, following the temporal order in Eq. (1.26). From a graph-theory point of view, this transformation is a dual-graph mapping: sites (nodes) in TB ↔ links in networks; hopping (links) in TB ↔ scattering nodes (nodes) in networks. It is worth to note that in the Floquet TB model with square lattice there is 2 sublattice degrees of freedom in the unit cell (gray area), whereas cyclic scattering process in the unit cell of the corresponding scattering network requires 8 wave amplitudes on the oriented links for a full description.

Following the original proposal [77, 86–88, 172], one can get another unitary operator $U(\boldsymbol{k})$ on the network of that form

$$U(\boldsymbol{k}) = \begin{bmatrix} 0 & 0 & 0 & S_4 T_{\boldsymbol{e}_1} \\ S_1 T_{\boldsymbol{e}_2} & 0 & 0 & 0 \\ 0 & S_2 T_{-\boldsymbol{e}_1} & 0 & 0 \\ 0 & 0 & S_3 T_{-\boldsymbol{e}_2} & 0 \end{bmatrix}. \tag{1.29}$$

$U(\boldsymbol{k})$ describes the scattering process on the basis of wave amplitudes $|\psi\rangle = [a_1, b_1, \ldots, a_4, b_4]^T$. The equivalence between Floquet topology characterized by $\tilde{U}(T, \boldsymbol{k})$ in the view of Floquet TB model and Floquet topology captured by $U^4(\boldsymbol{k})$ in the view of scattering networks can be proved by resorting to the concept of phase rotation symmetry [112]. The mapping applies broadly, as illustrated by the correspondence in Figs. 1.4(c, d) between Floquet TB model in honeycomb lattice and scattering network in Kagome lattice. Furthermore, the mapping can be more complex with the possible additions in time-Floquet systems, for example complex hopping terms and other temporal coupling statuses. Nevertheless, one can still build the matching unitary scattering network by comprehensively parameterizing scattering nodes and adding phase terms on the links.

In conclusion, this Floquet mapping remarkably unveils the potential of scattering networks in Floquet topological physics. In recent years, periodic unitary scattering networks have been shown to exhibit the anomalous Floquet insulating phase (AFI) [19–22, 71, 112, 148, 156–158, 163, 173, 174]. In addition, the use of topological scattering networks is motivated by their precision in modeling topological waves in photonic systems, such as systems comprising coupled resonator optical waveguides (CROWs) [14, 15, 160, 175–178] and programmable photonic platforms [179–181]. This privilege is attributed to the wider domain of validity for such systems than TB methods, because scattering networks accommodate both strong and weak coupling [112, 148], whereas TB model and coupled-mode theory (CMT) are restricted to weakly coupled high-Q resonators (sites). Furthermore, as elucidated in Sec. 1.2, linking Floquet systems to CC networks may provide essential insights into disordered systems through quantitative analysis, revealing scaling effects, critical exponents, and universality class [90, 96, 182], which are essential for understanding the topological phases and topological phase transitions in disordered systems. Therefore, with scattering networks, one can truly benefit from the triple advantages of the richer topological physics rooted in Floquet topology, quantitative results and scaling analysis of disorder effect on topological phases, and the potential for experimental application and future developments.

## 1.5 Motivation and structure of the thesis

This thesis is driven by the key objectives that arose in previous sections, which are summarized by the following overarching questions:

1. How to describe and understand the effect of distributed disorder on various kinds on A-class topological phases, and on their chiral edge transports?
2. Can disorder induce, enhance or guarantee chiral edge transport instead of impeding it?
3. What is the physical difference between chiral transports obtained from an anomalous or a Chern topological phase?
4. How to experimentally explore the interplay between Floquet topology and disorder by using scattering networks, to advance the field towards realistic applications?

This thesis focuses on unitary scattering networks with broken TRS, which is a prerequisite for genuinely operating in the A-class, and exhibiting unidirectional photonic edge states. Working with time-reversal invariant networks is not an option. As in prior arts, one may think of working with a TRS system with two time-reversed subspaces, however this cannot allow for a satisfactory study on disorder, as disorder would couple the two spins together, breaking the trick used to emulate the A-class.

This thesis is organized as follows.

- Chapter 2 lays the foundation of the work with a theoretical and numerical toolbox for scattering networks, including clean-limit honeycomb networks, their Bloch eigenequation, and the introduction of various distributed disorders (phase-delay links, scattering nodes, and network structure). Crucially, this framework also provides clear and mutually consistent observables for disordered systems regarding topological phase transitions and localization. These observables include band structures in infinite and semi-infinite networks, finite network calculation methods, localization length and scaling analysis, and topological invariants in disordered scattering networks.

- In Chapter 3, we study in detail the clean-limit honeycomb scattering networks introduced in Ch. 2 and identify conditions to obtain the three insulating phases- AFI, CI, and trivial. We then start to examine edge transport distinctions between the two topological phases, AFI and CI.
- In Chapter 4, based on key observations made in Ch. 3, we study the resilience of topological chiral edge transport in the presence of distributed disorder, in the form of random phase-delay fluctuations or variations in the scattering properties of the nodes. A remarkable robustness distinction is made between AFI and CI.
- Chapter 5 is dedicated to a third disorder type: the structural disorder. We will take a deeper look at it by providing a method to measure a topological scattering invariant in finite disordered scattering networks, and connect their non-trivial topology in the strong disorder to the physics of the anomalous Floquet Anderson insulator (AFAI).
- After that, in Chapter 6, we propose a unified framework to describe the effect of disorder on topology, and the crucial role of sample scaling on macroscopic scattering properties. This theory is a real space RG on unitary scattering networks, and allows to capture topological transports and critical behaviors in strongly disordered scattering networks. This RG frame is the last stop of my Ph.D. journey, which I expect can answer the questions you (readers) and I were wondering and curiosities we had about the physical origin of robustness in disordered topological systems.

# 2 Theory and analysis framework of disordered unitary scattering networks

The main results in this chapter are taken from the following published articles: (i) Zhe Zhang, Pierre Delplace, Romain Fleury, "**Superior robustness of anomalous non-reciprocal topological edge states**", *Nature*, 598, 293–297 (2021) (licensed under a Creative Commons Attribution 4.0 International License); (ii) Zhe Zhang, Pierre Delplace, Romain Fleury, "**Anomalous topological waves in strongly amorphous scattering networks**", *Science Advances*, 9, eadg3186 (2023) (open access, under a CC BY-NC or CC BY license); and (iii), the preprint in Zhe Zhang, et al, "**Renormalization group of topological scattering networks**", arXiv:2404.15866 (2024) (open access), with permissions of all co-authors and journals.

Since this thesis focuses on the topological phases in unitary scattering networks and the effects of disorder, there are two clusters of topics ("maps" and "tools") we (the "explorer") need to study before trying to find and validate new physics ("find the treasure").

The first cluster of topics contains several aspects of unitary scattering networks. Albeit we introduce scattering networks from their history and Floquet mapping in Ch. 1, we are still lack of knowledge regarding:

1. Which specific unitary scattering networks are we focusing on, and what constitutes their fundamental configuration in the clean-limit case?

2. Do these unitary scattering networks obey some symmetries or not ? Modern physics centers on symmetries. Systems preserving symmetries adhere to conservation laws, as elucidated by Noether's theorem. The information of network symmetries can therefore guide us in our theoretical and experimental efforts to understand the physics of photonic scattering networks.

3. How do waves/particles propagate within scattering networks? Answering this question requires detailed mathematical descriptions of their microscopic unitary scattering processes. Such description can also provide us with control knobs in both experiments and applications.

4. What types of disorder do we consider, and how do we construct and quantitatively characterize such disorders? These will constitute a numerical technique toolbox, central to our explorations in disorder physics.

5. Is there a difference between oriented scattering graphs and non-oriented non-reciprocal scattering networks? The Floquet mapping proved in Sec. 1.4 involves scattering networks with oriented links (CC networks). However, the scattering networks of our focus, which we implement in practice, are built by taking bidirectional waveguides as links, with non-reciprocal scatterers. Can we bridge the conceptual and practical gap between these two types of scattering networks, thereby establishing a clear connection between Floquet systems and scattering networks featuring bidirectional links?

After establishing "maps" for our exploration, namely the fundamentals of unitary scattering networks with or without disorder, we will then turn our attention to the needed "tools", aimed at deriving their physical properties through detailed theoretical and analytical frameworks. Indeed, we need theories and analysis frameworks about clear and mutually consistent physical observables, in order to capture topological characteristics, phase transitions, and localization in disordered scattering networks. The spirit we should keep in mind is: Physically, topological effects/invariants are linked to the transport/eigenstate response of a system when boundary conditions are varied e.g. the quantum Hall conductance [183] and polarization [184]. We will answer key considerations about how to study these physical observables:

1. Band structures are important as they facilitate the calculations of Chern numbers $C$ and gap invariants $W_\tau$, crucial for identifying topological properties in periodic scattering networks. They describes waves/particles' propagation within infinite networks or semi-infinite networks. In addition, they are helpful for checking chiral edge states and localization, since group velocity and positions of Bloch states are accessible from band structures.

2. While indispensable, band structures primarily serve as theoretical tools, predicated on the idealized assumption of networks of infinite or semi-infinite extent [I]. In practice, experiments pivot on real-space observables such as conductance and transmissions, bridging the gap between theoretical predictions and tangible outcomes. Therefore, real-space observables are crucial for both theoretical confirmations and experimental demonstrations, including transports in finite networks with external ports and eigenstates in finite closed networks. Transports are essential for confirming non-trivial topological phases, as topological edge states underpin unidirectional unitary transports, which must align with the topological invariant as implied by the well-known bulk-edge correspondence. Blocked transport is also an obvious observable related to localization.

---

[I] One possible experimental method to observe it is by applying twisted boundary condition.

3. Transport properties, especially under varied boundary conditions in finite networks, unlock insights into localization lengths, enabling us to categorize the network phase through scaling analysis: metal, topological insulator, or trivial insulator.

4. While transport and band structures provide preliminary insights into a network's topological phase, definitive theoretical and experimental validation of topological characteristics in disordered networks demands accessible topological invariants.

**In this chapter,** we aim to provide the toolbox needed to elucidate all of the above points. Equipped with the basic knowledge of unitary scattering networks and their analysis frameworks, we will be prepared to explore the interplay among unitary topology, disorder, and scattering in the networks, in subsequent chapters (Chs. 3-6).

**Organization of the chapter:** Sec. 2.1 covers the first cluster of topics regarding clean-limit honeycomb networks and their Bloch eigenequation, symmetries in photonic scattering networks, parameterization of unitary scattering processes, disorder types in unitary scattering networks, and mapping between two types of scattering networks. Secs. 2.2-2.5 provide the analysis frameworks of the second cluster of topics. Specifically, Sec. 2.2 elucidates analysis methods on band structures for periodic honeycomb networks and disordered networks. Sec. 2.3 discusses transport through external ports and cavity eigenstates in networks isolated from the external environment. In the ending of Sec. 2.3, we will examine an example in clean-limit scattering networks, to exhibit how analysis methods on band structures, topological invariants, transports, and eigenstates in finite closed networks coincide with each other. Such correspondence also works in disordered cases. Sec. 2.4 introduces scaling analysis and localization calculations. Finally, in Sec. 2.5, we propose a topological scattering invariant, which is measurable and applicable for any network even in the strong disorder cases where Anderson localization emerges.

## 2.1 Basics of scattering networks

This section details the configuration and basic physical context of *non-reciprocal scattering networks*. At the microscopic scale, the networks we consider are formed of interconnected unitary scatterers with three ports. This choice to work with three-port systems is motivated by three reasons. First, at the microscopic scale, scatterers with more than two ports are needed to construct complex networks. Second, although 2-port unitary scatterers can exhibit transmission nonreciprocity in the form of transmission phase asymetries (on off-diagonal elements of their $2 \times 2$ scattering matrix), they cannot exhibit nonreciprocity in transmission magnitude. Three-port appears here as a minimal number to do so[II]. Third, practically, three-port circulators are experimentally available and also the elementary component to construct multi-port non-reciprocal devices with versatile functionalities. One could, of course, work on a theory based on four-port unitary scatterer built networks, but this would only complicate

---

[II] Parameterization of $U(N)$ matrices is shown in Sec. 2.1.3.

the associated mathematics without bringing any new advantage. We also assume that the microscopic scatterers obey three-fold rotational ($C3$) symmetry[III].

We first check the configuration of honeycomb periodic scattering networks with non-reciprocal scatterers, regarded as pristine (clean-limit) scattering networks, and how Floquet band structure emerges. A non-reciprocal unitary scattering network is illustrated in Fig. 2.1a, which consists of general three-port non-reciprocal scatterers connected by bidirectional links in a honeycomb periodic structure. The links are standard monomode waveguides supporting forward and backward propagation. The scattering elements exhibit three-fold (C3) rotational symmetry, while the links impart a phase delay of $\varphi$, as represented in the zoom-in view of the unit cell (Fig. 2.1b). The scattering process is described by a unitary 3x3 asymmetric scattering matrix $S_0$, where $S_0^T \neq S_0$ means scattering nonreciprocity.

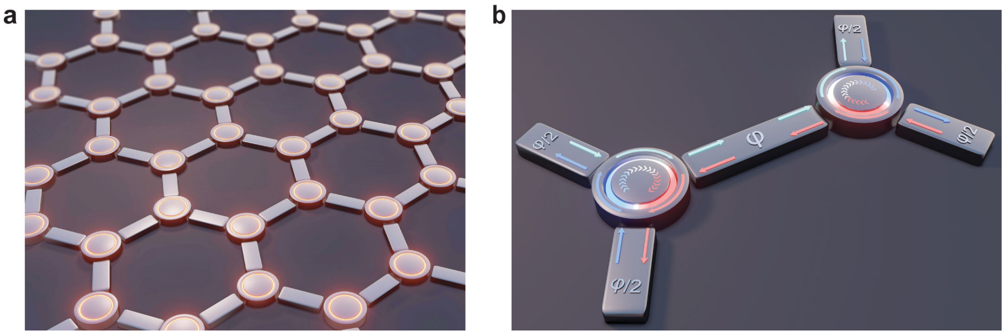

Figure 2.1: **Topological non-reciprocal scattering network in honeycomb lattice. a,** We consider a unitary scattering network made of three-port non-reciprocal elements, described by asymmetric unitary scattering matrices. **b,** Unit cell of the honeycomb lattice, highlighting the wave signals entering the non-reciprocal elements, their 120° rotational symmetry, and the reciprocal phase delay $\varphi$ imparted by the links. The network is described by a unitary unit-cell scattering operator $S(\boldsymbol{k})$, defining a Floquet unitary mapping with quasienergy $\varphi$.

### 2.1.1 Honeycomb non-reciprocal network configuration and Floquet band structure

In photonics, three-port non-reciprocal scatterers are referred to as circulators. For example, circulators operating in microwave frequency band are formed of a $C3$ symmetric resonant (central disk) on a ferromagnetic substrate (such as Yttrium iron garnet (YIG)) and penetrated by an external magnetic field that breaks time-reversal symmetry, as shown in Fig. 2.2a. The three ports are placed 120° apart from each other such that they are iso-spaced. The printed circuit board is sandwiched between two pieces of ferrite. Without magnetic fields, the Y-junction strip line supports two degenerate modes at $\omega_0$: right and left-handed. A magnetic field of 50 kA/m = 628 Oe, normal to the printed circuit board and polarizing the ferrite, lifts the initial degeneracy, with chiral modes at $\omega_+$ and $\omega_-$. When inputted at port 1, the superposition

---

[III] This is verified experimentally. On the theoretical front, this symmetry assumption will play an important role in Ch. 6, renormalization group theory.

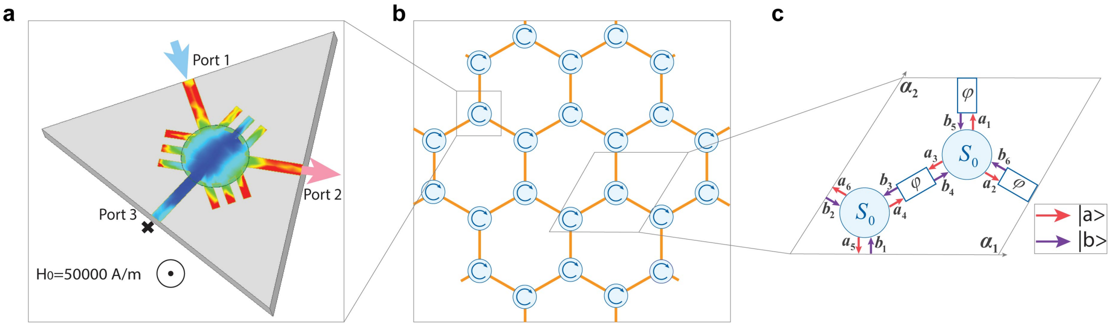

Figure 2.2: **Photonic honeycomb network and associated signal labelling convention in the unit cell. a,** Concrete practical implementation of 3-port circulators with a ferrite cavity circulator biased by an internal magnet providing a static magnetic field $H_0$. In a periodic honeycomb scattering network (**b**), we define state vectors $|a\rangle$ and $|b\rangle$, which represents signals propagating out and into the two circulators in the unit cell (**c**), respectively.

of the two excited modes makes a constructive interference (partial or full) at port 2 while destructive interference (partial or full) at port 3, therefore resulting in partial or full wave circulation from port 1 to port 2, port 2 to port 3, and port 3 to port 1. In the photonic scattering networks, we take such circulators as the scattering nodes in the crystalline networks with honeycomb lattice (Fig. 2.2b), where a unit cell consists of two 3-port circulators and three links which impart phase delay with value $\varphi$ (Fig. 2.2c).

Now, we derive the Floquet band structure in periodic honeycomb scattering networks and recognize that the phase delay $\varphi$ take the role of a quasienergy in the spectrum of the unitary operator describing the Bloch eigenproblem. Following this insight, in the remainder of this thesis, we will consistently use the terms phase-delay band structures/spectra instead of Floquet band structures/spectra.

To derive the eigenequation from the scattering matrix of the two circulators present in a honeycomb unit cell, we adopt the labelling scheme shown in Fig. 2.2c for the complex amplitudes of the waves propagating in and out of the 3-port circulators, which leads to

$$\begin{bmatrix} a_3 \\ a_1 \\ a_2 \\ a_5 \\ a_6 \\ a_4 \end{bmatrix} = \begin{bmatrix} 0 & S_0 \\ S_0 & 0 \end{bmatrix} \begin{bmatrix} b_1 \\ b_2 \\ b_3 \\ b_4 \\ b_5 \\ b_6 \end{bmatrix} \tag{2.1}$$

We then multiply Eq. (2.1) by a unitary permutation matrix $P_0$, which exchanges fifth row with sixth row, fourth row with fifth row, first row with third row, and first with second row, so that $(a_1, a_2, a_3, a_4, a_5, a_6)^T = P_0(a_3, a_1, a_2, a_5, a_6, a_4)^T$. Hence, noting $|b\rangle = [b_1, b_2, b_3, b_4, b_5, b_6]^T$

and $|a\rangle = [a_1, a_2, a_3, a_4, a_5, a_6]^T$, we get

$$|a\rangle = S_{\text{unit cell}}|b\rangle \qquad \text{with} \quad S_{\text{unit cell}} \equiv P_0 \begin{bmatrix} & S_0 \\ S_0 & \end{bmatrix}. \tag{2.2}$$

In general, $|a\rangle$ and $|b\rangle$ are functions of the position $\boldsymbol{r}$ of the unit cell: $|a\rangle = |a(\boldsymbol{r})\rangle, |b\rangle = |b(\boldsymbol{r})\rangle$ with $\boldsymbol{r} = n_1\boldsymbol{\alpha_1} + n_2\boldsymbol{\alpha_2}$, where $\boldsymbol{\alpha_1}$ and $\boldsymbol{\alpha_2}$ are Bravais lattice vectors shown in Fig. 2.2c, and $\boldsymbol{n} = \{n_1, n_2\}$ are integers.

With the phase-delay lines between circulators, we obtain:

$$\begin{cases} b_1(\boldsymbol{r}+\boldsymbol{\alpha_2}) & = e^{\mathrm{i}\varphi} a_1(\boldsymbol{r}) \\ b_2(\boldsymbol{r}+\boldsymbol{\alpha_1}) & = e^{\mathrm{i}\varphi} a_2(\boldsymbol{r}) \\ b_3(\boldsymbol{r}) & = e^{\mathrm{i}\varphi} a_3(\boldsymbol{r}) \\ b_4(\boldsymbol{r}) & = e^{\mathrm{i}\varphi} a_4(\boldsymbol{r}) \\ b_5(\boldsymbol{r}) & = e^{\mathrm{i}\varphi} a_5(\boldsymbol{r}+\boldsymbol{\alpha_2}) \\ b_6(\boldsymbol{r}) & = e^{\mathrm{i}\varphi} a_6(\boldsymbol{r}+\boldsymbol{\alpha_1}). \end{cases} \tag{2.3}$$

Looking for Bloch eigenstates, we obtain

$$|a(\boldsymbol{k})\rangle = e^{-\mathrm{i}\varphi} \Lambda(\boldsymbol{k}) |b(\boldsymbol{k})\rangle, \tag{2.4}$$

where $\Lambda(\boldsymbol{k}) = \mathrm{diag}\big(e^{\mathrm{i}\boldsymbol{k}\cdot\boldsymbol{\alpha}_2}, e^{\mathrm{i}\boldsymbol{k}\cdot\boldsymbol{\alpha}_1}, 1, 1, e^{-\mathrm{i}\boldsymbol{k}\cdot\boldsymbol{\alpha}_2}, e^{-\mathrm{i}\boldsymbol{k}\cdot\boldsymbol{\alpha}_1}\big)$ is a unitary matrix containing Bloch phases. Combining Eqs. (2.2) and (2.4), we obtain the eigenequation in the momentum space, formed by a unitary matrix $S(\boldsymbol{k})$, as

$$S(\boldsymbol{k})|b(\boldsymbol{k})\rangle = e^{-\mathrm{i}\varphi(\boldsymbol{k})}|b(\boldsymbol{k})\rangle, \tag{2.5}$$

where $S(\boldsymbol{k}) = \Lambda^{-1}(\boldsymbol{k}) S_{\text{unit cell}}$ is unitary, due to the unitarity of $\Lambda(\boldsymbol{k})$ and $S_{\text{unit cell}}$, which guarantees a real-valued phase $\varphi(\boldsymbol{k})$. The values of $\varphi(\boldsymbol{k})$, defined modulo $2\pi$, will be shown in the range $[0, 2\pi)$ as a function of $\boldsymbol{k}$, which defines the phase-delay band structure. This band structure is the analogue of the Floquet band structure in time-Floquet lattices where the phase delay $\varphi$ play the role of the quasienergy in Eq. (1.12). Such mapping also indicates that we can adjust phase-delay values in experiments to fix the operating point of practical networks[IV].

With the established eigenequation Eq. (2.5), we can compute quasienergy (Floquet) band structures in the honeycomb scattering networks, defined in $[0, 2\pi) \times BZ$. But before that, let us establish a few important considerations regarding symmetries.

---

[IV] This enables future applications on topological wave routing (Sec. 7.2.1).

### 2.1.2 Intrinsic symmetries in photonic systems

In this subsection, we focus on generalities regarding intrinsic symmetries related to time reversal operations, reciprocity, and Hermiticity. We first review these concepts in homogeneous media within the context of Maxwell's equations and scattering systems. Then, since tight-binding Hamiltonians and coupled-mode theory are widely used to analyze photonic systems, we also examine these concepts in Hamiltonians.

In continuous electromagnetic media [185–187], assuming time-invariance, linearity, and local anisotropic constitutive parameters, time-reversal symmetry (TRS)[V] implies real permittivity and permeability tensors: $\bar{\bar{\epsilon}}=\bar{\bar{\epsilon}}^*$ and $\bar{\bar{\mu}}=\bar{\bar{\mu}}^*$. Following Lorentz reciprocity theorem [49, 189], reciprocity implies symmetric permittivity and permeability tensors: $\bar{\bar{\epsilon}}=\bar{\bar{\epsilon}}^T$ and $\bar{\bar{\mu}}=\bar{\bar{\mu}}^T$. The concept of Hermiticity is obtained from the lossless condition, requiring $\bar{\bar{\epsilon}}=\bar{\bar{\epsilon}}^\dagger$ and $\bar{\bar{\mu}}=\bar{\bar{\mu}}^\dagger$ [49]. Hence, in time-invariant systems, any two out of TRS, Hermiticity, and reciprocity can lead to the third symmetry- only two of them are independent. Below, we take five examples of permittivity tensor of nonmagnetic media, whose symmetries are summarized in Table. 2.1:

$$\bar{\bar{\epsilon}}_0=\begin{bmatrix}\epsilon_{r0} & \epsilon_{r1} & 0\\ \epsilon_{r1} & \epsilon_{r0} & 0\\ 0 & 0 & \epsilon_{r0}\end{bmatrix},\bar{\bar{\epsilon}}_1=\begin{bmatrix}\epsilon_{r0}+\mathrm{i}\epsilon_{i0} & 0 & 0\\ 0 & \epsilon_{r0}+\mathrm{i}\epsilon_{i0} & 0\\ 0 & 0 & \epsilon_{r0}+\mathrm{i}\epsilon_{i0}\end{bmatrix},$$
$$\bar{\bar{\epsilon}}_2=\begin{bmatrix}\epsilon_{r0} & \mathrm{i}\epsilon_{i1} & 0\\ -\mathrm{i}\epsilon_{i1} & \epsilon_{r0} & 0\\ 0 & 0 & \epsilon_{r0}\end{bmatrix},\bar{\bar{\epsilon}}_3=\begin{bmatrix}\epsilon_{r0} & \epsilon_{i1} & 0\\ -\epsilon_{i1} & \epsilon_{r0} & 0\\ 0 & 0 & \epsilon_{r0}\end{bmatrix},\bar{\bar{\epsilon}}_4=\begin{bmatrix}\epsilon_{r0} & \mathrm{i}\epsilon_{i1} & 0\\ \epsilon_{i1} & \epsilon_{r0} & 0\\ 0 & 0 & \epsilon_{r0}\end{bmatrix}. \tag{2.6}$$

Table 2.1: Symmetries of the five examples of Eq. (2.6).

| | TRS $\bar{\bar{\epsilon}}=\bar{\bar{\epsilon}}^*$ | Reciprocity $\bar{\bar{\epsilon}}=\bar{\bar{\epsilon}}^T$ | Hermiticity $\bar{\bar{\epsilon}}=\bar{\bar{\epsilon}}^\dagger$ |
|---|---|---|---|
| $\bar{\bar{\epsilon}}_0$ | ✓ | ✓ | ✓ |
| $\bar{\bar{\epsilon}}_1$ | × | ✓ | × |
| $\bar{\bar{\epsilon}}_2$ | × | × | ✓ |
| $\bar{\bar{\epsilon}}_3$ | ✓ | × | × |
| $\bar{\bar{\epsilon}}_4$ | × | × | × |

For a scattering system with $N$ channels or ports, scattering matrix $S$ maps the vector of the incident wave amplitudes $|b\rangle$ into the vector of the scattered wave amplitudes $|a\rangle=S|b\rangle$. Due to Onsager-Casimir relation[51, 187, 190, 191], nonreciprocity is represented by $S\neq S^T$. Alternatively, the reciprocity of scattering matrix $S$ in photonic systems can also be obtained from the properties of dyadic Green functions (DGFs)[49, 189, 192], i.e. $\bar{\bar{G}}_{ij}=\bar{\bar{G}}_{ji}$. In addition, the concept of Hermiticity corresponds to energy flux conservation in scattering processes. In the context of Hamiltonians, the scattering matrix $S$ for a particle going through scattering is

---

[V] Time reversal operator $\mathscr{T}$ is represented by an anti-unitary operator, expressed by $\mathscr{T}=\mathscr{U}\mathscr{K}$, where $\mathscr{U}$ is an unitary operator and $\mathscr{K}$ is antiunitary operator (complex conjugation) [188].

defined from its time evolution operator as

$$S = \lim_{t_\pm \to \pm\infty} U(t_+, t_-) = \lim_{t_\pm \to \pm\infty} \mathscr{P} e^{-\mathrm{i}\int_{t_-}^{t_+} H(t)dt}. \tag{2.7}$$

Therefore, in this context, Hermiticity $H = H^\dagger$ is clearly equivalent to the unitarity of the scattering matrix $SS\dagger = \mathbb{I}$. In addition, such unitarity condition can also be directly proved from flux conservation, namely $\langle b|b\rangle = \langle a|a\rangle \equiv \langle b|S^\dagger S|b\rangle, \forall\ |b\rangle$.

For a Hamiltonian $H$, TRS means $H = H^*$. In most cases, inducing gain, loss, and phase differences of hopping break time-reversal symmetry [VI]. The reciprocity condition of $H$ can be read from the condition of $S = S^T$ via the exponential operation, expressed as $H = H^T$. Therefore, generally speaking, breaking TRS is neither a necessary nor a sufficient condition for nonreciprocity. However, in Hermitian and time-invariant systems, the condition of TRS is equal to the condition for reciprocity. To illustrate possible cases of Hamiltonians concerning three symmetries, we take five examples of 2 × 2 Hamiltonians, where the parameter $J$ is real:

$$\begin{gathered} H_0 = \begin{bmatrix} 0 & J \\ J & 0 \end{bmatrix}, H_1 = \begin{bmatrix} \mathrm{i} & J \\ J & -\mathrm{i} \end{bmatrix}, \\ H_2 = J\begin{bmatrix} 0 & \mathrm{i} \\ -\mathrm{i} & 0 \end{bmatrix}, H_3 = \begin{bmatrix} 0 & J \\ -J & 0 \end{bmatrix}, H_4 = J\begin{bmatrix} 0 & \mathrm{i} \\ 1 & 0 \end{bmatrix}. \end{gathered} \tag{2.8}$$

Their symmetries are summarized in Table. 2.2.

Table 2.2: Symmetries in photonic systems described by Hamiltonians in Eq. (2.8).

| | TRS $H = H^*$ | Reciprocity $H = H^T$ | Hermiticity $H = H^\dagger$ |
|---|---|---|---|
| $H_0$ | ✓ | ✓ | ✓ |
| $H_1$ | × | ✓ | × |
| $H_2$ | × | × | ✓ |
| $H_3$ | ✓ | × | × |
| $H_4$ | × | × | × |

In the practical model of our photonic circulators depicted in Fig. 2.2a, a gyrotropic magnetic material in the $xoy$ plane is subject to a static external magnetic field $H_0$ along the $z$ direction, and its permeability tensor is expressed as follows:

$$\bar{\bar{\mu}} = \begin{bmatrix} \mu_{r0} & \mathrm{i}\mu_{i1} & 0 \\ -\mathrm{i}\mu_{i1} & \mu_{r0} & 0 \\ 0 & 0 & \mu_0 \end{bmatrix}, \tag{2.9}$$

where $\mu_{r0} = \mu_0(1 + \frac{\omega_0\omega_m}{\omega_0^2-\omega^2})$, $\mu_{i1} = \mu_0\frac{\omega\omega_m}{\omega_0^2-\omega^2}$, $\omega_0 = \mu_0\gamma H_0$, and $\omega_m = \mu_0\gamma M_s$. $\gamma$ is called gyromagnetic ratio, and $M_s$ is the (DC) saturation magnetization [193]. The static magnetic field therefore breaks time-reversal symmetry and reciprocity, by checking $\bar{\bar{\mu}} \neq \bar{\bar{\mu}}^*$ and $\bar{\bar{\mu}} \neq \bar{\bar{\mu}}^T$, with-

---

[VI] However, there is a special case, alike $\bar{\bar{\epsilon}}_3$, which keeps TRS but non-Hermitian and non-reciprocal.

out breaking hermiticity. The scattering matrix of such circulators is therefore unitary and asymmetric.

### 2.1.3 Parameterization of scattering nodes

Until now, the form of the unitary asymmetric scattering matrix $S_0$ for the nodes within our networks has not been explicited. In this part, we parameterize such scattering process assuming the additional condition of 120$^{\mathrm{o}}$ rotational symmetry (C3 symmetry). This process is governed by scattering matrices $S_0$, which adhere to $C3$ symmetry and can be represented within the framework of $U(3)$ group theory. As we are dealing with a TRS breaking system, we firstly review known parameterization techniques for the general unitary group $U(n)$ alongside with the well-established Cabibbo-Kobayashi-Maskawa (CKM) model. The general parameterization of $U(N)$ classifies parameters into angle and phase parameters, and unambiguously provides the number of independent parameters required to describe a general $U(N)$ matrix. We discuss how to parameterize $C3$ and $U(3)$ matrices in the mathematical sense, before making the parameterization more physical using insight from coupled mode theory (CMT).

Proposed by Murnagham [194], parameterization of the $n$-dimensional unitary group $U(n)$ is the product of a unitary diagonal matrix containing $n$ phase terms and $n(n-1)/2$ matrices $J_{i,j}|_{i\neq j} \in U(N)$, whose main building block is a 2 × 2 matrix of the form:

$$\begin{bmatrix} J_{i,j}(i,i) & J_{i,j}(i,j) \\ J_{j,i}(i,i) & J_{i,j}(j,j) \end{bmatrix} = \begin{bmatrix} \cos(\theta_{i,j}) & -\sin(\theta_{i,j})e^{-\mathrm{i}\varphi_{i,j}} \\ \sin(\theta_{i,j})e^{\mathrm{i}\varphi_{i,j}} & \cos(\theta_{i,j}) \end{bmatrix}, \tag{2.10}$$

while the other diagonal elements $\{J_{i,j}(p,p) = 1|p \notin \{i,j\}\}$ are unity in $J_{i,j}$, and the other non-diagonal elements $\{J_{i,j}(p,q) = 0|p \neq q; p,q \notin \{i,j\}\}$ are vanishing. Specifically, $\theta_{i,j} \in [0,\pi)$, designated as the "angle parameter", controls the amplitude within the unitary matrix, while $\varphi_{i,j} \in [0,2\pi)$, known as the "phase parameter", dictates the phase terms. Consequently, to parameterize $U(n)$, there are $\frac{1}{2}n(n-1)$ angle parameters $\theta_{i,j}$ and $\frac{1}{2}n(n+1)$ phase parameters $\varphi_{i,j}$. For instance, the general parameterization of $U(2)$ is expressed as

$$S \in U(2); S = \begin{bmatrix} \cos(\theta)e^{\mathrm{i}\varphi_1} & -\sin(\theta)e^{\mathrm{i}\varphi_2} \\ \sin(\theta)e^{\mathrm{i}(\varphi_3-\varphi_2)} & \cos(\theta)e^{\mathrm{i}(\varphi_3-\varphi_1)} \end{bmatrix}, \tag{2.11}$$

where $\theta$ and $\varphi_i$ are angle and phase parameters respectively.

The parameterization of the unitary matrix transcends mere mathematical interest. In modern photonic networks, it enables the crucial capability to realize arbitrary discrete unitary transformations, facilitating arbitrary manipulation of quantum states in photonic networks, where product operations are executed via cascading transfer matrices of network blocks, and Eq. (2.10) is constructed using Mach–Zehnder interferometers (MZI) and tunable phase shifters [195]. In high-energy physics, this parameterization is instrumental in extracting the CP-violating phase from the CKM matrix, a critical component in understanding matterantimatter asymmetry [196, 197]. In applying unitary matrix parameterization to physical models, it is crucial to recognize that certain parameters hold more significance than others. To see it, given a definite $S \in U(N)$, we can map it into another unitary matrix $S' \in U(N)$ by multiplying it at left and at right by diagonal phase matrices $D_L = \mathrm{diag}(e^{\mathrm{i}\varphi_1^L}, \dots, e^{\mathrm{i}\varphi_n^L})$ and $D_R = \mathrm{diag}(e^{\mathrm{i}\varphi_1^R}, \dots, e^{\mathrm{i}\varphi_n^R})$, respectively. This operation physically corresponds to augmenting a unitary $n$-channel/port scatterer with a unitary 2-port non-reciprocal phase shifter at each port, with a scattering matrix described by

$$S_{\mathrm{NPS}} = \begin{bmatrix} 0 & e^{\mathrm{i}\varphi_A} \\ e^{\mathrm{i}\varphi_B} & 0 \end{bmatrix}. \tag{2.12}$$

Within scattering networks, this principle of reduction is equally applicable due to the interconnection of scatterers via phase delay links. In a sum, we can reduce the parameterization of physical systems by $2n-1$ phase parameters [VII]. This concept is recognized as the phase invariance property in the domain of high-energy physics [198]. For $U(3)$ parameterization, which in general contains three angle parameters $(\frac{1}{2}n(n-1)|_{n=3})$ and six phase parameters $(\frac{1}{2}n(n+1)|_{n=3})$ [194, 195, 199, 200], such reduction leads to the famous CKM matrix [196, 197], comprised of four parameters: three angle parameters $\theta_{12}, \theta_{13}, \theta_{23}$ and one phase parameter $\delta$, expressed as

$$S_{CKM} = \begin{bmatrix} c_{12} & c_{13}s_{12} & s_{12}s_{13} \\ c_{23}s_{12} & -c_{12}c_{13}c_{23} - e^{\mathrm{i}\delta}s_{13}s_{23} & -c_{12}c_{23}c_{13} + e^{\mathrm{i}\delta}c_{13}c_{23} \\ s_{12}s_{23} & c_{23}s_{13}e^{\mathrm{i}\delta} - c_{12}c_{13}s_{23} & -c_{13}c_{23}e^{\mathrm{i}\delta} - c_{12}s_{13}s_{23} \end{bmatrix}, \tag{2.13}$$

where $c_{ij} = \cos\theta_{ij}, s_{ij} = \sin\theta_{ij}$.

Now, let us try to apply $C3$ symmetry condition on the CKM parameterization. Yet, the general $C3$ and $U(3)$ matrix is not a simple subset of $S_{CKM}$. Starting from the definitions of $C3$ symmetry- the invariance under unitary transformation of cyclic permutation matrix, one can get

$$S_0 = \begin{bmatrix} a & b & c \\ c & a & b \\ b & c & a \end{bmatrix}. \tag{2.14}$$

Unitarity on $S_0$ then leads to two kinds of equations. The first class of equations is related with the energy conservation, namely

$$|a|^2 + |b|^2 + |c|^2 = 1, \tag{2.15}$$

---

[VII] We do not care about the overall phase. Therefore it is $2n-1$ rather than $2n$.

which indicates the parameterization as

$$\begin{cases} a = \cos(\theta_1) \\ b = \sin(\theta_1)\sin(\theta_2)e^{\mathrm{i}\varphi_1} \\ c = \sin(\theta_1)\cos(\theta_2)e^{\mathrm{i}\varphi_2}, \end{cases} \tag{2.16}$$

where $\theta_i$ and $\varphi_i$ are angle and phase parameters respectively. The second one is on the orthogonality among different columns of $S_0$, resulting in an equation

$$\cos(\theta_1)\sin(\theta_2)e^{-\mathrm{i}\varphi_1} + \cos(\theta_1)\cos(\theta_2)e^{\mathrm{i}\varphi_2} + \sin(\theta_1)\sin(\theta_2)\cos(\theta_2)e^{\mathrm{i}(\varphi_1-\varphi_2)} = 0. \tag{2.17}$$

By simplifications, we form Eq. (2.17) into

$$\tan(\theta_1) = -\frac{e^{\mathrm{i}(\varphi_1-2\varphi_2)}}{\sin(\theta_2)}\left[1+\tan(\theta_2)e^{\mathrm{i}(\varphi_1+\varphi_2)}\right]. \tag{2.18}$$

It is crucial to note that, in the parameterization of general unitary operators, angle parameters play a more significant role than phase parameters, since the scattering amplitude is directly controlled by the angle parameters $\theta_{i,j}$. As indicated by Eq. (2.18), selecting $\theta_2$ as a free parameter necessitates fixing $\theta_1$ to specific discrete values, rendering it dependent rather than independent. In addition, two phase parameters $\varphi_1$ and $\varphi_2$ are constrained by a condition ensuring the right part of the equation to be a real number. Hence, despite the derivations not yielding a closed form or parameterization with independent parameters for $C3$ and $U(3)$ matrices, we get an important information that the parameterization of $C3$ and $U(3)$ matrices should contain two parameters, in which one is an angle parameter and the other one is phase parameter. In the following, we find an alternative physically-relevant model of such system involving two of such independent parameters, in order to avoid dealing with the complexity of a parameterization based on Eq. (2.18).

Let's consider the practical physical model of lossless circulators with $C3$ symmetry [19]. To be more specific, these circulators consist of a circular resonator influenced by an external time-odd field, along with three equidistantly placed waveguides, all identically coupled to the resonator. Particularly, these models also contain two independent parameters. One is the strength of the external time-odd bias, such as the amplitude of the static magnetic field in photonic circulators [201] and the air velocity in acoustic circulators [191], while the other one is the resonator's quality factor. Therefore, it seems promising to obtain a simpler parameterization of $C3$ and $U(3)$ matrices from such circulator models.

Using temporal coupled mode theory (CMT) [36, 191, 201, 202] on photonic circulators, we consider the two resonant modes $|\psi_\pm\rangle$ with dipolar field profiles in the ferrite resonator, whose resonant frequencies are $\omega_+$ and $\omega_-$ with quality factor $Q_\pm$ respectively. With the bias field, Zeeman splitting lifts the degeneracy at $\omega_0$, inducing $\omega_+ \neq \omega_-$. Through three waveguides serving as external ports, we couple the two resonant modes $|\psi_\pm\rangle$ with the incoming waves (complex amplitudes $b_i, i = 1,2,3$) and outgoing waves (complex amplitudes $a_i, i = 1,2,3$)

propagating on the waveguides, in which coupling strength is quantitatively described by the inverse of decay times $\gamma_\pm = \frac{\omega_0}{2Q_\pm}$ for two modes respectively. When sending a signal with complex amplitude $b_i$ at port $i$, CMT lists the equations involving $b_i$ and waves amplitudes $(A_\pm)$ of the right-handed and left-handed modes, expressed as

$$\begin{cases} \frac{d}{dt}A_+ = (-\mathrm{i}\omega_+ - \gamma_+)A_+ + \sqrt{\frac{2\gamma_+}{3}}b_1 + e^{-\mathrm{i}2\pi/3}\sqrt{\frac{2\gamma_+}{3}}b_2 + e^{\mathrm{i}2\pi/3}\sqrt{\frac{2\gamma_+}{3}}b_3 \\ \frac{d}{dt}A_- = (-\mathrm{i}\omega_- - \gamma_-)A_- + \sqrt{\frac{2\gamma_-}{3}}b_1 + e^{\mathrm{i}2\pi/3}\sqrt{\frac{2\gamma_-}{3}}b_2 + e^{-\mathrm{i}2\pi/3}\sqrt{\frac{2\gamma_-}{3}}b_3, \end{cases} \tag{2.19}$$

where the phase terms are determined by the azimuth phases $e^{\pm\mathrm{i}\varphi_{xoy}}$ of $|\psi_\pm\rangle$ at the position of couplings. The output wave amplitudes $a_i$ at the three waveguides are then written by considering the interference between the direct reflection and the fields leaking out from each mode, expressed as

$$\begin{cases} a_1 = -b_1 + \sqrt{\frac{2\gamma_+}{3}}A_+ + \sqrt{\frac{2\gamma_-}{3}}A_- \\ a_2 = -b_2 + e^{\mathrm{i}2\pi/3}\sqrt{\frac{2\gamma_+}{3}}A_+ + e^{-\mathrm{i}2\pi/3}\sqrt{\frac{2\gamma_-}{3}}A_- \\ a_3 = -b_3 + e^{-\mathrm{i}2\pi/3}\sqrt{\frac{2\gamma_+}{3}}A_+ + e^{\mathrm{i}2\pi/3}\sqrt{\frac{2\gamma_-}{3}}A_-. \end{cases} \tag{2.20}$$

With the assumption of single harmonic $e^{\mathrm{i}\omega t}$ on complex amplitudes, the scattering matrix $S_0$ among three ports can be obtained:

$$S_0 = -I + \kappa^2 \begin{bmatrix} \sqrt{\gamma_+} & \sqrt{\gamma_-} \\ e^{\mathrm{i}\theta}\sqrt{\gamma_+} & e^{-\mathrm{i}\theta}\sqrt{\gamma_-} \\ e^{\mathrm{i}\theta}\sqrt{\gamma_+} & e^{-\mathrm{i}\theta}\sqrt{\gamma_-} \end{bmatrix} \begin{bmatrix} \frac{\mathrm{i}}{(\omega - \omega_+ + \mathrm{i}\gamma_+)} & 0 \\ 0 & \frac{\mathrm{i}}{(\omega - \omega_- + \mathrm{i}\gamma_-)} \end{bmatrix} \begin{bmatrix} \sqrt{\gamma_+} & e^{-\mathrm{i}\theta}\sqrt{\gamma_+} & e^{\mathrm{i}\theta}\sqrt{\gamma_+} \\ \sqrt{\gamma_-} & e^{\mathrm{i}\theta}\sqrt{\gamma_-} & e^{-\mathrm{i}\theta}\sqrt{\gamma_-} \end{bmatrix}, \tag{2.21}$$

where $I$ is a 3 by 3 identity matrix, $\kappa = \sqrt{2/3}$, and $\theta = 2\pi/3$. Due to $C_3$ symmetry, we have $\gamma_+ = \gamma_- = \gamma$. It can be proved that $S_0$ is unitary. In the above expression, despite being an important parameter for the cavity, $\gamma$ just introduces a scaling factor to all the frequency parameters ($\omega$, $\omega_+$, and $\omega_-$). In order to show a general parameterization, we transform $\omega - \omega_+$ and $\omega - \omega_-$ in Eq. (2.21), into two angle variables $\xi$ and $\eta$, by applying standard normalizations and arctangent transformations:

$$\begin{cases} \xi = \arctan(\frac{\omega - \omega_+}{\gamma}) \\ \eta = \arctan(\frac{\omega - \omega_-}{\gamma}), \end{cases} \tag{2.22}$$

where $\xi$ and $\eta$ are defined in $[-\pi/2, \pi/2)$ with a periodicity of $\pi$, and characterize the normalized deviation of the angular frequency $\omega$ from the right- and left-handed eigenvalues $\omega_+$ and $\omega_-$, respectively. Specifically, the condition $\xi = \eta$ corresponds to the reciprocal case, with no

Zeeman splitting ($\omega_+ = \omega_-$), while $\xi = -\eta$ represents the operation at the resonant frequency $\omega = \omega_0 = (\omega_+ + \omega_-)/2$. With the parameters $(\xi, \eta)$, the scattering matrix is rewritten as

$$S_0 = -I + \frac{2}{3}\begin{bmatrix} 1 & 1 \\ e^{\mathrm{i}\frac{2\pi}{3}} & e^{-\mathrm{i}\frac{2\pi}{3}} \\ e^{\mathrm{i}\frac{2\pi}{3}} & e^{-\mathrm{i}\frac{2\pi}{3}} \end{bmatrix} \begin{bmatrix} \cos\xi e^{\mathrm{i}\xi} & 0 \\ 0 & \cos\eta e^{\mathrm{i}\eta} \end{bmatrix} \begin{bmatrix} 1 & e^{-\mathrm{i}\frac{2\pi}{3}} & e^{\mathrm{i}\frac{2\pi}{3}} \\ 1 & e^{\mathrm{i}\frac{2\pi}{3}} & e^{-\mathrm{i}\frac{2\pi}{3}} \end{bmatrix}. \tag{2.23}$$

Therefore, a general $C3$ and $U(3)$ matrix is characterized by

$$S_0 = \begin{bmatrix} R & T_{CCW} & T_{CW} \\ T_{CW} & R & T_{CCW} \\ T_{CCW} & T_{CW} & R \end{bmatrix}, \tag{2.24}$$

where $T_{CW}$ and $T_{CCW}$ represent chiral clockwise (CW) and counter clockwise (CCW) transmissions, respectively, while $R$ is the reflection. They only depend on $\xi$ and $\eta$ [19]:

$$\begin{cases} R(\xi,\eta) & = -1 + \frac{2}{3}\cos\xi e^{\mathrm{i}\xi} + \frac{2}{3}\cos\eta e^{\mathrm{i}\eta} \\ T_{CW}(\xi,\eta) & = \frac{2}{3}\left[e^{\mathrm{i}\frac{2}{3}\pi}\cos\xi e^{\mathrm{i}\xi} + e^{-\mathrm{i}\frac{2}{3}\pi}\cos\eta e^{\mathrm{i}\eta}\right] \\ T_{CCW}(\xi,\eta) & = \frac{2}{3}\left[e^{-\mathrm{i}\frac{2}{3}\pi}\cos\xi e^{\mathrm{i}\xi} + e^{\mathrm{i}\frac{2}{3}\pi}\cos\eta e^{\mathrm{i}\eta}\right]. \end{cases} \tag{2.25}$$

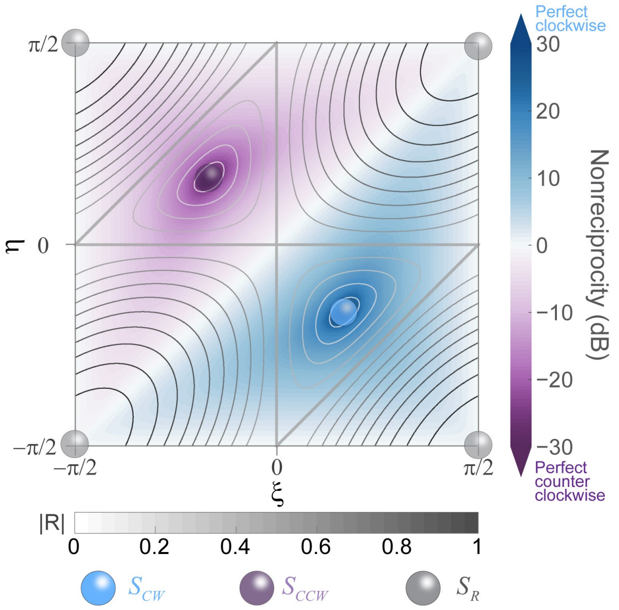

Figure 2.3: **Scattering properties of $S_0$ in $(\xi, \eta)$ parameter space.** Reflection (contour lines) and nonreciprocity (color map) of $S_0$ in its parameter space, defined by the two angle parameters $(\xi, \eta) \in [-\pi/2, \pi/2) \times [-\pi/2, \pi/2)$. Three special scattering matrices $S_R$, $S_{CW}$, and $S_{CCW}$, corresponding respectively to a fully reflective scatterer, a clockwise perfect circulator, and a counter-clockwise perfect circulator, are located on this plane.

By varying $\xi$ and $\eta$, we can generate $C3$ symmetric $U(3)$ scattering matrices $S_0(\xi,\eta)$ with variable reflection $R(\xi,\eta)$ and scattering chirality, which is quantified by the nonreciprocity level $NR(\xi,\eta) = T_{CW}/T_{CCW}$. This family of matrices is represented in Fig. 2.3, where the coloured density map represents $NR(\xi,\eta)$ in decibels, and the grey contours are for $R(\xi,\eta)$. There are special scattering matrices located at global extrema of $R(\xi,\eta)$ and $NR(\xi,\eta)$ on this parametric plane. They are $S_R$, $S_{CW}$, and $S_{CCW}$: The fully reflection (localized) matrix $S_R = I$ is obtained when $\xi$ and $\eta$ are equal to $\pm\pi/2$, whereas the chiral transport matrix $S_{CW}$ $(S_{CCW})$ is achieved under $\xi = -\eta = \pi/6$ $(-\pi/6)$, expressed as ideal clockwise and counterclockwise circulators

$$S_{CW} = \begin{bmatrix} 0 & 0 & 1 \\ 1 & 0 & 0 \\ 0 & 1 & 0 \end{bmatrix}, S_{CCW} = \begin{bmatrix} 0 & 1 & 0 \\ 0 & 0 & 1 \\ 1 & 0 & 0 \end{bmatrix}. \tag{2.26}$$

### 2.1.4 Disorder in scattering networks

In this part, we move away from the periodic honeycomb networks, and consider aperiodic macroscopic planar scattering networks[VIII]. These macroscopic networks are built by connecting the microscopic three-port scatterers ($S_0(\xi,\eta)$) using bidirectional links as shown in Fig. 2.4a, but the links may have different phases and the underlying structure may strongly depart from the pristine honeycomb. We recall that one can think of these links as lossless monomode waveguides characterized by the phase delay $\varphi$ that they impart to waves traveling one time along the length of the link, which is no longer constant. An example of an arbitrary macroscopic network is shown in Fig. 2.4b. In the Sec. 2.1.1, we already discussed periodic honeycomb networks, for which identical phase-delay links and identical three-port scatterers arranged in the honeycomb frame are used. We will refer to periodic honeycomb networks as pristine or clean-limit scattering networks, because it is an archetypal case in which no disorder is present.

In this thesis, we concentrate on types of disorder that are statistically uniform across the entire network area. In this part, we will figure out what kinds of disorder occur in macroscopic scattering networks, and how periodic honeycomb networks may be continuously transformed into disordered scattering networks. Specifically, we identify three types of disorder affecting macroscopic planar scattering networks. First, phase-link disorder affects the bidirectional links, altering their phase-delay values without modifying the underlying honeycomb network structure, and is represented by a probability distribution of phase-delay values $P(\varphi)$. This is illustrated in the left inset of Fig. 2.4c. Notably, there is a maximal level of phase disorder: phase-delay value is purely random when $P(\varphi)$ is a uniform probability distribution in $[0,2\pi)$. In fact, as phase-delay value $\varphi$ is quasienergy in the clean limit, fully random $\varphi$ can be regarded as completely randomized quasienergy, in which the statistically averaged observables

---

[VIII] The term "planar network" is the same concept as "plane graph" [203], where no link crosses with each other.

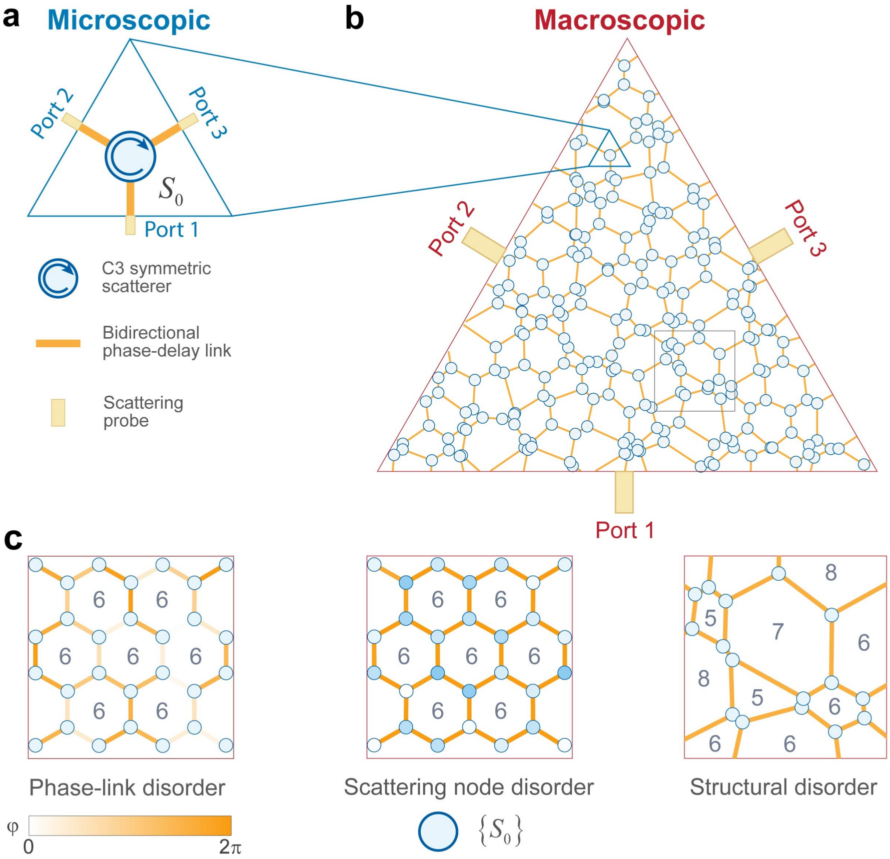
a
Microscopic
Port 2
Port 3
$S_0$
Port 1
C3 symmetric scatterer
Bidirectional phase-delay link
Scattering probe
b
Macroscopic
Port 2
Port 3
Port 1
c
Phase-link disorder
φ
0
2π
Scattering node disorder
$\{S_0\}$
Structural disorder
6
5
7
8

Figure 2.4: **Disordered scattering networks, from the microscopic to the macroscopic scale.** **a,** Unitary microscopic scatterers with three ports and three-fold rotational symmetry are used as building blocks to form macroscopic networks. The scattering detected at three scattering probes is described by the unitary matrix $S_0$. **b,** Macroscopic scattering network made of microscopic three-port scatterers $S_0$ interconnected by bidirectional phase-delay links. Three types of distributed disorder can be present. The macroscopic scattering properties of networks can be detected at three external probes, dictated by microscopic properties (disorder levels and types). **c,** Phase-link disorder (left), scattering-node disorder (center), and structural disorder (right). Phase-link disorder consists in taking a periodic network, e.g. a honeycomb arrangement, and adding random phase-delay fluctuations on each links. The second one is distributed disorder on scattering nodes, when keeping a honeycomb arrangement and identical phase-delay value on links but inducing perturbations on scattering properties of scattering nodes. Their microscopic scattering matrices are not identical, but form a set of unitary matrices $\{S_0(\xi,\eta)\}$. A more drastic form of disorder can take the form of deformations of the network structure, completely breaking the hexagonal structure (numbers count the number of sides forming each loop).

over many realizations are independent of quasienergy[IX]. Second, disorder can also occur independently at the network nodes, affecting the scatterers as depicted in the central inset. The scattering matrices of these scatterers are not identical, but form a statistical set $\{S_0(\xi,\eta)\}$. They can be statistically selected to lie within a specified region in the parameter space of $(\xi,\eta)$.

Third, one can imagine changing the structure of the network, creating in it loops that are no longer regular hexagons, but arbitrary irregular polygons (right inset in Fig. 2.4c). Such structural disorder, referred as amorphous disorder [204], can be continuously added to the honeycomb clean limit, following known Voronoi tessellation techniques [20, 205–207]. We use this method to construct a continuous amorphous deformation of periodic honeycomb non-reciprocal networks, controlled by a single parameter, the amorphous factor $\alpha$.

The Voronoi tessellation is constructed from a finite set of points $\{g_1,...,g_n\}$ called generators. Each generator $g_i$ corresponds to a polygonal cell $P_i$, which consists of all the points in a defined metric space $X$ whose distance to $g_i$ is less than or equal to its distances to the other generators [208]. Therefore, it can be formally defined as

$$P_i = \{x \in X | d(x,g_i) \le d(x,g_j), j \neq i\}, \tag{2.27}$$

where $d$ is the distance function in the metric space $X$.

The *weighted* Voronoi tessellation is a generalized version of the Voronoi tessellation, where each generator $g_i$ is weighted by $w_i$ such that generators with higher weights induce a larger polygonal cell by changing the local metric around them. The usual Voronoi tessellation is recovered when all the generators have the same weights. The weighted Voronoi diagram we adopt is known as a *Power diagram*, where the distance function between a point $x$ in the metric space $X$ and a generator $g_i$ weighted by $w_i$ is the power distance: $d(x,g_i) = d_E^2(x,g_i) - w_i^2$, where $d_E(x,g_i)$ is the Euclidean distance between $x$ and $g_i$. As shown in Figs. 2.5(a-b), we use the above tessellation to generate scattering networks made of three-port circulators and bidirectional links, by regarding the interfaces between cells as the network. In particular, the honeycomb network is generated, when applying the Euclidean distance, by using equal weights and arranging the generators in a triangular lattice, as shown in Fig. 2.5a. We obtain an amorphous network when the weights $w_i$ of the generators are taken randomly in the range $[0,M]$ with a uniform probability distribution. Then, the standard deviation of weights $\sigma = \frac{M}{2\sqrt{3}}$ quantifies the level of amorphism. As $M$ is of the order of $L_0^2$, where $L_0$ is the length of the links in the honeycomb network, we define the *amorphous factor* $\alpha = \frac{M}{L_0^2}$ as a normalized standard deviation, expressed by

$$\alpha \equiv \frac{2\sqrt{3}}{L_0^2}\sigma\,. \tag{2.28}$$

---

[IX] Or it will depend on the specified quasienergy. This property will be key to induce AFAI and distinguish AFI and CI without accessing the whole Floquet spectrum.

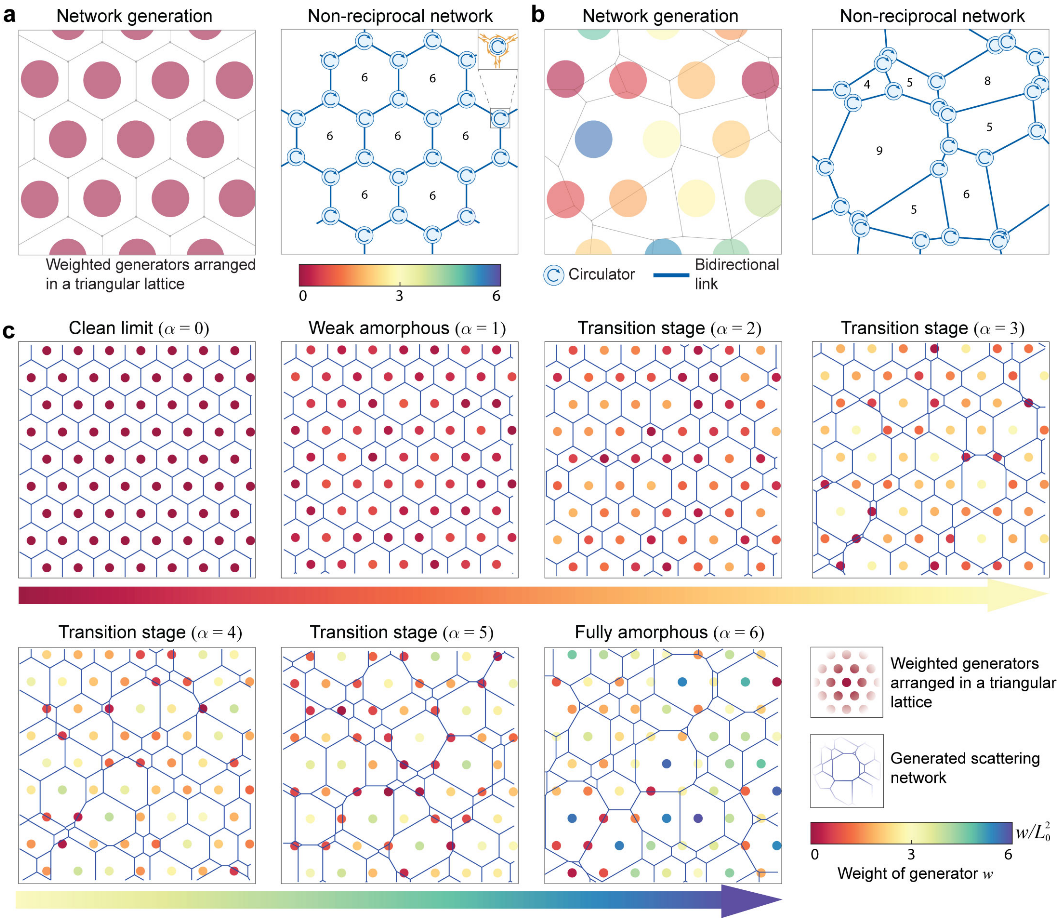
a
Network generation
Weighted generators arranged in a triangular lattice
Non-reciprocal network
0
3
6
b
Network generation
Circulator
Bidirectional link
Non-reciprocal network
c
Clean limit ($\alpha = 0$)
Weak amorphous ($\alpha = 1$)
Transition stage ($\alpha = 2$)
Transition stage ($\alpha = 3$)
Transition stage ($\alpha = 4$)
Transition stage ($\alpha = 5$)
Fully amorphous ($\alpha = 6$)
Weighted generators arranged in a triangular lattice
Generated scattering network
$w/L_0^2$
0
3
6
Weight of generator $w$

Figure 2.5: **Amorphous scattering networks generated from a weighted Voronoi tessellation.** The three-port circulators in scattering networks take the role of degree-3 nodes in the weighted Voronoi tessellation, while the bidirectional links connect degree-3 nodes. The weighted Voronoi tessellations are built by generators arranged in a triangular lattice. The equal weights of generators form a honeycomb crystalline network (**a**, clean limit, $\alpha = 0$), while the unequal weights give rise to an amorphous network (**b**, fully amorphous, $\alpha = 6$). **c,** We demonstrate how scattering networks at different amorphous levels are built from weighted generators arranged in the triangular lattice. At a given amorphous level $\alpha$, the weights $w$ of generators are randomly selected in a range of $[0, \alpha L_0^2]$ with a normal distribution, whose standard deviation is $\sigma = \frac{\alpha L_0^2}{2\sqrt{3}}$. Therefore, $\alpha$ is the normalized standard deviation of the weight ensemble.

In Fig. 2.5c, we illustrate the generations of scattering networks from the weighted Voronoi tessellation at several selected amorphous levels. To quantitatively understand what happens for networks upon increasing the amorphous level $\alpha$, we track both the link length variance and the number of sides of each loop in the network (numbers in Figs. 2.5(a-b)), as shown in Fig. 2.6. As $\alpha$ increases from 0 to 1.75, the links start to deform but the percentage of loops with $N = 6$ sides stays at 100% as in the clean honeycomb limit (Fig. 2.6a). Beyond this weakly amorphous regime, a transition occurs during which the percentage of loop 6 drops significantly as the one of loops with $N \neq 6$ increases. For $\alpha$ above 5, we enter a fully amorphous phase, characterized by a stabilized length variance (panel a) and a saturated distribution of loops of various sizes (panel b).

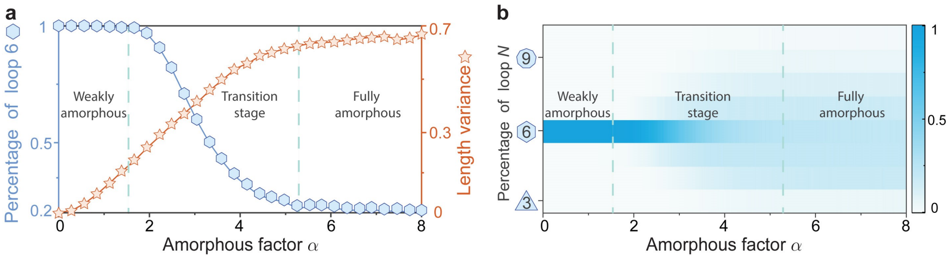

Figure 2.6: **Three amorphous stages revealed by the evolution of network statistics with $\alpha$.** With the statistics of loops and length variance of links in the generated scattering networks, three amorphous stages emerge. The networks statistics are computed from 1000 random realizations of networks made of 1000 nodes.

In particular, fully amorphous stage ($\alpha \gtrsim 5$) mean that amorphous disorder can be maximally strong in this regime, which is the maximal amorphism attainable on a Euclid plane. An example of fully amorphous networks at $\alpha = 6$ is exhibited in Fig. 2.5b.

It should be emphasized that amorphous networks have fluctuations on phase-delay values proportional to the link lengths, as amorphous disorder induces fluctuations on length of links and these links are practically constructed by lossless monomode waveguides. One can set a wavelength $\lambda_0$ of the lossless monomode waveguides and their corresponding length $l_c$ in the clean limit. A reasonable value of $l_c$ can be $l_c = 0.2\lambda_0$.

### 2.1.5 Mapping between three-port scattering networks with bidirectional phase links and scattering networks with oriented phase links

Up to now, we have studied the configuration of networks, their Floquet band structures, symmetries, as well as the parameterization of their scatterers and of various disorder types. We note that the scattering networks (CC networks) discussed in Ch. 1 consist of oriented links and connected scatterers. Mathematically, these oriented networks represent oriented Eulerian graphs[X], which can be randomized with the same types of disorder we just study,

---

[X] If one take scatterers as nodes and unidirectional links as links in oriented graph (Figs. 1.2 and 1.4), conservation of flow restricts the degree of nodes to be even, shaping it as a oriented (planar) Eulerian graph.

as pointed by Delplace [149] in a theoretical work addressing their topological classification. The non-reciprocal scattering networks analyzed in this thesis are seemingly different, since they feature bidirectional phase links instead of oriented ones, and three-port non-reciprocal scatterers instead of reciprocal ones. However, we will see in this section that there exists a one-to-one correspondence between both types of models. This is important to establish the connection with Floquet topology, as the Floquet mapping in Sec. 1.4 is built between time-Floquet systems and oriented CC networks. A pertinent question thus arises: "Can the non-reciprocal scattering networks with bidirectional links be mapped with time-Floquet systems?". The discussion in this part aims to fill this gap and establish a definitive mapping between two types of network models. For simplicity, we equate "oriented Eulerian graph" with "CC network", and "non-reciprocal network" with "scattering networks comprising three-port scatterers and bidirectional phase links".

Starting with the clean limit case, there exists a formal connection between a honeycomb lattice of circulators with bidirectional links and a Kagome network with oriented links. In the honeycomb circulator network, the scattering events occur at the non-ideal circulators through the scattering matrix $S_0$, while no backscattering occurs along the non-reciprocal links. We can equivalently consider the circulators as perfect, with the wave scattering events occurring along the links. Such a mapping is displayed in Fig. 2.7, where we have highlighted the different paths of the transmitted waves with different colors (these paths are defined only for the perfect circulator case). The resulting network is a Kagome lattice with oriented links inherited from the circulators. The scattering parameters entering the $S_{\text{unit cell}}$ matrices are now combined to enter three $2\times 2$ scattering matrices nodes $S_1$, $S_2$ and $S_3$, thus preserving the six degrees of freedoms per unit cell. Therefore, our non-reciprocal scattering network is formally analogous to a rigorously oriented Kagome graph, described by a unitary matrix, which can be mapped onto the Floquet eigenproblem of a time-Floquet lattice [112, 149], as shown in Fig. 1.4.

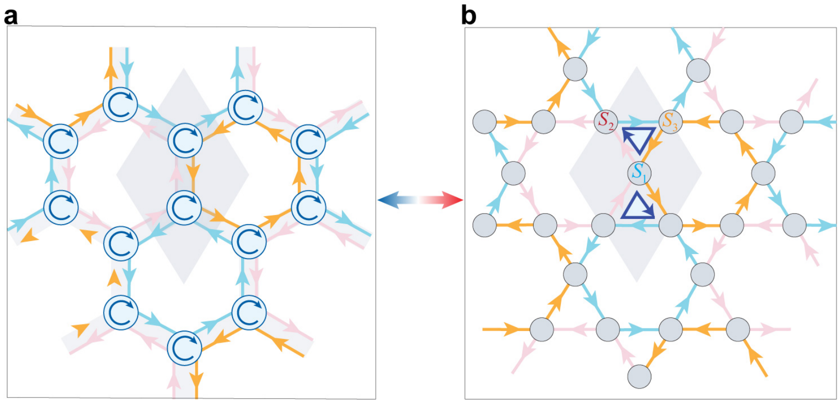

Figure 2.7: **Mapping between a non-reciprocal scattering network in honeycomb lattice and an oriented Eulerian graph in Kagome lattice.**

To show the universality of this mapping, an algorithm for generating random oriented Eulerian graphs (random CC networks) is adopted. As shown in Fig. 2.8a, a randomly generated oriented Eulerian graph [84, 109, 110, 149] describes the wave propagating along directional links and encountering scatterers at the nodes. For planar Eulerian graphs, Veblen theorem states that there always exists two kinds of decomposition of the graph, which consists in unions of disjoint simple cycles (i.e. closed walks containing as many edges as vertices). One of those decompositions is dubbed the *minimal* Veblen decomposition, and consists in fully reflected wave signals upon impinging the scatterers, i.e. analogous to the atomic limit of trivial insulators in solid state physics. In the minimal Veblen decomposition, each simple cycle (the uncolored polygons in Fig. 2.8a) consists in closed propagating loops of wave signals. The other decomposition, the *non-minimal* Veblen decomposition, is formed when all the wave signals are transmitted without scattering, and correspond to the non-atomic limit. For a periodic lattice, the Bloch bands of these two Veblen decompositions are flat and cannot be connected together without closing the bulk gap [112, 149]. Albeit the non-minimal decomposition exhibits closed loops (blue triangles in Fig. 2.8a), it surprisingly leaves a unidirectional boundary wave travelling around the whole graph (orange loop). Such a chiral wave indicates the existence of topological edge states in amorphous networks and aperiodic time-dependent Hamiltonians [149].

We now show how to translate a given oriented Eulerian graph (for example, Fig. 2.8a), into a non-reciprocal network made of 3-port circulators and bidirectional phase links (Fig. 2.8b). Since a graph can be decomposed into simple cycles, we rely on the mapping mechanisms of simple $N$-cycles (Fig. 2.8c) and degree-$M$ nodes (Fig. 2.8d), which connect the simple cycles together. Specifically, a simple cycle corresponds to an unitary non-reciprocal $N$-port scattering device, which can always be modelled by several 3-port non-reciprocal devices (i.e. 3-port circulators, light blue circles) connected by bidirectional links (deep blue lines). As for a degree-$M$ node, if one respectively regards the oriented links pointing to and out of a scatterer as incident and scattered waves, one can map it onto a $M/2$-port scattering device ($M$ being an even number). For $M = 4$, we map it into a perfect bidirectional line, and nodes with degrees $M > 6$ are modelled in the same way as in the $N$-cycle mapping.

In reverse, any non-reciprocal network (for example, Fig. 2.9a) can be converted into an oriented Eulerian graph (Fig. 2.9b) where the possible chiral edge state then becomes visible (orange oriented links). For this, we must make a choice and, for example, use exclusively the mapping mechanism between 3-port ciculators and cycles with $N = 3$, and the mechanism between bidirectional links and degree $M = 4$ nodes.

## 2.2 Momentum-space analysis for networks: Phase-delay band structures and topological invariants

Having covered the fundamentals of scattering networks, our attention shifts towards the toolbox needed to evaluate their physical properties. Band structures are of prime importance, since they enable Chern number $C$ and gap invariant $W_\tau$ necessitated by the Floquet topo-

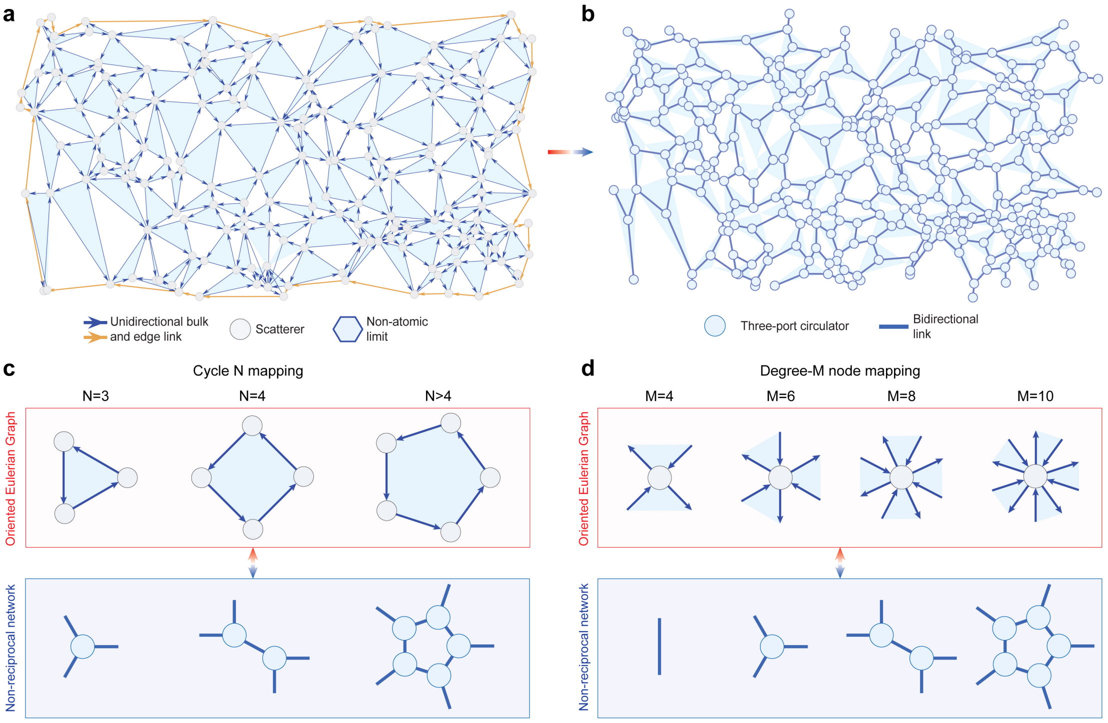
a
b
Unidirectional bulk
and edge link
Scatterer
Non-atomic
limit
Three-port circulator
Bidirectional
link
c
Cycle N mapping
N=3
N=4
N>4
Oriented Eulerian Graph
Non-reciprocal network
d
Degree-M node mapping
M=4
M=6
M=8
M=10
Oriented Eulerian Graph
Non-reciprocal network

Figure 2.8: **Implementation of an oriented Eulerian graph as a non-reciprocal 3-port circulators network. a,** Oriented Eulerian graph, depicting scattering signals in a scattering network. We emphasize the non-atomic limit, in which bulk signals travel in closed loops (following the blue arrows), leaving a large unidirectional loop along the edge (orange). **b,** Non-reciprocal network mapped from the oriented Eulerian graph in panel a. The network is made of three-port circulators connected by bidirectional links. We represent the closed loops of the non-atomic-limit as shaded blue triangles, for easy comparison. **c, d,** Mapping rules. Cycles of order $N$ (panel c) and nodes of degree $M$ (panel d) in oriented Eulerian graphs become specific circulator clusters in non-reciprocal networks. The mapping is defined such that the signal flows are the same in both representations.

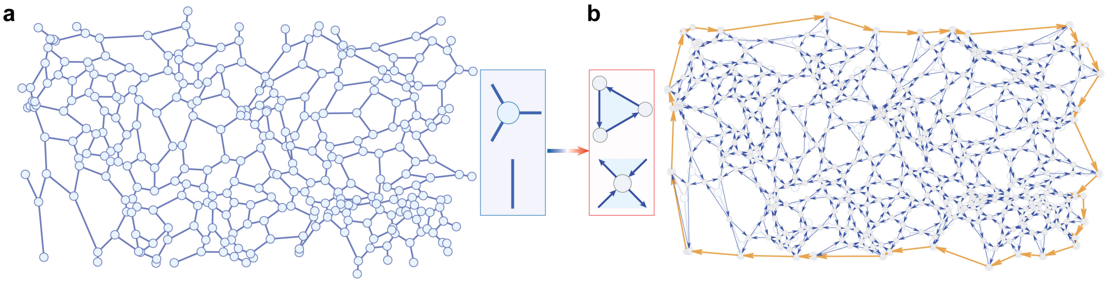

Figure 2.9: **Systematic mapping between amorphous non-reciprocal networks of 3-port circulators and random oriented Eulerian graphs.** For an arbitrary scattering network (panel **a**), we can describe the scattering process by an oriented Eulerian graph (panel **b**). The mapping is based on the simplest mechanism shown in the leftmost panels in Fig. 2.8c and d ($N = 3$ and $M = 4$).

logical band theory. They describes waves/particles' propagation within infinite networks or semi-infinite ones. In addition, they are helpful for checking chiral edge states and localization, since group velocity and positions of Bloch states are accessible from band structures.

### 2.2.1 Clean-limit case

In honeycomb networks extending infinitely in both $\boldsymbol{\alpha}_1$ and $\boldsymbol{\alpha}_2$ directions, we identify all possible extended modes $|b(\boldsymbol{k})\rangle$ with phase delay (quasienergy) $\varphi$ by solving the eigen-equation Eq. (2.5). As propagating waves experience spatially periodic scatterers, continuously translational symmetry is broken in the space, and therefore points $(\boldsymbol{k},\varphi)$ of all the modes form bands. Since these modes extend throughout the network's bulk, the resulting structure is referred to as the bulk band structure. Figs. 2.10(a-b) showcase two examples of bulk band structures within honeycomb networks, specifically for circulators $S_0(\xi,\eta)$ configured at $\xi = 2.5\pi/12, \eta = \pi/12$ and $\xi = 2\pi/12, \eta = 2\pi/12$, respectively. Adjacent bulk bands are separated by band gaps [XI], where photons are forbidden to propagate with certain phase-delay value $\varphi$ in any directions $\boldsymbol{k}$.

To determine the topological phases of periodic networks, as detailed in Eq. (1.1) of Sec. 1.1, we calculate the Chern number $C$ for phase-delay bands by substituting $|\psi\rangle$ with the eigenstate $|b(\boldsymbol{k})\rangle$, derived from Eq. (2.5). Moreover, given the Floquet topology of scattering networks, employing the topological gap invariant $W_\tau$ is crucial for identifying anomalous topological characteristics in these networks [112]. We check $C$ and $W_\tau$ of two examples in Fig. 2.10. We examine $C$ and $W_\tau$ for two cases illustrated in Fig. 2.10. Non-zero Chern numbers in panel (a) signify a Chern phase within the network, whereas panel (b) demonstrates a trivial phase through zero Chern numbers and gap invariants. This topological distinction exhibits the advantages of scattering networks: by tuning two knobs $(\xi,\eta)$, we can access different topological phases, which can be experimentally realized by reconfigurable scatterers or by operating at different frequencies. Furthermore, based on the bulk-edge correspondence [4, 7, 130], one can expect the existences of topological chiral edge states in a finite network made of circulators $S_0(\xi,\eta)|_{\xi=2.5\pi/12,\eta=\pi/12}$, which unidirectionally propagate along its boundaries.

To verify this, we consider a semi-infinite honeycomb network characterized by a ribbon-like supercell. This supercell adheres to periodic boundary conditions along $\boldsymbol{\alpha}_1 = \hat{\boldsymbol{e}}_x$ and incorporates open boundary conditions (OBCs) along the $\boldsymbol{\alpha}_2$ direction, simulating unitary reflections at both the top and bottom edges. Applying the Bloch theorem along the $\boldsymbol{\alpha}_1$ direction allows us to derive an eigenequation similar to Eq. (2.5), expressed as

$$\tilde{S}(k_x)|b(k_x)\rangle = e^{-\mathrm{i}\varphi(k_x)}|b(k_x)\rangle, \tag{2.29}$$

whose eigenphase $\varphi$ with momentum $k_x$ forms ribbon band structures. Their examples are shown in Figs. 2.10 (c-d). In the plot, we color each eigenstate depending on its participation

---

[XI] We do not discuss the Floquet winding metal case [141, 142], which has titled band gap in $[0,2\pi) \times BZ$.

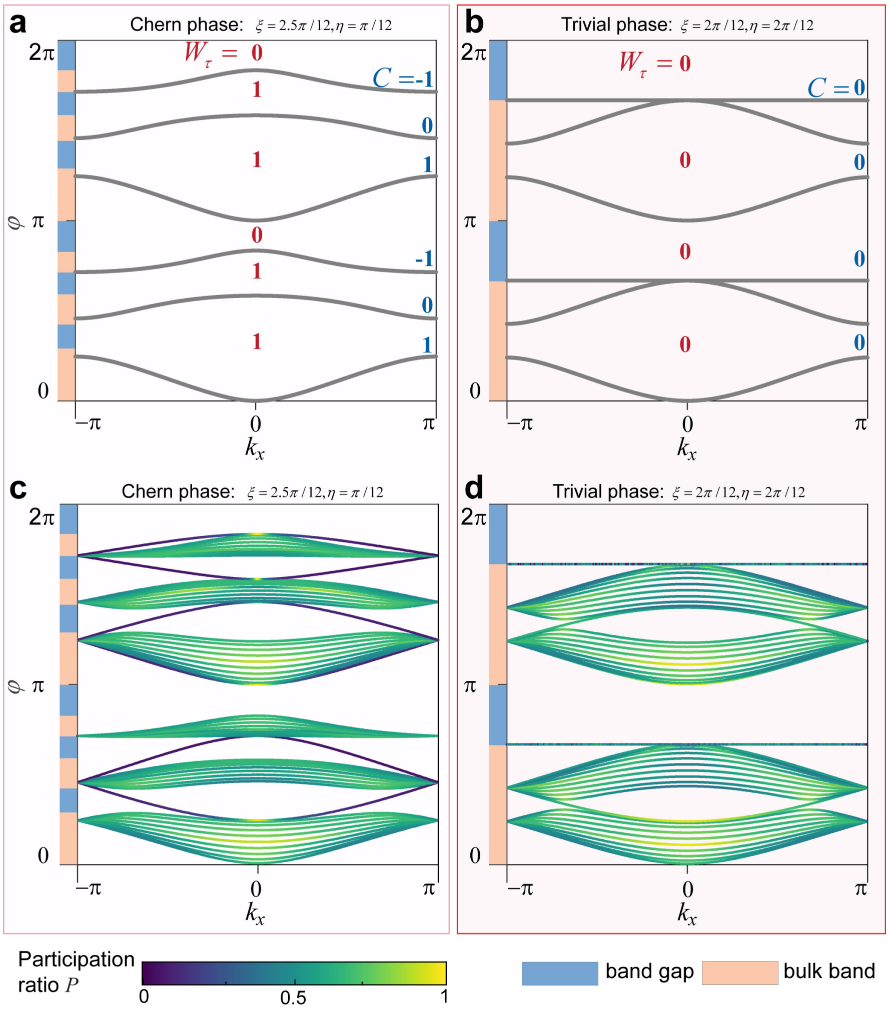

Figure 2.10: **Examples of bulk and ribbon band structures in the periodic honeycomb networks.** Bulk band structures for Chern (**a**) and trivial (**b**) phases in the periodic network. We indicate the calculated Chern number above each band, as well as the gap invariant $W_\tau$ in each gap. **c, d,** Ribbon band structures for the two examples. The eigenstates are colored according to their participation ratio $P$.

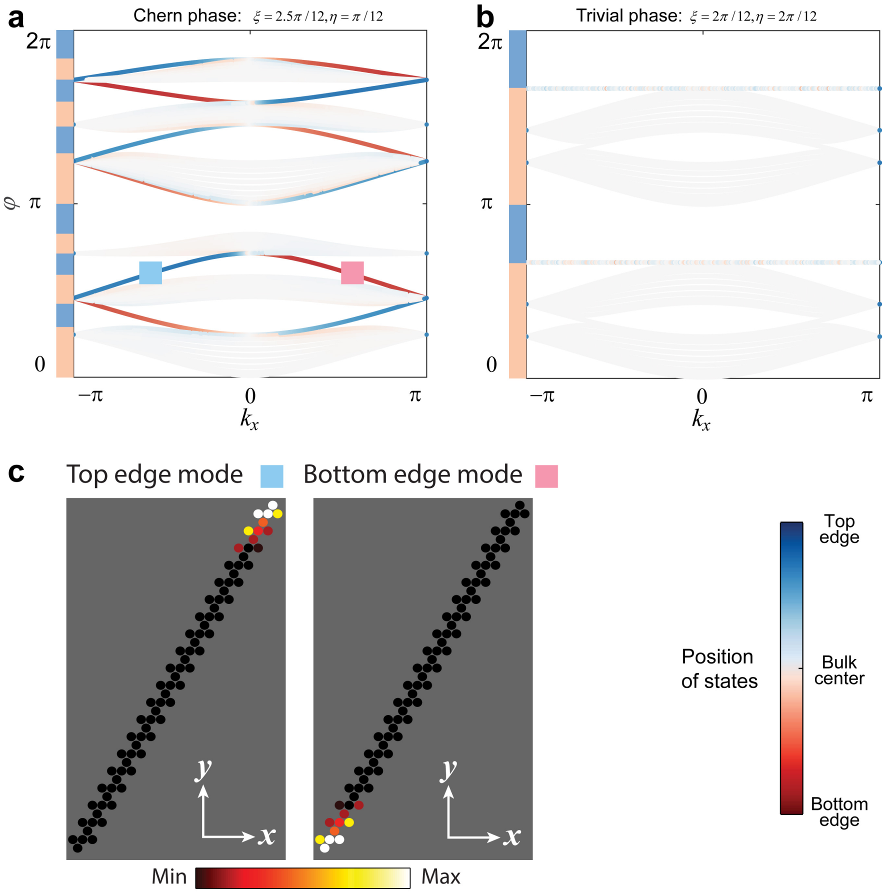

Figure 2.11: **Ribbon band structures colored with eigenstate positions. a, b,** Ribbon Band structures of a supercell colored by positions of eigenstates. In the Chern network (panel a), edge modes localized to the top and bottom in band gaps are shown in red and blue, respectively, while states in the trivial network (panel b) are always in the bulk. **c,** Supercell with examples of the field profiles of topological edge modes, corresponding to the markers in panel a.

ratio, expressed as

$$P = \frac{\left[\sum_i |b_i|^2\right]^2}{N \sum_i |b_i|^4}, \tag{2.30}$$

where $b_i$ is the amplitude of the state $|b\rangle$ at the port $i$. $N$ is the total number of wave signals in the supercell. This metric, crucial for analyzing localization phenomena in disordered and amorphous systems, ranges from 0 for completely localized states to values approaching 1 for fully delocalized states that encompass all sites within the sample [45, 209]. As the only difference between semi-infinite networks and infinite networks is the implementation of OBCs on the $y$ directions which creates boundaries at the top and bottom in the semi-infinite case, ribbon band structures inherit the bulk bands of bulk band structures, but are able to capture eigenmodes localized at the top and bottom boundaries. In Fig. 2.10d, absences of modes in band gaps confirm the trivial phase for the network made of circulators $S_0(\xi,\eta)|_{\xi=2\pi/12,\eta=2\pi/12}$ in panel b. Conversely, as predicted by the topological invariants in panel a, there are gapless edge states occupying some gaps in the ribbon band structures (panel c). These emerged states in the band gaps with low participation ratios are localized at the boundaries, while the bulk bands are composed of extended bulk states with high participation ratios. However, with only participation ratio, we cannot certainly see the chiral properties of these edge states. One way to achieve this is coloring the states in ribbon band structures with their averaged position. The corresponding results for two examples are shown in Fig. 2.11. Specifically, we identify two distinct types of edge states within the band gaps: those localized at the top boundary (colored blue), exhibiting a positive group velocity $v_g = \partial\varphi/\partial k_x$, and those localized at the bottom boundary (colored red), characterized by a negative group velocity. Such phenomenon indicates that these gapless edge states are chiral states, which propagate unidirectionally with no backscattering in the band gaps.

### 2.2.2 Disordered case

Within band theory, topological invariants are traditionally defined on the Bloch manifold, necessitating either continuous or discrete translational symmetry, as previously discussed. However, the presence of distributed disorder disrupts translational symmetry, rendering conventional topological band theory inadequate for capturing the system's topological characteristics. Pioneering studies on topological pumping within disordered quantum Hall effect (QHE) samples [8, 9] offer insights: analyzing how states respond to changes in boundary conditions reveals the system's topological properties.

To be more specific, in the Laughlin's pump model [9, 210, 211], the topological index of a two-dimensional (2D) electron gas penetrated by a magnetic field counts the number of electrons pumped per cycle which considers wrapping up the sample into a cylinder, as shown in the right panel of Fig. 2.12a. An additional magnetic flux $\Phi$ threads the cylinder, which plays the role of the adiabatic driven parameter in this topological pump. The effect of magnetic flux

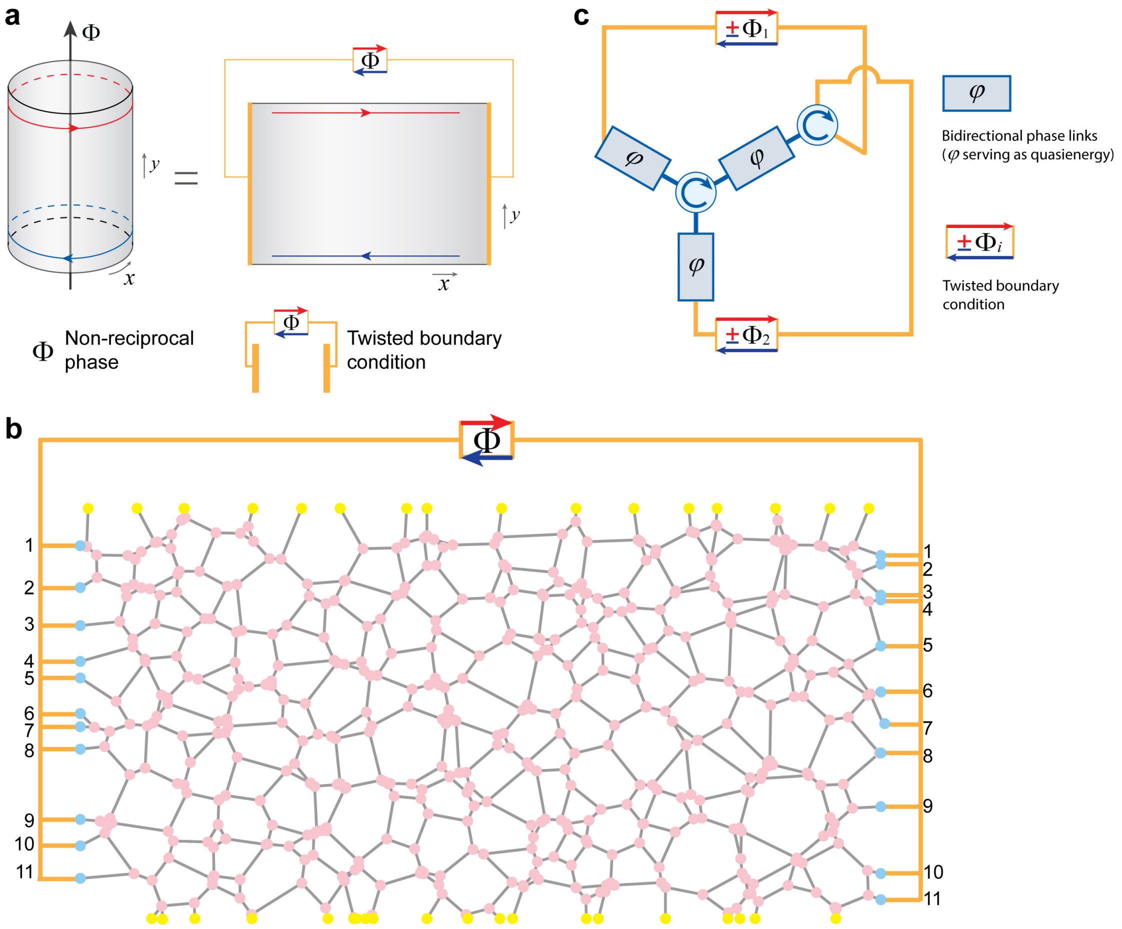
a
Φ
y
x
=
Φ
y
x
Φ Non-reciprocal phase
Φ
Twisted boundary condition
c
±Φ₁
φ
φ
φ
±Φ₂
φ
Bidirectional phase links (φ serving as quasienergy)
±Φᵢ
Twisted boundary condition
b
Φ
1
2
3
4
5
6
7
8
9
10
11
1
2
3
4
5
6
7
8
9
10
11

Figure 2.12: **Twisted boundary condition in scattering networks. a,** The magnetic flux $\Phi$ in the Laughlin's thought experiment (left) can be synthetically realized by the twisted boundary condition (TBC, right) consisting of direction-dependent phase delay $\Phi$. **b,** Illustration of a disordered finite network with TBC. Lateral ports, marked in blue and sharing the same index, are interconnected through TBC. In contrast, the ports at the top and bottom boundaries, highlighted in yellow, employ open boundary conditions (OBC). Any wave outgoing from port $i$ at the left boundary gains a phase term of $\Phi$ and incomes to port $i$ at the right boundary. Conversely, a wave traversing the reverse path experiences a phase shift of $-\Phi$. **c,** Honeycomb unit cell with two TBCs. By varying phase terms $\Phi_1 \in [0, 2\pi)$ and $\Phi_2 \in [0, 2\pi)$ which serves as $k_1 = \boldsymbol{k} \cdot \boldsymbol{\alpha_1}$ and $k_2 = \boldsymbol{k} \cdot \boldsymbol{\alpha_2}$ respectively, we can access the same phase-delay bulk band structure as that obtained from Eq. (2.5).

can be equivalently with a boundary condition, which is alike periodic boundary condition but with a twist phase term $\Phi$, therefore, termed as "twisted boundary condition (TBC)" (left panel in Fig. 2.12a). TBC compels photons to acquire an additional phase of $\Phi$ when tunneling through the boundary from left to right and to adopt a phase of $-\Phi$ when traversing from right to left.

The implementation of TBC on a scattering network is illustrated in Fig. 2.12b. Practically, TBC for photons is exactly a special non-reciprocal phase shifter, as the forward and backward waves experience distinct phase delays[XII]. For a disordered 2D sample with $N \times M$ unit cells, twisted boundary conditions in two directions ($\Phi_1$ and $\Phi_2$) can restore the topological argument in the clean limit, by

$$\begin{cases} |b(\boldsymbol{r}+N\boldsymbol{\alpha}_1)\rangle & = e^{\mathrm{i}\boldsymbol{k}\cdot N\boldsymbol{\alpha}_1}|b(\boldsymbol{r})\rangle \\ |b(\boldsymbol{r}+M\boldsymbol{a}_2)\rangle & = e^{\mathrm{i}\boldsymbol{k}\cdot N\boldsymbol{a}_2}|b(\boldsymbol{r})\rangle, \end{cases} \tag{2.31}$$

where $\boldsymbol{\alpha}_1$ and $\boldsymbol{\alpha}_2$ are the primitive vectors of the clean-limit networks. By setting $\Phi_1 = \boldsymbol{k}\cdot N\boldsymbol{\alpha}_1$ and $\Phi_2 = \boldsymbol{k}\cdot N\boldsymbol{\alpha}_2$, we establish that a disordered finite network with TBCs mirrors a large 2D supercell from a periodic network, effectively shrinking its Brillouin zone via the scaling of reciprocal vectors to $\boldsymbol{\beta}_i/N$, where $\boldsymbol{\beta}_i$ represents the lattice's original reciprocal vectors. In this sense, twist phase is related to the quasi-momentum of the eigenstates. For example, in the clean limit, the bulk band structure of a unit cell in Fig. 2.2c can be equivalently with all the eigenstates of this unit cell attached with two TBCs shown in Fig. 2.12c. TBCs along $\boldsymbol{\alpha}_1$ and $\boldsymbol{\alpha}_2$ directions impose $\Phi_1$ and $\Phi_2$ twist phases for waves crossing longitudinal and horizontal boundaries, respectively. This relationship is further confirmed by demonstrating that TBCs fulfill the role of $\Lambda(\boldsymbol{k})$, as detailed in Eq. (2.4). In fact, this connection provides a way to directly measure eigenstates and eigenvalues in the whole BZ [20, 212]. Consequently, employing the phase-delay bulk bands as outlined in Eq. (2.31) allows for the definition of Chern number $C$ within disordered networks. In addition, the disordered network with TBC shown in Fig. 2.12b can provide the ribbon phase-delay band structure of this supercell, which is helpful to check the localization of bulk states (flat bands) and to find mobility gaps accommodating topological edge states in disordered regimes [80, 213, 214].

Furthermore it is worth to note that Chern number $C$ in disordered networks with TBCs [215, 216] are equivalent to the real-space topological invariants in the thermodynamic limit, including noncommutative form[XIII] [55, 57, 217], Bott index [218–220], and local Chern marker [221].

---

[XII] The experimental implementation of this non-reciprocal phase shifter will be described in Ch. 5.

[XIII] It transforms the partial derivative and integral in Brillouin zone to the noncommutative form of real space.

## 2.3 Real space analysis of scattering networks: observables in finite networks

Having analyzed infinite and semi-infinite networks through momentum-space methods, we now examine real-space observables in finite networks. This includes transport through external ports and cavity eigenstates in networks isolated from the external environment. In the ending of this part, with an example, we show how real-space analysis, momentum-space analysis, and gap invariants are consistent with each other.

### 2.3.1 Transport with external ports

Topological insulators exhibit unidirectionally unitary transports, underpinned by topological edge states. This phenomenon aligns with the topological invariant as described by the bulk-edge correspondence. Therefore, understanding of transport properties in "open" scattering networks is crucial for theoretically confirmations of topological phases, experimental verification and applications of topological edge states. Additionally, establishing a relationship between the transport of an observable and its topological index can help explore the robustness of topological edge states against disorder.

We consider an arbitrary unitary scattering network formed by interconnecting scattering components. We assume that the network is now finite and open: $N_0$ ports are exterior probes, while the $N$ other ports of the scattering components are either connected to each other by phase delay lines (e.g. inside the bulk, simply connected (PBC), or TBC) or terminated with unitary boundary conditions (full reflection, e.g. on the edge). The total number of ports is $N + N_0$. Accordingly, one can write

$$S|b_{total}\rangle = |a_{total}\rangle, \tag{2.32}$$

where $S$ is a $(N + N_0) \times (N + N_0)$ unitary matrix composed of sub-blocks containing the scattering matrices of elementary components, converting the waves incoming at ports, with amplitude $|b_{total}\rangle$, to outgoing waves with amplitude $|a_{total}\rangle$. Since we can choose freely how we order the ports in these column vectors, we can classify them, starting on the $N_0$ first lines with the exterior ports, and filling up the rest with the interior ones, then

$$S = \begin{bmatrix} S_{ext} & S_{out} \\ S_{in} & S_{net} \end{bmatrix}, \qquad |a_{total}\rangle = \begin{bmatrix} |a_{probe}\rangle \\ |a_{net}\rangle \end{bmatrix}, \qquad |b_{total}\rangle = \begin{bmatrix} |b_{probe}\rangle \\ |b_{net}\rangle \end{bmatrix}. \tag{2.33}$$

Here, $S_{ext}$ is a $N_0 \times N_0$ matrix, describing a direct exterior coupling between the $N_0$ external probes. $S_{out}$ ($N_0 \times N$ matrix) depicts the coupling of waves from the network to the probes, while $S_{in}$ ($N \times N_0$ matrix) represents the inverse process. $S_{net}$ ($N \times N$ matrix) represents the coupling between ports in the network. On the other hand, from the interconnection information and unitary boundary conditions, we can form a unitary $N \times N$ connectivity matrix $C_{net}$ defined as with

$$C_{net}|b_{net}\rangle = |a_{net}\rangle. \tag{2.34}$$

From Eqs. (2.32) and (2.33), we get

$$S_{ext}|b_{probe}\rangle + S_{out}|b_{net}\rangle = |a_{probe}\rangle \tag{2.35}$$

$$S_{in}|b_{probe}\rangle + S_{net}|b_{net}\rangle = |a_{net}\rangle. \tag{2.36}$$

We want to characterize the relation between $|a_{probe}\rangle$ and $|b_{probe}\rangle$ through a scattering matrix $S_{probe}$ defined as

$$|a_{probe}\rangle \equiv S_{probe}|b_{probe}\rangle \ . \tag{2.37}$$

Substituting Eq. (2.34) into Eqs. (2.35) and (2.36), we find the expression

$$S_{probe} = S_{ext} + S_{out}(C_{net} - S_{net})^{-1}S_{in} \ . \tag{2.38}$$

As shown in Eq. (2.38), the total scattering matrix $S_{probe}$ among the external ports is the summation of two scattering terms. The first term $S_{ext}$ represents immediate scattering, as it is a block matrix of $S$ and does not contain any information about network interconnections $C_{net}$. Conversely, the second term, $S_{out}(C_{net} - S_{net})^{-1}S_{in}$, depicts scattering responses attributed to the network, in which $S_{in}$ describes the channels coupled into "Network Green function" $(C_{net}-S_{net})^{-1}$ before $S_{out}$ scatters photons out of the network. In fact, the formula in Eq. (2.38) can be seen as the scattering network version of the Mahaux-Weidenmüller formula usually used to express the scattering matrix of the probes in terms of a Hamiltonian description of the couplings [222–224]. It is worth noticing that although $S_{out}$ and $S_{in}$ are not unitary, the unitarity of $S$ and $C_{net}$ guarantee that $S_{probe}$ is unitary, whenever $C_{net} - S_{net}$ is invertible. This can be checked by a direct calculation, shown in Appendix. C.

The field map of the scattering network (i.e. $|a_{net}\rangle$ or $|b_{net}\rangle$) can then be obtained for a given excitation $|b_{probe}\rangle$ at the probes, by substituting the Eq. (2.34) into Eq. (2.36), yielding

$$|b_{net}\rangle = (C_{net} - S_{net})^{-1}S_{in}|b_{probe}\rangle. \tag{2.39}$$

In simulations and experiments, to faithfully reproduce the topological states in an infinite system, one can determine the size of a network (even disordered one) by a simpler rule. For 2D case, the network longitudinal and transverse sizes $L$ should follow $L >> \lambda$, where $\lambda$ is the typical decay length of the state at the phase-delay value $\varphi$ of the network. Otherwise, the bulk states are not insulating enough and contribute to the transports.

Furthermore, for precise evaluation of transport through networks, similar to quantum transport settings where additional sections ensure smooth transitions to ideal leads [83, 225–228], ports in the scattering network also require appropriate configurations to accurately capture the network's intrinsic scattering properties. We assume that photons enter through an external port $i$ and initially encounter a scatterer in the network. If this scatterer itself possesses a reflection at the port $i$, photons associated with such reflection are immediately reflected at the port $i$ rather than being reflected due to interfering with modes excited in the network, as indicated by the diagonal term in $S_{ext}$ of Eq. (2.38). To eliminate these immediate reflections at the external ports, one can opt for perfect circulators just at the external ports, whose chirality is the same with that of circulators in the networks. This port setting ensures all the inputted photons directly enter the network, which is similar to impedance matching.

It is also helpful to derive transfer matrix between two sides, which leads to the concept of conductance in scattering networks. Assume there are $N_0$ external ports at both left and right sides of a finite network. We represent the incoming and outgoing waves for left (right) side by $|b_L\rangle$ ($|b_R\rangle$ ) and $|a_L\rangle$ ($|a_R\rangle$), respectively. With Eq. (2.38), one get

$$S\begin{bmatrix}|b_L\rangle\\|b_R\rangle\end{bmatrix}=\begin{bmatrix}|a_L\rangle\\|a_R\rangle\end{bmatrix}. \tag{2.40}$$

We then form the following block representation of the scattering matrix $S$, as

$$S=\begin{bmatrix}S_{11} & S_{12}\\S_{21} & S_{22}\end{bmatrix}. \tag{2.41}$$

The conductance is defined as

$$G=\mathrm{Tr}\left[S_{12}^{\dagger}S_{12}\right]. \tag{2.42}$$

By assuming $S_{12}$ is invertible, we get

$$\begin{cases}|b_L\rangle=S_{21}-S_{22}S_{12}^{-1}S_{11}|a_R\rangle+S_{22}S_{12}^{-1}|b_R\rangle\\|a_L\rangle=-S_{12}^{-1}S_{11}|a_R\rangle+S_{12}^{-1}|b_R\rangle.\end{cases} \tag{2.43}$$

Therefore, we can define the transfer matrix $T$, which transfers waves at left external ports to waves at right external ports, as

$$T\begin{bmatrix}|b_L\rangle\\|a_L\rangle\end{bmatrix}=\begin{bmatrix}|a_R\rangle\\|b_R\rangle\end{bmatrix},\quad T=\begin{bmatrix}S_{21}-S_{22}S_{12}^{-1}S_{11} & S_{22}S_{12}^{-1}\\-S_{12}^{-1}S_{11} & S_{12}^{-1}\end{bmatrix}. \tag{2.44}$$

### 2.3.2 Cavity without external ports

When there are no external ports, a finite scattering networks becomes a cavity. To figure out its cavity eigenstates which forms a phase-delay spectrum, we look back at the Eqs. (2.32) and

(2.34), where zero external port means $|a_{total}\rangle = |a_{net}\rangle$ and $|b_{total}\rangle = |b_{net}\rangle$, forming

$$\begin{cases} S|b_{total}\rangle = |a_{total}\rangle \\ C_{net}|b_{total}\rangle = |a_{total}\rangle. \end{cases} \tag{2.45}$$

We can assume that there is a phase-delay term $\varphi$ on each interconnection and each unitary reflection [XIV]. As a result, $C_{net}$ can be decomposed into the multiple of a common phase term $e^{-\mathrm{i}\varphi}$ and a connectivity matrix $\tilde{C}_{net}$. This leads to an eigenequation for the cavity-like network, expressed as

$$\tilde{C}_{net}^{-1} S|b_{total}\rangle = e^{-\mathrm{i}\varphi}|b_{total}\rangle. \tag{2.46}$$

The eigenphases and eigenstates of $\tilde{C}_{net}^{-1}S$ construct the phase-delay spectrum. It is worth to noting that the phase-delay band structure of disordered networks with TBCs in Sec. 2.2 can be obtained by solving Eq. (2.46), in which $C_{net}$ is decorated with twisted phase terms $\Phi_1$ and $\Phi_2$ from TBCs. With the phase-delay spectrum, density of states can be obtained by following Appendix. A.

### 2.3.3 Mutually consistent observables in analysis

We already elucidated two main types of observables: band structures and topological invariants in momentum space for infinite or semi-infinite networks; transports and cavity eigenstates in finite networks. In the ending of this section, we take an example of a finite honeycomb network in the clean limit to show how to utilize them for analyzing topological features and localization-delocalization phenomena. In this example, the used circulators are of $\xi = -\eta = 3.5\pi/12$. Figure 2.13 examines the connections among topological invariants, band structures, edge transport across two external ports, and eigenstates in a closed network. When $\varphi$ falls in a topological band gap indicated by a non-vanishing gap invariant $W_\tau$, transmission is unity and mediated by the edge modes (top panel in Fig. 2.13b), and spectrum shows DOS, skin distance $d_s$, and participation ratio $P$ reaching low values, confirming the boundary localized states. Conversely, if $\varphi$ belongs to a trivial band gap, transmission is impeded due to vanishing DOS. Finally, if $\varphi$ falls in a bulk band, the transmission fluctuates with $\varphi$, depending on the excited bulk modal superposition interference at the output port, and their eigenstates in the close network are extended in the bulk (bottom panel in Fig. 2.13b).

Briefly, in a network with a phase-delay $\varphi$, transport between external ports—where some are with signals inputted and others are matched[XV], are governed by the superposition of eigenstates within the $\varphi - \delta\varphi/2$ to $\varphi + \delta\varphi/2$ range in the closed network. Moreover, when the size of the closed network approaches the thermodynamic limit, DOS($\varphi$) derived from its spectrum matches that calculated from the bulk band structure, and one can recover the bulk band structure by performing spatial Fourier transformation on all the eigenstates of

---

[XIV] Under disordered cases, $\varphi$ is an additional common term for all phase links.

[XV] At matched ports, photons can leave the network but no photon is inputted there.

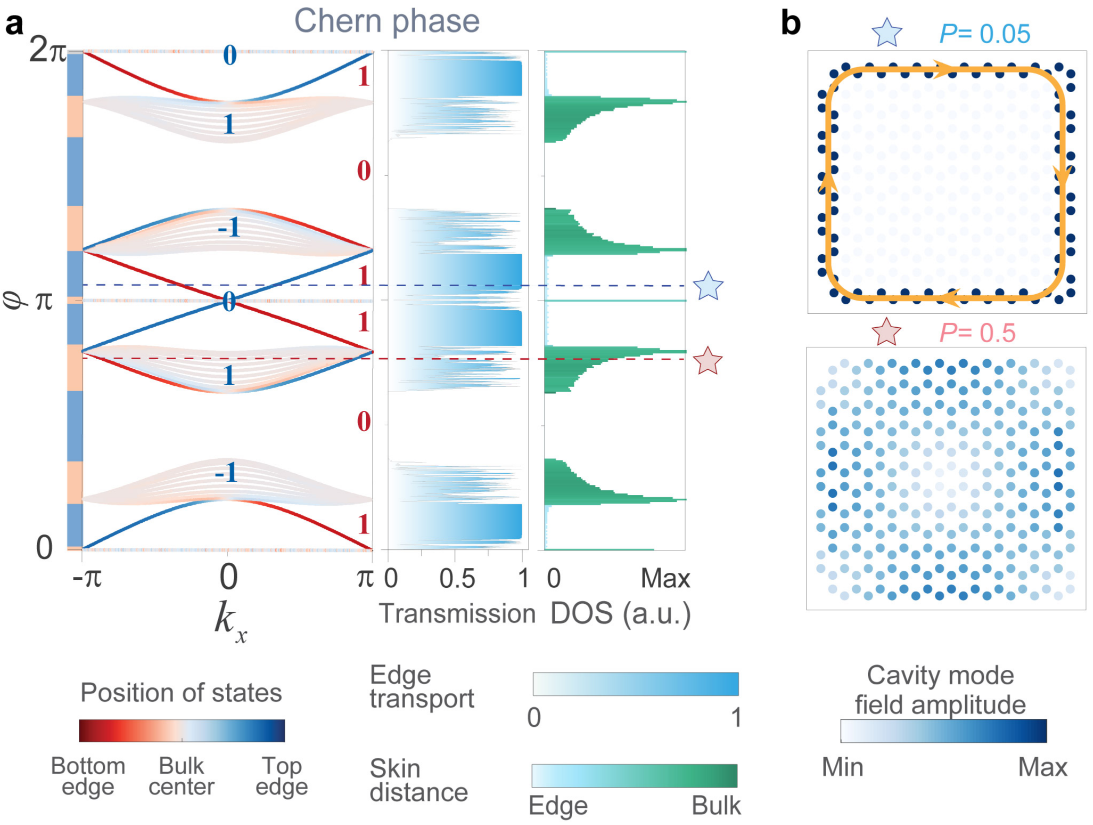

Figure 2.13: **Connections between momentum-space observables and real-space observables.** **a,** We take a clean-limit honeycomb network built by circulators of $\xi = -\eta = 3.5\pi/12$. The left panel displays invariants for infinite networks—Chern number $C$ in blue and gap invariant $W_\tau$ in red—alongside the band structures of a semi-infinite network. For each phase-delay $\varphi$, we correlate these momentum-space observables with transport metrics between two boundary ports in open networks (center panel) and the DOS of eigenstates in closed networks (right panel), highlighted by their skin distances. **b,** Profiles of eigenstate fields at two specific phase-delay values. The top profile represents topological eigenstates localized at the boundary in the closed network (low $P$), indicating unidirectional transport underpinned by non-trivial topology ($C \neq 0, W_\tau = 1$). Conversely, bottom profile shows a bulk eigenstate extending throughout in the network, characterized by a high $P$.

the closed network. This principle is utilized in photonic experiments through the design of sufficiently large structures (at least $10 \times 10$ unit cells) to measure DOS and bulk band structure [229–232].

These observables in infinite, semi-infinite, open, and closed networks are essential for characterizing the localization and delocalization phenomena in disordered scattering networks. For example, nonzero transport, with large $P$ of eigenstates and non-flat bulk bands for supercell, indicates the existence of delocalized states. Transport can vanish with flat bulk bands in band structures and low $P$ of eigenstates, if the randomness strength is sufficiently strong due to Anderson localization. This transport does not disappear abruptly; rather, it gradually shifts upward before annihilating within the spectrum [XVI] [233].

## 2.4 Localization length calculations and scaling analysis

Localization and correlation lengths play a central role in analyzing phase transitions and critical behaviors in disordered condensed matter systems [95, 101–104, 106–108, 234] and photonics [60, 61, 235–237]. Benefiting from the direct availability of transfer matrices, network models are particularly suited to quantitative scaling analysis and describing phase transitions. Early arts focused on scaling theory of localization [238, 239] and the study of metal-insulator transitions in QHE [84, 97, 98], exhibiting precise critical exponents. In recent years, these networks have been widely applied on disordered topological systems, to quantitatively characterize topological phase boundaries and their universality, including topological systems protected by time-reversal symmetry [99, 100, 103], in 2D or 3D [105]. In this section, we detail the transfer matrix method to study localization processes and topological phase transitions in unitary disordered scattering networks. We will apply this method in Ch. 6.

To derive the localization length, we work on a quasi one-dimensional (1D) network, whose total longitudinal size $M_x$ is much larger than its transverse size $L_y$. Both lengths are defined by counting the number of ports on the $x$ and $y$ directions, respectively. The number of ports on any opposite sides are equal. We look at the properties of the transfer matrix $T$ connecting the fields of the ports on the right boundary to the fields of the ports on the left boundary, i.e. in the $x$ direction. $T$ is then a $2L_y \times 2L_y$ pseudo unitary matrix [240], defined by the scattering relations among the $2L_y$ ports located on on the lateral sides (Eq. (2.44) in Sec. 2.3). Due to the pseudo unitarity of $T$, the eigenvalues of the $2L_y \times 2L_y$ Hermitian matrix $T^\dagger T$ can be written as $\exp(\pm 2X_j)$ with eigenstates $|\Psi_j^\pm\rangle$, where $X_j$ are Lyapunov exponents such that $0 < X_1 < X_2 < \cdots < X_{L_y}$. As the wave transport counted over $2L_y$ eigenchannels is dominated by the contribution of the smallest Lyapunov exponent $X_1 = \langle \Psi_1^- | T^\dagger T | \Psi_1^- \rangle$, the localization length $\lambda$ is defined as the inverse of the smallest Lyapunov exponent [95, 101, 239] as

$$\lambda = \lim_{M_x \to \infty} \frac{M_x}{X_1}. \tag{2.47}$$

Yet, calculating and decomposing $T$ leads to large numerical errors when $M_x$ is large (>20), yet $M_x$ should be at least millions to ensure $M_x > \lambda$. To reduce numerical errors in the determination of the localization length, we uniformly slice the long quasi-1D network along the $x$ direction, with a slice width $L_x$, and get slices indexed from $i = 1$ to $M_x / L_x$. We calculate the transfer matrix $T_i$ of each slice, and then multiply them by iterative QR decomposition

---

[XVI] A phenomenon called levitation and annihilation [67, 71].

[241]:

$$\begin{cases} T = \prod_{i}^{M_x/L_x} T_i; \\ T_1 = Q_1 R_1; \\ T_{i+1} Q_i = Q_{i+1} R_{i+1}, \quad i > 1. \end{cases} \tag{2.48}$$

Therefore, we get

$$T = Q_{M_x/L_x} \left[ \prod_{i}^{M_x/L_x} R_i \right] \equiv Q_T R_T, \tag{2.49}$$

where $R_T \equiv \prod_i^{M_x/L_x} R_i$ and $Q_T \equiv Q_{M_x/L_x}$. As Lyapunov exponents are exactly the diagonal elements of the upper triangular matrix $R_T$, we can therefore get

$$\lambda = \lim_{M_x \to \infty} \frac{M_x}{\min_j |\ln R_T(j,j)|}. \tag{2.50}$$

In this way, we maintain a good accuracy on the eigenvalue with modulus closest to unity. Generally, the smaller $L_x$ is, the more accurate $T$ is. Here, we take $L_x \in \{4, 8, 12, 16\}$. In Fig. 2.14a, we show a slice of such a system of length $L_x = 4$ ($L_x \ll M_x$ ), and of transverse size $L_y = 8$. We consider open boundary conditions (OBC) in the $y$-direction (Fig. 2.14a), namely edges with unitary reflection. As indicated by Eq. (2.50), calculating the exact localization length $\lambda$ requires taking $M_x$ to infinity. Also, in disordered networks, $T_i$ is taken from a statistical ensemble of finite quasi-1D network slices which are composed of specified microscopic scatterers and under prescribed disorder statistics. Therefore, it seems that one should take $M_x$ very large and average $\lambda$ over many calculations. Fortunately, as localization length $\lambda$ is a finite and self-averaging quantity, we can approximate $\lambda$ by only one calculation on a finite, but long enough, quasi-1D network with $M_x \in [5 \times 10^5, 2 \times 10^6]$.

One can identify whether a system is in an insulating or metallic phase by analysing how normalized localization length $\Lambda(L_y) = \lambda / L_y$ scales when increasing the width $L_y$, as demonstrated in prior arts [242]. This is traditionally done by checking the dependence of $\Lambda(L_y)$ on the transverse width $L_y$, when applying periodic boundary condition (PBC) in the $y$ direction (Fig. 2.14c, thus in a setting with no top and bottom edges). For a metal, $\Lambda(L_y)$ increases with $L_y$, and $\Lambda(L_y) \to \infty$ as $L_y \to \infty$. On the contrary, for an insulator, $\Lambda(L_y)$ decreases upon scaling $L_y$, and $\Lambda(L_y) \to 0$ as $L_y \to \infty$. At a critical transition, $\Lambda$ should be invariant upon scaling. This method, however, is not sufficient to distinguish topological and trivial insulators. To this end, one should repeat the study in the presence of edges, namely with PBC replaced by OBC [11]. Since non-trivial topology manifests itself by the existence of chiral edge states, $\Lambda(L_y)$ should increase monotonically, like for a metal. On the other hand, a topologically trivial insulating phase would be insensitive to the modification of the boundary condition [11], due to the absence of edge states. An example of this scaling analysis near a topological transition is

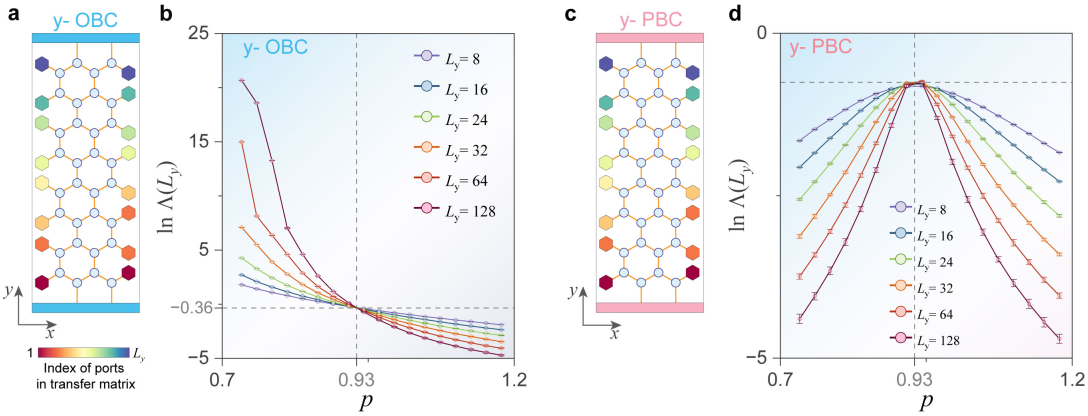

Figure 2.14: **Topological phase transitions by scaling analysis of the localization length. a, c,** A slice of a quasi-1D network with width $L_y = 8$ is used for iteratively calculating the transfer matrix. The longitudinal dimension contains four elementary slices, therefore $L_x = 4$. In panel a, we consider open boundary conditions (OBC) in the $y$-direction, namely edges with unitary reflection, while in panel c we apply periodic boundary condition (PBC) in the $y$ direction by wrapping the network into a cylinder. **b, d,** Example for scaling analysis. Consider evolution of the normalized localization length $\Lambda(L_y) = \lambda / L_y$ on the segment of $p \in [0.73, 1.18]$ under y-OBC (panel b) and y-PBC (panel d). $p$ is just a meaningless parameter to represent a line in the parameter space. $L_y$ is increased from 8 to 128. The left and right parts of the plot are topological and trivial phases, respectively, and are separated by the critical point $p \approx 0.93$ (dashed lines) characterized by scale invariance.

shown in Figs. 2.14(b, d), where the left part of the plot corresponds to a topological phase and the right part to a trivial insulating phase.

## 2.5 Topological scattering invariant in disordered scattering networks.

### 2.5.1 Topological invariants in disordered systems

Different theoretical approaches have been developed to tackle the topology of disordered systems, where the Brillouin zone cannot be used anymore. Various invariants have been identified, such as topological invariants with TBCs [215, 216] in the shrunken momentum space (in Sec. 2.2) and real-space topological invariants (noncommutative form [55, 57, 217], Bott index [218–220], and local Chern marker [221]).

However, these indices, based on the band invariant- Chern number, cannot capture anomalous topological phases in the context of disordered unitary systems. Other works addressed the topological characterizations of disordered unitary systems where anomalous phases may emerge, such as time-Floquet systems and scattering networks [132, 149, 163], but their potential experimental measurement remains elusive. Here, we introduce a novel topological index derived from the response of scattering matrices to twisted boundary conditions in our photonic scattering network, inspired by Laughlin's pump argument [173]. This index, therefore termed as "**Topological scattering invariant**", is accessible for any network and measurable in our experiments, via scattering measurements involving an exterior probe.

### 2.5.2 Topological scattering invariant

Physically, topological invariants are linked to the transport response of a disordered system when boundary conditions are varied e.g. the quantum Hall conductance [183] and polarization [184]. For instance, in disordered quantum Hall samples, the topological invariant with twisted boundary condition (TBC) is related with the number of pumped electrons by adiabatically changing magnetic flux piercing the system [9].

Transposed to scattering networks, this idea suggests the network setting shown in Fig. 2.15b, where the network with TBC in Fig. 2.12b is enclosed with $N_0$ external probes. With TBC, the wave is phase shifted by $\Phi$ ($-\Phi$) when propagating from the left to right (right to left) boundaries, respectively. At fixed $\Phi$, say for instance $\Phi = 0$, such non-reciprocal phase emulates a Bloch periodic boundary condition, guaranteeing that the eigenstates and eigenvalues of the system form a discretization of the band structure of an infinite strip in the $x$ direction, but finite in $y$. Such a discretization is schematically represented in 2.15c, for two bulk bands and one chiral edge state. The discrete set of eigenvalues (dots) sit on the band structure of the infinite strip, sampling it at a discrete number of points. Now, imagine that we increase the flux $\Phi$ adiabatically from 0 to $2\pi$ (we call this a cycle). Naturally, the discretized band structure must be the same at the beginning and end of this process. However, during this process, the points all move to the right, along the bands, since the increase of the Bloch phase imparts one quantum of momentum in the $x$ direction. Therefore, each point replaces its right-hand neighbor at the end of this adiabatic cycle.

The crux is now the following: Imagine that after fixing the phase delay $\varphi$ (for example at one of the dashed-yellow lines in the Fig. 2.15c), one is able to algebraically count the number of states which, during a cycle, cross this value of $\varphi$. For a bulk band ($\varphi$=$\varphi_0$), there must be as many states crossing it in one direction (upwards) than in reverse (downwards). Thus, one would find a zero net number of crossings. The situation would, however, be different for a situation where one would cross one or several chiral edge state bands ($\varphi$=$\varphi_1$), and counting the number of crossing would be the same as counting the number of edge states. Finally, in a spectral range where both bulk and edge states exist ($\varphi$=$\varphi_2$), the contributions of all the crossings with bulk states would compensate, leaving only those of the edge states. Thus, counting the number of crossings during a cycle is a direct count of the number of chiral edge states.

To perform this count in practice, we need an extra trick. The crossing of an eigenstate is a resonance: for a particular value of $\Phi$, we can maximally couple to an eigenstate[XVII].

---

[XVII] We cannot give the exact value for the maximal coupling $\Phi$; but from Fig. 2.15c there must be a crossing

Fortunately, resonances would influence a scattering measurement performed during the adiabatic cycle [223, 224, 243–246], as shown in Fig. 2.15b. Thus, we put $N_0$ external probes in Fig. 2.12, and assume that the system is large enough such that the weakly-coupled probes will not significantly disturb the states. It is possible that a given probe cannot detect all the resonances, as the amplitude of a state can vanish at the specific location of the probe. For example, the probe at the bottom edge cannot detect an edge state localized at the top. Thus, if we put probes at the bottom side, we can probe only the bottom edge states and almost all the bulk states.

In the following, we characterize the topological non-trivial pump in arbitrary scattering networks by the winding number of the determinant of $S_{probe}$ upon varying $\Phi$ from 0 to $2\pi$, as those windings count the resonances of $S_{probe}$ at a given $\varphi$ [223]. Indeed, the eigenvalues $\{e^{\mathrm{i}\theta_1},\cdots,e^{\mathrm{i}\theta_{N_0}}\}$ of $S_{probe}$ are distributed on the unity circle. As $S_{probe}$ recovers after one cycle of $\Phi$, the trajectories of eigenphase $\theta_j(\Phi)$ exhibit $2\pi$ normalized quantized phase accumulations [223, 224, 247]. Therefore, the winding number $W[\varphi]$ can be defined by the homotopy invariant ($\pi_1(U(N_0))=\mathbb{Z}$)

$$W[\varphi]=\frac{1}{2\pi}\int d\theta(\Phi)=\frac{1}{2\pi\mathrm{i}}\int d\Phi\Big(\frac{d\ln\det(S_{probe})}{d\Phi}\Big)=\frac{1}{2\pi\mathrm{i}}\int d\Phi\mathrm{Tr}\Big(S^{\dagger}_{probe}\frac{dS_{probe}}{d\Phi}\Big),\tag{2.51}$$

where $\theta(\Phi)$ is the sum of eigenphases of $S_{probe}$, given as

$$\theta(\Phi)=\sum_{i=1}^{N_0}\theta_j(\Phi).\tag{2.52}$$

Considering one exterior probe only ($N_0=1$), the eigenphase $\theta_1$ of $S_{probe}$ is exactly the probe reflection phase, due to the unitarity of $S_{probe}$.

Note that generally, a resonance induces a $\pi$ phase shift in the scattering states, therefore a $2\pi$ phase shift in the reflection phase ($N_0=1$), or in the phase of determinant of $S_{probe}$ (i.e. $\theta(\Phi)$). For a topologically non-trivial winding [9, 163, 223], the emergence of resonances in the course of varying $\Phi$ cannot be eliminated by a smooth deformation of the scattering matrix $S_{probe}$ of the system. It corresponds to the non-contractible loop, or non-trivial winding, of $\theta(\Phi)$, for which the resonance condition, wherever it sits on the circle, cannot be avoided, as shown in Fig. 2.15d. We can also define the fluctuation $\theta_F$ of $\theta(\Phi)$, expressed as

$$\theta_F=\max_{\{\Phi_1,\Phi_2\}}\Big[\int_{\Phi_1}^{\Phi_2}d\theta(\Phi)\Big].\tag{2.53}$$

Taking a finite honeycomb network in a Chern phase as an example, whose ribbon band structure is shown in Fig. 2.15e, we compute $\theta(\Phi)$ and the winding numbers $W[\varphi]$ at $\varphi=1.1$ (topological band gap, Fig. 2.15f), $\varphi=0.5$ (bulk band, Fig. 2.15g) and $\varphi=3$ (trivial band gap,

---

between the phase-delay (quasi-energy) line $\varphi=\varphi_0$ with the eigenstate movement from $n_k\to n_{k+1}$ induced by adiabatic cycle of $\Phi$.

Fig. 2.15h). As expected, a non-zero winding of the reflection coefficient is accompanied with a topological edge state, while bulk states and band gaps do not yield any winding. Yet, despite the absence of winding for $W[\varphi = 0.5] = W[\varphi = 3] = 0$ their fluctuations $\theta_F$ are very different, which could be used to distinguish the effect of bulk states from band gaps.

### 2.5.3 Relation with Wigner- Smith operator

To bring a deeper insight, the above physics and formula involving $\theta(\Phi)$ imply a relation between $\frac{d\theta(\Phi)}{d\Phi} = \mathrm{Tr}(S^{\dagger}_{probe}\frac{dS_{probe}}{d\Phi})$ and the Wigner-Smith operator [60, 248–250] $Q = -iS^{\dagger}\frac{dS}{dE}$ with density of states (DOS) $\rho(\omega) = \frac{c}{2\pi}\mathrm{Tr}(Q)$. As known, the time of resonances is directly related with density of states at a given $\varphi$ [60, 251]. The fluctuation $\theta_F$ of $\theta(\Phi)$ depicts the movement of the averaged center (expectation value of horizontal position operator) of wave packets during the pumping cycle. Therefore, we can identify the difference between the bulk bands ($W[\varphi] = 0$) with delocalized states and the trivial band ($W[\varphi] = 0$) by non-zero and zero $\theta_F$, respectively. Clearly, the above physics is universal and is valid for any system, in particular that we are not limited to the periodic ones. Consequently, the presented winding number of probe scatting matrices works for any planar network, even in the strong disorder cases where Anderson localization emerges.

To sum up, the main advantages of the proposed topological scattering index are that it provides a measurable and quantized value, defined on solid ground and applicable for any network even in the strong disorder cases where Anderson localization emerges. This topological scattering index just detects what happens at the very end of the sample. It is an observable which is easy to measure in the practice, via extracting the scattering matrix of $N_0$ external probes (we use $N_0 = 2$ in experiments).

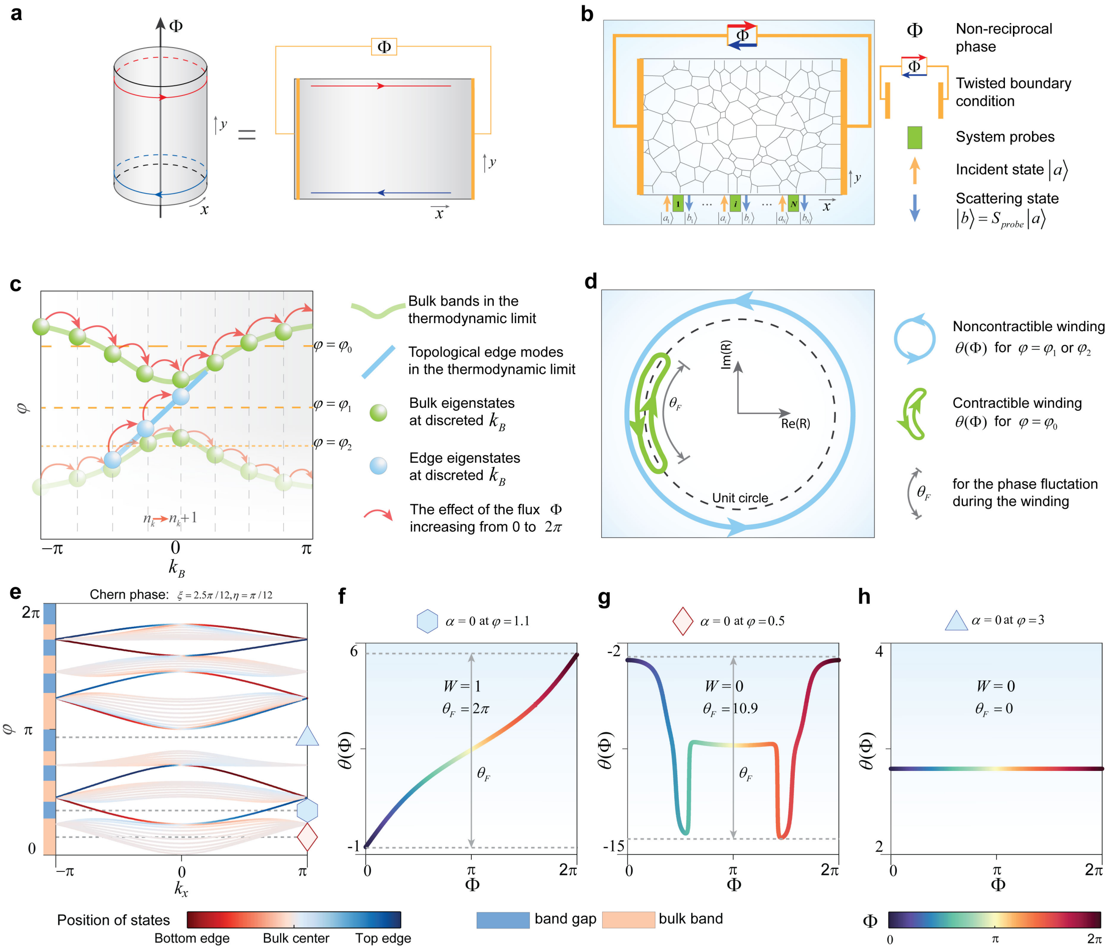
a
Φ
y
=
Φ
y
x
x
b
Φ
Non-reciprocal phase
Φ
Twisted boundary condition
System probes
Incident state $|a\rangle$
Scattering state $|b\rangle = S_{probe}|a\rangle$
y
x
c
Bulk bands in the thermodynamic limit
Topological edge modes in the thermodynamic limit
Bulk eigenstates at discreted $k_B$
Edge eigenstates at discreted $k_B$
The effect of the flux Φ increasing from 0 to 2π
$\varphi = \varphi_0$
$\varphi = \varphi_1$
$\varphi = \varphi_2$
$\varphi$
$n_k \to n_k+1$
−π
0
π
$k_B$
d
Im(R)
Re(R)
$\theta_F$
Unit circle
Noncontractible winding $\theta(\Phi)$ for $\varphi = \varphi_1$ or $\varphi_2$
Contractible winding $\theta(\Phi)$ for $\varphi = \varphi_0$
$\theta_F$
for the phase fluctation during the winding
e
Chern phase: $\xi = 2.5\pi/12, \eta = \pi/12$
2π
π
0
$\varphi$
−π
0
π
$k_x$
f
$\alpha = 0$ at $\varphi = 1.1$
6
-1
$W = 1$
$\theta_F = 2\pi$
$\theta_F$
$\theta(\Phi)$
0
π
2π
Φ
g
$\alpha = 0$ at $\varphi = 0.5$
-2
-15
$W = 0$
$\theta_F = 10.9$
$\theta_F$
$\theta(\Phi)$
0
π
2π
Φ
h
$\alpha = 0$ at $\varphi = 3$
4
2
$W = 0$
$\theta_F = 0$
$\theta(\Phi)$
0
π
2π
Φ
Position of states
Bottom edge
Bulk center
Top edge
band gap
bulk band
Φ
0
π
2π

Figure 2.15: **Topological invariant in scattering networks. a,** The magnetic flux $\Phi$ in the Laughlin's thought experiment (left) can be synthetically realized by the twisted boundary condition (right) consisting of direction-dependent phase delay $\Phi$. **b,** We probe the closed system by $N_0$ exterior probes, forming the scattering matrix $S_{probe}$. The topological index $W$ is then defined by the winding of the determinant of $S_{probe}$ in the complex plane, which is the winding of the probed reflection upon $N_0 = 1$. **c,** Schematic band structure in the thermodynamic limit and eigenphases of finite networks with the twisted boundary condition defined on discrete momentum $k_B$. The adiabatic cycle of $\Phi$ induces the successive replacements of eigenvalues from $n_k$ to $n_{k+1}$. **d,** The noncontractible and contractible windings. The contractible one (green) can be continuously deformed to a point which is topologically trivial, while the noncontractible one (blue) cannot be deformed to a point in a continuous way. **e- h,** The illustration of topological winding number $W[\varphi]$ for a finite Chern honeycomb network.

# 3 Topological scattering networks in honeycomb lattice

The main results in this chapter are taken from the published article in Zhe Zhang, Pierre Delplace, Romain Fleury, "**Superior robustness of anomalous non-reciprocal topological edge states**", *Nature*, 598, 293–297 (2021) (licensed under a Creative Commons Attribution 4.0 International License).

**In this chapter,** armed with solid foundations for describing scattering networks and their physical properties (Ch. 2), we begin our exploration with scattering networks in the clean-limit honeycomb lattice. We study under which circumstances the anomalous Floquet insulating phase (AFI) and Chern insulating phase (CI) exist in such clean-limit networks. We then explore the possible differences in edge transport between anomalous topological edge states and Chern edge states, in finite scattering networks. By inducing an abrupt change in phase links, we evidence a possible distinction in terms of robustness to phase fluctuations, motivating the study of the robustness of anomalous edge transport over the Chern one in distributed disordered cases, which is performed in the next chapter.

**Organization of the chapter:** The introduction in Sec. 3.1 aims to motivate the choice for topological unitary non-reciprocal scattering networks, namely the advantages of nonreciprocity and unitary topology. Sec. 3.2 will then exhibit the topological phases supported in scattering networks and their phase diagram. In Sec. 3.3, we numerically and experimentally examine differences between anomalous and Chern phases by studying transports in finite networks. In the end of this section, we explore the robust anomalous edge transport when an abrupt phase-link jump is introduced in the network. Finally, we show the experimental setups in Sec. 3.3.3.

**Notice:** Our studies in this chapter involve parameterization (Sec. 2.1.3), band structures (Sec. 2.2) and transports in open networks (Sec. 2.3).

## 3.1 Introduction

In the literature, topological unitary scattering networks have primarily been implemented in reciprocal photonic and phononic systems [14, 15, 148, 156–158, 160, 173, 175–178], exploiting two time-reversed subspaces. Yet, these subspaces cannot be completely decoupled and are severely affected by local defects and weak disorder. Therefore, robust topological photonic edge transport with genuine backscattering immunity is only achievable in systems that break time-reversal symmetry (TRS). On the contrary, our non-reciprocal scattering network is formally analogous to a rigorously oriented Kagome graph (Sec. 2.1.5), described by a unitary matrix $S(\boldsymbol{k})$, which can be mapped [112, 149] onto the Floquet eigenproblem of a time-Floquet lattice [111, 122, 123, 147, 252], with the phase delay of bidirectional links $\varphi$ taking the role of the quasi-energy. Consequently, we can truly benefit from the advantages of both nonreciprocity [253], and the potentially richer topological physics of Floquet systems [111]. This Kagome network is indeed known to display trivial, Chern and anomalous phases [112, 149].

In particular, it was shown that the existence of the anomalous phase is homotopically related to a critical symmetry point, called a phase rotation symmetric point [112], where the bands are perfectly flat and equidistant in quasi-energy. Such remarkable points are reached when the scattering nodes $S_1$, $S_2$, and $S_3$ are perfect transmitters so that trajectories in the Kagome network decompose into isolated oriented loops (Fig. 2.7). One of these configurations consists of isolated hexagons, that correspond to the blue point $S_{CW}$ in the parameter space $(\xi, \eta)$ in Fig. 2.3 for the non-reciprocal network in honeycomb. In fact, this unambiguously predicts that the topological phase surrounding these special points is anomalous, as long as the band gap remains open. This mapping motivates the exploration in the following section of the topological phase diagram in non-reciprocal scattering networks, which opens the possibility of an experimental implementation.

## 3.2 Anomalous topological phase and topological phase diagram

We use the model of Eq. (2.5) and theory in Sec. 2.2 to explore the parameters influencing potential topological phase transitions in the network. The individual reflection coefficient $|R|$ of non-reciprocal scatterers is found to be the main control lever for the closure of phase-delay $\varphi$ (quasi-energy) band gaps, as shown by the evolution of the bulk band structures for increasing values of $|R|$ in Fig. 3.1. Our model shows a systematic closing of two of the band gaps at $|R| = 1/3$ (denoted type 2, in red) while the others (type 1, in blue) vary only slightly, thus suggesting that topological phase transitions may be controlled by the individual scatterer reflectance.

To confirm this intuition, we probe the existence of edge modes for each of these situations by numerically calculating the band structure of a ribbon terminated by full-reflection boundary conditions at top and bottom. As depicted in Fig. 3.2a, both the low and high reflection cases

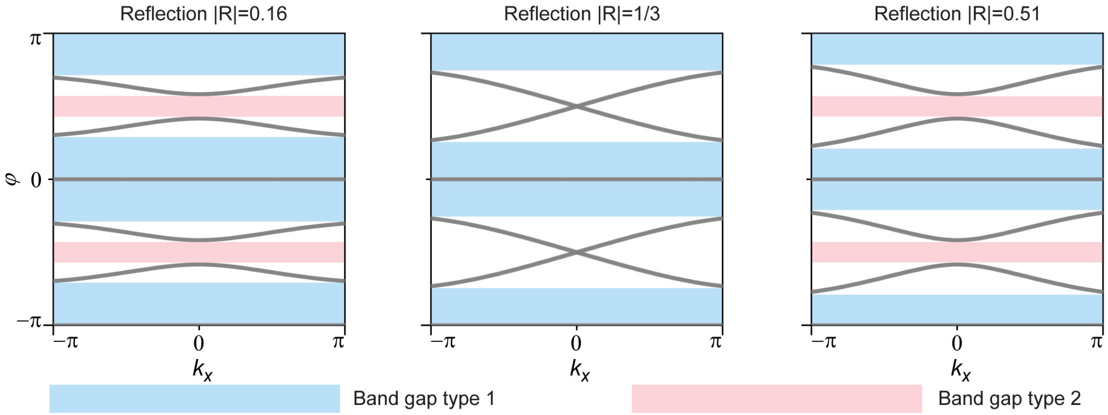

Figure 3.1: **Gap closing and reopening in phase-delay band structure at $|R| = 1/3$:** Evolution of the phase-delay band structure with the increase of the non-reciprocal elements' reflection from $|R| = 0.16$, (left, $\xi = -\eta = 2.5\pi/12$) to $|R| = 0.51$, (right, $\xi = -\eta = 3.5\pi/12$). At $|R| = 1/3$, (center, $\xi = -\eta = \pi/4$), the type 2 band gap closes, symptomatic of a topological phase transition.

(respectively on the left/right panels) exhibit chiral edge modes located at the walls either at the top (red line) or bottom (blue line), with profiles represented in Fig. 3.2b. The main difference is that the low reflection case has edge modes in every quasi-energy band gap, whereas at high reflection, they are found only in band gaps type 1. This low- $|R|$ behaviour is the hallmark of anomalous Floquet insulators (AFI)[111, 112, 123, 160], which possess topological edge states despite the Chern number of all surrounding bands being zero. In contrast, the high reflection case corresponds to the Chern insulator (CI). We map out in Fig. 3.2c the complete topological phase diagram for every possible realization of the scattering matrix $S_0$, represented by the angle parameters $\xi$ and $\eta$ (See details in Sec. 2.1.3 and Fig. 2.3). The CI and AFI regimes are shaded in red and blue, respectively. To connect this phase diagram with physically meaningful quantities, we plot it twice in the same parameter space, together with contour lines depicting the reflectance (Fig. 3.2c, left) and non-reciprocal isolation (right). Remarkably, the phase diagram unambiguously demonstrates the coincidence between the 1/3 reflection contours with the topological phase transition. Its centre and middle points of four sides, depicted by red triangles, correspond to a semi-metallic phase as shown in Figs. 3.3(b, d), with all band gaps closed, whereas the blue ($S_{CW}$) and purple ($S_{CCW}$) points are the perfect circulator case with $|R| = 0$ and infinite isolation, for which the bulk bands are flat and the edge modes are dispersionless (Fig. 3.3(a, c) for the blue point). Such critical condition corresponds to a phase rotation symmetric point [112], which can only occur in the anomalous (or trivial) phases.

For completeness, we provide the band gap map of the network together with the values of the homotopy invariant $W_\tau$ (Sec. 1.3) in Fig. 3.4. The white areas represent bulk bands. We focus on a segment $\xi = -\eta \in [\pi/6, \pi/2]$ in the parameter space, in which the reflection coefficient $R$ of the individual circulators correspondingly varies from 0 to 1. The blue areas represent band

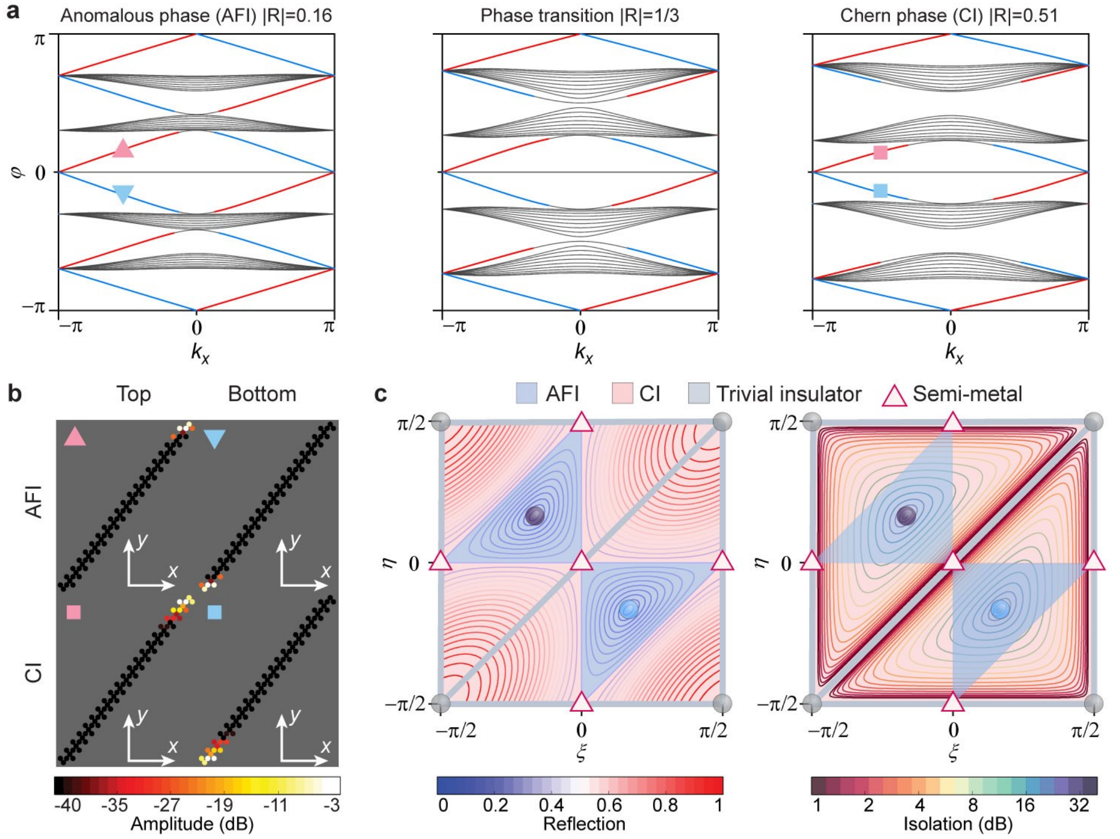

Figure 3.2: **Anomalous and Chern topological phases in non-reciprocal scattering networks. a,** Phase-delay band structures of a supercell with periodic boundary conditions along $x$ and unitary reflections at the top and bottom. The parameters are the same as in Fig. 3.1. The low reflection case is the anomalous topological phase, which features an edge mode in every quasi-energy gap. Conversely, the high reflection case supports edge modes only inside the type 1 band gaps, consistent with the Chern insulator phase. Edge modes localized to the top and bottom are shown in red and blue, respectively. **b,** Supercell with examples of Chern and anomalous topological edge modes profiles, corresponding to the markers in panel a. **c,** Topological phase diagram in the $(\xi,\eta)$ plane. The blue-shaded area corresponds to the anomalous phase, and the red one to the Chern phase. Left: comparison with the iso-reflection contours of the individual scatterers, demonstrating the coincidence between the topological phase transition and the $|R| = 1/3$ contour. Right: Comparison with the non-reciprocal isolation level of the individual scatterers $|S_0(2,1)/S_0(1,2)|$. On the thick gray lines, the scatterers are reciprocal. At the triangular red point, all band gaps close indicating a semi-metal, where phase transitions among AFI, CI and trivial phase happen. The blue and purple spheres represent the perfect circulator cases ($S_{CW}$ and $S_{CCW}$).

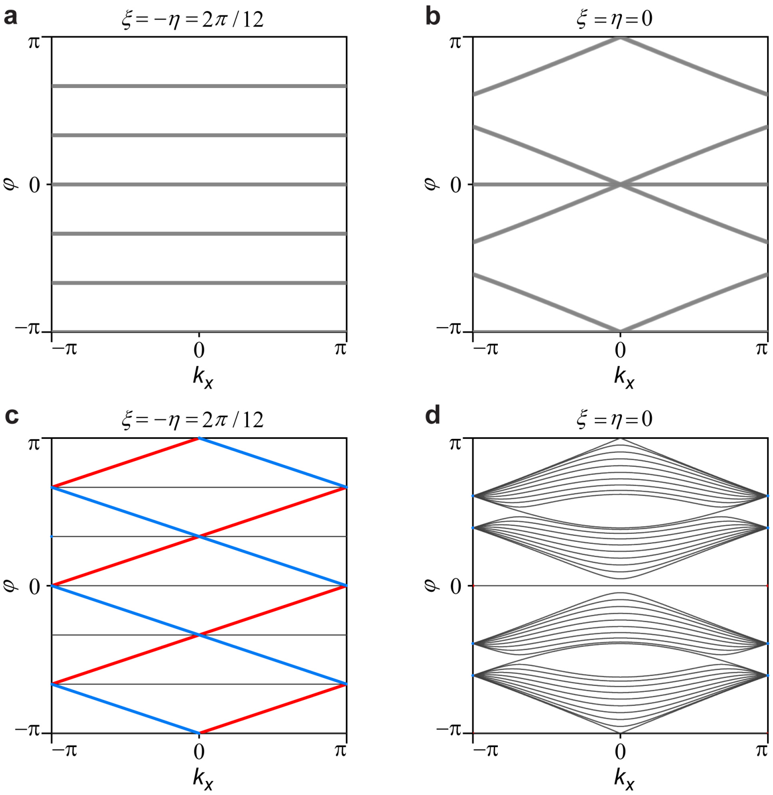

Figure 3.3: **Phase-delay band structures at two special points of the topological phase diagram. a, b,** Bulk band structures at the blue sphere (a) and red triangles (b) of the phase diagram of Fig. 3.2c. The blue and purple spheres correspond to a phase-rotation symmetric network of perfect matched circulators, thus in AFI phase. The red triangles represent a network of reciprocal resonant scatterers, with all band gaps closed. **c, d,** Ribbon band structures corresponding to panel a and b, respectively. The perfect circulator network features flat bulk band with dispersionless edge modes regardless of the value of the quasi-energy $\varphi$, which can only occur in the AFI phase.

gaps with values of the homotopy invariant $W_\tau = 1$, whereas red areas correspond to band gaps with a zero value of $W_\tau$.

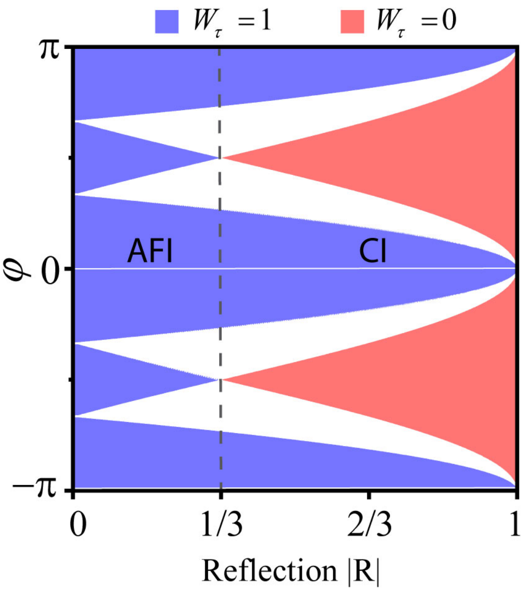

Figure 3.4: **Band gap map of the network.** We project the band structures on the segment of $\xi = -\eta \in [\pi/6, \pi/2]$ in the parameter plane. The band gaps are marked with gap invariant $W_\tau$: blue for 1 and red for 0, whereas white parts represent bulk bands. The topological phase transition at $|R| = 1/3$ is coincidence with the changes of gap invariants. Band structures in Fig. 3.2 ($|R| = 0.16, 1/3$ and $0.51$) and Fig. 3.3 ($|R| = 0$ and $1$) can be found in this band-projection map.

## 3.3 Transport distinctions in anomalous and Chern topological scattering networks

In this section, we focus on the transport properties for finite scattering networks with external ports and examine the associated difference between anomalous and Chern phases. To begin with, we consider a hexagonal finite scattering network in honeycomb lattice as shown in Fig. 3.5. To probe transport through this network, we assign three external ports at the network boundary, represented by green stars. The remaining boundary ports are configured for unitary reflection. In the scope of this section, we keep all the circulators in the network identical.

### 3.3.1 Transport distinctions of AFI and CI in the clean-limit network

First, we numerically examine how the distinctions in band structures for AFI and CI lead to different transport phenomena in the clean limit. In the finite open network constructed from identical circulators $S_0(\xi, \eta)$ and characterized by phase-delay $\varphi$, we initiate a wave signal at port 1 and check the amplitude of the signal received at port 2. In Fig. 3.6, we plot this transmission from port 1 to port 2 as a function of $\varphi$ and compare it with the phase-delay ribbon band structure of $S_0(\xi,\eta)$.

The parameters $(\xi,\eta)$ for AFI and CI are the same as those in Fig. 3.1, respectively. In the anomalous scattering network (panel a), the transmission in the phase-delay spectrum either reaches unity or exhibits non-zero values characteristic of metallic behavior, never being completely blocked at any phase-delay value, since AFI lacks trivial gaps. In contrast, the network in the Chern phase, despite showing unity and metal-like transmissions in certain phase-delay ranges, experiences complete transport blockages due to trivial band gaps.

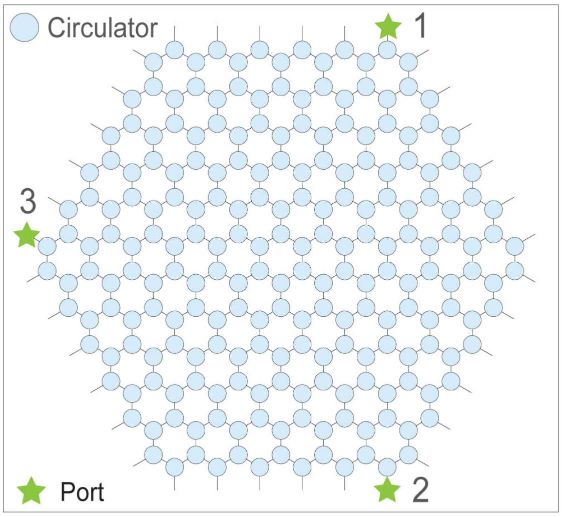

Figure 3.5: **Finite honeycomb scattering network with circulators $S_0(\xi,\eta)$ with three external ports.** Three ports are arranged at the boundary to examine transports through finite networks.

### 3.3.2 Experimental realizations for AFI and CI

Experiments were designed with the goal of being able to access both phases in samples allowing for extensive characterization, including field maps and scattering parameters. The non-reciprocal networks are designed and fabricated on 0.508 mm thick Rogers RT/duroid 5880 substrate (dielectric loss $\tan\delta = 0.0009$ at 10 GHz) with 35 $\mu$m thick copper on each side. Here, the non-reciprocal element is a surface mount microwave circulator UIYSC9B55T6 from UIY company, designed from a Y-shaped strip line on a printed circuit board [193]. Microstrip lines serve as phase delay links, with a width of 1.65 mm, corresponding to a standard 50 Ohms characteristic impedance. Microstrip transmission lines are known to behave as pure phase delays in this frequency range, since the propagation losses over so short distances are negligible (we indeed measured them to be 0.0167 dB/cm). In our experiment, we measure an individual circulator and retrieve its scattering matrix $S_U$ versus frequency $f$. Then we set the frequency bands for AFI and CI operations, by checking the position of the measured $S_U(f)$ in the topological phase diagram on $(\xi,\eta)$ plane (Fig. 3.2).

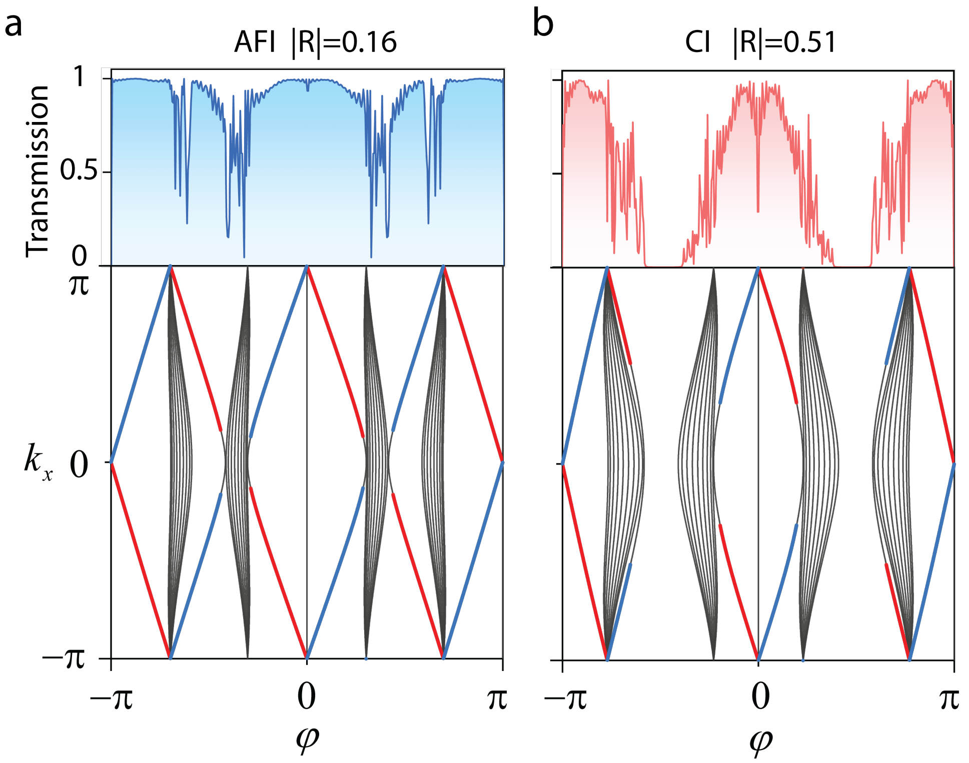

Figure 3.6: **Comparison between boundary-port transport properties and the ribbon band structures of anomalous and Chern phases.** We plot the simulated transmission between two boundary ports (port 1 and 2) through the hexagonal network (Fig. 3.5) as a function of $\varphi$, and compare it with the ribbon band structure. We assume a uniform distribution for the phase delay $\varphi$ and the circulator $S_0(\xi,\eta)$. **a,** Case of the anomalous phase in Fig. 3.1. **b,** Case of the Chern phase shown in Fig. 3.1.

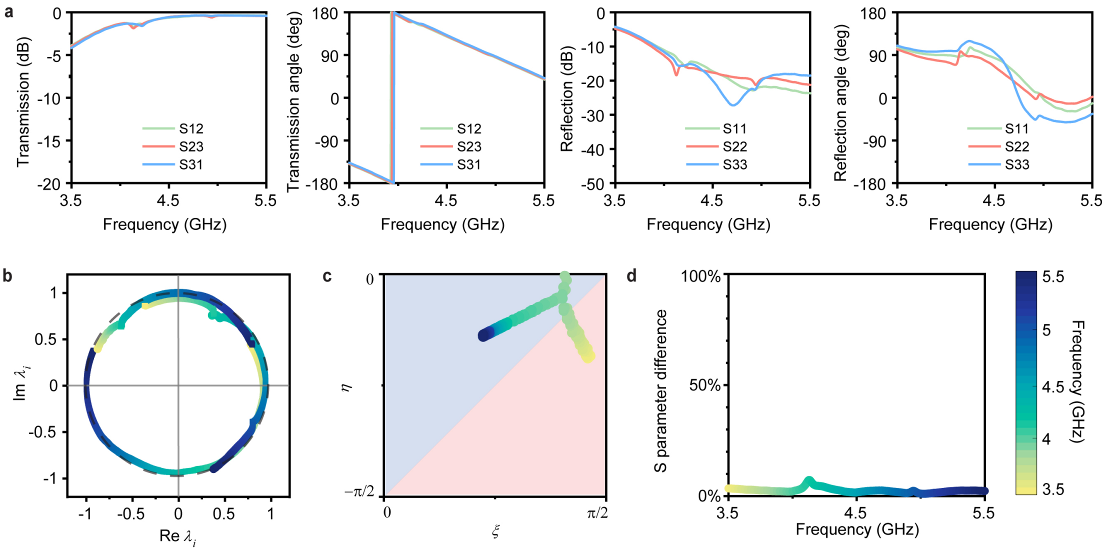

Figure 3.7: **Experimental validation of the model assumptions. a,** Validation of the $C3$ symmetry hypothesis. $C3$ symmetry holds when $S_0(1,2) = S_0(2,3) = S_0(3,1)$, as well as $S_0(1,1) = S_0(2,2) = S_0(3,3)$, which is the case in the considered frequency range. **b,** Validation of the unitary scattering properties: eigenvalues of the measured scattering matrix, with nearly-unitary behavior over the entire experimental bandwidth. **c,** $\xi$ and $\eta$ parameters used to approximate the real scattering matrix with a $C3$- symmetric unitary matrix. The red and blue areas are the Chern and anomalous phases respectively. **d,** Error in % made by approximating the real scattering matrix with Eq. (3.1) over the entire bandwidth.

We start by checking the validity of $C3$ symmetry and $U(3)$ assumptions made in Sec. 2.1.3, namely that the three-port scatterers have three-fold rotational symmetry (C3 symmetry), and that they are unitary. To do this, we measured the $3 \times 3$ scattering matrix $S_M$ of our circulators. We start with checking $C3$ symmetry, which implies that $S_M(1,2) = S_M(2,3) = S_M(3,1)$, as well as $S_M(1,1) = S_M(2,2) = S_M(3,3)$[I]. Fig. 3.7a plots the moduli and arguments of all these quantities in the considered frequency range $f \in [3.5, 5.5]$ GHz. From these plots, we see that although some small deviations from $C3$ symmetry are observed in the reflection coefficients, they correspond to fluctuations of reflection below −20 dB. We can then conclude that $C3$ symmetry is a valid assumption. Next, we check unitarity. Fig. 3.7b plots the eigenvalues of the measured scattering matrix versus frequency, in the complex plane. We can see that they are always very close to the unit circle, meaning that unitarity is also a very reasonable assumption. This is expected since we used a substrate with a small loss tangent of $10^{-4}$ and circulators with low insertion losses of 0.2 dB. Absorption is therefore not expected to alter the prediction of the unitary theory, but simply add an exponential decay that is most noticeable for large samples.

Now, we estimate the error that we make by modeling the real matrix $S_M$ with $S_0(\xi, \eta)$ in Eq. (2.25). To do this, we find the C3-symmetric unitary scattering matrix $S_U$ that is the closest to $S_M$. We get $S_U$ by rescaling the eigenvalues of $S_M$ to make them exactly unitary, keeping their arguments. We then determine the parameters $\xi$ and $\eta$ of $S_U$, which we plot against frequency in Fig. 3.7c. We then define a $s$-parameter error metric as

$$\epsilon_{diff} = \sqrt{\frac{1}{3}\Big[[S_M(1,1) - |S_U(1,1)|]^2 + [S_M(1,2) - |S_U(1,2)|]^2 + [S_M(2,1) - |S_U(2,1)|]^2\Big]}. \quad (3.1)$$

This quantity, depicted in Fig. 3.7d, represents the error that we make by using Eq. (2.25). We see that this error is below 5% for the whole frequency range, which unambiguously validates the relevance of Eq. (2.25). Furthermore, this mapping indicates that the topological phase of a scattering network can vary with its operation frequency $f$, if scattering matrices of scattering nodes are the functions of frequency $f$. This allows us to access both anomalous ($3.9 < f < 5.5$ GHz) and Chern phases ($3.5 < f < 3.9$ GHz) in only one fabricated scattering network by operating at different frequencies.

### 3.3.3 Experimental setups

The scattering parameters and field maps for circulators and fabricated networks are measured by a vector network analyser (VNA) R&S ZNB20, as illustrated in Fig. 3.8a. For the scattering parameter measurements for example results in Fig. 3.7, as they are multiport, we connect the two ports of the VNA to two ports of the measured devices, with the other ports perfectly matched with 50-ohm terminations (no reflection). For the field map measurements, we connect the signal input port of the measured network to VNA port 1, while perfectly matching the other ports of the network. We manually probe the field at the middle of the microstrip

---

[I] $S_M(2,1) = S_M(3,2) = S_M(1,3)$ is not checked as their amplitudes are quite small.

lines by using a coaxial probe, which is connected to VNA port 2, as shown in Fig. 3.8b.

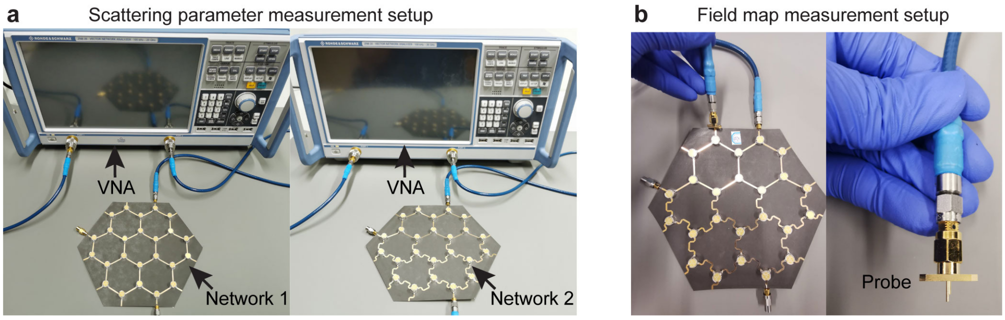
a
Scattering parameter measurement setup
VNA
VNA
Network 1
Network 2
b
Field map measurement setup
Probe

Figure 3.8: **Experimental setups for scattering parameter and field distribution measurements. a,** The setup consists of a vector network analyser (VNA) and two microwave non-reciprocal networks: N1 (left) and N2 (right). **b,** Field map measurement with a coaxial probe for measuring fields on the microstrip lines.

### 3.3.4 Robust anomalous edge states against an abrupt phase-delay jump

From the band structures in Fig. 3.1 and the transport results in Fig. 3.6, we can already intuitively expect the AFI edge transmission to be much more robust than the CI transmission to phase-delay (quasi-energy) fluctuations, even much larger than the band gap size. Indeed, the AFI phase occurs in the ballistic regime, in which reflections at nodes are low (Fig. 3.2), yielding relatively flat (slow) bulk bands and large topological band gaps. An abrupt jump of $\varphi$ within the lattice is very likely to land in a topological band gap, which necessarily carries an edge mode. Conversely, in the CI phase, the probability of an edge mode being destroyed by fluctuations larger than the band gap is much higher, due to the increased width of the bulk bands and the occurrence of trivial band gaps [II].

As an example of such a situation, let us consider the transport properties of edge modes in a finite non-reciprocal network with an abrupt phase-delay jump in the middle (Fig. 3.9a, right). As a reference, we also include the case of a uniform sample (left panel). The two hexagonal-shaped networks with three input/output ports follow the finite network in Fig. 3.5, as shown in the top row of Fig. 3.9a. Network 1 (N1) consists of uniformly distributed phase links $\varphi = \pi/8$, while for network 2 (N2), a phase-delay jump is introduced by changing all phase links in the bottom part to $\varphi = \pi/2$. With numerical simulations, we then compare the propagation of the anomalous and Chern edge modes, when exciting from port 1. The anomalous phase finds itself in topological band gaps at both $\varphi = \pi/8$ and $\varphi = \pi/2$ (Fig. 3.2a, left), whereas the Chern phase possesses a non-trivial band gap only at $\varphi = \pi/8$ (Fig. 3.2a, right). As shown in Fig. 3.9a, the anomalous edge mode crosses the interface completely unperturbed. In stark contrast, the Chern edge mode is unable to transmit to port 2 in the presence of the interface, and all the energy is guided to port 3.

---

[II] Such difference roots in the phase rotation symmetry [112], of which the clean-limit networks possess total flat bulk bands and can only be in anomalous or trivial phase.

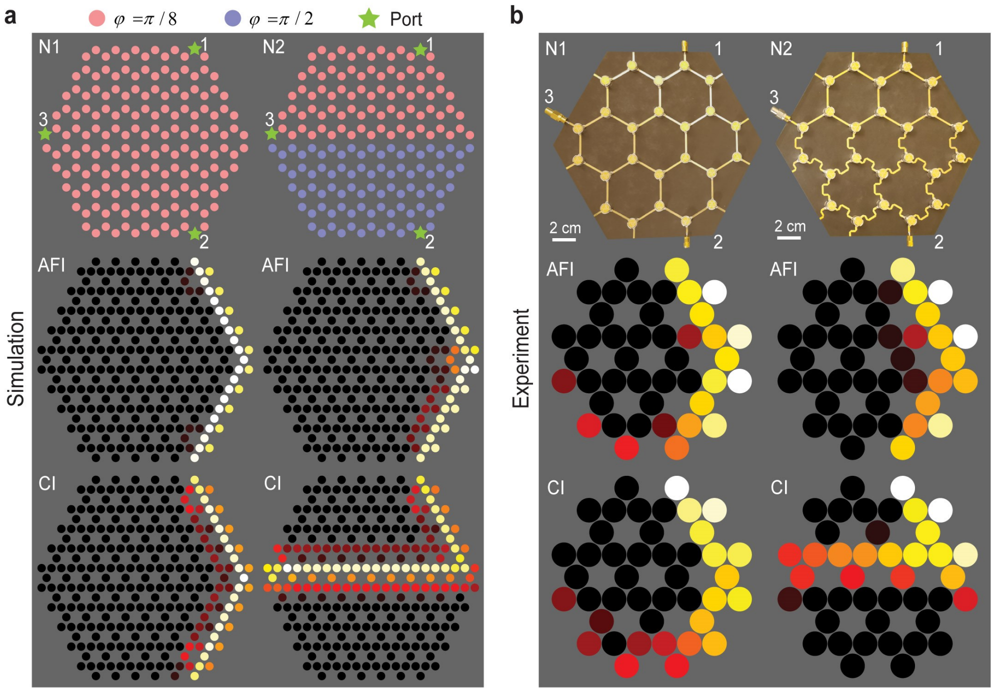

Figure 3.9: **Robustness of anomalous non-reciprocal topological edge transmission against abrupt phase-delay jump. a,** Numerical simulation of the steady-state energy propagation in finite non-reciprocal networks with different phase-link distributions. The signal is incident from port 1. The parameters used to generate the anomalous (center) and Chern (bottom) phases are the same as in Figs. 3.1 and 3.2. On the left, the phase-link distribution is uniform, with $\varphi = \pi/8$, and the energy can be transmitted to port 2 in both the anomalous and Chern phases. On the right, we introduce an interface and abruptly change the value of $\varphi = \pi/2$ for the bottom part. Only the anomalous phase is robust to this change, and keep transmitting to port 2. In the Chern phase, the edge mode travels along the interface and reaches port 3. **b,** Experimental validation at microwaves in a network made of ferrite circulators.

We validate experimentally this fundamental distinction between the anomalous and Chern phases by designing a non-reciprocal network operating at microwave frequencies. The scatterers are ferrite circulators connected with microstrip lines. Our experimental design, which takes into account both the frequency dispersion of the scatterers and delay lines, finds itself in the anomalous and Chern phases at 4.9 and 3.6 GHz, respectively. Modification of the phase delays of the links is induced by changing the total lengths of the microstrip lines with serpentine paths, whose phase delay $\varphi$ under a length $L$ at the frequency $f$ is expressed as $\varphi = \frac{2\pi f L\sqrt{\epsilon_{eff}}}{c}$, with $\epsilon_{eff}$ being the effective permittivity of the microstrip, obtained from an empirical microwave design formulas [193].

As shown in Fig. 3.9b, the measured field amplitude profiles confirm the resilience of the anomalous edge state to the phase jump, in perfect agreement with the numerical predictions. We also check the field maps upon exciting ports 2 and 3 as shown in Figs. 3.10 and 3.11. Their simulations and measured results are very well consistent with each other, exhibiting a robust anomalous edge transport circulating the whole hexagonal scattering network.

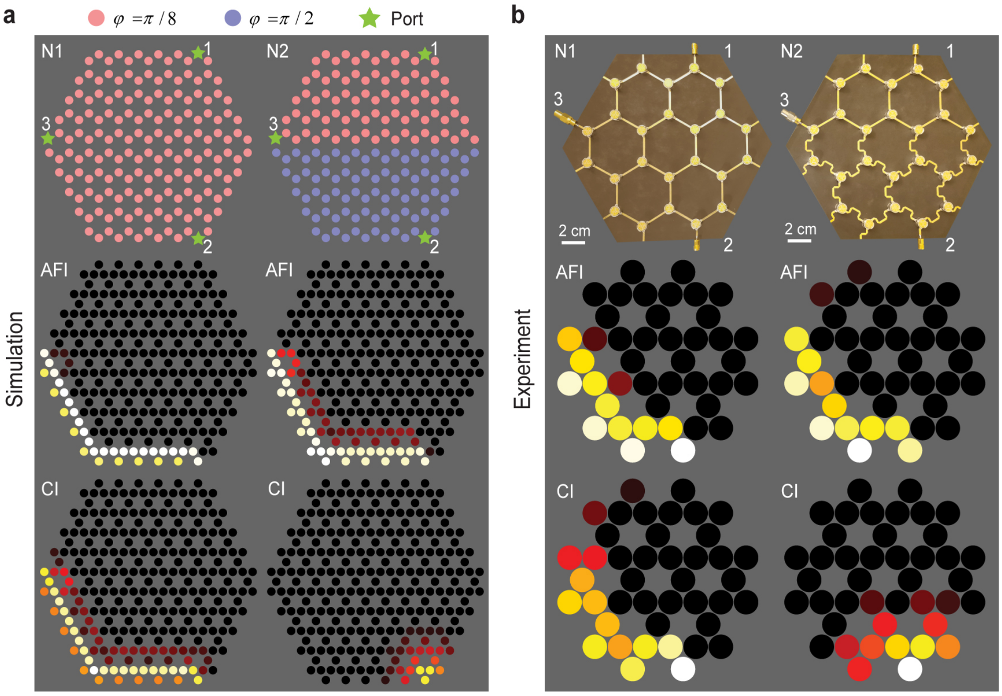

Figure 3.10: **Numerical and experimental field maps for excitation at port 2. a,** Numerical predictions for excitation at port 2 for the same system as in Fig. 3.9. While the anomalous phase supports transmission to port 3 regardless of the phase link distribution, the Chern phase possesses a trivial band gap at $\varphi = \pi/2$, and reflects all the energy incident from port 2, see bottom right plot (the field distribution exhibits exponential decay). **b,** Corresponding experimental data.

Further evidence is provided by the measured changes in scattering parameters over a frequency band. Indeed, as illustrated in Fig. 3.7c, the dispersion of circulators enables us to access the frequency bands in which networks operate in anomalous phase or Chern phase. As

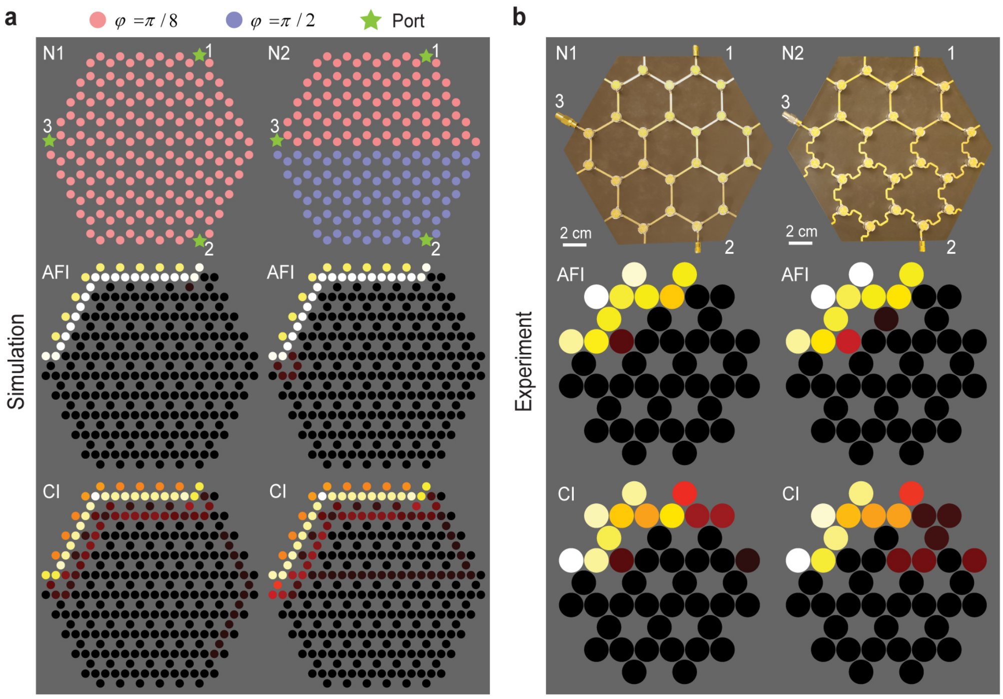

Figure 3.11: **Numerical and experimental field maps for excitation at port 3. a,** Numerical predictions for excitation at port 3 for the same system as in Fig. 3.9. Both the anomalous and Chern phases fall in topological band gap at $\varphi = \pi/8$, leading to transmission to port 1. **b,** Corresponding experimental data.

AFI and CI regimes are segregated by the reflection contour of $|R| = 1/3$ in the parameter space, this classification can also be simply achieved by checking the reflection of single scatterers, as shown in Fig. 3.12a. The blue-shaded area represents the bandwidth of the anomalous phase, indicating low reflection, where $|R| < -9.5$ dB, equivalent to $20 \cdot \log_{10}(1/3)$. By contrast, the red-shaded area shows the Chern phase with high reflection ($|R| < -9.5$ dB).

However, just because two topologically non-trivial phases are present doesn't guarantee the manifestation of topological edge states for a scattering network with a specified length $L$ of microstrip line operating at frequency $f$. Taking into account the frequency dispersion of the lines and circulators, we construct a more practical topological band gap map, shown in Fig. 3.12b, as a function of the effective length of the microstrip lines $L$ and the operating frequency $f$. In Fig. 3.12b, the blue and red regions correspond to band gaps with and without topological edge modes, respectively. The white regions represent bulk bands. Topological phase transitions happen at around 3.9 GHz and 7 GHz. With the aid of the map, we select $L_1 = 26.5$ mm and $L_2 = 37.5$ mm, which produce the conditions $\varphi = \pi/8$ and $\varphi = \pi/2$ in the simulations (Figs. 3.9a, 3.10a and 3.11a), respectively. As exhibited in Fig. 3.12c, the fabricated networks show the microstrip lines of $L_1$ (blue dashed region) and $L_2$ (red dashed region). Network 1 (N1) has a uniform length distribution of microstrip lines with $L = L_1$. For network 2 (N2), we introduce an interface and replace the bottom part with lines of different length $L_2$.

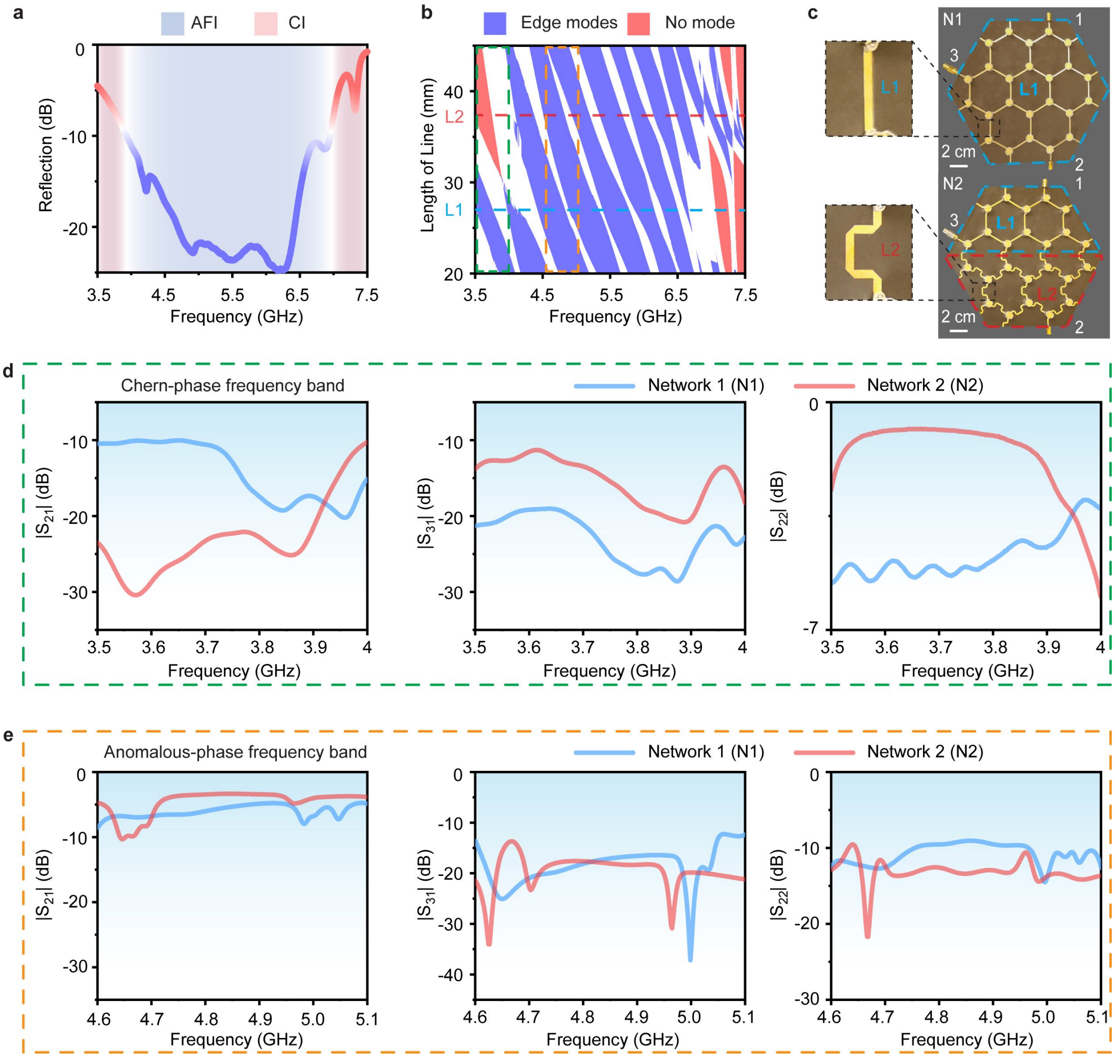

Figure 3.12: **Experimental network design and measured scattering parameters in bands of Chern and anomalous phases. a,** Measured reflection spectrum of an individual ferrite circulator. **b,** Topological band gap map predicted from the scattering data of individual circulators, when varying the length of the microstrip connections and the operating frequency. The frequency dispersion of the lines and circulators is taken into account. **c,** Design details of the experimental networks with/without the abrupt phase jump. **d,** Measured amplitudes of the scattering parameters $S_{21}$ (left), $S_{31}$ (mid), and $S_{22}$ (right) in the Chern-phase frequency band (green dashed box in panel b). **e,** Measured scattering parameters in the anomalous-phase frequency band (yellow dashed box in panel b).

We compare the changes of measured $S$ parameters within anomalous and Chern phase frequency bands, when inducing the abrupt phase jump in the scattering network, as shown in panels d and e of Fig. 3.12, respectively. Fig. 3.12d shows considerable differences between Chern-phase network 1 (N1) and network 2 (N2), from 3.5 GHz to 3.9 GHz for transmission from port 1 to port 2 ($S_{21}$, left), transmission from port 1 to port 3 ($S_{31}$, mid), and reflection at port 2 ($S_{22}$, right). These differences imply that Chern phases are not robust against strong perturbations of phase links. To be more specific, regarding N1, we see a high $S_{21}$ and a low $S_{31}$ denoting an edge mode from port 1 to port 2. Conversely, regarding N2, a low $S_{21}$ and a high $S_{31}$ imply a change of its wave propagation path due to the perturbation of phase links in the bottom part. The high $S_{22}$ (around $-1$ dB) of N2 indicates a trivial band gap for the bottom part of N2. In Fig. 3.12e, between anomalous-phase network 1 (N1) and network 2 (N2), in contrast to panel d, there are little differences of $S$ parameter ($S_{21}$, left; $S_{31}$, mid; $S_{22}$, right) between N1 and N2 under anomalous phases. It therefore provides additional evidences of the superior robustness of anomalous phases over Chern phases.

## 3.4 Conclusions

In this chapter, we investigated the anomalous Floquet topological phase (AFI) and the Chern insulating phase within a unitary wave network. This network was constructed from lossless three-port non-reciprocal scatterers interconnected by reciprocal phase-delay lines, analogously mapping to an oriented Kagome graph. By drawing parallels to the Floquet eigenproblem of a time-Floquet lattice, we delineated the topological phase diagram for periodic honeycomb scattering networks across the parameter plane of $(\xi, \eta)$, with the quasi-energy signified by phase delay $\varphi$. This diagram reveals three distinct phases: AFI, Chern phase (CI), and trivial phase. Both theoretical insights and experimental evidence based on introducing domains with different values of $\varphi$ suggest a potential superior robustness of anomalous transport against discrete variations in the phase imparted by the links. Motivated by such observations, the subsequent chapter aims at establishing quantitatively and statistically the superior robustness of AFI transport in situations where phase disorder is distributed across the sample and fully random.

# 4 Superior robustness of anomalous topological transport

The main results in this chapter are taken from the published article in Zhe Zhang, Pierre Delplace, Romain Fleury, "**Superior robustness of anomalous non-reciprocal topological edge states**", *Nature*, 598, 293–297 (2021) (licensed under a Creative Commons Attribution 4.0 International License).

In the previous chapter, we have discussed numerical simulations and experiments that suggest that the absence of trivial band gaps in the anomalous phase, contrary to the Chern phase, may lead to a superior resilience for anomalous chiral transport to phase fluctuations. This remains to be confirmed in more stringent situations where phase disorder takes the form of random fluctuations distributed over the sample. The question of other forms of disorder, such as disorder on the scattering properties of the circulators, also remains open.

**In this chapter**, we focus on the effect of distributed phase-delay and scattering-node disorder on topological scattering networks. It establishes the superior robustness against distributed disorder of anomalous topological transport over Chern topological transport. Our microwave experiments validate the existence of a stronger edge transmission channel in the anomalous phase. We apply our findings by prototyping and characterizing various prototypes with phase disorder and/or irregular shapes.

**Organization of the chapter:** In Sec. 4.1, we introduce the concept of topological robustness. In Sec. 4.2, we introduce random phase-delay disorder in the networks and compare the transport robustness of anomalous edge states with the Chern edge states, establishing the remarkable resilience of anomalous edge states. Sec. 4.3 demonstrates the superiority of the anomalous edge states in the case of scattering disorder. In Sec. 4.4, we experimentally confirm the exceptional resilience of the anomalous phase and demonstrate its operation by building a 6 port topological circulator with arbitrary shape. Sec. 4.5 further verifies the superior transmission robustness of anomalous phase by additional comparisons with other Chern phases characterized by various types of band structures. Sec. 4.6 concludes this chapter.

**Notice:** The investigations in this chapter employ the disorder realization and discussions from Chapter 2 on phase-delay disorder, scattering matrix disorder on nodes (in Sec. 2.1.4), and transports in open networks (Sec. 2.3).

## 4.1 Introduction

Among the unique and counterintuitive attributes of topological systems, topological robustness [4] against disorder and flaws is undoubtedly one of the most remarkable. This property shows ground-breaking application potential by relaxing the drastic constraints imparted by fabrication tolerances, and provides a way to seamlessly route energy and information in a wide variety of two-dimensional (2D) platforms [6, 7, 10, 13–15, 17, 23–25, 36, 37, 42–47, 51, 254–258], from quantum electronics [47] to classical photonic [6, 7] and phononic devices [23–25]. Topological edge states were found in systems with broken time-reversal symmetry, such as Chern insulators [10, 259], and then extended to time-reversal invariant scenarios, including the $\mathbb{Z}2$ [260] and other symmetry-protected schemes [35], simultaneously stimulating their classical analogues [13, 15, 36, 37, 147]. So far, Chern topological edge modes [10, 13, 17, 23, 36, 43–47, 258] undeniably represent the most reliable solution for point-to-point energy guiding, as they provide truly unidirectional, backscattering-immune wave transport at their boundaries [50]. They were reported in non-reciprocal artificial wave media, such as externally-biased magneto-photonic crystals [13] or mechanical systems [51] with moving [23, 36, 43, 44] or time-dependent [254, 258] elements. Albeit protected from the presence of local defects by the Chern number, the edge modes cannot survive the presence of distributed disorder of sufficiently strong magnitude [4, 6, 7, 10, 42], especially when the average amplitude of frequency fluctuations gets larger than the band gap size. This behaviour inherently confines the topological protection of Chern phases to small distributed disorder levels.

In this chapter, we demonstrate that in the case of the anomalous non-reciprocal topological phase, the edge transmission is quantitatively stronger than for the Chern phase, surviving parametric fluctuations of the phase much larger than the band gap size. We find such anomalous robustness in unitary scattering networks made of interconnected non-reciprocal resonant scatterers coupled by non-directed phase links. We compare quantitatively the robustness of transmission through the anomalous and Chern channels to phase-link disorder and scattering disorder on nodes, by statistical averaging over many disorder realizations. Our experiments at microwave frequencies confirm the superior resilience of the anomalous transmission channel over the Chern one. We apply our findings to the design of ideally robust networks with arbitrarily located ports and irregular shapes, including a 6-port circulator.

## 4.2 Superior robustness of AFI against random phase-delay disorder

From the results revealed in the last Chapter, the resilience of anomalous edge transport in interface scenarios, involving two periodic networks, raises the question of its generalization to distributed non-uniform phase-delay (quasi-energy) perturbations. To answer quantitatively, we consider the same hexagonal network as in the left of Fig. 3.9a, and impose site-dependent disorder to the phase links, with fluctuations of strength $\delta_\varphi$ randomly drawn with uniform probability in the interval $\pi/8+\left[-\delta_\varphi/2, \delta_\varphi/2\right]$. We then numerically extract the transmission from ports 1 to 2 for 1000 realizations of disorder, and plot its magnitude versus $\delta_\varphi$ in the top panel of Fig. 4.1. The solid lines represent the ensemble average, and the dashed lines are the first and last quartiles (Q1 and Q3). In the clean limit ($\delta_\varphi = 0$), both AFI and CI phases show high transmission, since the edge states exist in both cases and are unperturbed (Fig. 3.9a). We now turn on the disorder, up to the maximal possible strength, which corresponds to randomly drawn values in the entire $2\pi$ phase-delay (quasi-energy) range, much larger than the band gap size of both AFI and CI phases (roughly $\pi/4$). Upon increasing $\delta_\varphi$, the average transmission in the Chern case quickly drops to low values. Remarkably, the AFI transmission shows a markedly different behaviour, remaining near 90% even when $\delta_\varphi$ reaches $2\pi$ (fully random case). Note that this exceptional robustness does not require to reach the critical condition $|R| = 0$, since the figure is generated for $|R| = 16\%$. Such statistically stable transmission constitutes a solid evidence of the superiority of anomalous non-reciprocal topological networks, which survive phase disorder levels arbitrarily larger than their band gap size. The subtle physics behind this exceptional resilience will be elucidated in an upcoming chapter, with the help of a renormalization group theory in Ch.6.

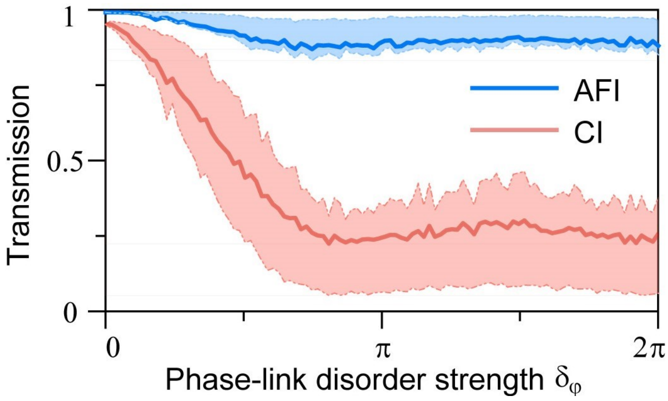

Figure 4.1: **Superior robustness of anomalous non-reciprocal topological edge transmission against phase-delay disorder.** Transmission between ports 1 and 2 in a disordered system with randomly-generated phase delays. The phases are uniformly drawn in an interval $\left[-\delta_\varphi/2, \delta_\varphi/2\right]$ around $\varphi_c = \pi/8$. Solid lines represent the value of transmission averaged over 1000 realizations of disorder, and the dashed lines are the first and last quartiles (Q1 and Q3). The anomalous edge transmission channel can survive disorder strengths up to a full $2\pi$ rotation.

To check how wave propagates through disordered network via anomalous edge states, we check field maps for several selected phase-link disorder levels: the clean limit $\delta_\varphi = 0$ (left), weak fluctuation $\delta_\varphi = \pi/4$ (mid) , and the fully random case $\delta_\varphi = 2\pi$ (right), as shown in Fig. 4.2. In both panels, the top row shows the numerically predicted field map, and the bottom row provides information about the considered particular disorder realization. The left column shows the perfectly ordered system, the middle column shows a realization of random phase delays with strength of fluctuations $\delta_\varphi = \pi/4$, and the last column is the fully disordered case, $\delta_\varphi = 2\pi$. Only the anomalous edge mode in panel (a) survives full random phase disorder.

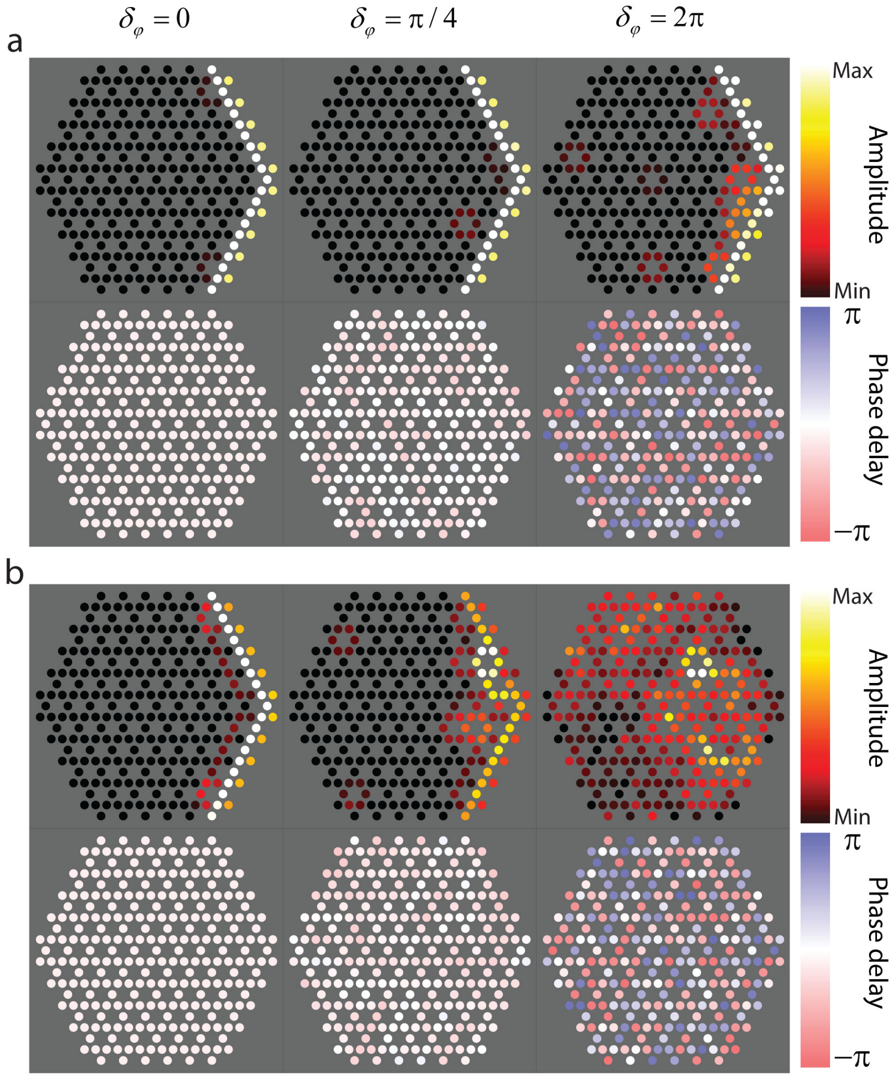

Figure 4.2: **Field maps anomalous (a) and Chern (b) edge mode transmissions at several phase-delay disorder levels.**

We now delve deeper into the exceptional resilience of anomalous edge transport against distributed phase-delay disorder $\varphi$. We analyze networks formed by circulators within the parameter range $\xi = -\eta \in [\pi/6, \pi/2]$, previously examined in Fig. 3.4, where the reflection coefficient $|R|$ shifts from 0 to 1, marking a topological phase transition at $|R| = 1/3$. Utilizing the configurations and disorder models outlined in Fig. 4.1, we evaluate the mean transmission from port 1 to port 2 across these networks as the disorder intensity $\delta_\varphi$ in the phase links increases, depicted in the left panel of Fig. 4.3. Initially, for a uniform phase-delay $\varphi_c = \pi/8$, both Chern and anomalous networks contain high transmissions due to stable edge states, even under mild disorder. Yet, as the disorder reaches $\delta_\varphi = \pi/2$, Chern network transmissions significantly diminish, virtually disappearing at $\delta_\varphi = \pi$. In stark contrast, anomalous networks maintain near-perfect edge transmission, demonstrating their remarkable robustness, even under the highest disorder intensity $\delta_\varphi = 2\pi$.

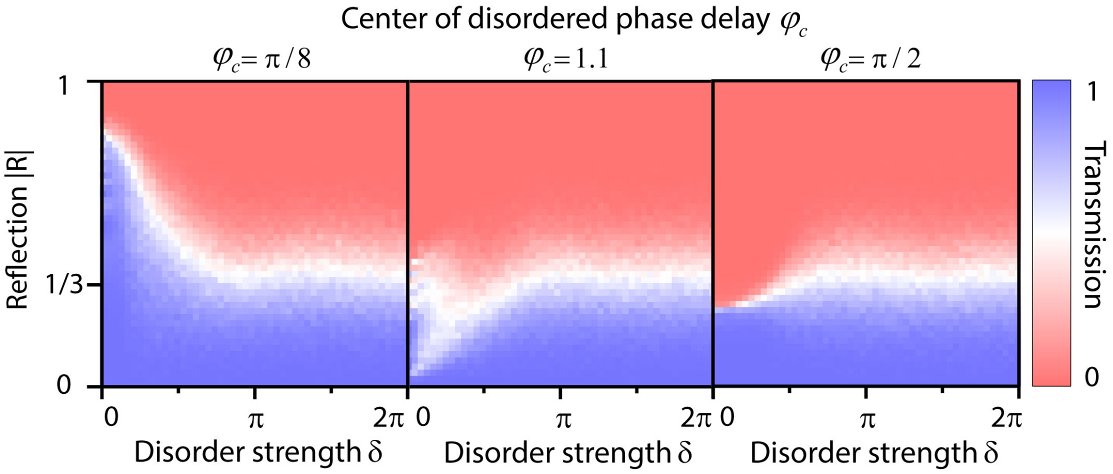

Figure 4.3: **Superior robustness of anomalous edge transport regardless of the center of disordered $\varphi$.** The phase-delay value in the clean-limit networks is termed as $\varphi_c$, which is also the center of disordered phase delay, since disordered phase delay $\varphi$ is randomly drawn from $\varphi_c + [-\delta_\varphi/2, \delta_\varphi/2]$ in a uniform probability distribution.

Furthermore, we change the center of disordered $\varphi$ from $\varphi_c = \pi/8$ to $\varphi_c = 1.1$ (Fig. 4.3, mid) and $\varphi_c = \pi/2$ (Fig. 4.3, right); we then increase the disorder intensity continuously from the clean-limit condition to the fully disordered stage. As demonstrated in Fig. 4.3, although clean limit and associated transitions observed in the weak disorder regime depend on $\varphi_c$, the transmission in Chern phases invariably diminishes to negligible levels under moderate disorder intensity. In contrast, while transmissions in anomalous networks may fluctuate due to bulk states in the clean limit and weak disorder case, they ultimately exhibit high edge transmissions in the strong disorder regime. Focusing on the fully disordered phase-link scenario to analyze the average transmission through the network is physically relevant, as the phenomena at $\delta_\varphi = 2\pi$ demonstrate independence from the central values of disordered phase delays.

We computed the average transmission for fully-random phase-link disorder at each point of our phase diagram, i.e. for all possible tunings of the band structure (Fig. 4.4b). Intuitively, in the fully-random ($2\pi$ strength) phase-link disorder, the value of the transmission depends on the ratio in amplitude between the bandwidths of all the bulk bands, the trivial gaps, and the gaps hosting chiral edge modes. In particular, by reducing the band widths, one increases the transmission, even for the Chern phase.

Note that this mechanism is nonetheless more efficient for the anomalous phase than for the Chern phase. Indeed, the anomalous phases are related by a continuous deformation

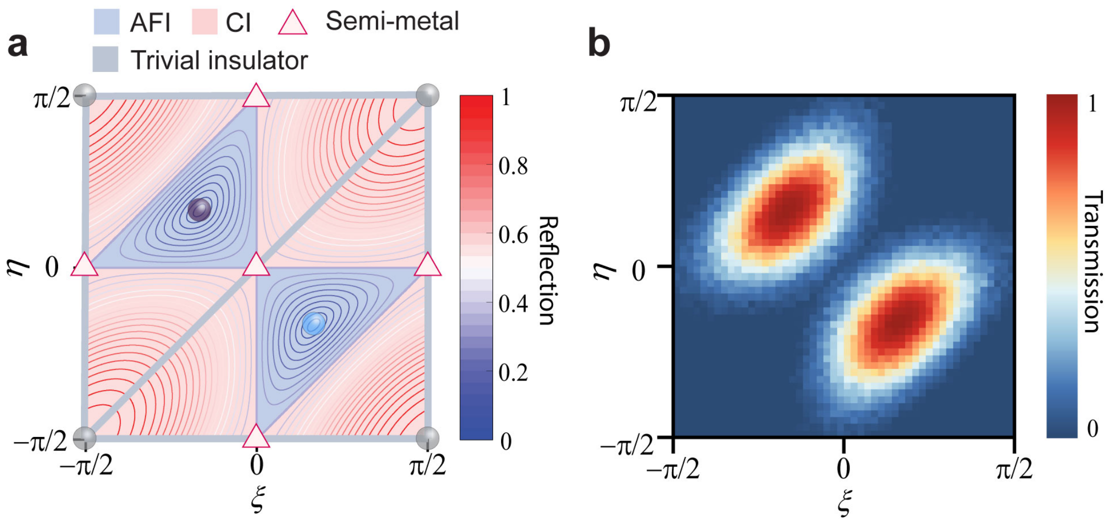

Figure 4.4: **Average transmission in the fully disordered phase-link case for all possible networks in the parameter space. a,** Reminder of the topological phase diagram for all possible $S$-matrix, parameterized by $\xi$ and $\eta$. **b,** Corresponding averaged transmission in the fully-disordered case. The average transmission in the Chern phase is much lower than the average transmission in the anomalous phase.

(that does not close a gap) to a phase-rotation symmetric point, where all the bulk bands are flat [112]. Owing to the topological nature of the Chern numbers and of the $W_\tau$ indices, the Chern phases in scattering networks cannot be continuously deformed to such a special point, otherwise the Chern numbers would be zero. Therefore, their band widths have a minimal finite value that always reduces the transmission compared to the contribution of an edge mode. This favors the anomalous phases that can reach a perfect $T = 1$ transmission even in the fully-random phase link disorder, by tuning the scattering parameters at the blue/purple points in Fig. 4.4a.

Owing to this impossibility to flatten all the bulk bands, and of course to the existence of trivial gaps, it is thus clear that even an optimized Chern phase - i.e. by fine tuning the scattering parameters to maximize the topological gaps and to minimize at the same time both the trivial gaps and the band widths- cannot reach the perfect transmission $T = 1$ in the fully-random phase-link disorder configuration. This said, there is of course nothing that prevents this optimized Chern phase to have a higher transmission than the worse fine-tuned "anti-optimized" anomalous phase (i.e. with band widths as large as possible). The question is then: is this comparison, between the best optimized Chern phase and the worse "anti-optimized" anomalous phase, representative of the average Chern and anomalous cases?

Fig. 4.4b answers this question. In Fig. 4.4b, we find that the anomalous phases have a typical transmission much higher than the Chern ones, and that the average transmission (over scattering parameters of the phase diagram) of the anomalous regime is also mush higher than that of the Chern phase. We also find that there are very small regions where we can pick parameters so that the transmission of the anomalous phase is smaller than the highest possible transmission of the Chern phases. However, such regions only appear close to the transition lines where the gaps are small, and both the optimized Chern and "anti-optimized" anomalous systems collapse to a nearly insulating phase. Elsewhere, when the gaps are well resolved, the transmission in the anomalous phase is close to 1 while the transmission in the Chern phase is close to 0. In Ch. 6, we will deeply understand such distinct behaviors for anomalous and Chern phases in strong disorder regime, by using RG theory and scaling analysis on scattering networks.

## 4.3 Superior robustness of AFI against distributed disorder on scattering nodes

Besides disorder on the phase links, one could indeed imagine another type of physically relevant disorder: on the $S$ matrices of the scatterers themselves (on the network nodes). Scattering matrix disorder altogether includes fluctuations of the circulator matching (reflection coefficient) and nonreciprocity level, which could occur due to finite geometrical tolerances in the circulator fabrication process.

We start with the Chern phase, for which the scattering matrices must belong to the bottom right red triangle shown in the $\xi$ and $\eta$ plane in Fig. 4.5. We consider the same hexagonal sample as in the studies of phase-delay disorder (Sec. 4.2), with the same input and output ports on the top right and bottom right corner, respectively. The clean-limit network is made from uniform scatterers $(\xi_c, \eta_c)$ that are precisely in the middle of the Chern phase (Figs. 4.5(a,b), left). When setting $\varphi = \pi/8$, this network exhibits an edge mode along its edge, connecting the two ports (Fig. 4.5c, left).

For disorder on the scattering matrices of the nodes, we pick $S_0(\xi, \eta)$ randomly within the Chern or anomalous phases, with the phase delay $\varphi$ held constant at $\pi/8$. $S_0(\xi, \eta)$ is chosen at random from a parametric region centered around the clean-limit parameters $(\xi_c, \eta_c)$. The extent of this region, and thus the intensity of disorder, is determined by the parameter $\delta_s$, which therefore serves as the disorder strength. We now consider the same hexagonal network as in Fig. 3.9 (left), but now each scatterer can have a different scattering matrix. Turning on the disorder level to $\delta_s = 50\%$, we allow the $S$ matrices of the individual circulators to fill up 50% of the triangular area of the Chern phase. Note that this corresponds not only to reflection disorder (mismatch) but also to disorder in the degree of nonreciprocity (the isolation), as shown in Fig. 4.6(a,b) (middle column). The edge mode is already completely destroyed. The situation is even worse for fully random disorder that covers $\delta_s = 100\%$ of the triangular Chern phase.

Now, let us compare with the anomalous phase, for which the scattering matrices belong to the upper left blue triangle shown in the $\xi$ and $\eta$ plane in Fig. 4.6. By checking the excited field maps of Fig. 4.6c, we see a totally different behavior: the anomalous edge mode transmission is

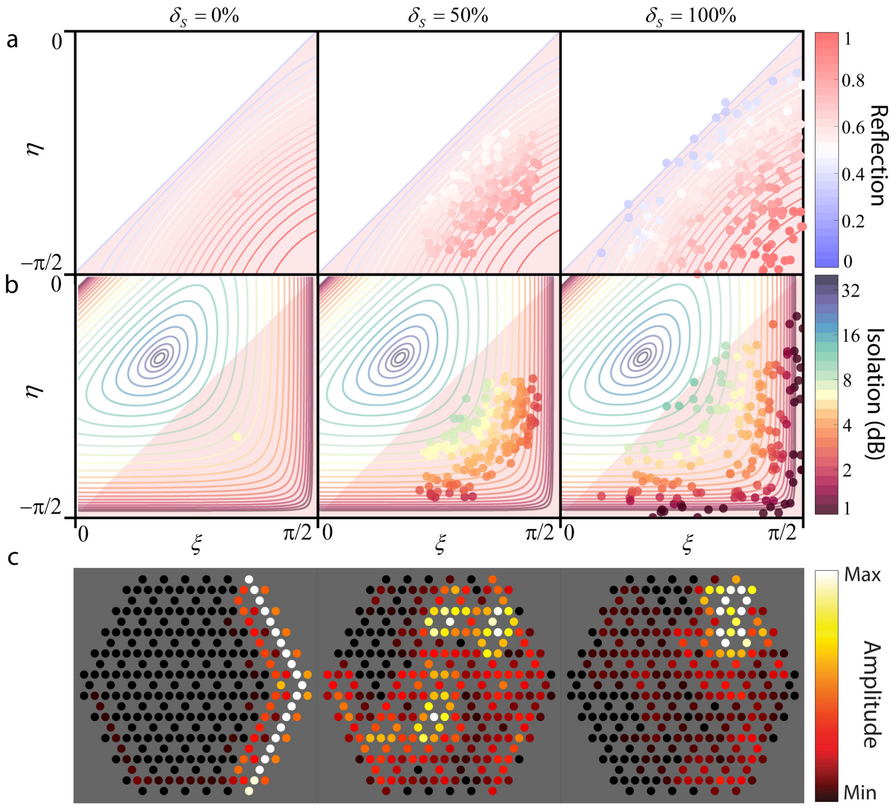

Figure 4.5: **Effect of scattering matrix disorder on the Chern edge mode transmission.** We take the same hexagonal network as in Fig. 4.2, but now each scatterer is randomly selected from a region in the parameter plane, an area whose size depends on the disorder level $\delta_S$. The left column shows the perfectly ordered system, the middle column shows a realization of random scattering disorder filling 50% of the Chern phase, and the right column shows a realization with 100% disorder, namely with scattering matrices anywhere inside the Chern phase. **a, b,** Repartition of the scattering matrices within the Chern phase (bottom right red triangle). The color map shows the corresponding reflection (panel a) and non-reciprocal isolation (panel b) values. **c,** Corresponding field maps, showing the sensitivity of Chern edge modes to scattering disorder.

not affected much and is robust even for 100% disorder in $S$-parameters within the anomalous phase.

The superiority of the anomalous phase over the Chern one in the case of scattering disorder can be quantitatively demonstrated by exploring many realizations, and performing ensemble averaging. The transmission statistics are shown in the bottom panel of Fig. 4.7. We see that the anomalous transmission can tolerate 100% disorder in the choice of scattering matrices, whereas the Chern one falls after 25%. The reason for this surprising behavior is that in a disordered Chern phase (random $|R| > 1/3$), transmission is mediated by both bulk and edge modes, but is blocked by trivial gaps, whereas in the anomalous case (random $|R| < 1/3$), those trivial gaps are absent. This shows that the superior robustness of the anomalous phase is not

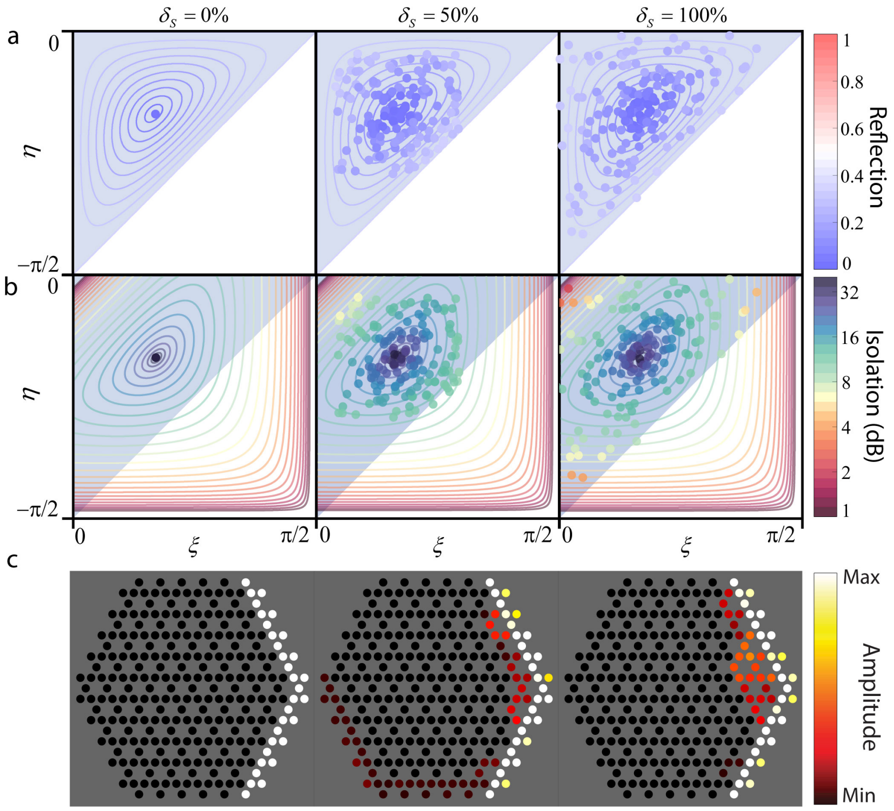

Figure 4.6: **Effect of scattering matrix disorder on the anomalous edge mode transmission.** Same as Fig. 4.5 but the study is performed for the anomalous phase (top left blue triangle). Unlike the Chern one, the anomalous edge mode transmission is very robust even for fully random scattering matrix disorder.

restricted to phase-link disorder, but also to the other possible source of disorder: fluctuations of the scattering matrices.

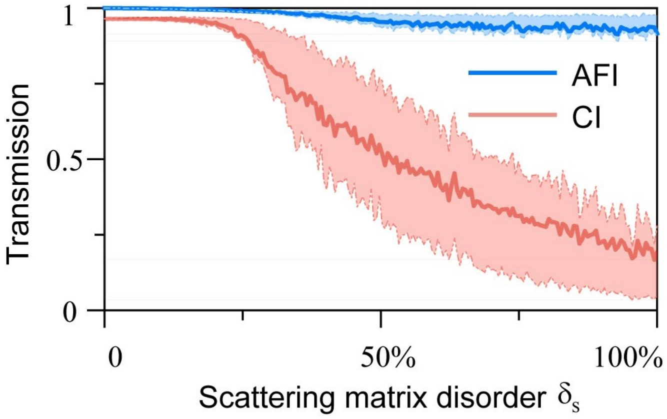

Figure 4.7: **Superior robustness of the AFI phase to scattering disorder.** We impose scattering matrix disorder on the scatterers with a given phase-delay value ($\varphi = \pi/8$). Transmission in the anomalous channel is also more resilient to this disorder type.

## 4.4 Experiments

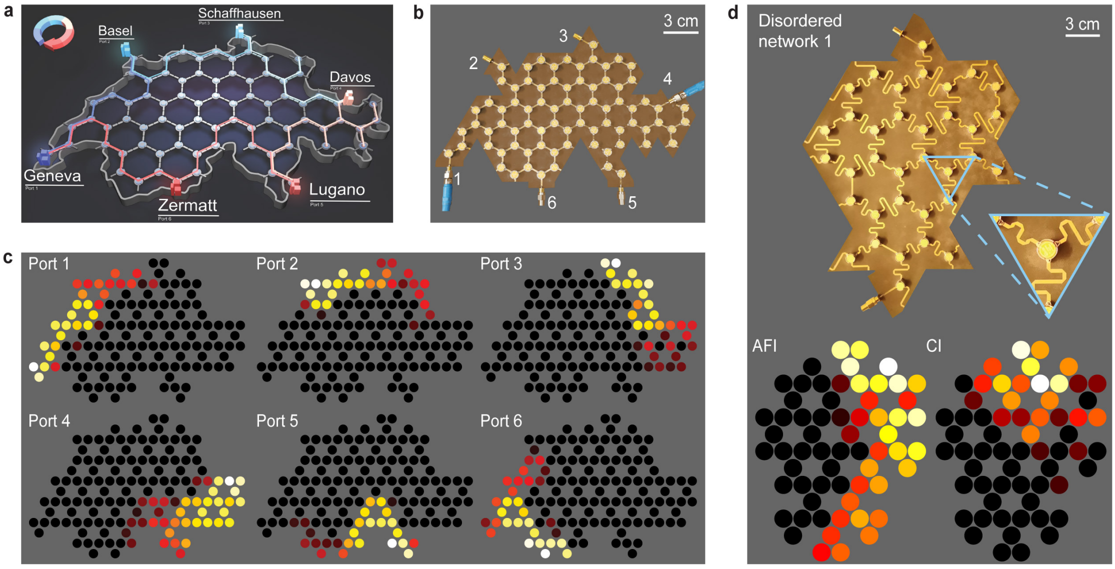
a
Basel
Schaffhausen
Davos
Geneva
Zermatt
Lugano
b
3 cm
1
2
3
4
5
6
d
Disordered network 1
3 cm
AFI
CI
c
Port 1
Port 2
Port 3
Port 4
Port 5
Port 6

Figure 4.8: **Experiments on irregularly shaped and disordered networks. a,** We consider a network shaped like the map of Switzerland, and placed six ports on the external boundary at six city locations. **b,** Photograph of the associated prototype. **c,** Experimental field maps upon sequential excitation of this 6-port system. **d,** Experimental validation of robust anomalous transmission in a two-port system with randomly-disordered phase links under the largest possible disorder strength ($\delta_\varphi = 2\pi$). Top: photograph of one of our prototypes. Bottom: Measured field maps in the AFI and CI cases. The AFI edge mode reaches port 2, while the Chern one is blocked.

We validate the extraordinary resilience of the anomalous transmission by performing experiments on irregularly shaped disordered networks. First, we demonstrate the use of anomalous phases in a practical scenario, where an anomalous non-reciprocal topological network is used to create a robust 6-port circulator with arbitrary shape and port locations. The prototype is shaped like Switzerland, and we place 6 ports at the locations of six boundary cities (Fig. 4.8a). We aim at connecting each city to its clockwise closest neighbour, with strong non-reciprocal isolation to any other city. A picture of the fabricated prototype is shown in Fig. 4.8b. We sequentially excite each input of this six-port non-reciprocal network, and report the measured experimental field maps in the AFI band (Fig. 4.8c). Despite the presence of finite fabrication tolerances, such as the inaccuracy in the surface mounting process of the elements, and shrinking effects due to the employed reflow oven method, and regardless of the tortuous shape of the border, we observe the expected clockwise non-reciprocal circulation of the energy.

Second, we provide an experimental validation of the superiority of the anomalous transmission in the presence of fully random phase delays. We built five new prototypes with randomly drawn realizations of phase link disorder (fully random case), implemented by varying the length of the serpentine paths connecting the scattering nodes. The two-port disordered networks (DN) are numbered from 1 to 5, and have an irregular external shape. DN1 is shown in Fig. 4.8d. The measured field maps in the AFI and CI phases show that only the anomalous channel survives such strong distributed perturbations, consistent with our statistical studies. Fig. 4.9 shows the other four results. Furthermore, this superior robust transport of anomalous edge states is observed in the whole anomalous frequency bands. Fig. 4.10 shows the averaged transmissions counted over measured results on five prototypes. Anomalous transports (panel b) are 15 dB higher transports in the Chern bands (panel a). This difference cannot be attributed to the minor loss difference of circulators in the two frequency bands (Fig. 3.7b), and is consistent with the field maps showing a clear edge transport only in the anomalous band.

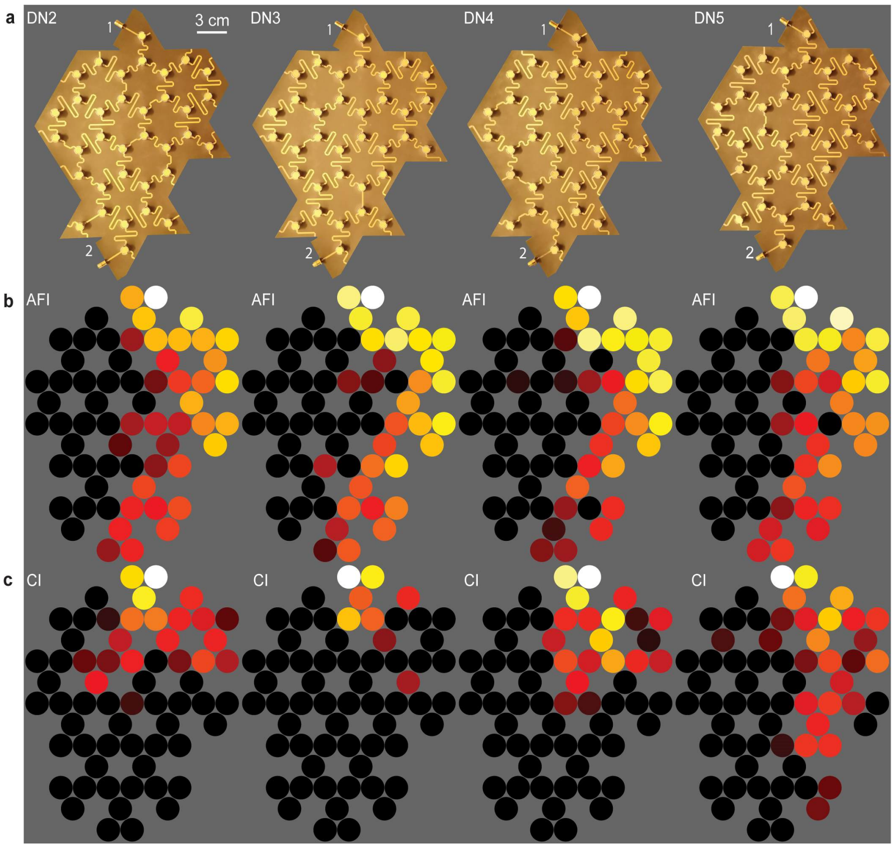

Figure 4.9: **Experimental validation of anomalous phase disorder robustness in four other prototypes with distinct disorder realizations. a,** Pictures of the prototypes, having the same irregular shape but different phase delay distributions implemented by varying the geometry of the serpentine links. **b,** Measured field maps in the AFI phase. **c,** Measured field maps in the CI phase.

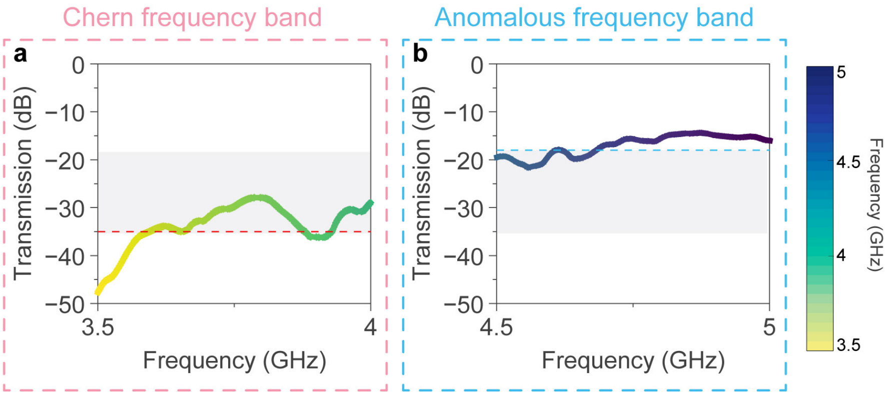

Figure 4.10: **Measured transports averaged over five prototypes in anomalous and Chern frequency bands.** Anomalous edge transports (**a**) are 15 dB higher than transports in the Chern frequency band (**b**).

## 4.5 Robustness comparisons with other Chern phases

Here, we further verify the superior transmission robustness of the anomalous phase by extra comparisons with other Chern phases characterized by various types of band structures. Our extra study shows that even by working with Chern phases with less trivial band gaps or more edge states in the topological gaps, we cannot reach the same level of robustness than the anomalous phase. For easy reference, we note $M$ the number of trivial band gaps of a band structure.

We firstly study the case of Chern phase with a single trivial band gap ($M = 1$), which is less than the number of trivial band gaps of the Chern phase shown in Fig. 3.1 ($M = 2$). In our network, such a phase cannot be directly obtained, because the matrix $S(\boldsymbol{k})$ satisfies the relation $PS(\boldsymbol{k})P^{\dagger} = -S(\boldsymbol{k})$, where $P = \mathrm{diag}(\mathbb{I}_{3\times 3}, -\mathbb{I}_{3\times 3})$. The relation implies that the bulk band structures have $\pi$-translation symmetry, forcing the gaps to close and open by pairs. This $\pi$-translation symmetry can be broken if we introduce an extra unitary 2-port reciprocal scatterer in the middle of the connecting links.

Specifically, by setting the reflection of this extra scatterer to 0, we recover the previous network discussed in the above sections. However, playing with the reflection level of this extra scatterer allows us to extend our parameter space and reach even the cases where $M$ is even. We generate the cases $M = 0, 1,$ and 3 with their ribbon band structures shown in Fig. 4.11. The phase $M = 0$ is the anomalous phase, and $M = 2$ is the Chern phase already reported in Fig. 3.2a in Sec. 3.2. Next, we perform a statistical transmission analysis on a finite network with 1000 different realizations of phase link disorder, with range up to $2\pi$. Panel b shows the results. Clearly, even the $M = 1$ case, despite having a small trivial band gap (its size is around $\pi/6$), is largely affected by the disorder. $M = 3$ is worse than the case $M = 2$ presented in Fig. 4.1, as expected.

In addition, we considered the three cases shown in Fig. 4.12, whose band structures are characterized by Chern numbers with absolute values of 1, 2, and 3 respectively (to increase the Chern numbers, we stacked several networks with Chern phases with $C = 1$ together and coupled adjacent layers weakly with unitary directional couplers). The Chern gaps have, consequently, 1, 2 and 3 edge modes per edge (the band structure is for a ribbon, as Fig. 3.1, with edge modes at both top, in red, and bottom, in blue). Next, we consider the transmission averaged over 1000 realizations of phase link disorder for the three cases (panel b). We observe that an increase of the number of edge modes does not improve the transmission. This is actually expected: the input power has to split over the various available transmission channels. Each transmission channel will contribute to transport and undergo a different phase shift when disorder is imparted, before interfering at the output port. This interference is statistically detrimental to power transmission, a phenomenon known as multi-mode interference, as exploited for example in multi-mode fiber optical sensors.

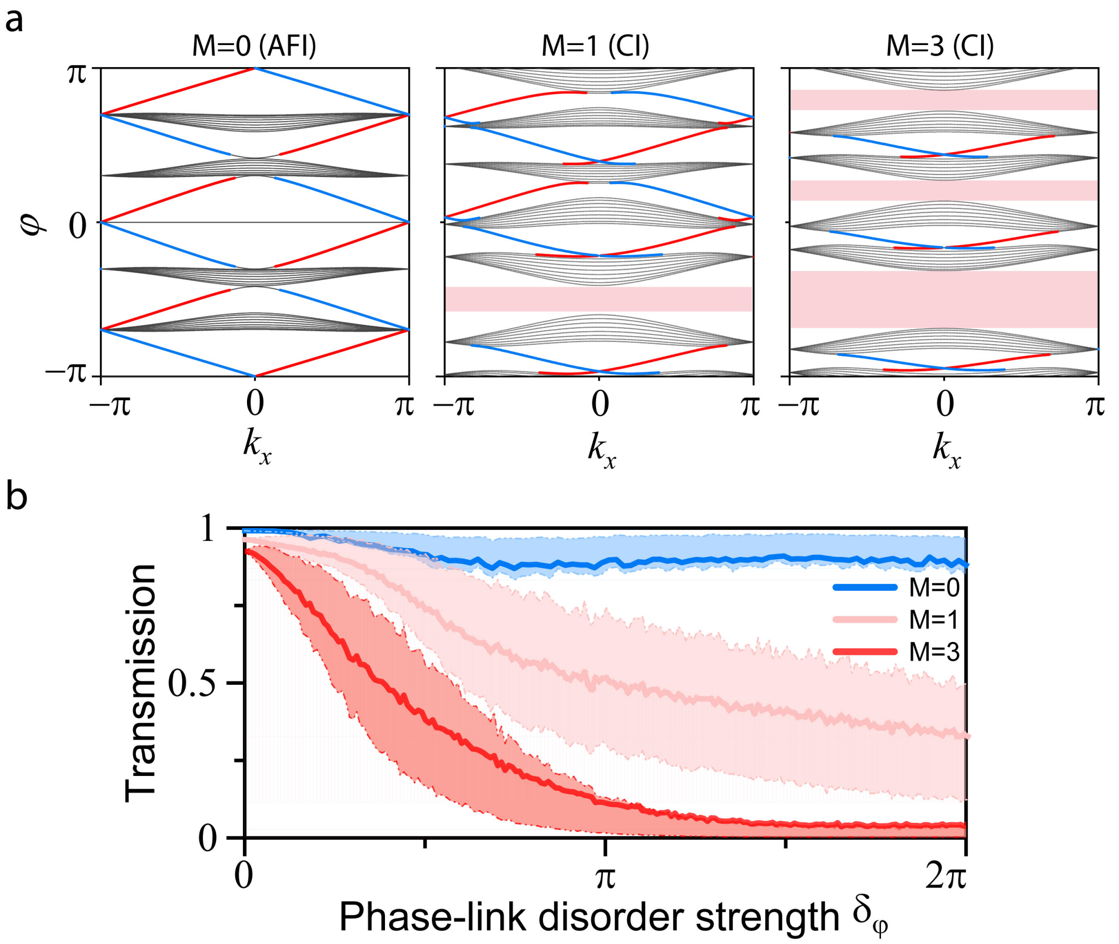

Figure 4.11: **Effect of the number of trivial band gaps (noted $M$) on the robustness of the edge mode transmission to phase link disorder. a,** Ribbon band structures. We compare the case of the anomalous phase (left), in which all band gaps exhibit edge modes, to the case of a Chern phase with a single trivial gap ($M = 1$, center), which is the most favorable scenario for Chern. For a complete comparison, we also take the case $M = 3$ (right). The case $M = 2$ is already studied in Fig. 4.1. **b,** Transmission statistics (average, Q1 and Q3) for the three cases for 1000 realizations of random disorder.

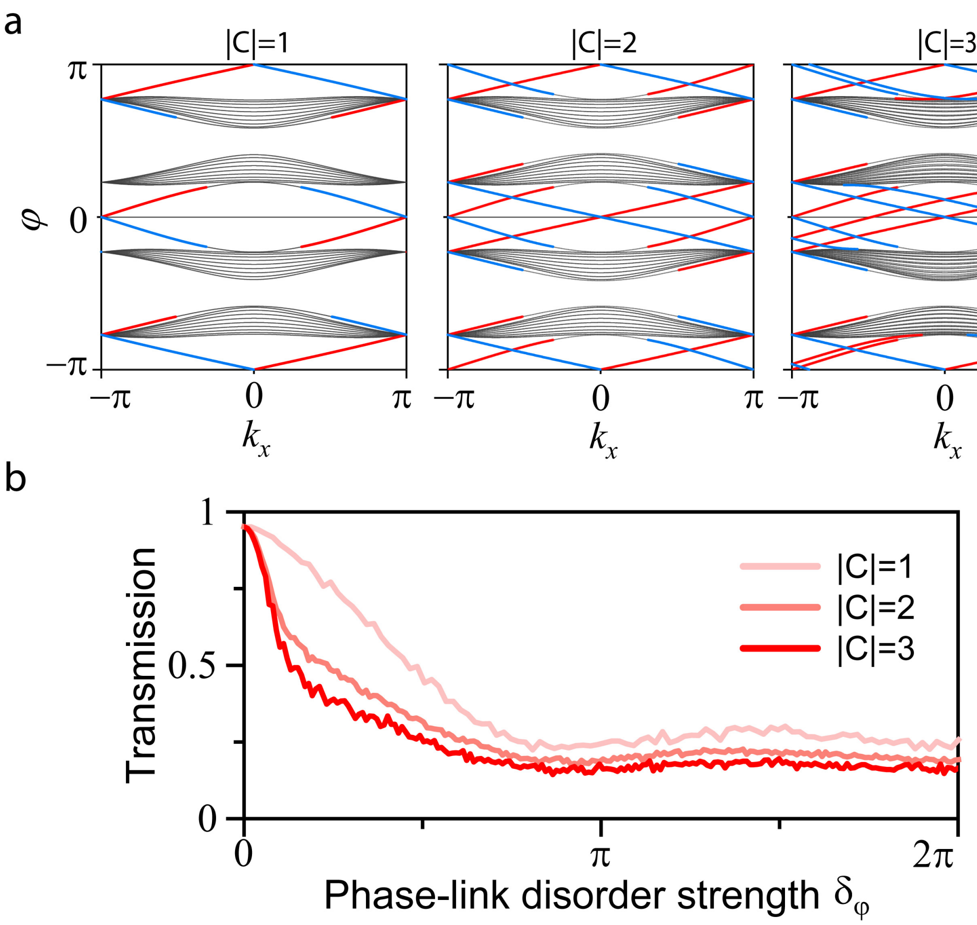

Figure 4.12: **Effect of the number of Chern edge modes on the transmission robustness. a,** Band structures. We compare three different Chern phases with one (left), two (center) and three edge modes (right) in the non-trivial gaps. **b,** Transmission averages for 1000 realizations of random phase disorder. As for transmission between two antennas in a multi-mode environment, the input power has to split over the various transmission channels which interfere at the output. Disorder creates random interference between the different channels at the output, which is statistically detrimental to transmission.

## 4.6 Conclusion

We showed that the difference between anomalous and Chern non-reciprocal topological networks is more than a mere theoretical distinction: there exists a physically observable difference when they are subject to distributed disorder in terms of the resilience of the edge transmission channel. We studied the general conditions to obtain such an unusual effect in systems made of unitary three-port scattering matrices connected by phase links and established the superior robustness of the anomalous edge transmission over the Chern ones to phase link disorder of arbitrarily large values. We confirmed experimentally the exceptional resilience of the anomalous phase, and demonstrate its operation in various arbitrarily-shaped disordered multi-port prototypes. Our results pave the way to efficient, arbitrary planar energy transport on 2D substrates for wave devices with full protection against large fabrication flaws or imperfections.

Consequently, networks in anomalous phase can be differentiated from those in the Chern phase by introducing strong disorder into the phase links and examining the edge transport. In sufficiently large disordered networks, high transmission through edge states indicates the presence of the anomalous phase; otherwise, the network is either in the Chern phase or close to a phase transition (Finite size effect). In this way, the topological phase can be directly and briefly characterized from transports without requiring the entire phase-delay spectrum (quasi-energy) measurement, thus easing the characterization process.

With the maximum phase-link disorder ($\delta_\varphi = 2\pi$), the phase-delay values on links adhere to a uniform probability distribution across the interval $[0, 2\pi)$, regardless of the central value of the disordered phase delay $\varphi_c$, attributed to the periodic nature of phase terms. Indeed, $\varphi_c$ acts as an additional, uniformly applied phase-delay value across all disordered phase links. Crucially, $\varphi_c$ is therefore related with the spectrum of a closed network discussed in Sec. 2.3. As a result, the nearly unity anomalous edge transport, regardless of $\varphi_c$ in strong disorder regime for anomalous phase, implies that there are topological edge states throughout the phase-delay spectrum- a signature of anomalous Floquet Anderson insulator (AFAI). In the next Chapter, we continue to discuss the distinct resilience of anomalous topological phase against amorphous disorder, i.e., a disorder that breaks the honeycomb structure. We will theoretically and experimentally confirm their relation with AFAI through supercell band structure, transport, and measurements of topological scattering invariants.

# 5 Anomalous topological waves in strongly amorphous scattering networks

The main results in this chapter are taken from the published article in Zhe Zhang, Pierre Delplace, Romain Fleury, "**Anomalous topological waves in strongly amorphous scattering networks**", *Science Advances*, 9, eadg3186 (2023) (open access, under a CC BY-NC or CC BY license).

Ch. 4 focused on the effects of phase-delay disorder and scattering nodes disorder in topological unitary scattering networks with a honeycomb arrangement. We discovered that anomalous topological edge states survives within these disordered networks, even at the highest levels of disorder, while Chern edge states collapse and are obstructed. In Ch. 4, we confirmed experimentally the exceptional resilience of the anomalous phase, and demonstrated it in various devices.

However, structural disorder (amorphism), a type of disorder prevalent in nature, remains largely unexplored in topological physics. This disorder breaks the hexagonal loops in honeycomb networks as introduced in Sec. 2.1.4. We are intrigued by how amorphous networks evolve under continuous increase in structural disorder. Furthermore, in Ch. 4, we only examined the transport properties in a finite network, but without rigorously evaluating their potential topological origins. Moreover, concerning disorder-induced localization, we are keen to determine whether Chern networks succumb to Anderson localization. To unveil all the above mysteries, we need to exploit all the analysis methods for disordered networks prepared in Ch.2.

**In this chapter,** we predict and demonstrate a novel topological photonic phase that withstands arbitrarily high levels of amorphism in scattering networks. This topological phase's resilience to strong disorder can only be comprehended within the Floquet topological framework, as it exhibits completely flat bulk bands but possesses topological edge states at any phase-delay (quasi-energy) value, therefore an anomalous Floquet Anderson Insulator (AFAI). The interplay between amorphism and topology triggers, enhances and guarantees the nucleation of robust topological wave energy transport.

**Organization of the chapter:** In Sec. 5.1, we introduce amorphous topological insulators and briefly discuss about findings in this chapter. In Sec. 5.2, we start from oriented scattering graphs and exploit a simple non-atomic limit displaying an unidirectional boundary state to construct anomalous topological edge states that are immune to Anderson localization regardless of the level of amorphism. Sec. 5.3 shows the remarkable resilience of anomalous edge states, by numerically and experimentally comparing its transports in irregular interfaces with the usual edge states of the Chern phase (which are trivialized by strong amorphism). In Sec. 5.4, we utilize transports, eigenstate in closed finite networks, supercell band structures, and topological scattering invariants, and find that topological networks surviving in the strong disorder are actually an AFAI. In Sec. 5.5, we implement our strategy for electromagnetic waves, by constructing non-reciprocal scattering networks operating in the GHz range. We experimentally show the topological edge transport in samples with maximal amorphism, by combining transmission and topological invariant measurements. Sec. 5.6 draws a conclusion for this chapter.

**Notice:** Without the loss of generality, in numerical studies, we take the Chern network ($\xi = 2.5\pi/12, \eta = \pi/12$) and trivial network ($\xi = 2\pi/12, \eta = 2\pi/12$) shown in Fig. 2.10 (Sec. 2.2), as well as the anomalous network ($\xi = 2.5\pi/12, \eta = -2.5\pi/12$) shown in Figs. 3.1 and 3.2. They are used as typical examples for three phases in scattering networks, to show the phenomena unveiled in this Chapter.

Our studies in this chapter involves the disorder realizations of amorphous disorder in Sec. 2.1.4 and mapping shown in Sec. 2.1.5. The applied observables in disordered networks include supercell band structures (Sec. 2.2), transports in open networks and eigenmodes in closed networks (Sec. 2.3), and the topological scattering invariant (Sec. 2.5).

## 5.1 Introduction

Amorphous solids [204], materials that do not exhibit any structural long-range order, represent the majority of the solids found on Earth. Amorphous materials such as glasses, metals, plastics and semiconductors provide unique mechanical [261], electrical [262] and optical [263] properties. Yet, the physics traditionally associated with periodic structures often breaks in amorphous systems. An important example is the topological classification of matter [34, 112, 264], which inherently applies to periodic insulating structures based on their intrinsic and crystalline symmetries, and has recently stimulated the exploration of fascinating phenomena, including robust energy transport in electronic [4, 265] and classical wave [18, 19, 36, 160] systems. Actually, the concept of topology is not fundamentally limited to systems with spatial translation symmetry, as implied by early observations of the quantum Hall effect in disordered samples [54], and theoretical predictions in non-commutative geometry [55, 57]. Recently, topological edge states were shown to be robust to small structural disorder until the close of mobility gaps [219, 266–268]. Recent works have theorized amorphism-induced topology in random fermionic tight-binding lattices [163, 205, 269–272] and quantum spin liquids [206, 207], and performed experiments with mechanical systems [45]. However, all these prior arts were limited to weak levels of amorphism, as stronger levels of amorphism unavoidably close the mobility gaps via Anderson localization, and destroy the topological phase. In addition, the non-trivial topology of amorphous phases has so far only been numerically confirmed using either local Chern markers [221] or Bott index [269] calculations, and a direct experimental measurement of an amorphous topological invariant is still crucially missing.

In this chapter, we investigate, design and experimentally demonstrate a topological regime surviving arbitrarily large levels of amorphism, and prove its topological origin by direct topological invariant measurements. Starting from oriented scattering graphs, we exploit a simple non-atomic limit displaying an unidirectional boundary state to construct anomalous topological edge states that are immune to Anderson localization regardless of the level of amorphism. We implement our strategy for electromagnetic waves, by building non-reciprocal scattering networks operated in the GHz range. We experimentally show the topological edge transport in samples with maximal amorphism, by combining transmission and topological invariant measurements. Those direct measurements are substantiated with numerical studies on supercell band structure, transport, eigenstates in closed network, and topological invariant. They together unveil a striking transition mechanism- the evolution from anomalous topological insulator in the clean limit to anomalous Floquet Anderson insulator (AFAI) driven by strong amorphism. Within this mechanism, the interplay between amorphism and topology triggers, enhances and guarantees the nucleation of robust topological wave energy transport.

## 5.2 Amorphous non-reciprocal networks

The existence of anomalous chiral edge states in networks, periodic or amorphous, can be easily understood from the oriented graphs picture (See mapping details in Sec. 2.1.5): the wave propagates along the oriented links of the graph in a given direction and scatters at the nodes (Fig. 5.1a). If one tunes the scattering parameters of each node such that the wave is fully transmitted into only one link, one can end up with a configuration where the wave is trapped around minimal circuits in the bulk (blue loops), but can circulate around the system through the outermost exterior links (orange loop). Such a configuration is a two-dimensional analog of the non-atomic limit of the Su–Schrieffer–Heeger (SSH) model where the atoms in the bulk of the chain pair to form uncoupled diatomic molecules, leaving an isolated single atom at each extremity of the chain. In our case, it turns out that this surrounding circuit precisely corresponds to an ideal anomalous chiral edge state that decouples from the rest of the bulk, as opposed to more conventional edge states of Chern phases that do not support a similar graph interpretation [112]. The existence of such unidirectional surrounding circuits is guaranteed for planar oriented graphs [149] with equal numbers of incoming and outgoing modes at each node, known as Eulerian graphs (Sec. 2.1.5). Remarkably, it does not depend on the spatial arrangement of the nodes of the graph nor on the length of the links. This suggests that the anomalous chiral edge states of scattering networks are robust to arbitrarily large amorphism (Fig. 5.1a, bottom panel).

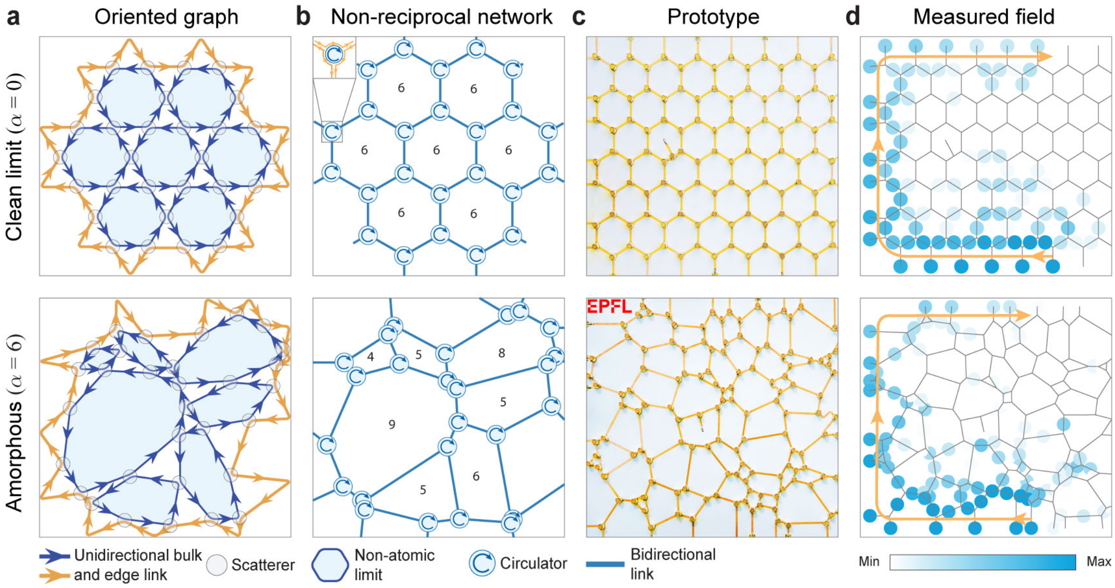
a
Oriented graph
b
Non-reciprocal network
c
Prototype
d
Measured field
Clean limit ($\alpha = 0$)
Amorphous ($\alpha = 6$)
6
4
5
8
9
EPFL
Unidirectional bulk and edge link
Scatterer
Non-atomic limit
Circulator
Bidirectional link
Min
Max

Figure 5.1: **Anomalous edge states can survive any level of amorphism. a,** Random oriented scattering networks. Anomalous topological edge states occur in any scattering signal graphs, when a limit can be found in which bulk signals travel in closed loops (in blue), leaving a large signal loop on the edge (in orange). This picture is valid not only for periodic systems (top row, honeycomb case), but should also be true for any level of amorphism (bottom row). We validate this idea by mapping the oriented graphs (panel **a**) to practical scattering networks made of three-port circulators linked with reciprocal connections (panel **b**). We built prototypes (panel **c**) operating around 5.7 GHz and experimentally observed the resilience of anomalous edge states to strong levels of amorphism (panel **d**).

Guided by this insight, we propose a physical realization of such amorphous insulators in Fig. 5.1b, by the complete mapping between oriented graphs and non-reciprocal networks made of circulators. The circulator networks are generated using a weighted Voronoi tessellation, picking random weights on a triangular generator set lattice (see Sec. 2.1.4 for details). The weight standard deviation defines a dimensionless amorphous factor $\alpha$ that allows us to describe the continuous deformation from the clean-limit honeycomb lattice (top row, $\alpha = 0$), to a highly amorphous regime (bottom row, $\alpha = 6$). We implemented this strategy into two electromagnetic prototypes made of GHz circulators connected by microstrip lines (panel c). The measured electric field maps (panel d) confirm the existence of the anomalous edge state even when $\alpha = 6$. The level of amorphism used in this experiment is very strong, as evidenced from the evolution of network statistics with $\alpha$, shown in Fig. 2.6.

## 5.3 Exceptional resilience of anomalous edge states to strong amorphism

In order to evidence the remarkable resilience of anomalous edge states to a high level of amorphism, we now compare them with the usual edge states of the Chern phase regarding transports in irregular interfaces. We then confirm it experimentally.

### 5.3.1 Transport comparison

In the clean limit of the honeycomb lattice, trivial, Chern and anomalous phases can be engineered according to the degree of reflection and nonreciprocity of the circulators (Sec. 3.2). We use this property to numerically investigate the fate of wave propagation along anomalous-trivial and Chern-trivial interfaces, comparing the clean case to the strong amorphous limit (Fig. 5.2a).

While in the clean limit ($\alpha = 0$, top row), the two configurations both display the expected chiral mode along the interface, in the strong amorphous regime ($\alpha = 8$, bottom row) the anomalous edge state is the only one to survive. The Chern-trivial interface configuration no longer benefits from a topological protection, as the input wave has localized. In other words, both topologically trivial and Chern insulators transit toward a topologically trivial Anderson insulator in the strongly amorphous regime, in sharp contrast with the anomalous phase, suggesting the existence of a topological amorphous phase immune to Anderson localization. We confirm experimentally the topological distinction between the two amorphous phases, respectively obtained by building an amorphous network in the regime $\alpha = 6$, made of two domains that respectively correspond to Chern and anomalous phases in the clean limit (Fig. 5.2b). We observe the unidirectional propagation of an interface state, from the top to the bottom (Fig. 5.2c), and a chiral edge state circulating the anomalous part (Fig. 5.2d), in agreement with a difference of topology between the two strongly amorphous networks.

### 5.3.2 Design of Chern network

Here, we discuss about the design of the Chern network used in the interface configuration of Fig. 5.2, which is achieved by inserting additional scatterers between the circulators. This trick is necessitated by the impossibility to obtain the Chern and anomalous phase with the same circulators at the same frequency (indeed, until now, the main control knob to switch from the Chern to the Anomalous phase has been the operating frequency). In Fig. 5.3, we show how we design a Chern honeycomb network starting from the anomalous one, by adding a reciprocal unitary scatterer in the middle of the phase delay link (design used in Fig. 5.2b). Following our method in Sec. 2.1.1, we gather all the wave signals into four signal vectors $|a\rangle$ (waves leaving the circulators), $|b\rangle$ (waves coming into the circulators), $|c\rangle$ (wave coming into the scatterers) and $|d\rangle$ (wave leaving the scatterers). This leads to an eigenequation and with examples of band structures shown in Figs. 5.3(b-d). The scatterers scattering matrix is

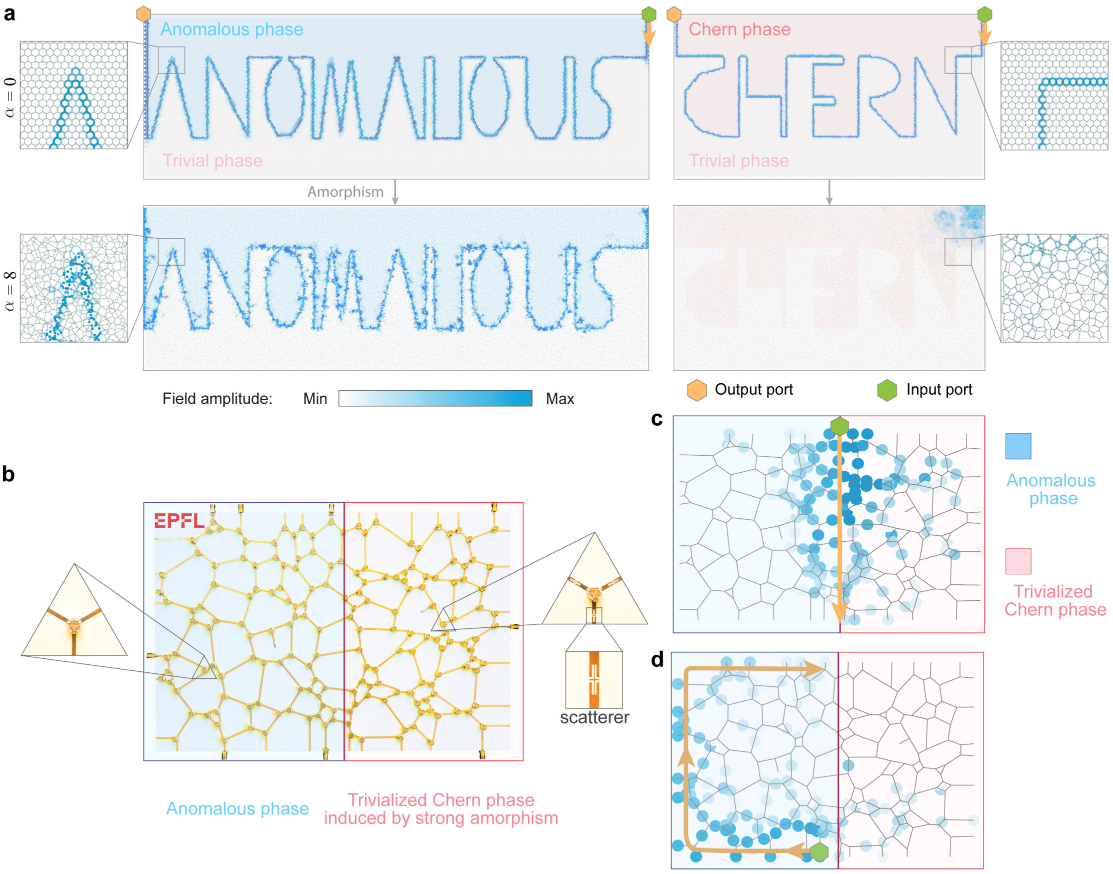
a
Anomalous phase
Trivial phase
Chern phase
Trivial phase
$\alpha = 0$
Amorphism
$\alpha = 8$
Field amplitude: Min Max
Output port
Input port
b
EPFL
scatterer
Anomalous phase
Trivialized Chern phase induced by strong amorphism
c
d
Anomalous phase
Trivialized Chern phase

Figure 5.2: **Exceptional resilience of anomalous edge states to strong amorphism.** We compare the resilience of the anomalous edge mode to amorphism with the one of a standard Chern edge mode, when propagating along a domain wall with a trivial insulator. **a,** In the clean limit ($\alpha = 0$, first row), both anomalous and Chern phases provide a robust channel with unitary transmission. Then, we impart strong amorphism ($\alpha = 8$, second row). Only the anomalous interface state survives. Conversely, the Chern case undergoes Anderson localization. **b,** Experimental demonstration of the topological distinction between anomalous (left) and trivialized Chern (right) phases in the strong amorphous limit ($\alpha = 6$). The trivialized Chern phase is obtained by adding amorphism to a Chern crystal, which differs from an anomalous phase only by the presence of extra scatterers between the circulators. **c, d,** Measured field map when exciting the interface from the top (panel c) and bottom (panel d), confirming the existence of a topological state at the interface and its chiral circulation around the anomalous network domain.

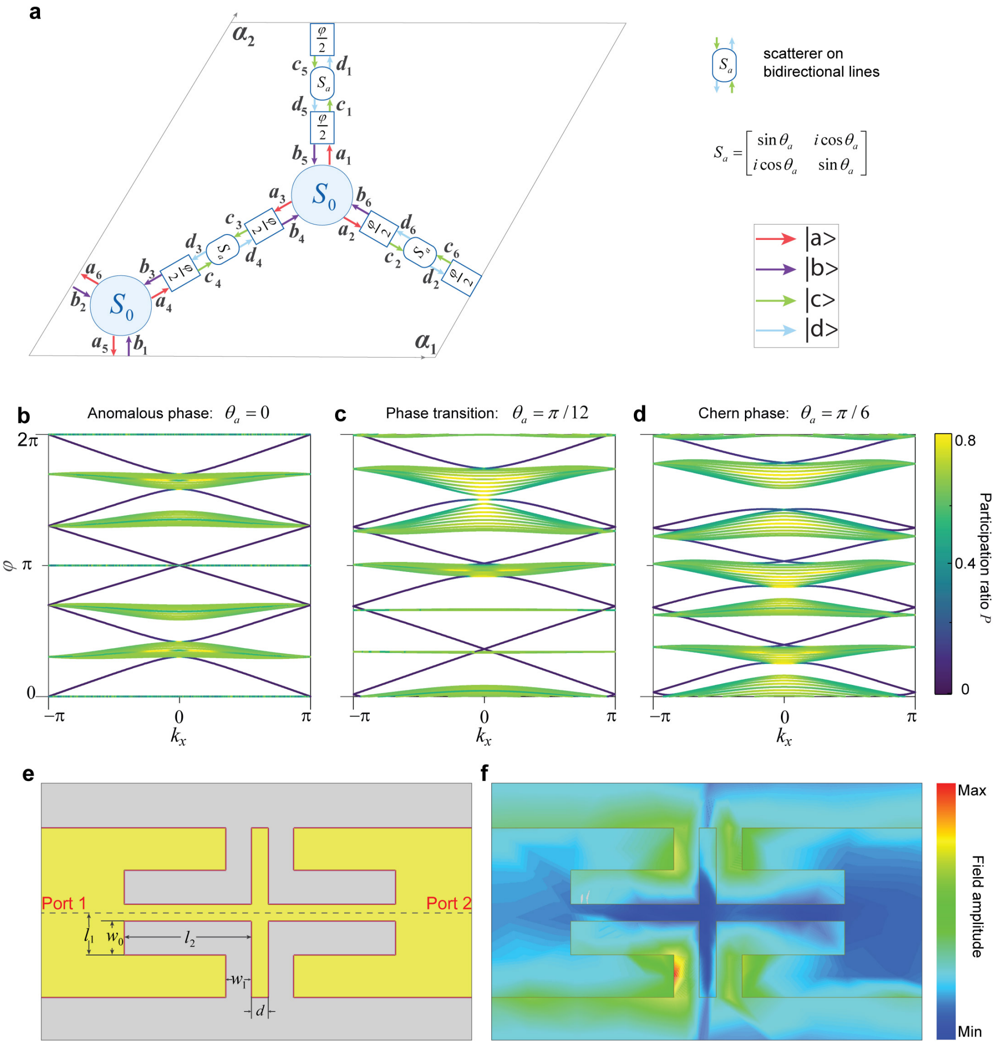

Figure 5.3: **Design of a Chern network by adding reciprocal scatterers in the middle of the phase delay lines of an anomalous network. a,** Unit cell with extra scatterer at the center of each phase delay line. We parameterize its scattering matrix by $\theta_a$. The case of $\theta_a = 0$ reduces to the no scatterer configuration shown in Fig. 2.2c. **b-d,** Examples of ribbon band structures for scatterers with $\theta_a = 0$ (panel b, repeat the left panel in Fig. 3.2a), $\pi/12$ (panel c) and $\pi/6$ (panel d) with circulators parameterized by $\xi = -\eta = \frac{2.5\pi}{12}$. Starting from the no scatterer case in anomalous phase (panel b), scatterers with higher reflection in $\theta_a = \pi/6$ result in a Chern phase (panel c), mediated by a phase transition at $\theta_a = \pi/12$ (panel b). **e,** The practical design of the scatterer with $\theta_a = \pi/6$. **f,** Simulated field map when exciting the wave at port 1. The lower field amplitude at port 2 is consistent with a power reflection of 25% induced by the scatterer.

parameterized by the angle $\theta_a$, where $\sin\theta_a$ controls the reflection level. When the scatterers do not contribute the reflection ($\theta_a = 0$), the honeycomb network is in an anomalous phase (one edge mode in each gap). However, switching $\theta_a$ to $\pi/6$, which corresponds to reflecting 25% of the power results in a Chern honeycomb network (at least one gap is trivial). We then design and simulate a simple scatterer satisfying this condition using full-wave simulations (ANSYS HFSS), as shown in Figs. 5.3(e-f). This scatterer satisfies $\theta_a = \pi/6$.

## 5.4 Amorphism-enhanced anomalous topological phase: AFAI

To shed light on how this amorphous anomalous phase emerges from the clean limit, we compute the evolution of the transmission coefficient between two ports in open finite networks, evolution of spectra in closed finite networks, supercell band structures, and evolution of topological invariant, when increasing the amorphous factor $\alpha$ from the clean limit to the fully amorphous regime. With the analysis on these observables, we confirm that strongly amorphous networks with anomalous edge states have blocked bulk transports consistent with their flat bulk bands but nearly unity edge transports confronting with topological edge states at any phase-delay value in a spectrum. Consequently, they are in anomalous Floquet Anderson insulating (AFAI) phase. This unique Floquet topological phase, proposed Rudner and his colleagues [123], has no counterpart in Hamiltonian topological insulators, and has been only theoretically analyzed in the context of quantum systems. Disorder flatten bulk bands and gapless unidirectional edge states in an AFAI system [71, 132, 149, 169, 170] indicates the latent relations with topological robustness. On the other hand, from the view of phase rotation symmetry [112], systems with flat bulk bands can only be AFI at the perfect circulator points or trivial one at the perfect reflection point. In the strong disorder regime, all transports via bulk states are suppressed therefore making bulk bands flat in the thermodynamic limit. As a result, phase rotation symmetry also points out a possibility of AFAI in the strong disorder regime.

### 5.4.1 Transports through amorphous networks

To begin with, we check the transmission between two ports of a finite anomalous network when increasing the amorphous factor $\alpha$ (Fig. 5.4). The ports are located either both on the edge (top) or both inside the bulk (bottom). In the clean limit ($\alpha = 0$), the bulk band structure is well defined in terms of the link phase delay $\varphi$ between the nodes whose possible values form bands (see left panel of Figs. 3.1 and 3.2a). For a given value of $\varphi$, the network is either in a topological gap with a chiral edge state or in a bulk band (blue and light orange regions near the vertical axes in Fig. 5.4a, respectively). In the weakly amorphous range, the transmission remains consistent with that of the clean limit: edge transmission is always unity in the anomalous topological gaps, and fluctuates within bands, whereas bulk transmission vanishes in the gaps but remains finite in the bulk bands. This reminiscence of the clean limit band structure completely disappears in the fully amorphous regime, which is characterized by unitary edge transmission and zero bulk transmission, regardless of $\varphi$. This is the smoking gun of anomalous Floquet Anderson insulator (AFAI) [131, 132, 163–170]. It shows that strong amorphism drives a global enhancement of the edge transmission and of the bulk insulation when compared to the clean limit.

The transition of the bulk bands into topological amorphous insulators is by no mean trivial. Fixing $\varphi = 1.1$, we now track the evolution of the excited field by plotting its distribution at selected values of $\alpha$ (Fig. 5.4b). In the clean limit (top row), the field is delocalized regardless of the position of the ports, consistently with the existence of a bulk band. This clean-limit picture remains valid when $\alpha$ is increased a little, within the weakly amorphous regime. For $\alpha = 2$, we reach a transition where the bulk transmission has been reduced and the field map shows that the states excited by the bulk and edge probes are much less delocalized. Keeping increasing $\alpha$, the field excited in the bulk localizes around the input port, whereas the edge scenario exhibits a robust chiral edge channel, with enhanced edge localization under strong amorphism.

The nucleation of amorphism-enhanced anomalous topological phase (AFAI) in anomalous scattering networks is markedly different from the behavior of trivial and Chern insulators, which both undergo a trivial Anderson localization transition, both with nearly zero edge and bulk transmissions. Here, we complete the picture by repeating the study for the Chern and trivial insulating phases. The results are shown in Figs. 5.5 and 5.6. Similarly to the anomalous case, Chern and trivial networks in the weakly amorphous regime inherit the properties of the clean limit: the bulk transmission remains finite in the bands, and the edge transmission vanishes in a trivial gap. However, contrary to the anomalous phase, they both end up not transmitting anything under strong amorphism.

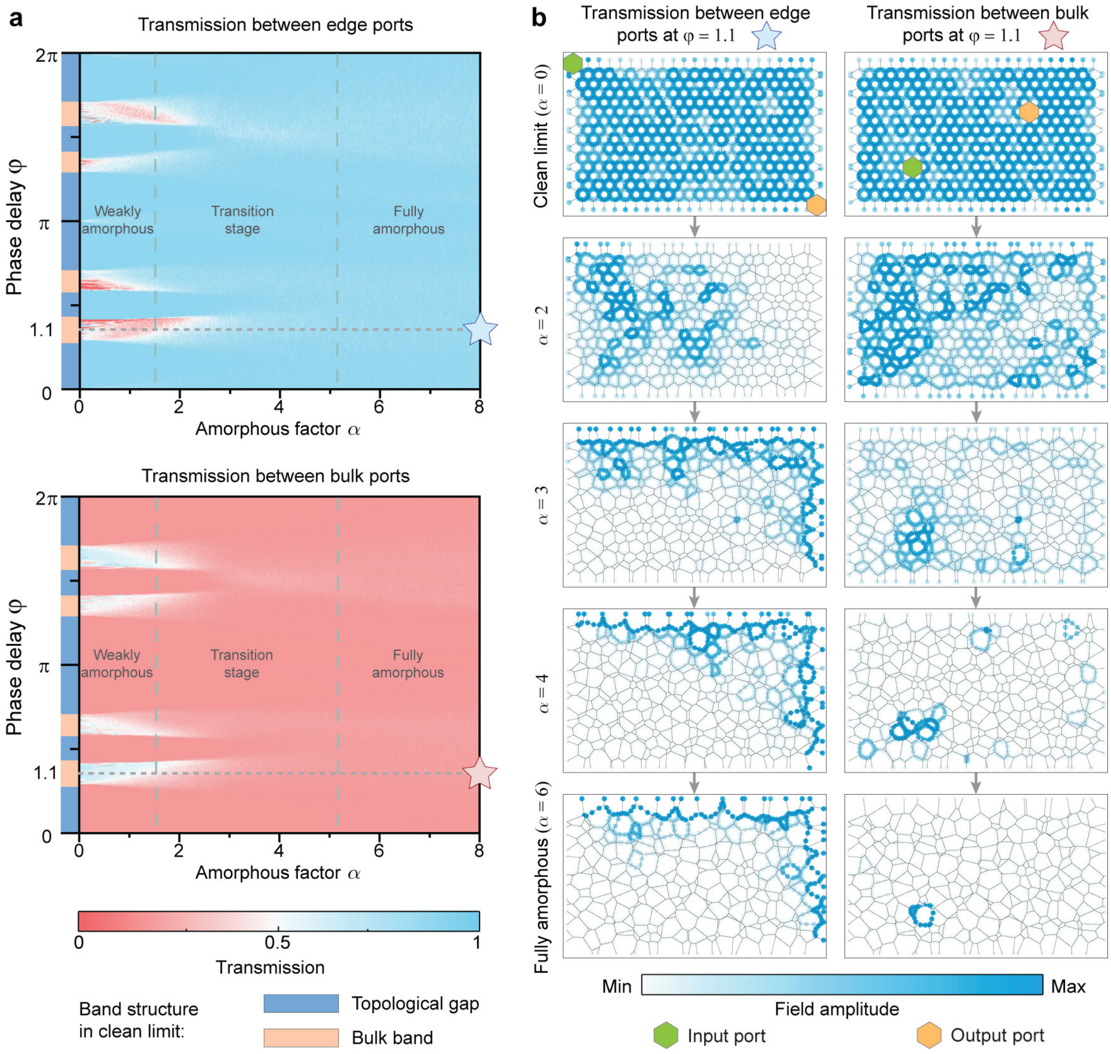

Figure 5.4: **Amorphism-enhanced edge transmission and bulk insulation of the anomalous phase.** We consider the evolution of the anomalous edge and bulk transmissions when increasing the level of amorphism, for any value of the phase delay $\varphi \in [0, 2\pi]$ of the reciprocal links, defined in the clean limit. Each point corresponds to an average over 200 realizations of randomly generated scattering networks, with some examples shown in panel (b). **a,** In the weakly amorphous regime, the edge (top) and bulk (bottom) transmissions are consistent with the clean limit band structures, with large edge transmission only in the topological gaps, and non-zero bulk transmission only in the bulk bands. After the transition stage, the edge transmission is enhanced to 1 and the bulk transmission is pinned to zero regardless of the value of $\varphi$. This confirms the nucleation of a single amorphism-enhanced anomalous topological phase (AFAI), which now spans the full $2\pi$ range.

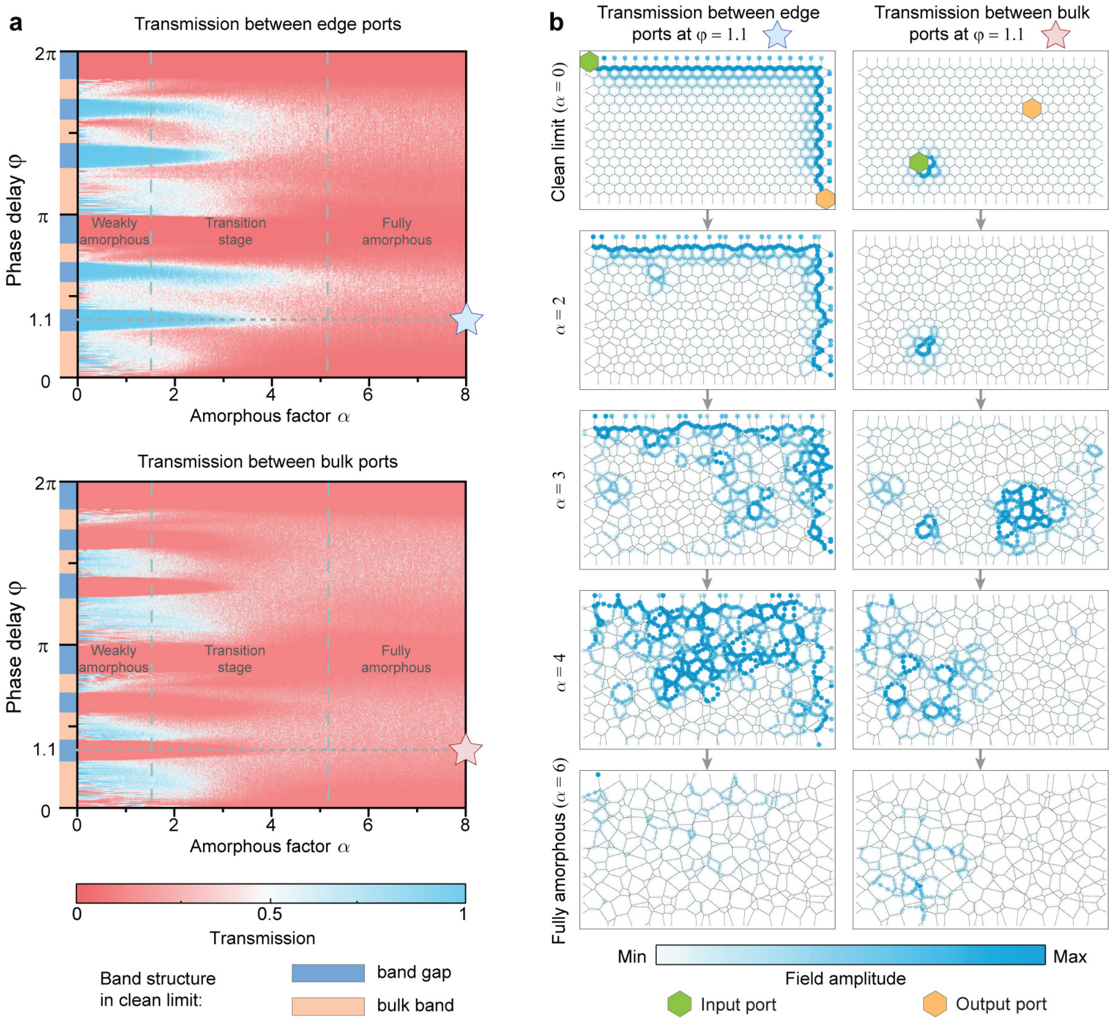

Figure 5.5: **Chern networks become trivial when networks are strongly amorphous.** We calculate the evolution of edge and bulk transmissions for Chern networks upon increasing the level of amorphism, while keeping the other settings of numerical calculations as in AFI case (Fig. 5.4). **a,** In the weakly amorphous regime, the edge and bulk transmissions stay consistent with the clean-limit band structures, with some of the gaps being trivial and other topological. However, in the transition stage, the bulk and edge transmissions gradually go to zero, due to the close of all topological band gaps. Under strong amorphism, the Chern network becomes a trivial insulator. **b,** Examples of amorphous networks and simulated fields of edge and bulk transmissions at $\varphi = 1.1$ (dashed line marked with stars in panel a), located in a topological band gap in the clean limit. Starting from the clean limit (first row) to the intermediate amorphous level ($\alpha = 3$, third row), edge channels show unitary transmission with fields localized at the boundary albeit degrading a little due to amorphism. However, the edge state collapses and gets localized at the input port. The examples in the panels confirm the Anderson transition of Chern networks induced by strong structural disorder.

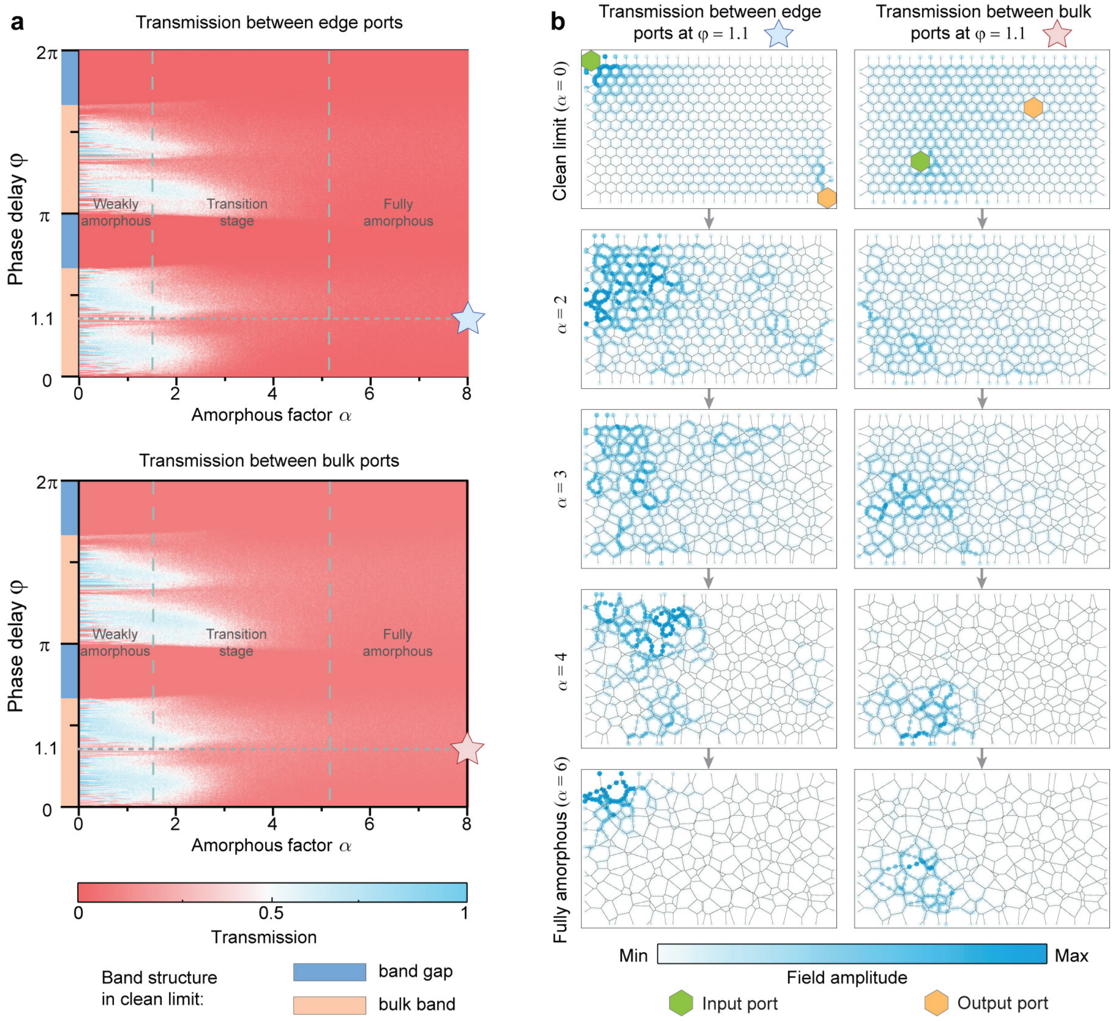

Figure 5.6: **Trivial insulating networks under amorphism.** We consider the evolution of edge and bulk transmissions for trivial networks upon increasing the level of amorphism, while keeping the other settings of numerical calculations as in AFI case (Fig. 5.4). **a,** For trivial networks in clean limit, there are distinct bulk bands, corresponding to the non-zero edge and bulk transmissions. This persists in the weakly amorphous regime. However, in the transition stage, localization starts regardless of $\varphi$, accompanied by suppressed edge and bulk transmission. **b,** Examples of amorphous networks and simulated fields of edge and bulk transmissions at $\varphi = 1.1$ (dashed line marked with stars in panel a, which finds itself in a bulk band in the clean limit. The field profiles gradually localize when increasing the amorphous factor (from top row to bottom row).

### 5.4.2 Spectra of closed amorphous networks

After the analysis of wave transports between external ports in finite networks, we remove the ports and report phase-delay spectra in closed finite networks. We look at properties related to eigenstates, including the density of states (DOS), participation ratio $P$ defined in Eq. (2.30), skin distance $d_s$ defined in Eq. (A.2), and classify the states between bulk or edge. The results in this part unveil that with increasing amorphous level, bulk states do not disappear but populate the whole spectrum. However, these bulk states do not contribute to any transport in strongly amorphous networks, as they become localized. For anomalous networks, strong amorphism transforms a bit of bulk states into edge states, which therefore fill in all the phase-delay values in the spectrum.

In Fig. 5.7, we compute the density of states (DOS) and the participation ratio $P$ (defined in Eq. (2.30)) for the three possible topological phases of honeycomb networks, and then we increase the amorphous factor $\alpha$. The phase delay $\varphi \in [0, 2\pi)$, well defined in the clean limit, can be seen as the additional phase term, which is uniformly applied on each phase link. We normalize density of states DOS($\varphi$) by the DOS($\varphi_0$) of the clean limit, where $\varphi_0$ finds itself in a topological band gap. In the clean limit, DOS and $P$ are consistent with the transports (Sec. 5.4.1) and band structures in Figs. 2.10 and 3.2a (left panel). Continuously increasing the amorphous factor, we observe that the states spread out to occupy the full $\varphi$ spectral range, ultimately occupying all values in $[0, 2\pi)$ with low participation ratio.

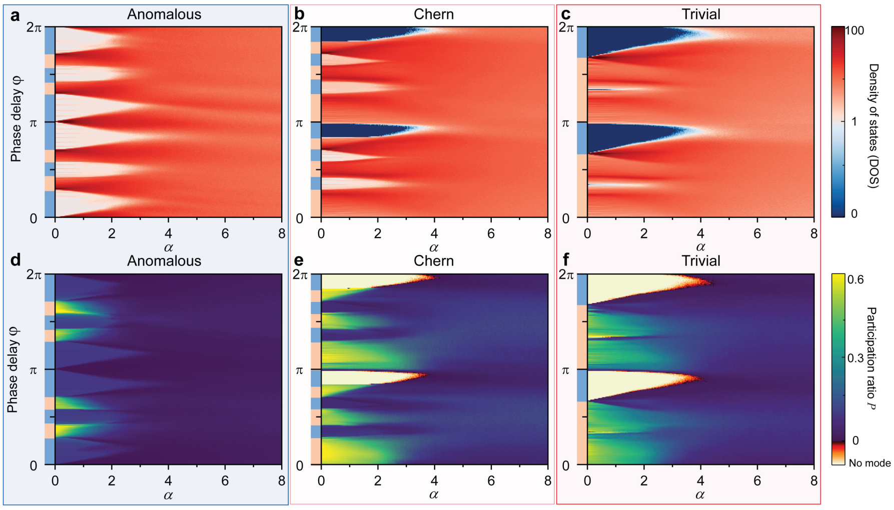

Figure 5.7: **Amorphism localizes the states and populates them in the entire phase delay spectrum.** We solve the eigenstates of finite anomalous (left, **a** and **d**), Chern (middle, **b** and **e**) and trivial (right, **c** and **f**) networks when increasing the level of amorphism, whose eigenphases are phase delay $\varphi$. We calculate the density of states (top row, in logarithmic scale) and participation ratio $P$ (bottom row). As a result of strong amorphism, states populate the whole $\varphi$ spectrum and become localized for all three kinds of networks.

However, distinct transitions happen for three kinds of networks, if one studies the details of the eigenstates. As defined in Eq. ((A.2)), we can calculate the skin distance $d_s(|b\rangle)$ of an eigenstate $|b\rangle$, which captures the averaged position of an eigenstate $|b\rangle$. In Fig. 5.8a, we consider the percentage of skin distance counted over all states for amorphous level $\alpha \in [0, 8]$. Surprisingly, there is a huge difference between the peak of the weakly amorphous distribution and the peak of the fully amorphous one, mediated by a transition from bulk states to edge states during $\alpha \in [1.75, 5]$. As a comparison, we perform the same statistics for Chern and trivial networks, and report them in Figs. 5.8(c-d). It clearly shows that in the fully amorphous regime, both Chern and trivial networks end up with trivial amorphous networks, with large skin distances, in stark contrast with the anomalous case, whose states are localized near the edge.

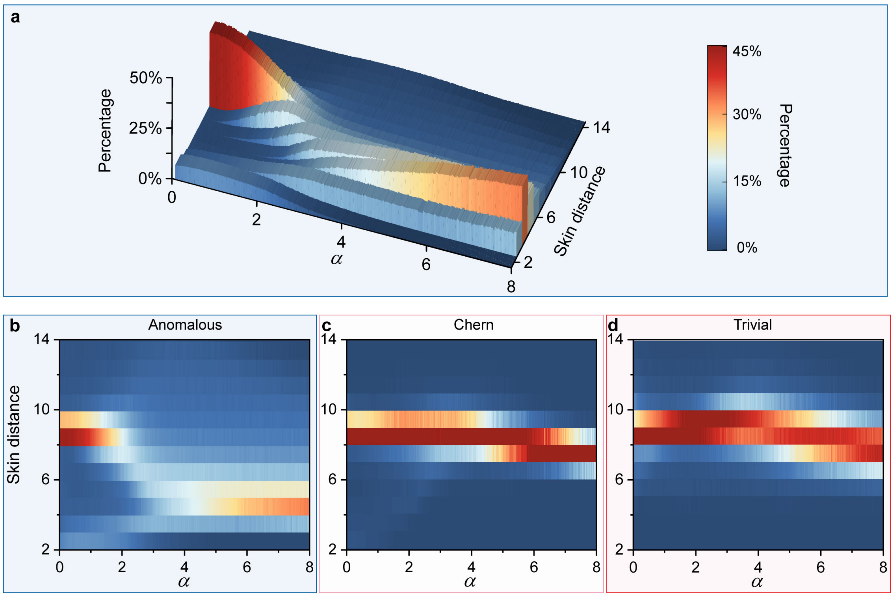

Figure 5.8: **Unique transition in anomalous networks driven by strong amorphism. a,** We consider the evolution of skin distances for eigenstates in finite anomalous networks upon increasing $\alpha$. At a given value of $\alpha$, 200 realizations of amorphous networks are randomly generated with a network thickness around 16. In the clean limit, most of the states are in the bulk with skin distance around 9. A few of them have a skin distance of 3, corresponding to the edge states. With strong amorphism, the bulk peak disappears, leaving only one peak with skin depth centered around 5, i.e. close to the edge. **b-d,** Comparison of skin distances among anomalous (b), Chern (c) and trivial (d) networks under strong amorphism. We perform the same calculations in Chern and trivial networks as that in panel a. For Chern and trivial networks, strong amorphism leaves the states in the bulk, and never creates additional edge states.

In addition, we can classify edge states or bulk states by looking at the skin distance. Based on Fig. 5.8, we decided to adopt a threshold $\tau_b = 5$. A state $|b\rangle$ can be regarded as an edge state, if $d_s(|b\rangle) < \tau_b$ and $P(|b\rangle) < 0.05$ (localized at the boundary). Otherwise, it is classified as a bulk state. Following this rule, we calculate the percentage of edge states and percentage of bulk states upon increasing the amorphous factor $\alpha$. As shown in Fig. 5.9, it is clear that Chern and trivial networks experience the same localization process, ultimately exhibiting trivial networks with all states localized by strong amorphism. However, despite the localization of states, anomalous networks show a different localization transition: they keep gaining more edge states at the expense of the number of bulk states. This striking phenomenon highlights a unique process of conversion from bulk states to edge states that occurs in anomalous networks under the effect of amorphism.

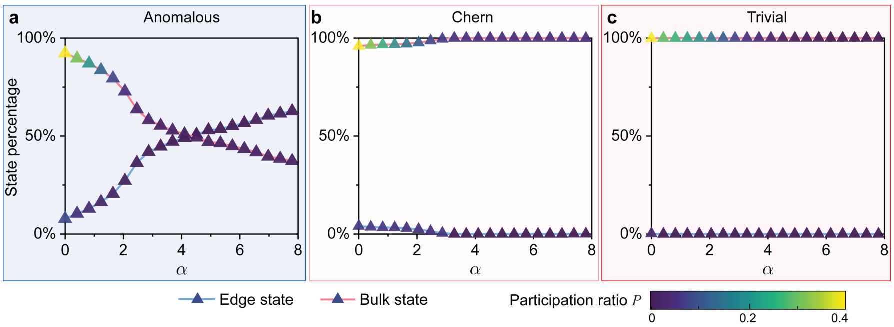

Figure 5.9: **Strong amorphism creates new edge states in anomalous networks.** We classify eigenstates in finite networks to be bulk or edge state, and color them with their averaged participation ratio $P$. We perform the calculations for anomalous (**a**), Chern (**b**) and trivial (**c**) networks when increasing amorphous factor $\alpha$. Only the anomalous networks own edge states in the full amorphous regime, while Chern and trivial networks become trivial amorphous insulator. The number of anomalous edge states increase with $\alpha$, at the expense of the bulk states.

### 5.4.3 Supercell band structures of amorphous networks

Up to now, in anomalous amorphous networks, transports tell us that there is unitary edge transport for any value of phase delay throughout the spectra, along with suppressed bulk transports. Eigenstates in closed networks confirms that the eigenstates populating the whole spectra driven by amorphous disorder, and some bulk states can gradually turn into edge states upon increasing its disorder level, while the other bulk states get localized. However, it will be great if we could confirm that these edge states in the anomalous amorphous networks are really chiral, and the bulk states are localized with nearly vanishing group velocity. As discussed in Sec. 2.2, these phenomena can be visualized by putting twisted boundary condition on the lateral sides for the closed networks, forming supercell band structures.

We consider a finite network with twisted boundary condition (TBC) in the $x$ direction and open boundary conditions in the $y$ direction, as shown in Fig. 2.12b. The non-reciprocal $\Phi$ or the synthetic magnetic flux through the cylinder flux $\Phi$ plays the same role as momentum $k_x$ in the $x$ direction. Therefore, we use $k_x$ here as the horizontal axis. In the clean limit ($\alpha = 0$), the band structures for the anomalous, Chern and trivial honeycomb networks are shown in Figs. 5.10(a-c). In this clean limit, we recover band structures consistent with that computed previously in Figs. 2.10 and 3.2a (left panel), but folded and projected due to the longer length of the unit cell in the $x$ direction (Details discussed in Sec. 2.2). Then, we switch on the amorphous disorder to the level of $\alpha = 6$ (fully amorphous regime, Figs. 5.10(d-f)). The eigenvalues now occupy all the possible values of $\varphi$ and all the states have a low participation ratio, which is consistent with the participation ratio of the eigenstates of finite systems shown in Fig. 5.7.

We now show the differences of behavior of anomalous, Chern and trivial networks, when we impart strong amorphism, namely: (i) the unique transition of anomalous networks to enhanced chiral edge states which populate the phase-delay spectrum, and (ii) the trivial Anderson localization of Chern and trivial networks. To be more precise, we zoom in Figure 5.10 and focus on the band structures around some typical values of phase delay $\varphi$ marked by hexagons, rhombuses and triangles in the anomalous, Chern and trivial networks, respectively. The blue markers are in the band gaps of the clean limit, while the red ones find are in the bulk bands. In the zoomed band structures shown in Figs. 5.11-5.13, we repeat the same plots but color the states according to three metrics: their averaged position in the $y$ direction, participation ratio $P$ and skin distance $d_s$.

Fig. 5.11 focus on the anomalous case. Regardless of the range of $\varphi$ in the clean limit, the spectra in the fully amorphous case exhibit flat bands whose gaps are occupied by chiral edge states (Fig. 5.11). It means that all the bulk states are localized, while chiral edge states populate all the phase delay $\varphi$ spectrum, confirming the enhanced anomalous edge transport and bulk insulation in Fig. 5.4. In contrast, band structures for Chern (Fig. 5.12) and trivial (Fig. 5.13) networks only display isolated flat bands in the strong amorphous limit, indicating the transition to topologically trivial amorphous insulators. The above spectral calculations confirm and supplement the transport, eigenstates results in Secs. 5.4.1 and 5.4.2.

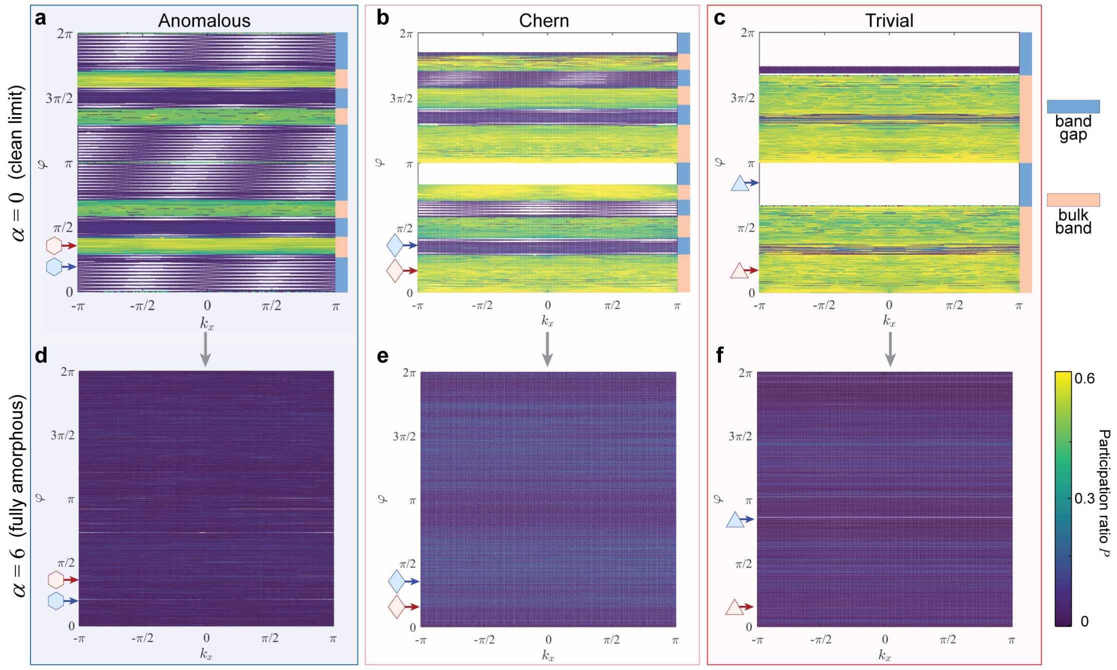

Figure 5.10: **Band structures of networks in clean limit and in fully amorphous regime in the cylinder geometry.** We regard a finite network as a super unit cell and assume Bloch wave with momentum $k_x$ along the $x$ direction. The cylinder band structures are computed by solving the formed eigenproblem, whose eigenphase is the phase delay $\varphi$. We consider anomalous networks in the honeycomb ($\alpha = 0$, **a**) and fully amorphous ($\alpha = 6$, **d**) cases with network thickness of 9. As references, we calculate the cylinder band structures of Chern (**b** and **e**) and trivial (**c** and **f**) networks in the clean (top row) and strong amorphous limits (bottom row).

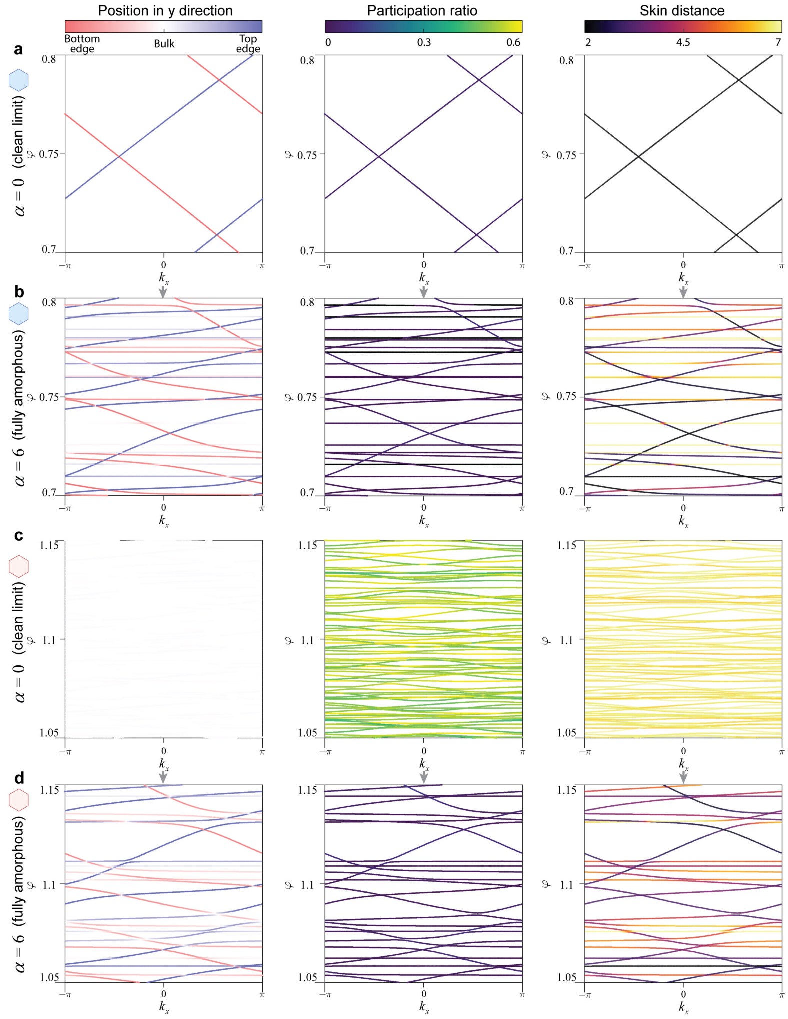

Figure 5.11: **Strong amorphism enhanced anomalous topology: AFAI. a,** The cylinder band structure in Fig. 5.10a, zoomed in the phase delay range $\varphi \in [0.7, 0.8]$, supports chiral edge states in the clean limit. We color states with averaged positions regarding the $y$ (non-periodic) direction (leftmost panel), participation ratios (middle panel) and skin distances (rightmost panel). **b,** Zoomed cylinder band structure (Fig. 5.10d) in the same phase delay range as in panel a. The spectrum of $\varphi \in [0.7, 0.8]$ is filled with several nearly flat bands, consisting of states with high skin distances (namely in the bulk). Surprisingly, these flat bands are linked by gapless states, which are localized at the top (blue) or bottom (red) edge depending on the slope sign of the gapless states. This means that the gapless states are chiral edge states persisting in the strong amorphous regime, while bulk states are localized. **c,** The cylinder band structure in Fig. 5.10a for a honeycomb network zoomed in the phase delay range $\varphi \in [1.05, 1.15]$, where bulk states dwell. **d,** The cylinder band structure in Fig. 5.10d zoomed in the phase delay range $\varphi \in [1.05, 1.15]$. The gapless chiral edge states between flat bands indicate a non-trivial transition driven by strong amorphism.

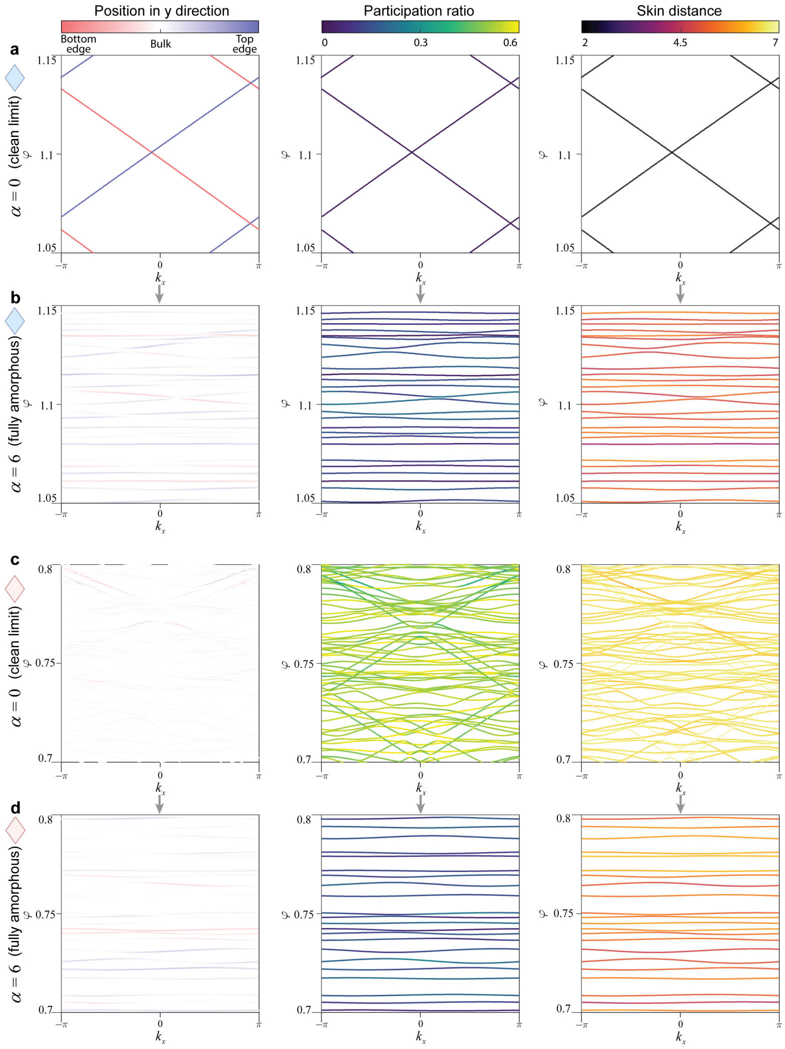

Figure 5.12: **Trivialization and localization in Chern networks induced by a strong amorphous disorder. a,** The cylinder band structure in Fig. 5.10b, zoomed in the phase delay $\varphi \in [1.05, 1.15]$, supports topological edge states in the clean limit. **b,** Zoomed cylinder band structure (Fig. 5.10e) in the same phase delay range as panel a. The spectrum of $\varphi \in [1.05, 1.15]$ is filled with many flat bands, consisting of states localized in the bulk. However, unlike the anomalous case, there is no gapless states, indicating the trivialization of Chern network. **c,** Cylinder band structure of Fig. 5.10b for a honeycomb network, zoomed in the phase delay range $\varphi \in [0.7, 0.8]$, where bulk states dwell. **d,** Cylinder band structure of Fig. 5.10e zoomed in the same phase delay range as panel c. The flat bands comprising localized bulk states are isolated in the $\varphi$ spectrum, suggesting a strong amorphism induced Anderson localization of states.

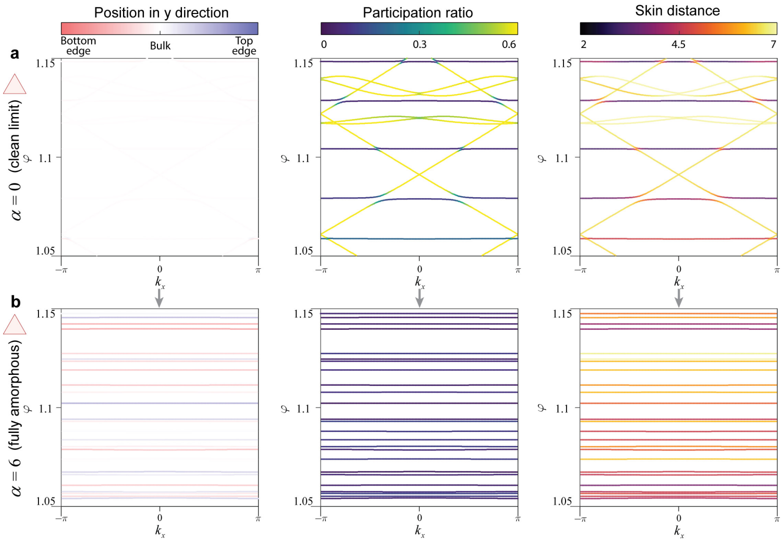

Figure 5.13: **Localization in trivial networks in the fully amorphous regime. a,** The cylinder band structure in Fig. 5.10c, zoomed in the phase delay $\varphi \in [1.05, 1.15]$, supports bulk states in the clean limit. **b,** Zoomed cylinder band structure (Fig. 5.10f) in the same phase delay range as panel a. The spectrum in the range $\varphi \in [1.05, 1.15]$ is filled with isolated flat bands, consisting of states localized in the bulk. It suggests the strong amorphism induced localization in trivial networks.

### 5.4.4 Topological scattering invariant for amorphous networks

After studying transports in open networks, eigenstates of closed networks, and supercell band structures for disordered scattering networks, one can believe that anomalous scattering networks in strongly amorphous regime are of AFAI, with a high degree of certainty. To complete the picture, we propose to confirm the topological origin of the chiral edge states by calculating the topological scattering invariant. To do so, we utilize the theory introduced in Sec. 2.5.

Fig. 5.14 shows the numerically calculated winding numbers of randomly generated networks for all levels of amorphism and values of $\varphi$. For anomalous networks (panel a), the phase diagram suggests that the effect of amorphism is first to localize the bulk states, creating a topological mobility gap. This is confirmed by participation ratio of eigenstate calculations in closed networks (Fig. 5.7). Besides, we also find that the anomalous supercell band structure displays flat bulk bands with topological gapless chiral edge states in between (Figs. 5.11 and 5.14). Therefore, one can be convinced that anomalous networks in fully amorphous regime are in anomalous Floquet Anderson insulating phase. In contrast, when starting from a Chern phase (panel b), the topological gaps close as both bulk and edge states localize, creating a trivial amorphous insulator. Performing a statistical study at $\varphi = 1.1$ with 200 realizations, Fig. 5.14c shows that topological transitions have to be understood in a statistical sense: the proportion of realizations with non-trivial winding number changes smoothly when increasing $\alpha$ through the transition stage.

In a sum, the non-trivial topological edge states and transports in anomalous networks are induced, enhanced and guaranteed by strong amorphism.

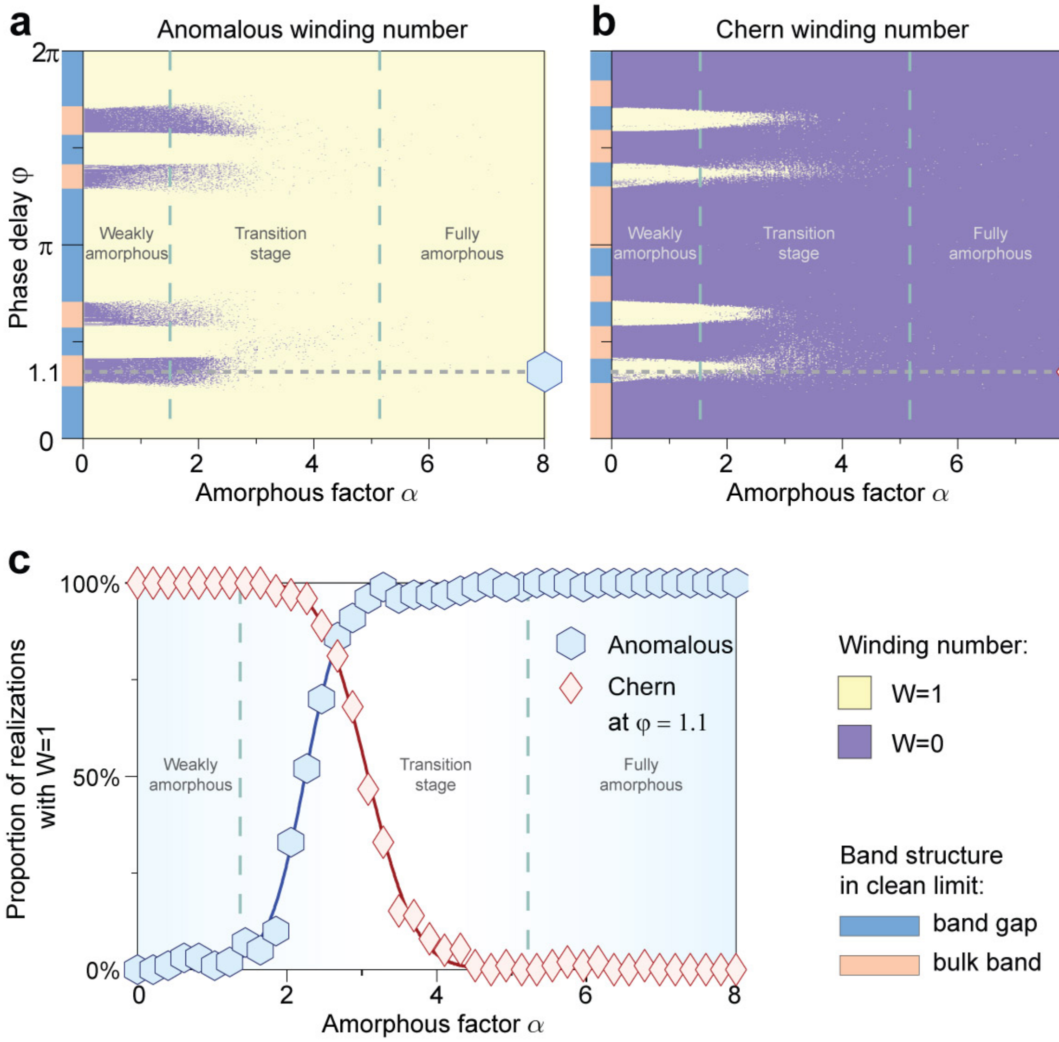

Figure 5.14: **Emergence of anomalous Floquet Anderson insulating phase (AFAI) in anomalous scattering networks when inducing strong amorphism. a, b,** Amorphism-induced topological phase transitions. For each amorphous level $\alpha$ and phase delay $\varphi$, we calculate the winding number $W$ of a randomly generated network. In the weakly amorphous regime, the bulk bands of the anomalous network (a) persist with trivial windings, while the Chern networks (b) exhibit a robust non-trivial topology only near the Chern gaps already present in the clean limit. Under moderate levels of amorphism, opposite transitions occur for the two phases. The occurrence of Chern networks (b) with non-zero winding decreases to zero, consistent with a trivial Anderson insulator. Very differently, anomalous networks (a) undergo a topologically non-trivial Anderson transition to be AFAI, as the entire spectrum becomes topological and bulk bands are flatten by strong amorphism. **c,** Statistical study of the proportion of realizations with non-trivial winding versus $\alpha$, performed on 200 random realizations of amorphous networks with phase delay $\varphi = 1.1$.

## 5.5 Measurement of topological scattering invariant in the strongly amorphous regime

In this section, we introduce the experimental methods involved in the measurement of the scattering topological invariant. We then exhibit the design and measured scattering properties of the non-reciprocal phase shifter implementing the twisted boundary condition used in our direct measurements of the topological scattering invariant. With experiments on edge and bulk transports, we examine the trivial scattering networks, where strong amorphism induces Anderson localization. Finally, we report the results of the direct measurements of topological invariants. We could observe the distinct transitions happens for anomalous and Chern networks when inducing strong amorphism consistent with the statistical study in Fig. 5.14c.

### 5.5.1 Measurement methods and bulk ports

The scattering parameters and field maps of fabricated honeycomb and amorphous networks are measured by a vector network analyzer (VNA; ZNB20, R&S). For field map measurements, we connect the signal input port of the measured device to VNA port 1 and measure the transmission by the near-field probe connected with VNA port 2. As shown in Figs. 5.15(a-b), the field probe made from coaxial lines couples with the vertically polarized near field of microstrip lines, due to the guided mode of quasi-TEM on the line. The bulk excitation is achieved by designing a port at the back, which transits the wave from the coaxial cable to microstrip line (Figs. 5.15(c-d)). In the fabricated networks, we drill a metalized hole, in which we insert the inner connector of the coaxial cable.

### 5.5.2 Experimental realization of twisted boundary conditions

Our reconfigurable non-reciprocal phase shifter prototype is shown in Fig. 5.16a. It consists of two identical reconfigurable reciprocal phase shifters, put in parallel, connected at the two junction points by two circulators. External voltages exerted on the anodes control the reciprocal phase shifters, altering the capacitance of varactors. Radial stubs are used as low-pass filter to isolate the microwave frequency wave from the static voltage control circuits. With high-pass filters to isolate the static voltages from each other, $V_1$ (top one) and $V_2$ (bottom one) independently adjust the phase-shift values in transmission from port 1 to 2 and transmission from port 2 to 1, respectively. All the components are built on 1.016mm thick Rogers RO4350B laminates with 1oz copper layers on the top and bottom sides. The varactors are SMV2020-079LF of silicon hyperabrupt junction varactor diode (Skywork Co.).

To synthetically achieve the adiabatic cycle of magnetic flux $\Phi$ in such photonic platform, each reciprocal reconfigurable phase shifter should cover a continuous phase shift range of at least $2\pi$, when tuning the static voltage in the operating frequency band of our non-reciprocal networks ($f \in [5.4, 7]$ GHz). To reach this goal, we adopt a reconfigurable reflective-type

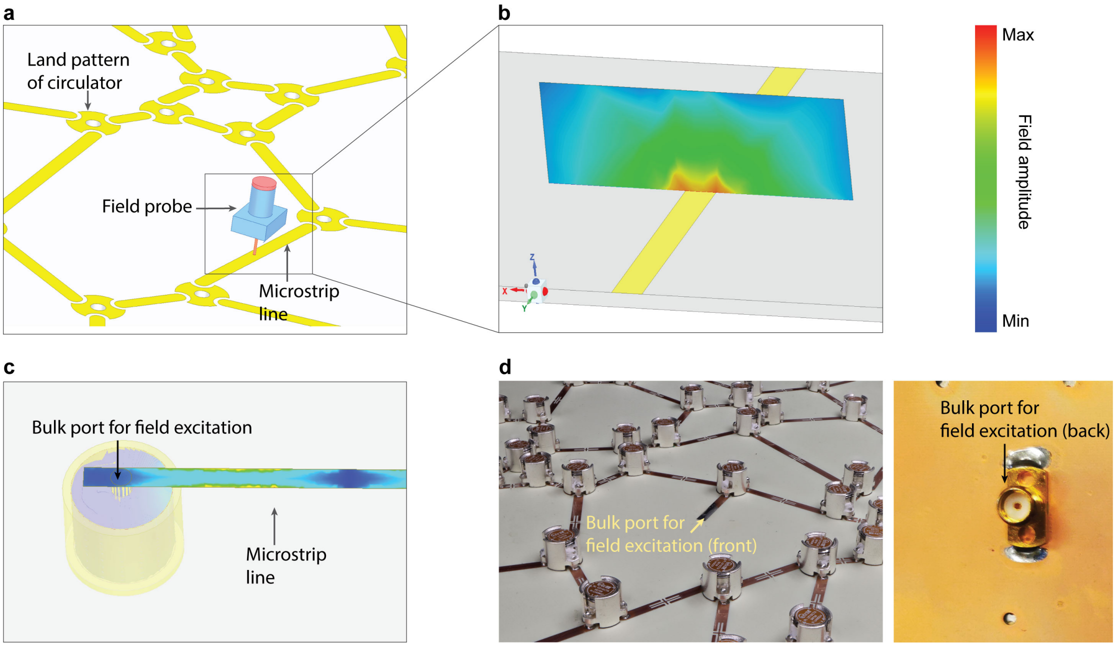
a
Land pattern of circulator
Field probe
Microstrip line
b
Max
Field amplitude
Min
c
Bulk port for field excitation
Microstrip line
d
Bulk port for field excitation (front)
Bulk port for field excitation (back)

Figure 5.15: **Measurement method and bulk port design. a,** We use the coaxial probe to couple with the near field of microstrip line. **b,** The near field of microstrip line. **c,** The design of the port used for bulk excitation and field map upon feeding the port. **d,** Zoomed in view of the bulk port in the prototype.

analogue phase shifter, which is compact and able to continuously shift phase values. The designed single reconfigurable phase shifter is composed of three parts: two high pass filters, a 90 degree hybrid coupler and two reflective loads. We input microwave at port 1 and show the simulated field map of the phase shifter in Fig. 5.16b. The 90 degree hybrid coupler is used for wide-band impedance matching. In addition, the field shows that the designed low pass filter exhibits nice isolation between the microwave frequency wave and static voltage control source. The reflective loads contribute to having an access to a large range of phase shifts. The basic phase-shift mechanism is the following: taking a typical resonator with resonant frequency $f_0$ as a example, when tuning the resonant frequency from $f_1$ to $f_4$, the phase reaction at $f_0 = (f_2 + f_3)/2$ can be nearly altered by $\pi$ (Fig. 5.16c) [273, 274]. For a reflective load, when the resonant frequency is tuned by changing the capacitance of varactors, the range of phase shift can be around $2\pi$. One can further increase the range by combining several resonators (here we use two).

Based on the measured scattering matrix of the fabricated reconfigurable non-reciprocal phase shifter, Fig. 5.16d shows how to set the applied voltages $V_1$ and $V_2$ for realizing a given non-reciprocal phase $\Phi$. As shown in Fig. 5.16e, the measured maximal phase-shift range in the operating frequency band of networks is beyond $2\pi$, which enable the topological invariant measurement in the whole band. To wrap the networks to be a cylinder in the topological invariant measurements, we fabricate eight reconfigurable non-reciprocal phase shifters. The standard deviation of the measured phase shifts for these 8 devices is close to zero (Fig. 5.16f).

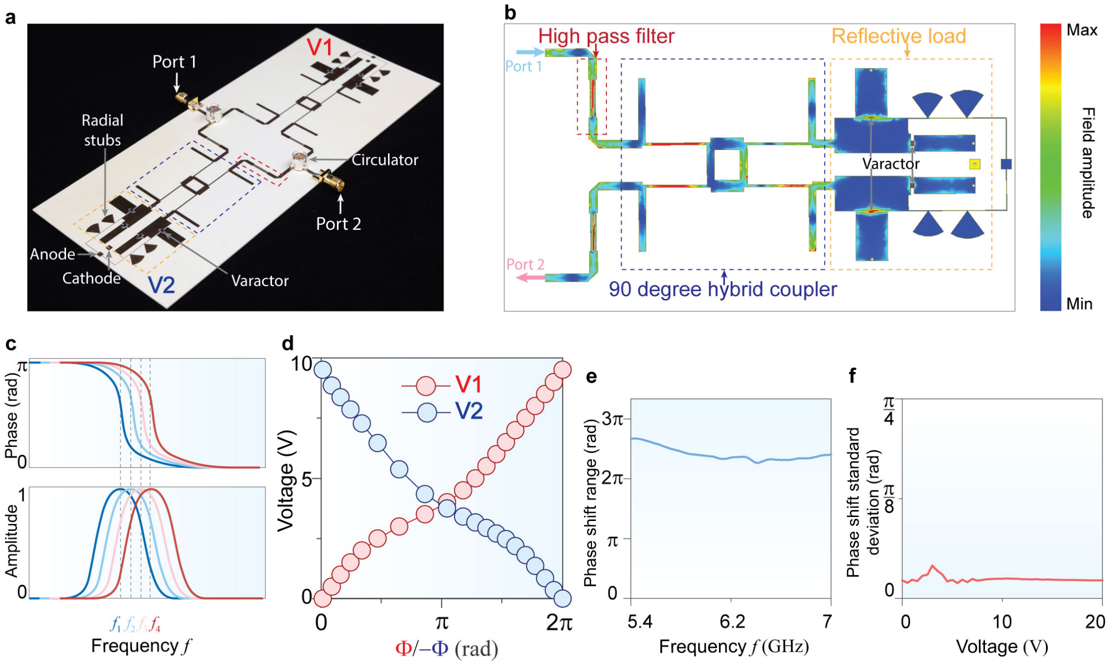

Figure 5.16: **Design and measurement of our reconfigurable non-reciprocal phase shifter (twisted boundary condition). a,** Prototype of a reconfigurable non-reciprocal phase shifter. **b,** Simulated field map (input at port 1) of the reconfigurable phase shifter. It comprises three parts: two high pass filters, one 90-degree hybrid coupler and two reflective loads with four varactors controlled by static voltages. **c,** Mechanism of phase shift induced by resonant frequency shifts. For a typical resonator, when tuning the resonant frequency from $f_1$ to $f_4$, the phase reaction at $f_0 = (f_2 + f_3)/2$ can be nearly altered by $\pi$. A reflective load therefore exhibits a $2\pi$ range of phase shifts. **d,** Applied voltages $V_1$ and $V_2$ to realize a given synthetic magnetic flux $\Phi$, used in our winding number measurements. **e,** Measured phase-shift range in $f \in [5.4, 7]$ GHz. **f,** Standard deviation of the measured phase shifts for the 8 phase shifters involved in the twisted boundary condition, at 5.6 GHz.

### 5.5.3 Experimental observation of Anderson localization in trivial scattering networks induced by the strong amorphism

In this part, as a reference, we performed experiments for trivial networks to check the wave localization induced by the strong amorphism, as revealed in Fig. 5.17. The zoomed-in inset shows a 3-port resonator, achieving the parameters $\xi = \eta = \pi/6$, whose band structures are shown in Fig. 2.10(b, d). The measurements show that regardless of the states in the clean limit, the trivial network always turns to insulating through the whole structure. The blocked transports for excitation at edge or bulk ports indicate trivial localization induced by amorphism, validating numerical results in Figs. 5.6 and 5.13.

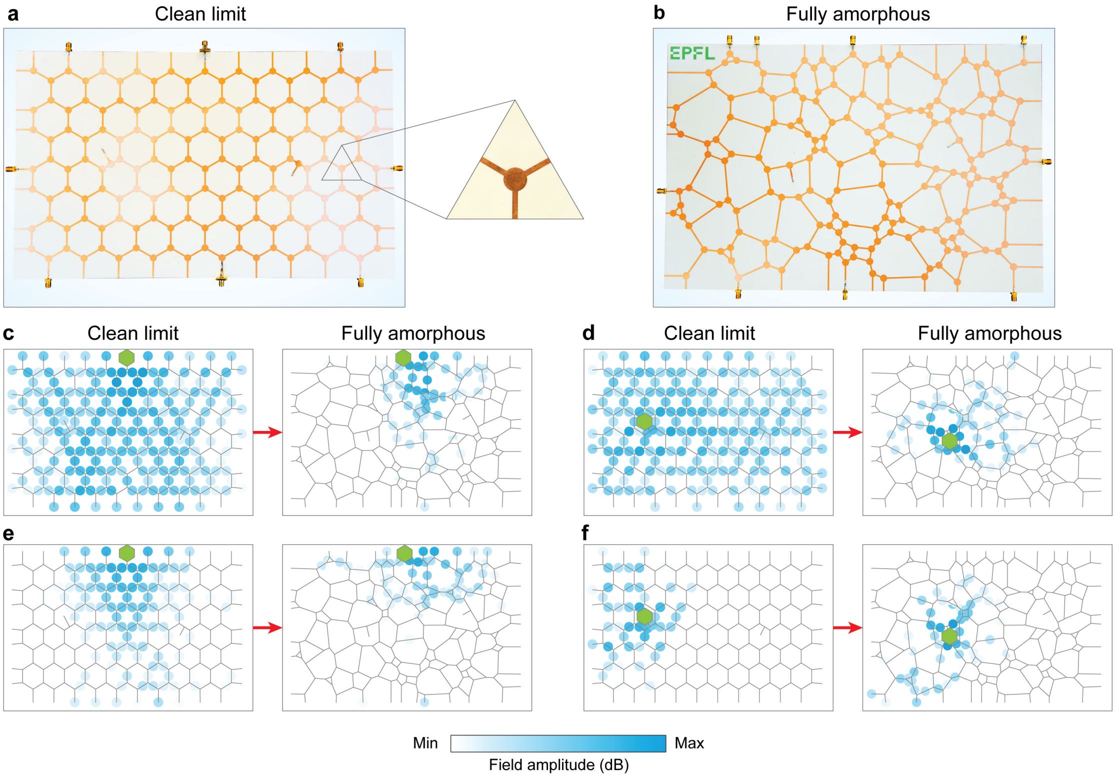

Figure 5.17: **Measured field maps of trivial networks. a,** Prototype of trivial network in the clean limit. **b,** Prototype of trivial network in the fully amorphous regime. We keep the same network but replacing the 3-port circulators to be 3-port resonators. **c-f,** We measured the field maps excited at the edge port (panel c and e) and bulk port (panel d and f) starting from bulk state (panel c and d) or band gap (panel e and f) in the clean limit.

### 5.5.4 Direct measurement of topological indices for anomalous topological networks in the strongly amorphous regime.

We now provide a direct experimental evidence of the topological character of the anomalous amorphous insulating phase. We start from a finite strongly amorphous network and endow it with a twisted boundary condition on its lateral sides, effectively wrapping it up into a cylinder

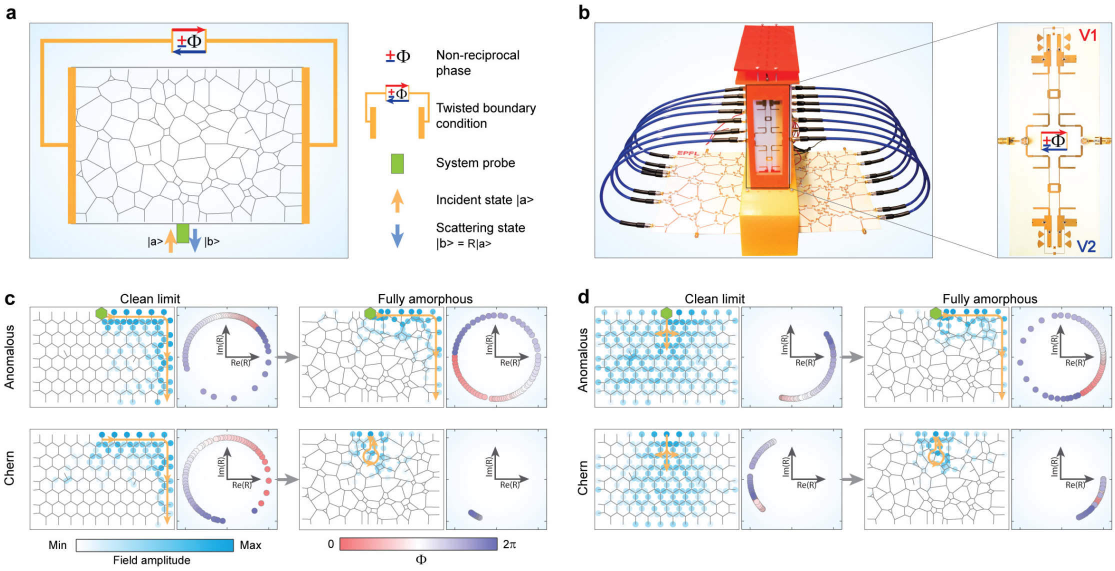

Figure 5.18: **Direct measurement of topological indices in the strongly amorphous regime. a,** Scheme for measuring the topological index of amorphous scattering networks. We impart a twisted boundary condition to the scattering network, wrapping up the sample into a cylinder. The boundary condition links the left and right boundaries with a non-reciprocal phase $\Phi$. The topological index $W$ is the winding of the reflection coefficient $R$ measured at the external probe, when $\Phi$ is varied over all angles. **b,** Picture of the experimental setup, with the microwave non-reciprocal phase shifter shown in the inset. The value of $\Phi$ is controlled by external d.c. voltages $V_1$ and $V_2$. **c, d,** Measured winding numbers and corresponding field maps, when starting from different situations in the clean limit. In panel c, we start with anomalous and Chern networks in a topological gap, whereas in panel d, we start inside bulk bands. The measurements show that regardless of the starting point in the clean limit, the anomalous network is always topological under strong amorphism. Conversely, the Chern network always becomes a trivial insulator.

(Fig. 5.18a). The twisted boundary condition imposes a direction-dependent phase delay ($\Phi$ from left to right, and -$\Phi$ in reverse), which plays, in this photonic system, the same role as the synthetic magnetic flux $\Phi$ threading the cylindrical electronic sample considered in Laughlin's thought experiment [9, 16, 173, 210]. The system is then probed through one external port at the bottom edge. The topological invariant $W$ is defined as the winding number of the probe's reflection coefficient $R$ when $\Phi$ is adiabatically varied from 0 to $2\pi$ [223, 224, 247], that is $W = \frac{1}{2\pi \mathrm{i}} \int_0^{2\pi} \mathrm{d}\Phi\, R^* \frac{\partial R}{\partial \Phi}$. The twisted boundary conditions is implemented by the non-reciprocal phase shifter described previously (Fig. 5.18b), in which the direction-dependent phase delays are set by external voltages $V_1$ and $V_2$.

Figure 5.18c reports the measurement of the reflection coefficient's winding for the anomalous phase in the clean limit, and compares it with the one obtained in the strongly amorphous regime ($\alpha = 6$). As a reference, we also performed a measurement starting from a Chern insulator. For clarity, we plot as well the field maps measured when disconnecting the twisted boundary condition. Whereas both anomalous and Chern phases do wind in the clean limit, only the anomalous phase shows a nonzero winding when strong amorphism is present. Such non-zero winding is always accompanied with edge transport. In Fig. 5.18d, we repeat the experiment but starting from non-insulating samples. In the clean limit, $W$ is zero in both cases as expected for bulk bands. Turning on strong amorphism, the Chern sample remains topologically trivial, whereas we now measure a non-zero winding for the anomalous one. Such opposite topological transitions for both the Chern and anomalous cases are consistent with our theoretical prediction in Fig. 5.14. Our measurements prove the topological origin of the edge states, and the emergence of a topological phase under very strong amorphism.

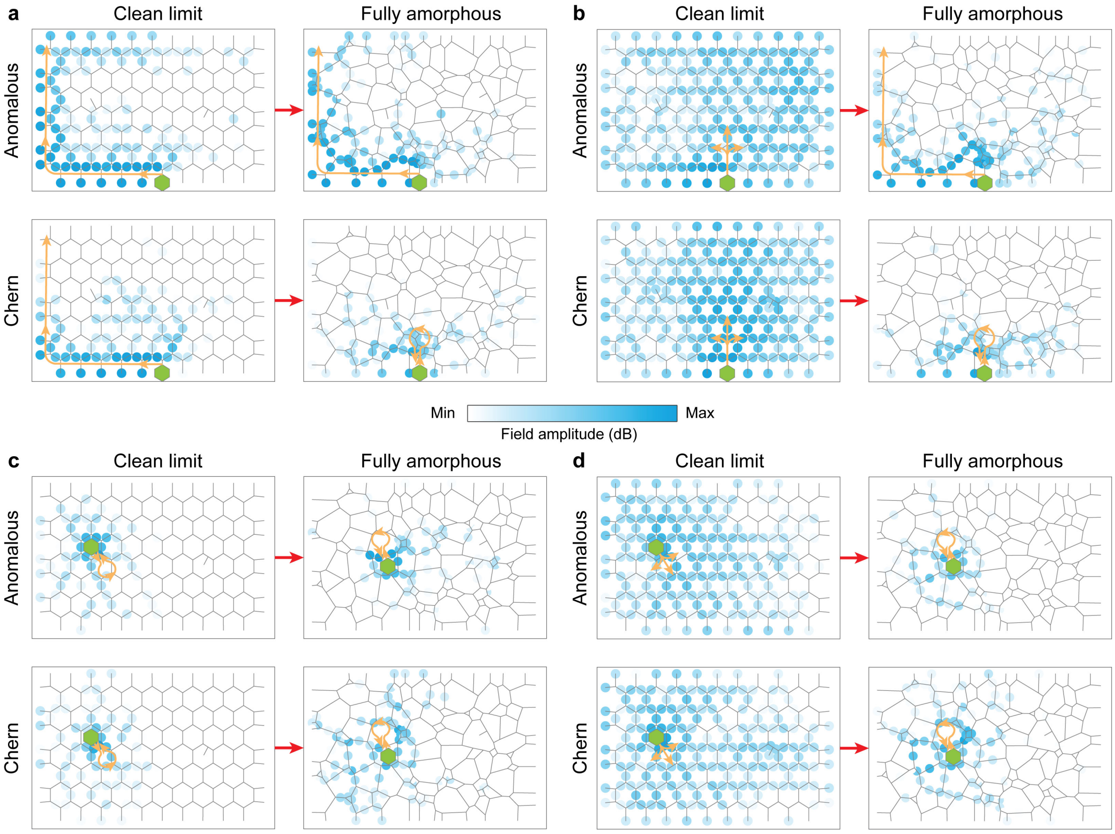

Figure 5.19: **Experimental validation of the chiral edge state in the amorphous anomalous network.** Keeping the measurement setting in Figs. 5.18(c- d), We change the position of input port to the port located at the bottom edge (**a, b**) or in the bulk (**c, d**).

We now supplement the edge transports in Fig. 5.18 with edge transports excited from a bottom port and bulk transport cases with excitation inside the network, as shown in Fig. 5.19. The measurements show that regardless of port positions for wave excitation, for any state in the clean limit, anomalous networks always exhibit edge states in the fully amorphous regime with bulk insulation. However, Chern networks always get localized under strong amorphous disorder, ending up as trivial amorphous insulators.

Finally, as a confirmation for the striking phenomena of strong amorphism enhanced anoma-

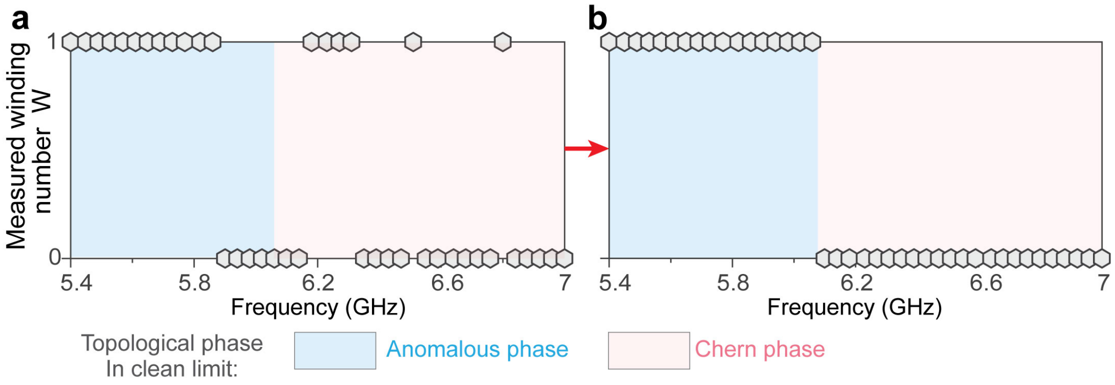

Figure 5.20: **Measured topological invariant in the operating band for honeycomb and fully amorphous networks.** Measured topological invariants versus frequency in the clean limit (**a**), and in fully amorphous networks (**b**). From the measurement of the reflectance of a single circulator, we obtained the theoretical frequency ranges of anomalous (5.4 – 6.05 GHz) and Chern (6.05 – 7 GHz) phases in the clean limit. In these ranges, both anomalous and Chern phase can wind in the topological gaps), and do not wind in bulk band (and in trivial gaps, for the Chern phase). However, remarkably, after inducing strong amorphism, the anomalous phase always winds, and the Chern one became completely trivial.

lous network and trivialized Chern network, we provide the measured topological scattering invariants over a broad frequency range, both for the clean limit and the fully amorphous cases (Fig. 5.20) . In the clean limit (panel c), both the anomalous and Chern phases support frequency ranges with trivial or non-trivial windings. Indeed, the anomalous phase winds in every gap, and does not wind in bulk bands, whereas the Chern winds in Chern gaps, but does not wind in trivial gaps or bulk bands. However, in the amorphous case (panel d), the anomalous phase always winds, while the amorphous phase coming from the Chern case is always trivial. This clearly confirms the enhancement of the anomalous phase due to amorphism, and the destruction of the Chern phase.

## 5.6 Conclusion

We reported the resilience of the anomalous topological phase even in amorphous networks, demonstrating resilience against high degrees of amorphism, evading Anderson localization, and reaching anomalous Floquet Anderson insulating phase. The robustness of this phase is elucidated through intuitive arguments grounded in graph theory. Through detailed analyses—including transport studies, supercell band structures, eigenstates in closed networks, and topological scattering invariants—we unravel the intricate localization mechanisms underpinning the emergence of anomalous amorphous topological insulators, affirming their classification as AFAI. We implemented it for electromagnetic waves in non-reciprocal scattering networks and experimentally demonstrated the existence of unidirectional edge transport in the strong amorphous limit. We proposed a practical method to perform direct topological invariant measurements in finite aperiodic samples.

Although Chapter 4 primarily focused on transport studies for examining anomalous topological scattering networks under strong disorder, the analytical framework, localization mechanism, and the conclusion that these networks exhibit AFAI characteristics are broadly applicable, encompassing networks with disorder in phase-delay links or scattering nodes. By performing the same analysis in this chapter, one can find that the anomalous topological networks robust to maximal phase-link disorder and scattering matrix disorder are also of AFAI, in which topological edge states occupy all the spectrum and bulk bands are totally flat (not shown for "brevity"). We envision a new class of topological systems in which strong disorder including all types of disorder-phase links, amorphism, and scattering matrices on nodes- is no longer a hindrance, but can be used as a new degree of freedom to induce, control and strengthen the robustness of unidirectional wave energy transport.

In a sum, we now have noticed that transitions happen differently for some scattering networks in the parameter space, when inducing strong disorder into networks. We performed extensive experiments and numerical studies on several examples, via observables from transports, supercell band structures, eigenstates in closed network, and topological invariants. In the next chapter, we try to unify all our observations with a unique framework, to define precise topological phase diagrams in the presence of disorder and elucidate the critical behaviors occurring in the strong disordered regime, which are not accessible in our analysis so far, due to computational limitations and finite-size effects. In addition, we will delve into phase transition occurring in disordered networks, examining their critical phenomena.

# 6 Real-space renormalization group scheme

This chapter contains adapted text and results from the following preprint: Zhe Zhang, et al, "**Renormalization group of topological scattering networks**", arXiv:2404.15866 (2024), with permissions of all co-authors.

Ch. 3 made a thorough discussion about how the anomalous Floquet topological phase and the Chern phase emerge in non-reciprocal scattering networks made of three-port circulators interconnected by bidirectional phase-delay links. Ch. 4 and Ch. 5 demonstrated that some chiral topological edge states, most of which are in the anomalous topological phase, can survive the addition of strong levels of distributed disorder in the network, in the form of arbitrary phase fluctuations, disordered scattering matrices on nodes, or even a randomization of its structure [19–22, 170]. These topological scattering networks in the strong disorder regime are confirmed to be of anomalous Floquet Anderson insulating phase (AFAI). These observations were validated by direct transport evaluation and measurements of topological invariants in strongly amorphous cases [19, 20].

Yet, predicting whether a given periodic network will be topological or not when disorder is imparted remains a challenge, because the reason why networks can retain a non-trivial topological nature in drastically aperiodic settings is still not completely understood. For example, some honeycomb topological networks supporting chiral edge states in this clean limit remain topological when adding disorder, whereas some others do not and trivially localize. This behavior seems to be related to the networks being either in the anomalous or Chern phases in the clean periodic limit, although counter-examples can be found near topological phase transition boundaries. Such phenomena appear to indicate the existence of unexplored critical topological transitions in disordered networks, which by essence cannot be understood from standard approaches relying on topological band theories.

**In this chapter,** we explore a general real-space renormalization group (RG) approach for scattering models, which is capable of dealing with strong distributed disorder without relying on the renormalization of Hamiltonians or wave functions. Such scheme, based on a block-scattering transformation combined with a replica strategy, is applied for a comprehensive study of strongly disordered unitary scattering networks with localized bulk states, uncovering a unique connection between topological physics and critical behavior. Our RG theory leads to topological flow diagrams that unveil how the microscopic competition between reflection and nonreciprocity leads to the large-scale emergence of macroscopic scattering attractors, corresponding to trivial and topological insulators. Our findings are confirmed by a scaling analysis of the localization length (LL) and critical exponents, and experimentally validated. The results not only shed light on the fundamental understanding of topological phase transitions and scaling properties in strongly disordered regimes, but also pave the way for practical applications in modern topological condensed-matter and photonics, where disorder may be seen as a useful design degree of freedom, and no longer as a hindrance.

**Organization of the chapter:** In Sec. 6.1, we introduce renormalization group approach and briefly discuss about our RG theory. In Sec. 6.2, we show examples introducing the problem of predicting the emergence of chiral edge states upon scaling. Secs. 6.3, 6.4, and 6.5 focus on networks with strong phase-link disorder, elucidating our scattering RG theory, replica method and results (Sec. 6.3), its validation by scaling analysis of the localization length (Sec. 6.4), and an experimental validation of RG flows (Sec. 6.5). In Sec. 6.6, we extend the RG analysis to structural network disorder (amorphism). In Sec. 6.7, we conclude our results and discuss their implications.

**Notice:** The studied disordered scattering networks in this chapter contain phase-link disorder or structural disorder (amorphism). We fix scattering matrices for all scattering nodes to be identical, therefore excluding scattering matrix disorder on nodes. The reason is two-fold: the parametrization of these scattering matrices constitutes the parameter space; one can still use RG and scaling analysis on networks with disorder on scattering nodes, which won't alters our conclusion on critical distributions. This chapter include the parameterization in Sec. 2.1.3 and disorder realizations of phase-delay disorder and amorphous disorder in Sec. 2.1.4. The applied observables in disordered networks are transports in open networks (Sec. 2.3) and localization length and scaling analysis (Sec. 2.4).

## 6.1 Introduction of renormalization group

The renormalization group (RG) [275–278], which offers valuable insights on the connection between physical phenomena occurring at very different scales, may provide a way to probe the uncharted connection between scattering processes occurring at the microscopic scale, and macroscopic transport properties of large samples, which are related to the scaling of insulating phases and their topology [79, 92, 94, 279, 280] in periodic or aperiodic scenarios [1]. RG is a conceptual frame: it catches large-scale behavior, predicting macroscopic physical observables while smearing out local fluctuations. Conceptual advances in the use of RG in condensed matter physics have led to important developments. For instance, recent works applied tensor-networks RG on state entanglement to describe symmetry-protected topological order [281, 282], perturbative RG on Hamiltonians to deduce the topological phase diagrams under local disorder [283], and momentum space-RG on Berry curvatures to identify topological transitions in periodic structures [284]. However, RG approaches proposed in the context of topological physics have focused on either periodic systems, or systems with local disorder by renormalizing the Hamiltonians or the wave function. The case of topological transitions and scaling effects in systems with very strong non-local disorder, i.e. disorder of arbitrary strength distributed over their entire area, is still largely unexplored [56, 132, 285, 286]. Moreover, despite much interest in topological scattering networks and their potential applications in photonics [14, 15, 160, 175–180] and electromagnetic systems [157, 287–289], a unifying RG theory to understand these topological systems is still crucially lacking. RG on strongly disordered networks is expected to shed light on the competition between localization and topology in a broad range of scenarios, by revealing how microscopic scattering properties affect macroscopic topological transport.

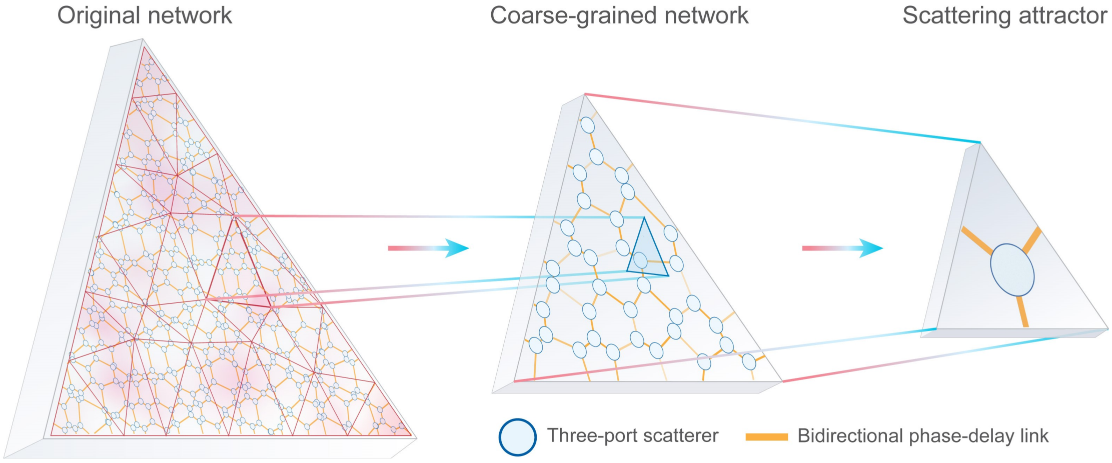

Figure 6.1: **Block scattering transformations for a renormalization group of unitary scattering networks.** Starting with an arbitrary scattering network composed of three-port unitary scatterers connected by reciprocal phase links (left), we perform block-scattering transformations to extract the key scattering properties of each triangular sub-blocks, which are replaced by a three-port unitary scattering matrix (center). This results in a coarse-grained network. By iteratively applying this transformation, we finally get to a single three-port scatterer described by a unitary 3 by 3 matrix $S_F$, which we call the scattering attractor of the network (right). If the RG procedure is successful, the scattering attractor $S_F$ summarizes whether the initial network is a trivial insulator (if $S_F$ is a full reflection matrix) or a topological insulator ($S_F$ is a circulator).

Our real-space renormalization group focuses on unitary scattering networks. It unveils the intricate physical mechanisms behind the persistence of topological edge states in systems with strong distributed disorder. Instead of playing with Hamiltonians or wave functions, we focus on network models and propose block-scattering transformations that preserve the key scattering properties of each block during scaling, namely flux conservation, reflection level, and scattering chirality. The block-scattering transformation (Fig. 6.1) is composed of three steps: partitioning the original network triangularly, replacing each block subnetwork by a simpler three-port scatterer, and interconnecting together these three-port scatterers into a new coarse-grained network, on which the procedure can be repeated. The goal of the RG theory is therefore to leverage iterative block-scattering transformations until one converges to a three-port scattering attractor that captures the essential information about the macroscopic scattering of the network, namely whether chiral transport occurs on the edges or if incident waves coupled to the edge are just reflected. Intuitively, we expect three possible scattering attractors (Fig. 6.2). Chiral topological systems would be attracted to unitary scattering matrices that describe clockwise or counter clockwise perfect circulation. The clockwise circulator $S_{CW}$ (matrix shown in the figure inset), and its transpose $S_{CCW}$ are the only two possibilities compatible with edge transport (we ignore transmission phases for now). On the other hand, systems that trivially localize would be attracted to the identity matrix $S_R$, if we ignore reflection phases. This later case corresponds to full reflection as the input waves excite localized modes. We apply this RG theory on two examples of fully disordered networks, either with a honeycomb structure subject to arbitrary phase fluctuations on the hexagonal links, or a fully random structure with arbitrary planar connectivity. We obtain RG topological phase diagrams that elucidate the intricate competition between microscopic reflection and chirality. We unveil the critical phenomena occurring at the transition between trivial and topological disordered networks, by exploring the evolution of RG flows upon scaling and studying the critical probability distributions of microscopic scattering matrices. This block-scattering RG approach leads to a better understanding of topological phase transitions and scaling properties in scattering networks models with strong disorder, broadening the scope of renormalization group approaches to topological unitary systems.

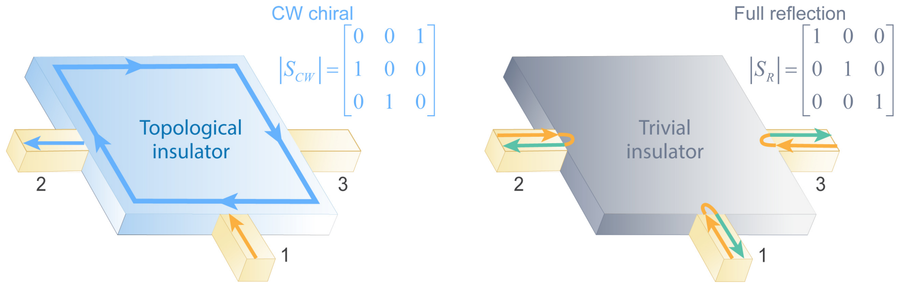
CW chiral
$|S_{CW}| = \begin{bmatrix} 0 & 0 & 1 \\ 1 & 0 & 0 \\ 0 & 1 & 0 \end{bmatrix}$
Topological insulator
2
3
1
Full reflection
$|S_R| = \begin{bmatrix} 1 & 0 & 0 \\ 0 & 1 & 0 \\ 0 & 0 & 1 \end{bmatrix}$
Trivial insulator
2
3
1

Figure 6.2: **Trivial and topological systems and their scattering attractors.** We consider three matched probes (in yellow) placed at arbitrary positions on the boundary of a 2D insulator. This is the minimal number of probes allowing the detection of chiral edge transport. For a topological insulator (left, blue), we expect that as the system size increases, the scattering matrix at the probes converges to the one of a clockwise ($S_{CW}$) or counter clockwise ($S_{CCW}$) unitary circulator. On the other hand, the probe scattering matrix for an ideal trivial insulator (right, gray) would converge to a full reflection matrix $S_R$. Therefore, we expect $S_{CW}$ ($S_{CCW}$) and $S_R$ to represent possible scattering attractors in any valid RG theory.

## 6.2 Two examples of disordered scattering networks: from microscopic to macroscopic scale

At the microscopic scale, the networks we consider are formed of interconnected unitary scatterers with three ports as shown in Fig. 2.4b. Such structure is maintained through renormalization iterations until converging to the attractor, which is again a three-port unitary scatterer. This choice to work with three-port systems is motivated by two reasons. First, at the microscopic scale, scatterers with more than two ports are needed to construct complex networks. Second, at the macroscopic scale of the attractor, it wouldn't be possible to detect chiral edge transport with only two ports, and three-port appears here as a minimal number to do so [290]. One could, of course, build a theory based on four-port unitary scattering, but this would only complicate the associated mathematics without bringing any new advantage. Yet, one could object the following: what if the initial network contains scatterers with arbitrary numbers of ports? Well, in this case, we can always make a first coarse-grained iteration, and this operation would reduce all subsequent iterations back to the three-port case. We will also assume that the scatterers that compose the initial networks obey three-fold rotational ($C3$) symmetry. However, we will assume that $C3$ symmetry is not in general enforced on the entire network, and the connections between the scatterers do not fulfill this symmetry. This means that after the first RG iteration, the scattering matrices in the coarse grain picture are no longer $C3$ symmetric. Nevertheless, for representing the evolution of these matrices during RG iterations, we will perform ensemble averaging, which will restore $C3$ symmetry for sufficiently large statistical ensembles. For all these reasons, three-port scatterers described by a $C3$ and unitary ($U(3)$) scattering matrix $S_0$ play a crucial role in our scheme. In panels a and b of Fig. 6.3, We show two examples of microscopic building blocks, whose scattering matrices $S_1$ and $S_2$ are given in the figure.

Macroscopic planar networks are then built in the usual way, namely by connecting such $S_0$ scatterers using bidirectional links with phase delay $\varphi$. In the pristine or clean-limit scattering networks, as shown in the Fig. 6.4a, the clean-limit networks made of $S_1$ is in the Chern phase, due to the non-zero Chern number of several bands. Its bulk bands in specified ranges of $\varphi$ are consistent with the finite two-port transmissions and high density of states (DOS) in the finite network, while the topological band gaps are consistent with the unity transports and DOS. Its trivial band gap is represented by blocked transmission and zero DOS. Contrarily, the periodic $S_2$ network (Fig. 6.4b) is in the anomalous phase, evidenced by the vanishing Chern numbers and the existences of topological edge states in every band gap. There is no trivial gap in the anomalous phase. In a sum, although periodic $S_1$ network and periodic $S_2$ network are of distinct topological phases, whose difference featured by vanishing trivial band gaps, both networks can support diffusive waves in the bulk, and most importantly both exhibit topological unidirectional edge waves.

We focus instead on network models subject to distributed disorder including phase-link disorder (Figs. 6.3(c-d)) and amorphism (network structure disorder, Figs. 6.3(e-f)). The networks we work with in this chapter are always at maximally strong levels. The macroscopic scattering

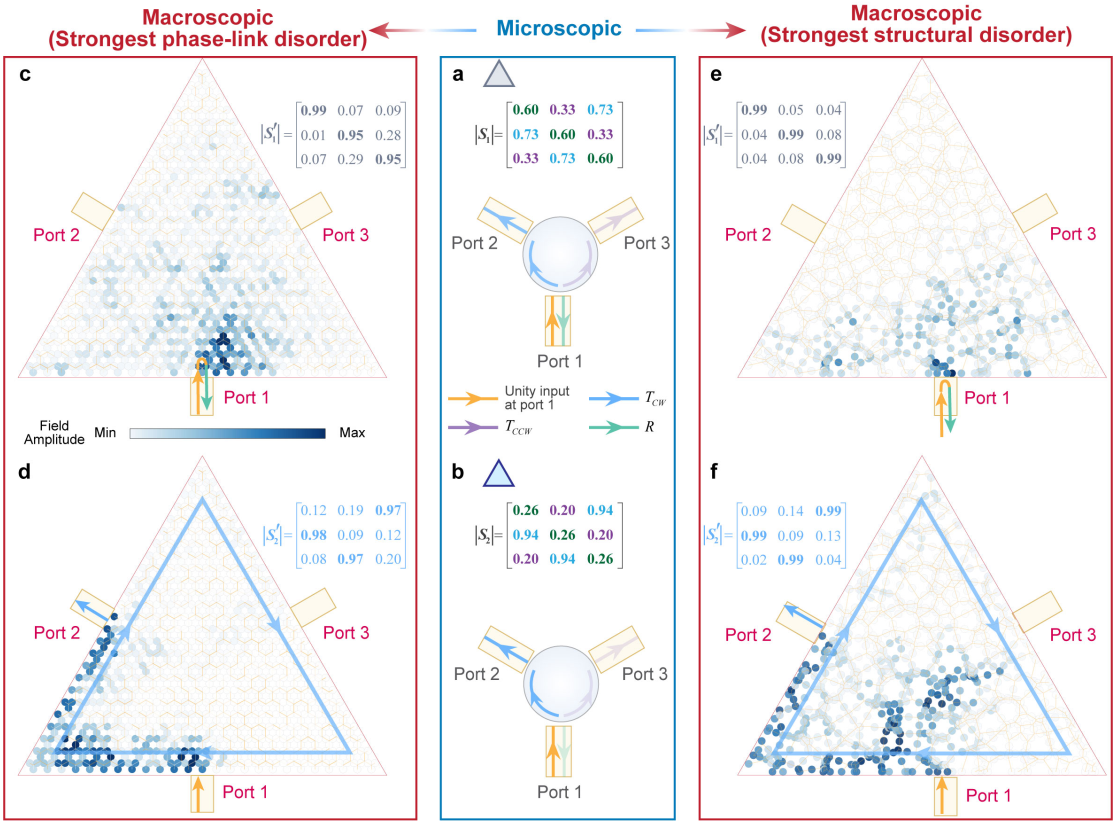
Macroscopic
(Strongest phase-link disorder)
Microscopic
Macroscopic
(Strongest structural disorder)
c
$|S_1'| = \begin{bmatrix} 0.99 & 0.07 & 0.09 \\ 0.01 & 0.95 & 0.28 \\ 0.07 & 0.29 & 0.95 \end{bmatrix}$
Port 2
Port 3
Port 1
Field Amplitude
Min
Max
d
$|S_2'| = \begin{bmatrix} 0.12 & 0.19 & 0.97 \\ 0.98 & 0.09 & 0.12 \\ 0.08 & 0.97 & 0.20 \end{bmatrix}$
Port 2
Port 3
Port 1
a
$|S_1| = \begin{bmatrix} 0.60 & 0.33 & 0.73 \\ 0.73 & 0.60 & 0.33 \\ 0.33 & 0.73 & 0.60 \end{bmatrix}$
Port 2
Port 3
Port 1
Unity input at port 1
$T_{CW}$
$T_{CCW}$
$R$
b
$|S_2| = \begin{bmatrix} 0.26 & 0.20 & 0.94 \\ 0.94 & 0.26 & 0.20 \\ 0.20 & 0.94 & 0.26 \end{bmatrix}$
Port 2
Port 3
Port 1
e
$|S_1'| = \begin{bmatrix} 0.99 & 0.05 & 0.04 \\ 0.04 & 0.99 & 0.08 \\ 0.04 & 0.08 & 0.99 \end{bmatrix}$
Port 2
Port 3
Port 1
f
$|S_2'| = \begin{bmatrix} 0.09 & 0.14 & 0.99 \\ 0.99 & 0.09 & 0.13 \\ 0.02 & 0.99 & 0.04 \end{bmatrix}$
Port 2
Port 3
Port 1

Figure 6.3: **Examples leading to trivial and topological macroscopic properties, under phase-link disorder and structural disorder (amorphism). a, b,** We choose two microscopic scattering matrices $S_1$ (a) and $S_2$ (b), located at $\xi = -\eta = 2.8\pi/12$ (gray triangle) and $\xi = -\eta = 3.8\pi/12$ (blue triangle). Scattering flows are shown by coloured arrows, illustrating $T_{CW}$ (blue), $T_{CCW}$ (purple), and $R$ (green), when a unity wave is incident from port 1 (yellow arrow). $S_1$ and $S_2$ both exhibit clockwise chirality with some reflection, and are relatively close to each other on the parameter plane (Fig. 2.3). These matrices are then used to form networks with maximal phase-link disorder (**c- d**) or structural disorder (**e- f**). We computed field maps when inputting a signal at port 1, and calculated the associated macroscopic scattering matrices. $S_1$ always leads to a trivial insulator with full external reflection, whereas $S_2$ exhibits topological edge states in both cases.

networks are then probed via three external scattering probes, defining a macroscopic unitary scattering matrix $S_0^{'}$ exemplified by $S_1^{'}$ and $S_2^{'}$ shown in Figs. 6.3(c-f). The first goal of RG is to establish a link between the microscopic scattering $S_0$ and the macroscopic one $S_0^{'}$, and unveil the role of disorder in this mapping. The second goal of RG is identifying the limit of $S_0^{'}$ when the macroscopic system gets infinitely large (we call this limit the thermodynamic limit), to unveil the relation between scattering attractors and topological phases. This is made possible by the fact that $S_0^{'}$ can contain the signature of topological edge transport, even under strong disorder [224, 244, 291].

The connection between $S_0$ and $S_0^{'}$ is by no mean trivial. Some numerically tractable examples

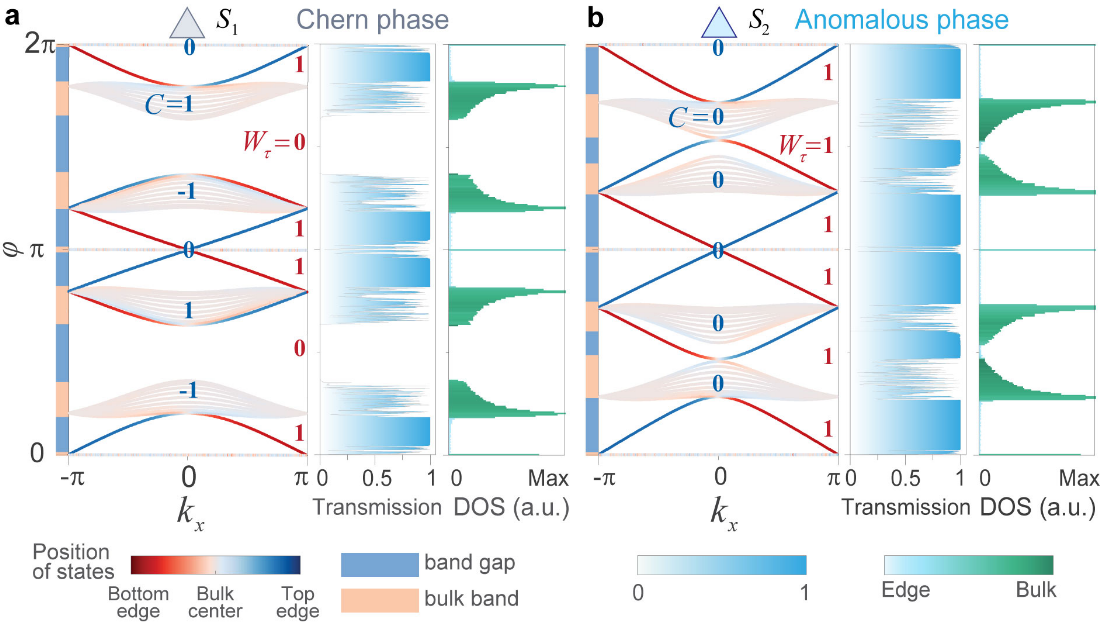

Figure 6.4: **Topological phases and observables.** Band structures of a supercell, two-port transmissions, density of states (DOS) for the periodic $S_1$ (panel **a**) and $S_2$ (panel **b**) networks. The blue and red numbers on the bands represent the calculated Chern numbers $C$ and gap invariants $W_\tau$, respectively. $S_2$ network is of anomalous phase, which features the zero Chern numbers and topological gapless edge states $W_\tau \neq 0$ accommodated in each band gap. As a contrary, $S_1$ network is in Chern phase, as demonstrated by the non-zero Chern numbers. In the finite honeycomb networks, we can identify the band structure by checking DOS (rightmost) and two-port transmission (center) versus quasi-energy (namely, phase delay value, $\varphi$). The unity transmission is mediated by topological edge states with low DOS, while the vibrating finite transmission along with high DOS indicates bulk states in bands.

with relatively large sizes are shown in Fig. 6.3. Field maps are computed numerically assuming input from the bottom port. Note that $S_1$ and $S_2$ are both of the same chirality and differ only slightly in their level of reflection and nonreciprocity. Despite of this, we observe a completely opposite macroscopic scattering behavior in the networks originating from $S_1$ and $S_2$. In the case of $S_1$ (Figs. 6.3(c,e)), the input wave seems to localize around the input port and end up being reflected. Conversely, with $S_2$ a clear edge transport channel appears and connects the input port to the next port on the left. If we could numerically access the thermodynamic limit, we would expect a convergence of the macroscopic scattering matrices $S_1^{'}$ and $S_2^{'}$ to $S_R$ and $S_{CW}$ (the values of $S_1$ and $S_2$ for the finite systems considered here are shown within the figure). We also found even more surprising examples of systems behaving totally differently for the two types of disorder, when starting from scattering matrices with reflectance slightly lower than 1/3 (not shown for brevity). Explaining the emergence or non-emergence of unidirectional edge states in networks with distributed disorder requires a unified scheme capable of accessing the macroscopic properties of arbitrarily large systems with no additional computational cost. In the next section, we describe a RG theory that sheds light on these examples and unveils a microscopic competition between reflection and chirality, that translates into a macroscopic competition between disorder and topology, explaining the emergence of critical behaviors associated to topological transitions in the thermodynamic limit.

## 6.3 RG on scattering networks with phase-link disorder

### 6.3.1 Iterative block-scattering transformations

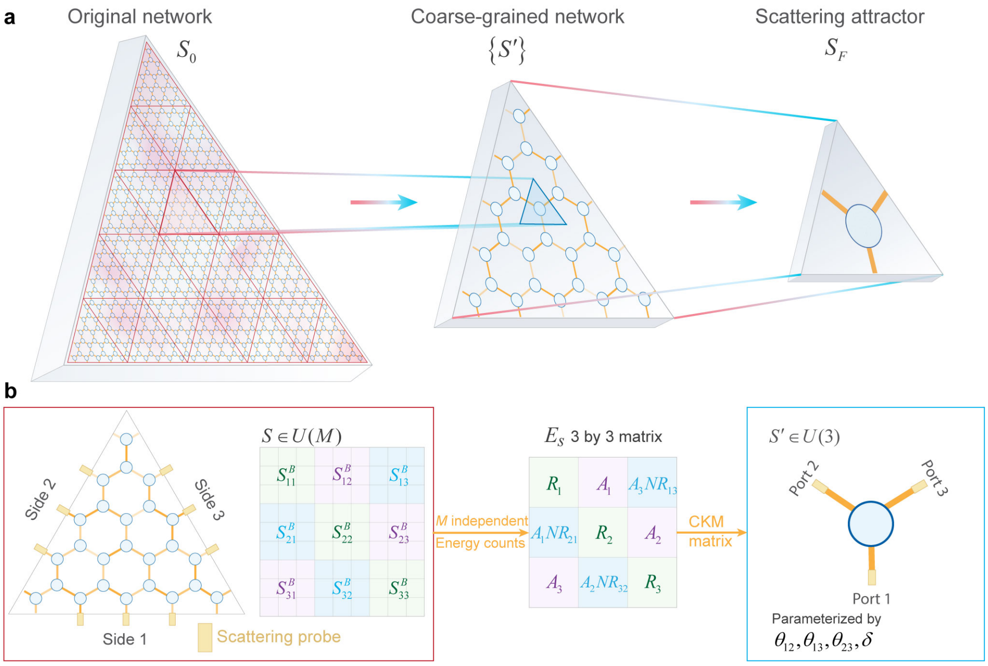
a
Original network
$S_0$
Coarse-grained network
$\{S'\}$
Scattering attractor
$S_F$
b
Side 1
Side 2
Side 3
Scattering probe
$S \in U(M)$
$S^B_{11}$ $S^B_{12}$ $S^B_{13}$
$S^B_{21}$ $S^B_{22}$ $S^B_{23}$
$S^B_{31}$ $S^B_{32}$ $S^B_{33}$
M independent
Energy counts
$E_S$ 3 by 3 matrix
$R_1$ $A_1$ $A_3NR_{13}$
$A_1NR_{21}$ $R_2$ $A_2$
$A_3$ $A_2NR_{32}$ $R_3$
CKM
matrix
$S' \in U(3)$
Port 1
Port 2
Port 3
Parameterized by
$\theta_{12}, \theta_{13}, \theta_{23}, \delta$

Figure 6.5: **Renormalization group of a unitary scattering network with phase-link disorder.** **a,** Schematic of the block-scattering transformation. **b,** Procedure for the replacement of a triangular block scattering network (described by a large unitary scattering matrix $S \in U(M)$) by a single three-port scatterer (described by a 3×3 scattering matrix $S' \in U(3)$). The reduction of matrix size is performed by partitioning $S$ into nine 3×3 blocks according to the three sides, then summarizing some key dimensionless quantities, namely *nonreciprocity and reflection* into an energy matrix $E_S$ (center panel). $A_i (i = 1, 2, 3)$ are variables to be determined in order to restore unitarity. This is done using CKM matrix parameterization, and we recover the corresponding unitary matrix $S' \in U(3)$ (rightmost panel).

The type of phase-disordered networks we focus on in this section is shown in Fig. 6.5. They are composed of identical scattering matrices $S_0(\xi, \eta)$ connected in a honeycomb structure with phase-link disorder. The phase $\varphi$ of each link is drawn from a uniform distribution in the range $[\varphi_0 - \Delta\varphi/2, \varphi_0 + \Delta\varphi/2]$ (Fig. 6.5). We also focus on the case of the strongest possible disorder level $\Delta\varphi = 2\pi$, although any other range is in principle accessible. As discussed in the introduction, the RG theory contains three steps. First, we subdivide the original network into triangular blocks by applying a standard Delaunay triangulation, whose generators are on a triangular lattice. Second, each triangular block is replaced by a single three-port scatterer, whose scattering matrix $S' \in U(3)$ must be deduced from the scattering properties of the block. In the final step, by considering the dual graph of the triangulation graph, we can form a coarse-grained network by arranging the matrices $S'$ on the nodes, and connect them with new phase links randomly drawn from the same uniform distribution as the original ones. The RG transformation is then iterated, replacing the original network by the coarse-grained one. Each iteration reduces the size of the network by a scaling factor equal to the number of scatterers $P$ in the triangular blocks ($P$= 25 in panel a). After $n$ iterative transformations, a 3-port scatterer therefore represents $25^n$ scatterers in the original network. At the end, we get a single three-port attractor $S_F \in U(3)$.

The backbone of the RG theory is therefore the block-scattering transformation, namely the protocol of replacing the large unitary scattering matrix of a triangular block by a small one. Two pivotal questions arise when trying to define such a protocol: "What scattering matrix should be associated to a triangular block ?" and "What kind of physical information should be preserved when this block scattering matrix is compressed into a 3×3 matrix?". To address the first question, we note that a triangular block may have a large number of ports on its edges, which at the end should be concatenated into a single one. A simple proposition to achieve this concatenation would be to close all edge ports with full-reflections, leaving only three of them, one on each edge. However, such a solution would not consider the fact that the connections between adjacent triangular blocks are actually distributed over many ports along the edge, allowing to couple together various modes of such triangles. To take this into account, we do not select only one, but $M_i$ ports along the boundary of the $i$th side of the triangle, as shown on the left of Fig. 6.5b. On each side, these open ports are chosen to be adjacent, and we avoid choosing the ones around the corners. All the other ports are closed with a fully reflective boundary condition. This allows defining a unitary scattering matrix $S \in U(M)$, with $M = \sum M_i$, which summarizes the transport and reflection at the scale of a block. Therefore, the problem of replacing the block scattering network by a three-port scatterer is equivalent to reducing the large unitary matrix $S \in U(M)$ to a much smaller one, $S' \in U(3)$.

This takes us to our second pivotal question. To preserve the important physics while smearing out microscopic details, such reduction of scale must carefully maintain the scattering properties that matter in the trivial or topological localization processes occurring during scaling. Intuitively, the level of *nonreciprocity and reflection* of a triangular block are important. We evidence these two properties in $S$ by partitioning it into nine 3×3 blocks, according to the side of the triangle,

$$S = \begin{bmatrix} S^B_{11} & S^B_{12} & S^B_{13} \\ S^B_{21} & S^B_{22} & S^B_{23} \\ S^B_{31} & S^B_{32} & S^B_{33} \end{bmatrix}. \tag{6.1}$$

Next, we note that the reduction of $S \in U(M)$ to $S' \in U(3)$ should follow a few principles. The first one is the fact that the quantities that we are trying to keep during the reduction should not depend on the size of the block network or the number of probes we choose. The second principle is that we should reflect accurately the way with which energy incident on one side of the triangular block is reflected and transmitted to the other two sides. One may start, following Landauer-Büttiker formalism [60, 225], by expressing the overall energy transport from side $i$ to side $j$ as

$$T_{ji} = \mathrm{Tr}(S^B_{ij}(S^B_{ij})^\dagger), \tag{6.2}$$

however this quantity depends on block size and number of probes. Instead, we can consider the overall nonreciprocity of the energy transport between side $i$ and $j$, represented by

$$NR_{ji} = T_{ji}/T_{ij}. \tag{6.3}$$

The overall reflection $R_i$ for the side $i$ of a triangular block may be represented by the quadratic mean of all the reflection of the probes on this side, expressed as

$$R_i = \sqrt{\sum_{p=1}^{M_i} |S^B_{ii}(p,p)|^2/M_i}. \tag{6.4}$$

After extracting the nonreciprocity and reflection of the block, $NR_{ji}$ and $R_i$, we can summarize this information about $S$ into a 3×3 matrix $E_S$ (Fig. 6.5b, center), defined as

$$E_S = \begin{bmatrix} R_1 & A_1 & A_3 \cdot NR_{13} \\ A_1 \cdot NR_{21} & R_2 & A_2 \\ A_3 & A_2 \cdot NR_{32} & R_3 \end{bmatrix}, \tag{6.5}$$

where $NR_{ji}$ and $R_i$ serve as the non-diagonal and diagonal terms respectively. Here, $A_i (i = 1,2,3)$ are variables to be determined so that we can recover a genuine unitarity scattering matrix from $E_S$. Note that $E_S$, by itself, is not unitary and contains only amplitude information. The recovery of a unitary matrix from the matrix $E_S$ is not a trivial task. Indeed, the general parameterization of $U(3)$ matrices implies that we have to recover in general three angle parameters $(\frac{1}{2}n(n-1)|_{n=3})$ and six phase parameters $(\frac{1}{2}n(n+1)|_{n=3})$ [194, 195, 199, 200]) (see details in Sec. 2.1.3). Fortunately, the problem of recovering a unitary scattering matrix from amplitude measurements is a known problem in high energy physics, solved by the Cabibbo–Kobayashi–Maskawa (CKM) matrix parameterization [196, 197]. This method implies that the recovery of a unitary matrix from an energy-related matrix can focus on finding four parameters (three angle parameters $\theta_{12}, \theta_{13}, \theta_{23}$ and one phase parameter $\delta$), as exemplified by the successful recovery of the quark-mixing matrix from experimental measurements. Appendix. D details how to adapt CKM parametrization to the recovery of one possible candidate of a 3×3 unitary matrix $S' \in U(3)$, by first transforming $E_S$ to a double stochastic matrix. We stress that many different choices for $S' \in U(3)$ are possible. However, they all differ by different phases, whose particular choice does not matter for RG due to the fact that random phase disorder is anyways present in the network (Fig. 6.5b rightmost).

### 6.3.2 Replica scheme

Having explained how the block scattering transformation is implemented, we are in principle ready to look at results from applying RG to large networks. Before doing so, however, one needs to think about two important practical aspects: (i) how to best describe the state of the network at a given iteration; and (ii), how to ensure that the iterative RG algorithm is computationally efficient. The first point is addressed by remembering that we want to track the convergence to a potential scattering attractor. Therefore, what matters is to monitor the evolution of the set of $U(3)$ scattering matrices $\{S'_n\}$ during RG. This can be performed by averaging them over the network. This average is trivial to take for the initial network, which is composed of identical $C3$ and $U(3)$ matrices $S_0$. At any other iteration number $n$, the $S'_n$ in the network are in principle all different and no longer obey $C3$ symmetry. However, we remark that averaging over a sufficiently large set would restore $C3$ symmetry, since the choice of the port labels (1 , 2 and 3) for each $S'_n$ is arbitrary (when labeling them clockwisely), eventually allowing for the data to be tripled, making the average invariant with respect to 120-degree rotations. Thus, a first way to represent the state of the network at a given iteration is a point representing this average in the $(\xi,\eta)$ parameter plane. This is equivalent to say that the statistic average of the scattering properties $\{S'_n\}$ in the $n_{th}$ coarse-grained network takes the form of a $C3$ symmetric unitary matrix, namely

$$\langle S'_n\rangle \equiv \begin{bmatrix} \langle R_n\rangle & \langle T_{CCW,n}\rangle & \langle T_{CW,n}\rangle \\ \langle T_{CW,n}\rangle & \langle R_n\rangle & \langle T_{CCW,n}\rangle \\ \langle T_{CCW,n}\rangle & \langle T_{CW,n}\rangle & \langle R_n\rangle \end{bmatrix}. \tag{6.6}$$

During the iterative RG procedure, the block-scattering transformation of the system from one scattering state $\langle S'_{n-1}\rangle$ to the next $\langle S'_n\rangle$ can thus be represented by the motion of this point, discretely jumping on the $(\xi,\eta)$ plane of Fig. 2.3. Starting from the point representing the original scatterer $S_0$ on the $(\xi,\eta)$ plane, we can watch the trajectory formed by the successive locations of $\langle S'_n\rangle$, which defines a renormalization-group flow [275]. Such flow can either lead the system towards a stable fixed point (a scattering attractor), the only exceptions being the cases that start on unstable fixed points. Such fixed points reveal themselves by looking at the probability distributions of $T_{CW,n}$, $T_{CCW,n}$, and $R_n$, denoted by $P(T_{CW,n})$, $P(T_{CCW,n})$, and $P(R_n)$. For example, if $P(T_{CW})$, $P(T_{CCW})$, and $P(R)$ remain invariant under the block-scattering transformation, we know that we have reached a scale invariant point. An attentive reader may object that such an averaging procedure performed on the RG theory of Fig. 6.5 may be unpractical: since the size of the system shrinks at each iteration, the size of the set $\{S'_n\}$ depends on $n$, which is problematic to develop a rigorous statistical study of the flow over many iterations. At the same time, the numerical calculations of block networks and unitary matrix transformations increase exponentially with system's size, preventing us from working with very large systems. To be more specific, the number of calculations grows exponentially in $P_0 \cdot P^n$ as a function of RG iterations $n$. $P$ and $P_0$ are defined as the number of microscopic scatterers in a block network and that in the final coarse-grained network, respectively. $P$ serves as the scaling factor, and $P_0$ is required to be in a large scale close to the thermodynamic limit [275, 276, 292, 293]. The problem of developing a consistent statistical description of the network and the one of computational efficiency are therefore intertwined.

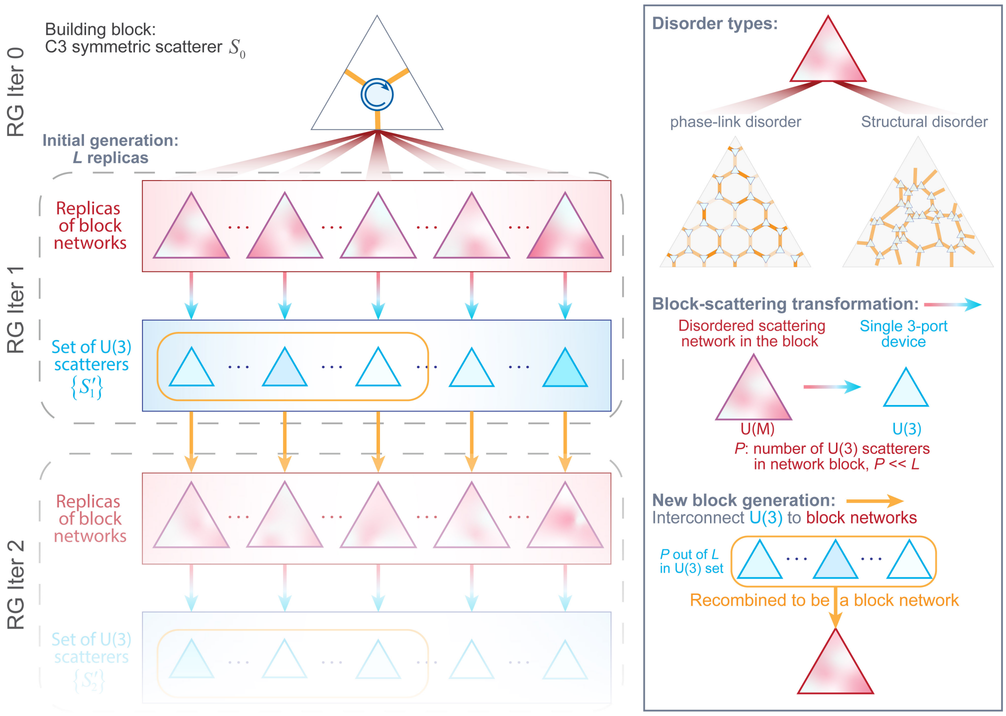
Building block:
C3 symmetric scatterer $S_0$
RG Iter 0
Initial generation:
L replicas
Replicas of block networks
RG Iter 1
Set of U(3) scatterers $\{S'_1\}$
Replicas of block networks
RG Iter 2
Set of U(3) scatterers $\{S'_2\}$
Disorder types:
phase-link disorder
Structural disorder
Block-scattering transformation:
Disordered scattering network in the block
Single 3-port device
U(M)
U(3)
P: number of U(3) scatterers in network block, P << L
New block generation:
Interconnect U(3) to block networks
P out of L in U(3) set
Recombined to be a block network

Figure 6.6: **Numerical RG scheme of disordered scattering networks.** We assume that scattering networks is under a kind of disorder (phase-link one or structure one, left inset) described by a specified statistics $P_{disorder}$. To start with, by taking the microscopic three-port scatterer $S_0(\xi,\eta)$ as building blocks, we construct $L$ replicas of triangular block networks (red triangles) for the RG iteration 1. Each replica is in the same network disorder statistics $P_{disorder}$, and contains $P(P \ll L)$ microscopic scatterers. Secondly, we apply block scattering transformations, which turn each block network into a $U(3)$ scatterer (blue triangles). The scattering matrix set $\{S'_1\}$ of these $U(3)$ scatterers represents the scattering properties of RG iteration 1. Thirdly, to generate block scattering networks of the iteration 2, we construct $L$ replicas of triangular block networks in the disorder statistics $P_{disorder}$, and most importantly each replica is composed by $P$ scatterers randomly selected from the set $\{S'_1\}$. By iteratively performing the above three-step process, we obtain the sequence of $\{S'_n\}$, the flow of probability distributions ($P(T_{CW,n})$, $P(T_{CCW,n})$, and $P(R_n)$), and the averaged scattering properties $\langle S'_n \rangle$.

We handle this issue by enhancing the RG theory with a well-known strategy, which is able to successfully depict the effect of disorder especially in spin glass, and known as the replica scheme [30, 294–297]. As shown in Fig. 6.6, our numerical RG scheme is based on the transformation of the $U(3)$ scatterer set $\{S'_n\}$, each element of which is transformed from one of $L$ replicas of triangular block networks by applying block-scattering transformations. To be more specific, let us assume: the disorder (phase-link one or structure one) in scattering networks conforms to a specified statistics denoted as $P_{disorder}$. For the first RG iteration, we generate $L$ triangular networks- namely block networks, each of which contains $P$ microscopic scatterers described by $S_0(\xi,\eta)$ and are generated as a replica following the statistics $P_{disorder}$. Each replica of block scattering networks is then transformed into a $U(3)$ scatterer, by applying block-scattering transformations. The scattering matrix set of these $L$ scatterers forms the $U(3)$ matrix set $\{S'_1\}$. To construct a block scattering network of the next iteration, we generate a network in the same statistics of disorder ($P_{disorder}$), whose $P$ microscopic scatterers are randomly selected from the set $\{S'_1\}$. Repeating such construction $L$ times, we obtain $L$ replicas of block networks for the second iteration. To make sure the sampling is random enough, we follow the condition $L \gg P$. Now, RG calculation proceeds by starting all over again, with the block scattering networks of iteration 2 as the block scattering networks of iteration 1.

In a sum, conceptually, what our numerical RG scheme performs is horizontally taking the statistic average of replicas and vertically sustaining the system close to the thermodynamic limit (under large enough $P$). As we keep the constant replicas for each iteration, the number of calculations is reduced to the linear function of $n$, expressed as $nL$. The constant size of the set $\{S'_n\}$ also allows us to perform the evolution of probability distributions with enough samples for statistics, which describes how the scattering properties of disordered network are transformed when networks are scaled up. The size $P$ can be maintained relatively small[I], as long as accurate statistics can be performed, making it possible to look at arbitrarily large numbers of RG iterations at relatively low computational cost, and explore the physics occurring at very different scales.

### 6.3.3 Results for random phase-link disorder

Taking the matrices $S_1$ and $S_2$ used in Fig. 6.3 as examples, we use the replica scheme and go through seven RG iterations. The results are presented in Fig. 6.7. Consistent with the finite-size simulations of Fig. 6.3, $S_1$ and $S_2$ are found to converge to opposite attractors: $S_R$ for $S_1$ (Fig. 6.7a), indicating a trivial insulator, and $S_{CW}$ for $S_2$ (Fig. 6.7e), indicating a topological insulator. To see how the macroscopic scattering properties change upon scaling up the disordered networks, we track the evolution of $P(T_{CW})$, $P(T_{CCW})$, and $P(R)$ during iterations. As shown in Figs. 6.7(b, f), after five iterations the attractors are almost reached: although both systems are initially clockwise chiral, only disordered systems based on $S_2$ maintain high values of $T_{CW}$ at large scales. Conversely, for large enough disordered networks based on $S_1$, $T_{CW}$ and $T_{CCW}$ gradually disappear, while the probability of observing full reflection is close to unity after the fifth iteration. These distinct behaviors are further confirmed by the evolution of the averages $\langle T_{CW}\rangle$, $\langle T_{CCW}\rangle$, and $\langle R\rangle$, exhibited in Figs. 6.7(c, g). A visual summary of this process is obtained by plotting the RG flows, starting from the initial point $S_2$

---

[I] The numerical RG results shown in this chapter are under the setting with $L = 4000, P = 100$ and $M_1 = M_2 = M_3 = 3$ or 5. The only restriction for $P$ is guaranteeing that the block network has a bulk, namely network depth at least 3, as the topological effect needs a definition of bulk. The selections of $P$ and $L$ only affect the resolution of boundary.

($S_1$) in the parameter space, and going through a discrete trajectory to reach $S_{CW}$ ($S_R$).

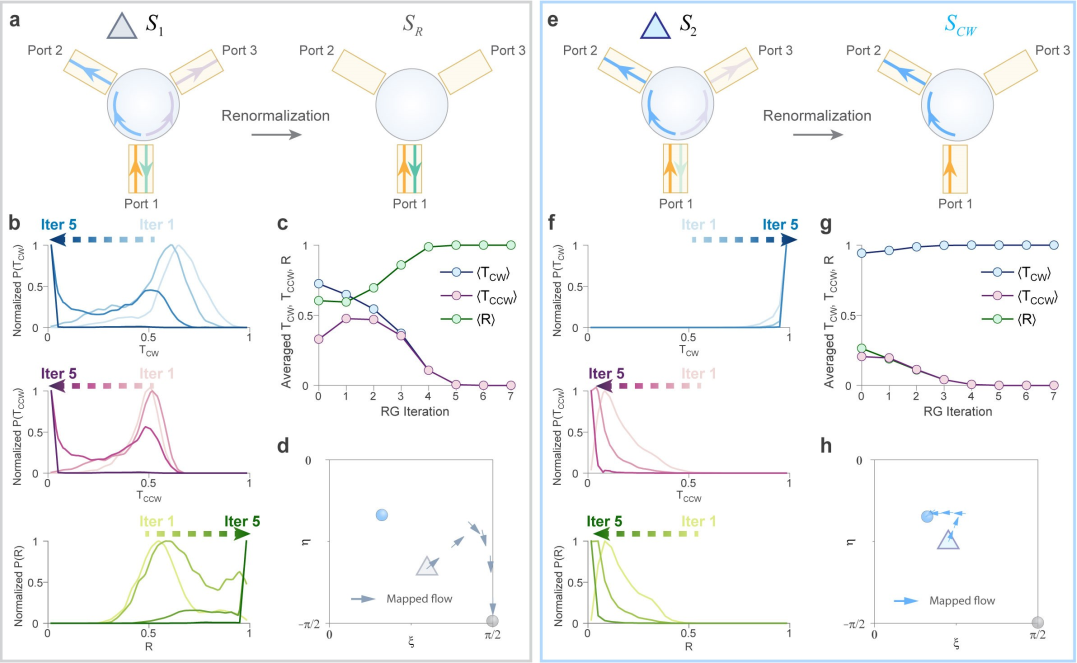

Figure 6.7: **Two examples of RG on scattering networks with random phase-link disorder. a, e,** Two opposite scattering attractors are reached for $S_1$ (a) and $S_2$ (e). During RG, macroscopic disordered networks built from $S_1$ and $S_2$ converge to the trivial attractor $S_R$, and the clockwise chiral one $S_{CW}$, respectively. **b, f,** Evolution of the distributions $P(T_{CW})$, $P(T_{CCW})$, and $P(R)$ upon RG, for the case of $S_1$ (b) and the case of $S_2$ (f). These distributions represent how the macroscopic scattering properties continuously evolve when scaling up the networks. **c, g,** We summarize the distinct behaviors of $S_1$ and $S_2$ networks by plotting the statistic averages of these distributions upon scaling, $\langle T_{CW}\rangle$, $\langle T_{CCW}\rangle$, and $\langle R\rangle$. **d, h,** RG flows. The averaged scattering properties of networks at each iteration are mapped to a point on the parameter space introduced in Fig. 2.3. The trajectory of the point forms the RG flow, showing the evolution of the macroscopic scattering properties as the network is repeatedly scaled up during RG.

This procedure, performed so far for only two initial scatterers $S_1$ and $S_2$, can be repeated for all possible initial scatterers that belong to the $(\xi,\eta)$ plane, obtaining a RG phase diagram for phase-link disorder. The RG phase diagram summarizes, for each $S_0(\xi,\eta)$, the attractor reached by large disordered networks built from $S_0$ (Fig. 6.8a). There are two topological phases of opposite chirality, depending on whether large systems converge to $S_{CW}$ or $S_{CCW}$. They are separated by the trivial phase, composed of systems that converge towards the full-reflection attractor $S_R$ upon scaling. At the interfaces between systems converging to $S_{CW}$ (or $S_{CCW}$), and systems converging to $S_R$ , a topological phase transition occurs, which is related to the presence of a critical metal with infinitely long correlations. As a result, the RG approach requires more iterations around these transition lines to start choosing an attractor, consistent with the observation of a extremum of the number of RG iterations required for convergence

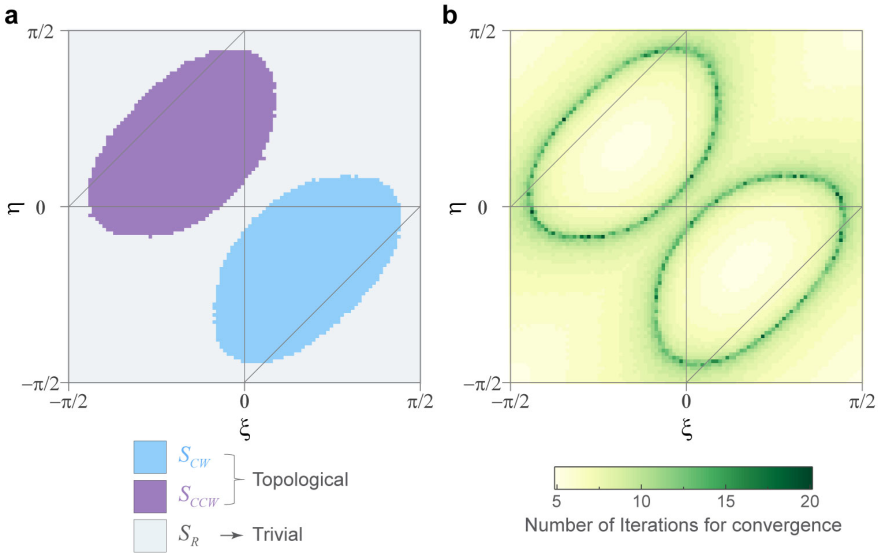

Figure 6.8: **RG phase diagram. a,** Phase diagram obtained by summarizing, for each network built from $S_0(\xi,\eta)$, which RG scattering attractor is reached in the thermodynamic limit or large systems. **b,** Number of RG iterations required to reach a fixed level of convergence to the scattering attractor. Local maxima are obtained at the phase transition, which is a signature of scaling invariant behaviors.

at the boundary, as shown in Fig. 6.8b.

To better represent the process of converging towards stable fixed points, we plot the associated RG flow diagram, shown in Fig. 6.9. Any initial value of $(\xi,\eta)$ in the blue (purple) region leads to a trajectory heading to the clockwise chiral attractor $S_{CW}$ ($S_{CCW}$). However, any point starting in the grey region goes to the fully reflective attractor $S_R$. The interface between the two regions are critical lines connecting six unstable fixed points (saddle points) of the RG flow. Any point with arbitrary small deviations from the critical lines will flow away from the critical condition, and eventually converge to a stable fixed point. In such disordered systems, a topological phase transition is equivalent to the crossing of a critical line, which represent systems that reach an exact balance between nonreciprocity and reflection upon scaling.

To complete the picture, we explore RG as close as possible to the critical scattering matrix located on the line between $S_1$ and $S_2$ in the parameter space. Note that we cannot exactly locate the exactly the critical scattering matrix, thus we choose a point very close to the critical scattering matrix $S_c$, but on the side of $S_{CW}$. We expect that such a point would behave similarly as $S_c$ during RG, at least during the first iterations, before it starts moving toward the attractor. As shown in Fig. 6.10, the probability distributions $P(T_{CW})$, $P(T_{CCW})$, and $P(R)$ are invariant in the first eleven iterations, which is indeed a symptom of the scale invariance expected for critical phenomena. Furthermore, the critical probability distributions of $T_{CW}, T_{CCW}, R$ represented in Fig. 6.10d establish a reference to determine whether a disordered network with arbitrary disorder will be topological or trivial in the thermodynamic limit.

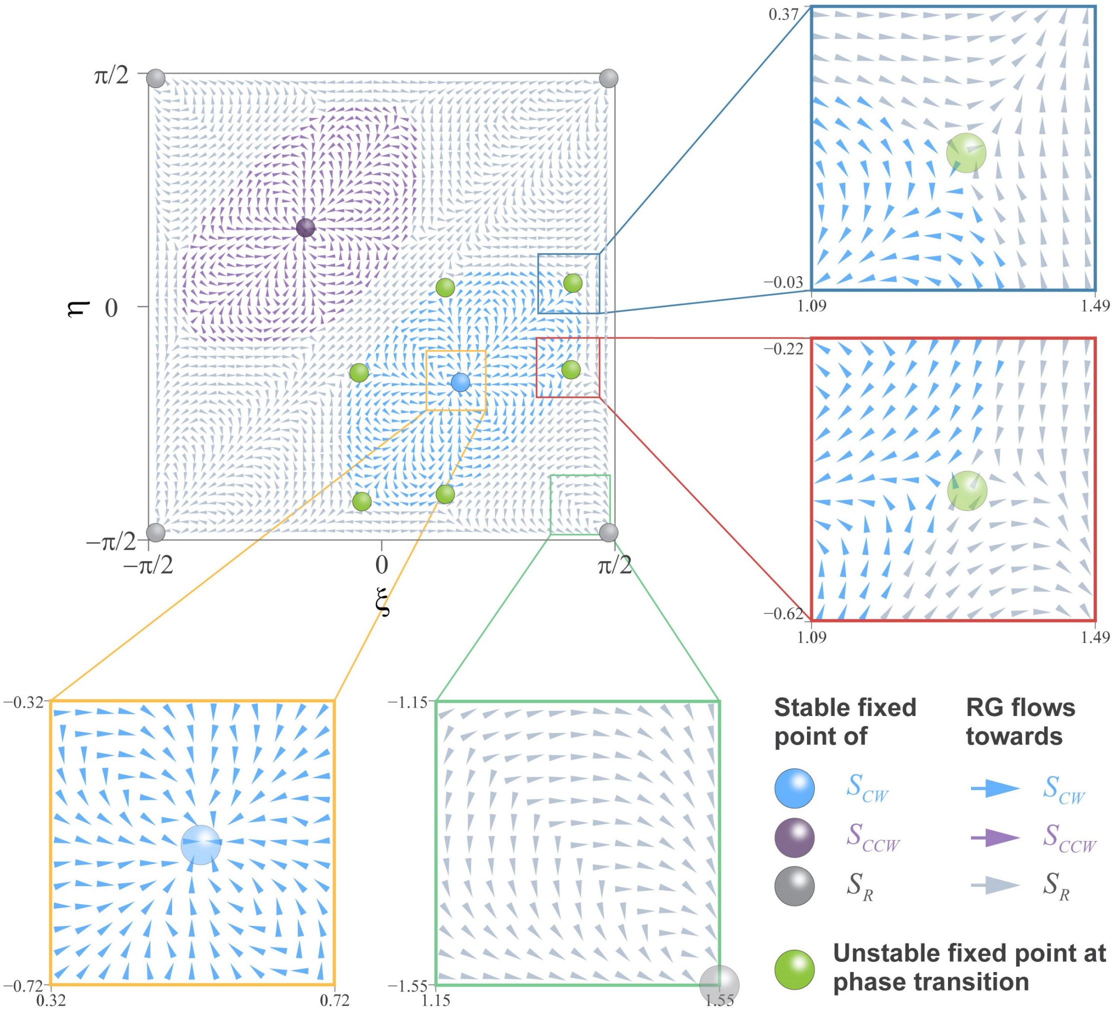

Figure 6.9: **RG flow diagram.** Arrows in the flow diagram indicate the effect of successive RG transformations on the macroscopic scattering properties of scaled networks. Non-zero flow divergence confirm that the points $S_{CW}$, $S_{CCW}$, and $S_R$ located at the centers of three phases are stable fixed points (a zoomed in view is provided by the two bottom insets). Six saddle points (green) define unstable fixed points located on the topological phase boundary.

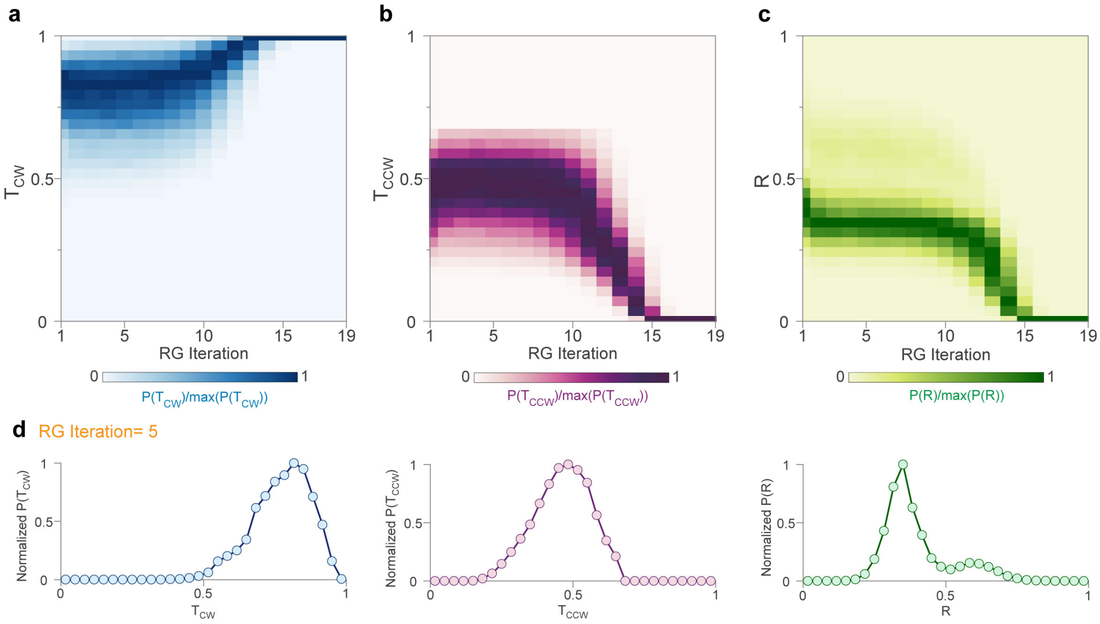

Figure 6.10: **Critical scattering properties. a-c,** Evolution of $P(T_{CW})$, $P(T_{CCW})$, and $P(R)$ of the scattering matrix at the point $\xi = -\eta = 0.92$, which is close to the critical point between $S_1$ and $S_2$, but on the side of $S_{CW}$. The probability distributions of $T_{CW}, T_{CCW}, R$ are invariant over the first ten RG scaling iterations, consistent with critical behavior. **d,** Corresponding critical probability distributions at the topological phase transition in phase-disordered honeycomb scattering networks.

It should be emphasized that the above critical distributions for phase transitions between trivial and topological insulators describe a totally different physical situation from the metal-insulator transition of quantum Hall effect already captured by CC networks [84, 88, 89, 91–95]. For CC networks governed by quantum percolation, the phase diagram consists instead of two phases, metal and insulator, and is described by a single scalar quantity $T$. In contrast, disordered topological scattering networks are described by the distributions of the three quantities $T_{CW}, T_{CCW}, R$ required to describe the topological criticality, which would no be possible with a single scalar quantity $T$ that contains no information about the chirality of the transport.

## 6.4 Scaling analysis of the localization length

In this section, we confront the phase transition boundary obtained from RG in the previous section to the one obtained from a different, computationally more intensive method based on calculating the localization length. The agreement between these independent results confirm the quantitative accuracy of the RG theory. As a by-product of the localization length study, we obtain insights on the topological phase diagram of phase-disordered networks and shed light on the associated critical phenomena.

### 6.4.1 Localization length and critical exponents

In this part, we utilize transfer matrix method on finite quasi-1D network discussed in Sec. 2.4, and perform localization length calculations and scaling analysis, to quantitatively characterize topological phase boundaries and their critical behaviors. In Fig. 6.11a, we show a slice of quasi-1D network with $L_x = 4$ and $L_y = 8$. In Fig. 6.11b, we show the results of such scaling analysis, with OBC applied in the $y$ direction (Fig. 6.11a). We vary the network parameters along the line $\xi = -\eta$, ranging from 0.73 to 1.18, expecting to cross the phase transition. We observe a monotonically increasing $\Lambda(L_y)$ in the range $0.73 < \xi < \xi_c \approx 0.93$, where $\xi_c$ denotes the critical value for which $\Lambda(L_y)$ is scale-invariant, marked by a dashed line. Conversely, $\xi_c < \xi < 1.2$ exhibits an insulator behavior. To determine whether the range $0.73 < \xi < \xi_c$ corresponds to a metal or a topological insulator, we changed the boundary conditions to PBC as shown in Fig. 6.12. which reversed the scaling behavior of the localization length, excluding the metal. Therefore, we conclude that disordered networks with $0.73 < \xi < \xi_c$ are topological insulators, whereas $\xi_c < \xi < 1.2$ are trivial insulators. Numerically, the topological criticality at $\xi_c \approx 0.93$ can be identified by a local minimum in the standard deviation of $\Lambda(L_y)$ for a set of $L_y$, represented as $\sigma_{\Lambda(L_y)}$ in Fig. 6.11c.

To extract the critical exponent $\nu$, we focus on a smaller range around the transition, shaded in orange in Fig. 6.11c. The scaling of $\Lambda$ in the vicinity of the critical point $\xi = \xi_c \approx 0.93$ is shown in Fig. 6.11d. If the localization length $\lambda$ diverges following the power law

$$\lambda \sim |\xi - \xi_c|^{-\nu}, \tag{6.7}$$

with the scaling ansatz, the normalized localization length $\Lambda(L_y, \xi)$ can be expanded as

$$\Lambda = \Lambda_c + \sum_{q=1}^{Q_1} a_q \left[ (\xi - \xi_c) L_y^{\frac{1}{\nu}} \right]^q + \sum_{q=0}^{Q_2} b_q \left[ (\xi - \xi_c) L_y^{\frac{1}{\nu}} \right]^q L_y^z, \tag{6.8}$$

where the third term is a finite effect correction [298], with $z$ defined as a negative exponent. Therefore, in the limit of $L_y \to \infty$, Eq. (6.8) recovers the standard form of single-parameter scaling as

$$\lim_{L_y \to \infty} \Lambda := \Lambda_c + \sum_{q=1}^{Q_1} a_q \left[ (\xi - \xi_c) L_y^{\frac{1}{\nu}} \right]^q. \tag{6.9}$$

With the help of Eq. (6.8) and using $Q_1 = 5$ and $Q_2 = 2$, we fit the data in Fig. 6.11d and obtain all the parameters $\nu, \xi_c, \Lambda_c, z$, as well as the coefficients $a_1, a_2, a_3, a_4, a_5, b_0, b_1, b_2$. To reduce the statistical error, we averaged the result over 100 disorder realizations. Fig. 6.11e plots the single parameter scaling function $\Lambda(L_y, \xi)$ (solid line) together with the data (dots) as a function of $L_y$. Our estimation lead to the critical exponent $\nu_1 = 2.4246 \pm 0.0970$ and critical length $\Lambda_c = 0.7020 \pm 0.0077$ for the critical boundary at $\xi = -\eta \approx 0.9301$. We observe that the value of $\nu_1$ and and $\Lambda_c$ are very close to the ones reported for QHE [97], which is not surprising since they are both topological insulators belonging to class A [97, 98, 106].

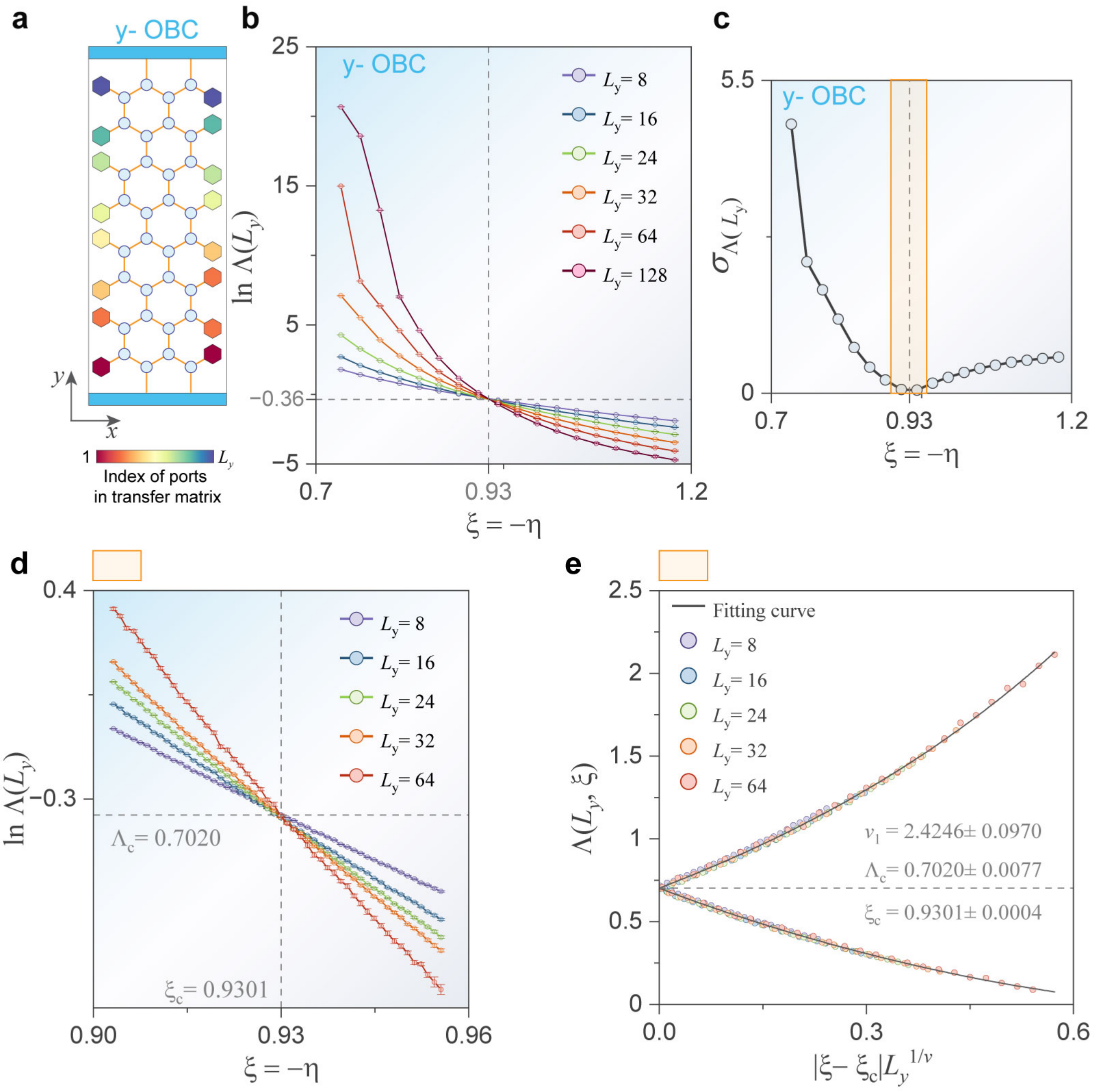

Figure 6.11: **Topological phase transitions and critical behaviors by a scaling analysis of the localization length. a,** A slice of a quasi-1D network with width $L_y = 8$ is used for iteratively calculating the transfer matrix. The longitudinal dimension contains four elementary slices, therefore $L_x = 4$. **b,** Evolution of the normalized localization length $\Lambda(L_y) = \lambda/L_y$ with the width $L_y$ on the segment of $\xi = -\eta \in [0.73, 1.18]$. $L_y$ is increased from 8 to 128. Error bars are smaller than the markers. The left and right parts of the plot are topological and trivial phases, respectively, and are separated by the critical point $\xi_c \approx 0.93$ (dashed lines) characterized by scale invariance. **c,** Criticality can be numerically identified as the local minimum of the standard deviation of the normalized localization length, $\sigma_{\Lambda(L_y)}$. **d,** Zoomed-in results of $\Lambda(L_y)$ scaling in the vicinity of $\xi = -\eta = \xi_c$ (marked as yellow region in panel c). The dashed view near the critical point $\xi = -\eta = \xi_c = 0.9301$ and $\Lambda_c = 0.7020$. **e,** Single parameter scaling function $\Lambda$ fitted from the data in panel d. We obtain a critical exponent $\nu_1 = 2.4246 \pm 0.0970$. The error bars correspond to the 95% confidence intervals estimated from the Monte Carlo simulations.

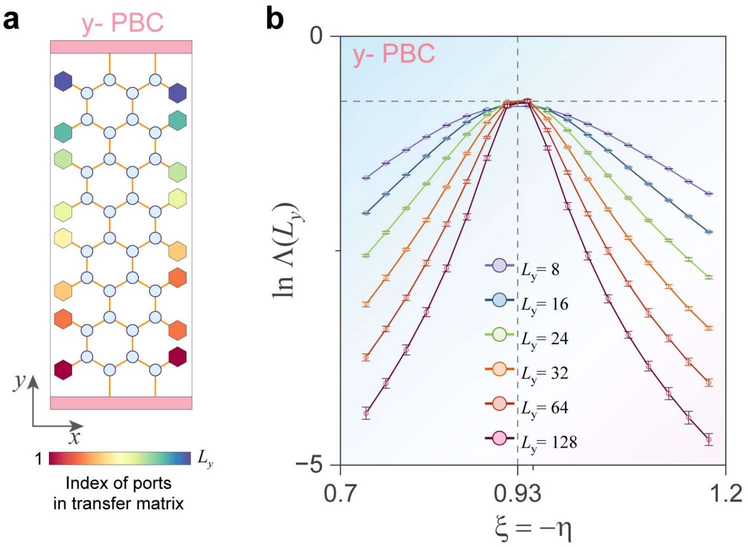

Figure 6.12: **Scaling of $\Lambda(L_y)$ under y-periodic boundary conditions in the vicinity of the critical point $\xi_c \approx 0.93$ on the line of $\xi = -\eta$. a,** Periodic boundary condition along y direction eliminates edge effects including topological edge states. **b,** Two sides of the dashed line both show decreasing $\Lambda(L_y)$ when increasing width $L_y$ from 8 to 128, a hall marker of insulating phases, indicating an insulator-insulator transition.

### 6.4.2 Topological phase diagrams comparisons and two critical exponent values

The study of the previous section can be repeated for any point of the phase diagram, in order to directly confront the topological boundary predicted by RG to the one obtained from the scaling analysis of the localization length. The later can be obtained by looking at the location of local minima of $\sigma_{\Lambda(L_y)}$ in the parameter space, plotted in Fig. 6.13a. In Fig. 6.13b, we show the direct comparison of the phase boundaries obtained from localization length calculations (dashed line) and from RG (solid lines). We observe a very good agreement between the two, validating the validity of our RG theory, with percent-level quantitative accuracy. In terms of numerical efficiency, the time cost of RG calculation for one point of the phase diagrams is a few seconds, (minutes very close to critical points), versus several hours for the corresponding localization length calculations, performed on the Intel(R) Xeon(R) Platinum 8360Y processors.

Surprisingly, we found that the critical behaviors vary discretely on the topological phase boundaries. More specifically, they are of two kinds, and change at the RG flow saddle points. The values of the two distinct critical exponents are $\nu_1 \approx 2.43$ and $\nu_2 \approx 3.33$, and their locations are shown in Fig. 6.13c. A detailed example for $\nu_2 \approx 3.33$ in the vicinity of $\xi = -\eta \approx 0.0947$ is shown in Fig. 6.14, which is also found on the segment $\xi = -\eta \in [0, \pi]$, on the other side of the phase diagram. A given segment connecting two unstable fixed points (saddle points) in the RG flow diagram exhibits a constant critical exponent value, which changes when crossing saddle points. We conjecture that such distinct critical behaviors originate from distinct types

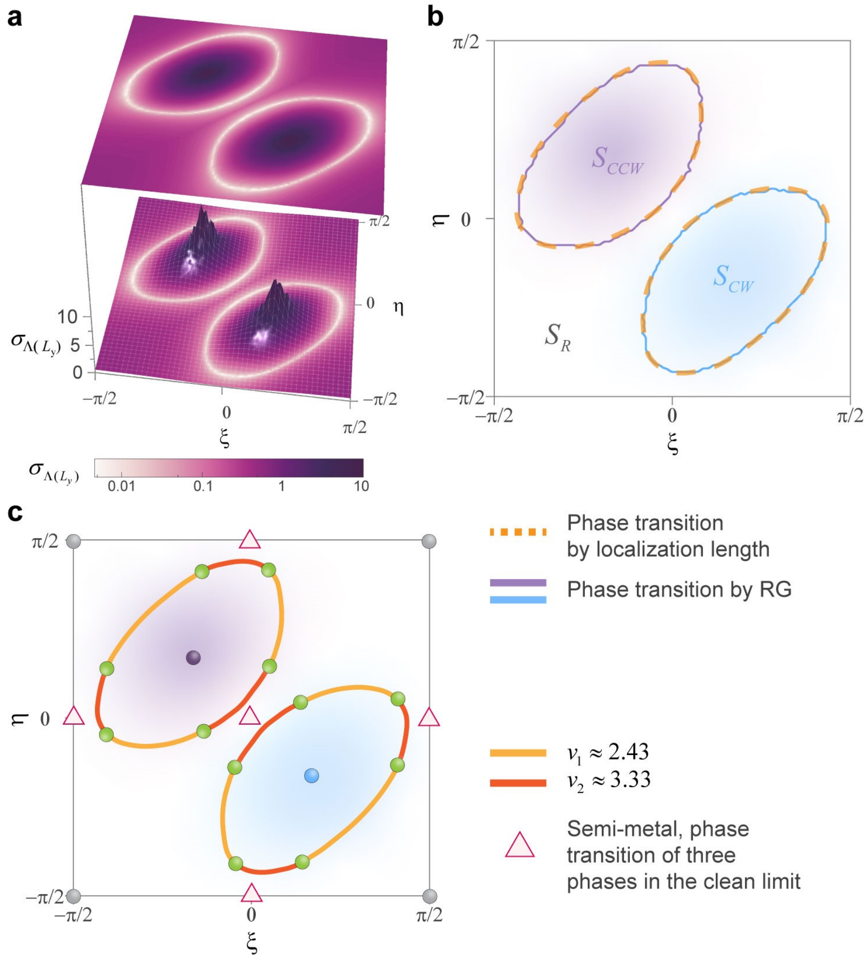

Figure 6.13: **Comparisons of the topological phase diagrams and critical behaviors obtained from RG and LL analysis.** **a,** In LL analysis, the boundaries of topological phases are revealed by the local mimima of $\sigma_{\Lambda(L_y)}$. **b,** Direct comparison of the RG and LL topological phase diagrams. They agree with percent-level accuracy. **c,** Critical exponent distribution on the phase boundaries. Two values of critical exponents - $\approx 2.43$ (orange) and $\approx 3.33$ (red)- emerge along the critical boundary, and change only at the RG unstable fixed points, which are saddle points of the RG flow.

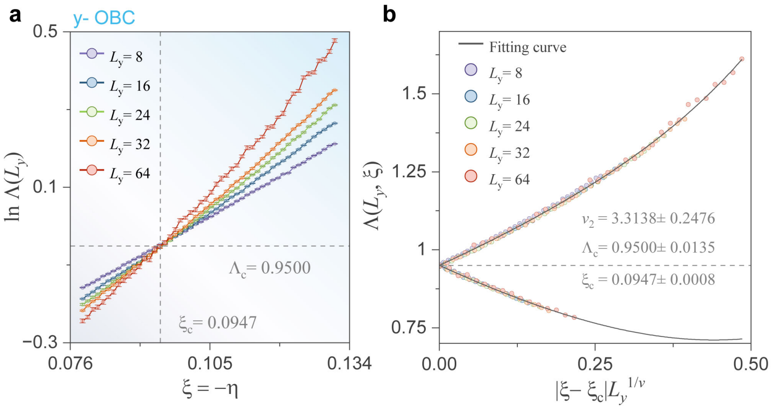

Figure 6.14: **Scaling analysis in the vicinity of another type critical point:** $\xi_c \approx 0.0947$ **on the line of** $\xi = -\eta$**. a,** $\Lambda(L_y)$ at different parameters versus $L_y$, changing from 8 to 64. **b,** Fitted curved and critical parameters with the ansatz of single parameter scaling. Critical exponent $\upsilon_2$ is estimated to be 3.3138 with critical $\Lambda_c \approx 0.9500$, distinct with the critical exponent $\upsilon_1$ in the vicinity of $\xi_c \approx 0.9301$.

of topological phase transitions, which we can clearly see on the clean-limit topological phase diagram. The critical segments with $\upsilon_1$ are associated to the topological phase transition between the anomalous and Chern phases in the clean limit (Fig. 3.2), whereas the ones with $\upsilon_2$ can be attributed to more complex phases transitions at the semi-metal points in the clean limit, where three topological phases meet: anomalous, Chern, and trivial insulators.

## 6.5 Experiments

We performed experiments by using again our prototypes DN1-5 with random phase link disorder. We added a port on the edge to make the prototypes three port networks, and show a picture of one of them in Fig. 6.15a. At each frequency, we can not only measure the microscopic scattering properties of a single circulator $S_0(f)$, but also the macroscopic scattering properties of the networks $S_1'(f)$, taken at three external probes located on the boundary. The difference between $S_0(f)$ and $S_1'(f)$ is the experimental RG flow, shown by coloured arrows in Fig. 6.15c. As the measurements of networks involve one probe per side, we compare the measured flow with the numerical RG flow obtained for $M_i = 1, i = 1,2,3$, shown by smaller arrows in the background. Clearly, the measured RG flow in the blue region points toward the center of blue region, namely the $S_{CW}$ attractor, consistent with the numerical RG predictions. On the contrary, the flow measured in the grey region heads to the fixed point of $S_R$, as expected from theory. Slight discrepancies between measured and predicted flows are observed nearby the critical boundary. They are attributed to the limited number of disorder realizations, as well as the limited size of the networks, which is not large enough to capture accurately the thermodynamic limit near critical boundaries. Nevertheless, our experiments substantiate the predicted RG flow and the convergence of large networks towards scattering attractors by confirming experimentally the accuracy of block-scattering transformations.

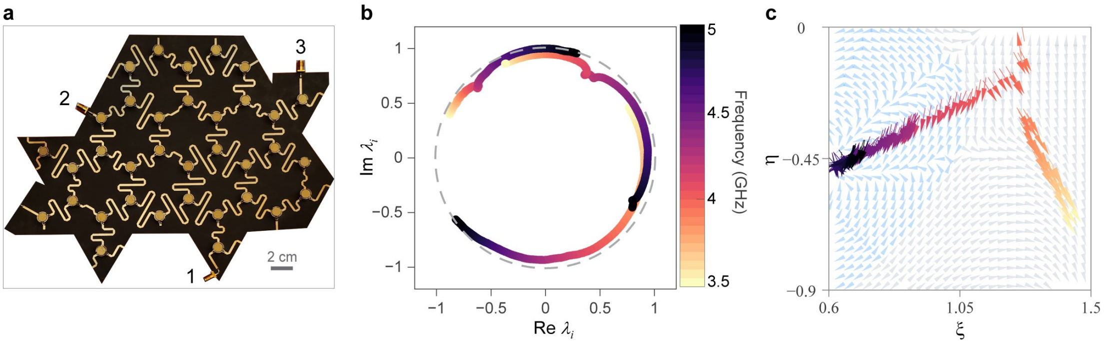

Figure 6.15: **Experimental validation of renormalization group flow. a,** Photograph of one of our 5 prototypes. We experimentally validate the scattering RG flow by using microwave networks made of ferrite circulators interconnected by microstrip lines. The ferrite circulators serve as microscopic three-port scatterers, and their scattering matrix depends continuously on frequency, allowing us to access a continuous family of networks with different attractors simply by varying the frequency of operation. The random phase-link disorder is realized by varying the length of the meandering microstrips that connect the circulators together. The 5 prototypes correspond to different realizations of disorder. At each frequency, we can measure the microscopic scattering properties of a single circulator, as well as the macroscopic scattering properties of the networks, taken at three external probes located on the boundary. This allows us to experimentally extract the RG flow. **b,** Experimentally measured eigenvalues of the scattering matrix of the circulators, confirming the quasi-unitarity of the microscopic scattering process over the experimental frequency band (3.5 – 5 GHz). **c,** Measured RG flow (colored arrows) averaged over the five different disorder realizations. The arrows composing the background are numerical predictions of the RG flow ($M_i = 1, i = 1,2,3$).

We are able to confirm that the presence of phase-link disorder enhances the chirality of the transport when comparing $S_1'(f)$ to $S_0(f)$, when the networks fall in the region of attraction of $S_{CW}$. Such results shed light on the origin of topological chiral edge states in samples with strong distributed disorder.

## 6.6 RG on scattering networks with structural disorder

In this section, we therefore turn our attention to another type of disordered scattering networks with structural disorder. We implement our RG theory to explore topological phase diagram and RG flows in such amorphous scattering networks. In the following, we focus on scattering networks at the strongest level of structural disorder $\alpha = 8$. More information about network statistics as a function of $\alpha$ can be found in Sec. 2.1.4.

The RG of amorphous networks is essentially similar to the one of phase-disordered honeycomb lattices. The implementation of the RG theory on structurally disordered networks still relies on the same three steps (block division, transformation, and reconstruction). However, the Delaunay triangulation yielding the block division comes with a twist. Since we are dealing with networks with structural disorder at level $\alpha$, the Delaunay triangulation is no longer

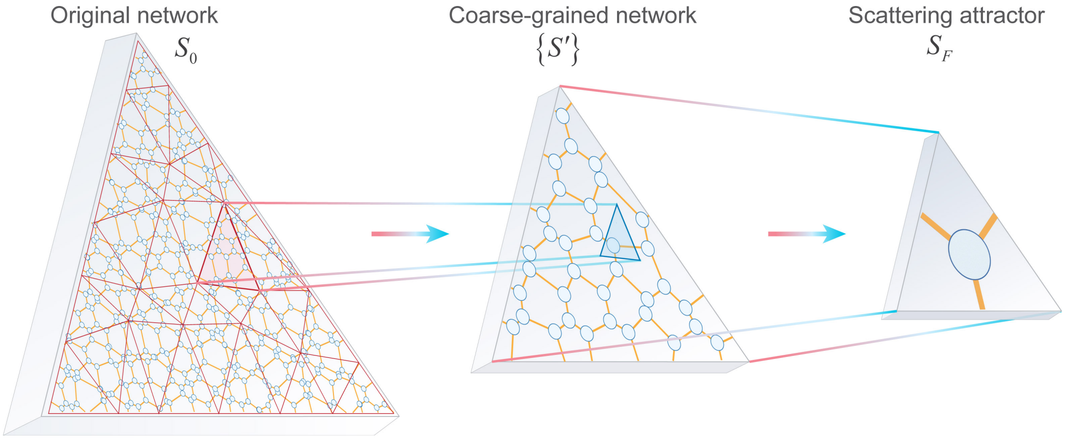

Figure 6.16: **Renormalization group of a unitary scattering network with structural disorder.** As for the case of phase-disorder, the block-scattering transformation follows the three key steps of block division, transformation and reconstruction. The only difference is that the Delaunay triangulation is no longer regular. The transformation is used iteratively until one obtains a $U(3)$ attractor $S_F$. In practice, this scheme is implemented via the replica scheme described in the section 6.3.2.

regular, but also at level $\alpha$ (Fig. 6.16, leftmost). Following this, the dual graph that is used to interconnect the newly generated scatterers into a coarse-grained network (Fig. 6.16, center), is also at disorder level $\alpha$.

The topological phase diagram obtained from RG is shown in Fig. 6.17a. It exhibits smaller topological phases than the phase diagram observed in honeycomb networks with random phase-link disorder (Fig. 6.8). The phase boundary is confirmed by looking at the number of RG iterations needed for convergence into $S_F$ (Fig. 6.17b), whose local maxima indicates the scale invariance of networks located at the phase transition. Albeit with a slightly different topological range, the structure of the RG flow is very similar to the one found in the previous section, and exhibits the same landscape of stable and unstable fixed points as in Fig. 6.9, highlighting some for of critical universality between the two different kinds of disordered networks.

## 6.7 Conclusion

We have presented a real-space renormalization group (RG) theory for unitary scattering network models, which offers significant insights into the emergence of topological edge states in large systems with strong distributed disorder. The method can reduce the microscopic scattering processes occurring in any unitary network into a $3 \times 3$ unitary scattering attractor that summarizes the key macroscopic scattering properties emerging at large scales. By introducing the block-scattering transformation, we focus on preserving key information about transport chirality and reflection, smearing out microscopic fluctuations into a macroscopic description of the scattering process. The combination of block scattering transformations

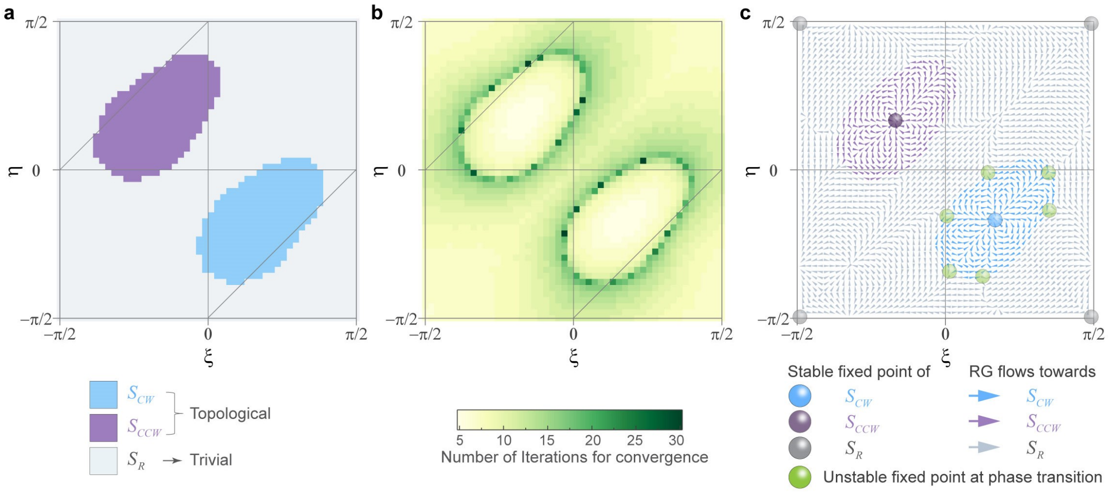

Figure 6.17: **RG topological phase diagram and flow diagram for networks under the strongest structural disorder. a,** Topological phase diagram obtained from RG, representing the RG scattering attractor $S_F$ for all possible choices for the microscopic scattering matrix in the parameter space. **b,** Corresponding number of RG iterations required to converge to the attractor. **c,** RG flow diagram, showing the transformation of networks upon iterative application of RG.

and the replica strategy was shown to lead to a numerically-efficient RG theory, capable of handling simultaneously an arbitrary number of RG iterations while performing Monte-Carlo simulations on disorder realizations. Our RG theory is capable of discerning between topological and trivial disordered networks, since their correspond to distinct scattering attractors. Its implementation on two types of disordered networks not only clarifies the necessary microscopic conditions for constructing macroscopic topological networks, but also uncovers the unique critical phenomena occurring at topological phase boundaries, as well as the physics of disorder-resilient chiral edge transport. In addition, the quantitative accuracy of our RG framework is demonstrated through an independent scaling analysis of the localization length of quasi-1D networks, which predicts the same topological phase diagram as the RG theory, with percent-level accuracy. As a by-product, we were able to elucidate the intricate critical phenomena occurring at the transition between disordered topological and trivial insulators, with critical exponents that take discrete values on the boundary, only changing at the RG flow saddle points. Finally, these theoretical advancements are complemented by experimental verifications performed on microwave scattering networks, which are consistent with the calculated RG flow.

# 7 Conclusion and outlook

## 7.1 Conclusions

In this thesis, we undertook a comprehensive exploration of topological scattering networks, focusing specifically on unitary (Floquet) topology and the significant impacts of disorder. These scattering networks are made of three-port non-reciprocal unitary scatterers interconnected by bidirectional phase-delay links. Through a combination of theoretical analysis, numerical simulations, and experimental validations, the conducted investigations revealed the robustness of topological phases, particularly emphasizing the resilience of chiral transport in anomalous Floquet insulators (AFI) against various types of distributed disorder.

### Results summary

The journey began with a general introduction presenting the motivation of the thesis and global aspects of topological insulators. Following up the introduction, we have assembled and discussed in Chapter 2 practical and mutually consistent concepts, including band structures for infinite and semi-infinite networks, transports and eigenstates in finite networks, scaling analysis with localization length calculations, and topological scattering invariants, to be ready to tackle the adventurous study of the topological properties of disordered network systems.

The major achievements of this thesis include:

1. Identification of Floquet topological bands in honeycomb scattering networks with broken TRS, where phase-delay mirrors quasienergy. Their topological phase diagram contains three phases: anomalous Floquet topological phase (AFI), Chern phase (CI), and trivial phase.
2. Distinction between AFI and CI lies on the topological robustness against strong distributed disorder. Anomalous topological edge transports show superior robustness over Chern edge states, under disorder in any type- disorder on phase-delay values (randomized quasienergy), structural disorder (amorphism), and disorder on scattering

nodes. Anomalous topological waves can persist against the strongest disorder on phase delays and amorphism. These topological networks under strong disorder are of AFAI, where topological edge states are ubiquitous in the quasienergy spectrum and bulk states are fully localized. Such a phenomenon can only be understood in the Floquet topology frame.

3. Findings are experimentally validated by photonic scattering networks operating in microwave frequency bands by probing transports and scattering matrices. Various types of disorders are implemented and examined. Topological invariants are measured even in disordered networks by implementing a designated device realizing twisted boundary conditions.

4. Definition of a real-space renormalization group (RG) driven by block-scattering transformations on unitary scattering networks. Such a unified theory unveils the intricate physical mechanisms behind the persistence of topological edge states in systems with strong distributed disorder, substantiated by RG topological phase and flow diagrams. The obtained critical probability distributions of microscopic scattering properties are the boundary between AFAI and trivial Anderson insulators, which can be the guideline for practically constructing topological networks. RG theory is further validated by scaling analysis of the localization length (LL) and critical exponents, and experimentally confirmed by building microwave scattering networks with fully disordered phase links.

### 7.1.1 Theoretical contributions

The theoretical framework developed in this manuscript has considerably contributed to the understanding of topological robustness in scattering networks. In Chapters 3-5, by implementing the analysis tools described in Chapter 2, we established the superior robustness of the anomalous topological phase in unitary scattering networks. In addition, we have evidenced the persistence of topological edge states within the anomalous topological phase, even under severe disorder conditions, by developing a novel real-space RG approach. This methodology not only diverges from traditional Hamiltonian renormalization techniques but also provides practical guidelines for the design of robust topological photonic systems. The critical probability distribution can serve as a guideline for the practical construction of topological networks.

### 7.1.2 Experimental realizations and implications

The experimental aspect of this thesis not only validated the theoretical predictions, but also demonstrated how topological invariants can be observed and measured in disordered networks. The implementation of the twisted boundary conditions via a specially designed device played a key role in this achievement, enabling the direct observation of the topological properties. These experiments underline the practical potential of AFIs in real-world applications, ranging from photonic devices to quantum computing platforms.

## 7.2 Future directions

We now outline possible future directions for the presented work.

### 7.2.1 Applications: robust and versatile topological photonic manipulations

Traditionally, Chern insulators can be used to guide an edge mode between two domains having different Chern numbers. However, when the disorder is larger than the band gap, such insulators can be trivialized. In addition, changing Chern numbers require local control of the external magnetic polarization (e.g., by reversing the magnetic field) [299–301]. Non-reciprocal unitary scattering networks unlock opportunities to exploit the anomalous phase as an extra degree of freedom, forming edge states at Chern-anomalous boundaries that do not require a modification of the magnetic bias, but simply a contrast in the scattering properties. This makes it possible to harness the rich topological features of Floquet systems, thus leveraging non-reciprocal advantages for genuine back-scattering immune wave manipulations.

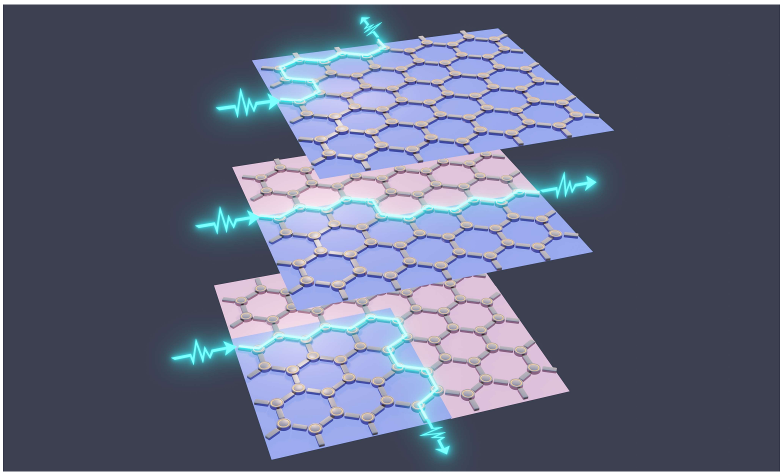

Figure 7.1: **Wave routing with superior topological protection.** By using domain walls between AFI (blue) and CI/trivial insulator (red), one can build dynamically reconfigurable unidirectional photonic paths from any input to any output on a 2D photonic chip, despite using a uniform magnetic bias.

As illustrated in Fig. 7.1, the first envisaged application is the topological routing of a given wave. The essence of topological wave routing lies in the creation of a domain wall. On either side of the boundary, network domains find themselves in gaps (band gaps or mobility gaps) and have different gap invariants, the difference of which is exactly the number of topologically protected edge states accommodated at the domain wall. The reconfigurability of wave routing relies on the tunable phase-delay links or scatterers. Looking at the tuning of the phase delay spectrum under a fixed phase delay band structure, the phase-delay links can be adjusted in a first domain exactly in the trivial band gaps, while the phase-delays links are maintained in the topological band gap in the other domain. This approach modifies the band structure in a specific domain of the network, as illustrated in Fig. 5.3, resulting in a trivial

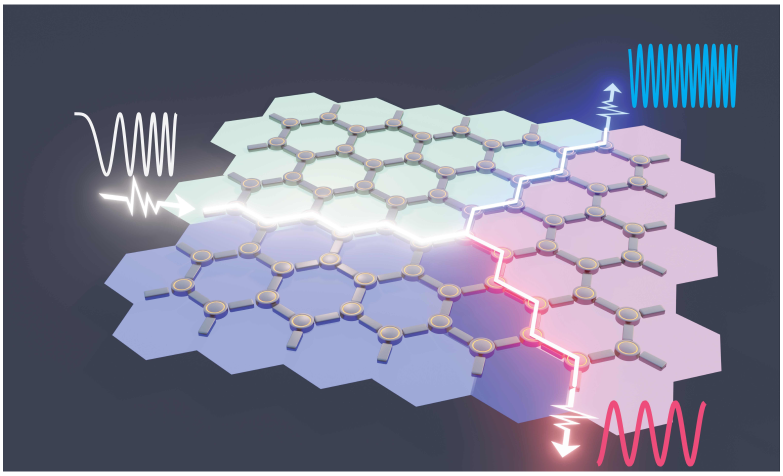

Figure 7.2: **Topological filters and multiplexers.** Unidirectional filters and multiplexers may find applications in protected communication systems. They can be based on topological domain walls among anomalous, Chern, and trivial phases occurring in non-reciprocal scattering networks.

band gap at a predetermined phase-delay value. Moreover, by taking advantage of the unique effects of disorder on topological phase, disorder on phase-links or additional scatterers can also be used to trivialize Chern networks, while maintaining the other domain of the network in the anomalous phase.

Building on the fundamental functionality of topological waveguiding, Fig. 7.2 shows an example of topological filters and multiplexers. Anomalous topological networks uniquely allow the adjustment of local phases and impedance mismatches without disturbing the unidirectional flow of energy, providing an ideal platform for engineering poles and zeros in order to challenge traditional filter design paradigms, including the trade-offs between performance and complexity.

Beyond traditional wave phenomena, the results and frameworks presented in this thesis also offer promising future for topologically robust operations in quantum photonic networks [177, 178, 302–305], as these networks are also constructed by multiple unitary scattering processes. For instance, anomalous topological edge states can be harnessed to protect entanglements [306], quantum information processing [307, 308], and communication [309, 310], against any disorder in the quantum networks [288, 311, 312]. Furthermore, in the realm of quantum photonic networks, the experimental realization of arbitrary $U(N)$ operators is essential to perform various state operations, for which the transfer matrix method proposed by Reck *et al* [195] is widely used. It incorporates a $2N \times 2N$ unitary scattering matrix $S$ with zero diagonal blocked matrices $S(1:N, 1:N) = \mathbf{0}$ and $S\big[(N+1):2N,(N+1):2N\big] = \mathbf{0}$. Consequently, the transfer matrix on the off-diagonal block $T = S\big[1:N,(N+1):2N\big]$ can be of $U(N)$ group. However, this approach depends heavily on the assumption that the diagonal blocks of the matrices are zero, which implies the absence of reflections in Mach-

Zehnder interferometers (MZI). A mathematical and physical question arises: "Is it possible to implement arbitrary $U(N)$ operators within non-reciprocal scattering networks?". We believe that a completely new parameterization of the $U(N)$ matrices will first be required, in order to create the corresponding scattering network block by block.

### 7.2.2 Further explorations on network models

We focused during this thesis on 2D planar networks characterized by unitary scattering processes. Generalizing the network models beyond these conditions opens new research avenues. Firstly, although practical continuum structures are confined to 3D, network models enable the exploration of higher-dimensional structures, by constructing appropriate connections [313–315]. Non-reciprocal scattering networks allow us to study higher-dimensional Floquet topological states and their localization properties. Since systems of different dimensions exhibit distinct localization-delocalization transitions [316], it would be interesting to unveil new disorder-induced phase transition phenomena in the higher dimensional non-reciprocal networks. Alternatively, three phase-delay links in a unitcell can have independent phase terms- $\varphi_1$, $\varphi_2$, and $\varphi_3$- which synthetically form a five-dimensional compact space for a 2D planar scattering networks [317–321]. Secondly, by keeping the positions and scattering properties of scattering nodes, non-planar connections can be integrated into scattering networks and can therefore potentially lead to topological phase transitions as they act as disorder. For example, to model the practical radiation couplings between scatterers in a given distance range, non-planar connections are placed among scatterers [322–324]. Finally, breaking the unitary conditions opens the way to the exploration of the interplay between non-Hermitian physics, Floquet topology, and non-reciprocal scattering, where intriguing phenomena such as skin effect and exceptional points could be of research interest.

### 7.2.3 Disorder effects on topological phases for non-interaction electron and time-driven systems

The history and motivations of scattering network models reveal two distinct trajectories: one focuses on modelling disorder in non-interacting electron systems, while the other draws parallels with Floquet topology. The interplay between unitary topological phases and various types of disorder, as discussed through scattering network models in this thesis, offer the possibility to elucidate the counter-intuitive effects of disorder in electronic systems. For example, network models have recently been applied to explain flat bands in twisted bilayer graphene (TBG) [325–329].

Returning to unitary topology, one of the most intriguing prospects for time-driven systems is the further investigation of the Floquet topological robustness against disorder. The synergy between Floquet engineering and disorder unveils new avenues for discovering disorder-induced topological phases, including the potential emergence of anomalous Floquet topological insulators in highly disordered regimes. Understanding these phenomena could lead to the design of Floquet photonic systems that maintain topological edge states and functionalities even under significant structural imperfections or environmental fluctuations. Currently, the realm of disorder in time-driven systems [330, 331] and their topological phases [131, 132, 163–170] remain largely unexplored. In addition, the advancement of experimental techniques to realize and manipulate disordered Floquet topological photonic systems is crucial. Challenges include, but are not limited to, non-quantized transport, which is non-unitary due to the frequency conversions induced by the time modulation, as well as the lack of platforms capable of tuning various parameters in the time-driven mechanism, etc. The development of versatile and programmable photonic platforms able to dynamically tune disorder and Floquet parameters would indeed enable the experimental exploration of theoretical predictions and practical applications of anomalous topological phase and AFAI in devices ranging from lasers and sensors to communication technologies. In summary, observational studies of topological time-driven photonic systems are still lacking, and their AFAI awaits for a suitable platform to be probed.

### 7.2.4 Potentials for scattering RG theory

We believe that the proposed scattering-based RG is general and broadly extends a theoretical toolbox that may find direct applications in network models used in condensed-matter and disordered topological physics. In the longer term, we envisage that the block scattering transformation introduced in this work may also be useful in the study and understanding of large network models in communication systems, or in the development of physical neural networks based on scattering. With our methodologies and numerical framework, a potentially interesting future direction may be to explore other complex systems in the spirit of scattering, by grid discretization into networks or even by developing a continuous form of scattering RG that would address physical systems beyond networks. This could potentially unravel new aspects of the intricate interplay between topology, disorder, and scaling. Practically, conducting research in that direction would pave the way to the design of more resilient and efficient devices in photonic, electromagnetic, and quantum computing networks, by establishing disorder as a general degree of freedom instead of a hindrance in the management and design of topological properties.

## 7.3 Conclusion

In this thesis, we systematically studied the interplay between unitary topology and disorder in unitary non-reciprocal scattering networks through various but consistent analysis methods designated for disordered networks. We theoretically unveiled and experimentally validated the superior robust topological phase in unitary scattering networks, namely the anomalous Floquet topological phase, and proposed a unified scattering-based RG theory for the determination of the topological properties in disordered unitary scattering networks. The knowledge acquired here not only deepens our comprehension of topological matter but also paves the way for the development of robust and efficient electronic, photonic, and quantum devices. As we venture into the future, I hope that the foundations laid by this work may inspire other researchers on continued innovation and exploration in the fascinating interplay between topological physics and disorder.

# A Density of states and skin distance definitions

For a large enough network without external ports, we can obtain the density of states (DOS) directly from the network spectrum (Details of spectrum discussion in Sec. 2.3.2). The density of states DOS($\varphi$) for a given phase delay $\varphi$ is defined as $N(\varphi)/\delta\varphi$, where $N(\varphi)$ is the number of states whose eigenphases lie in the range $[\varphi, \varphi+\delta\varphi]$. We can normalize DOS($\varphi$) by the clean limit one, DOS($\varphi_0$), for which $\varphi_0$ lies in a topological band gap.

To identify the localization properties of an eigenstate $|b\rangle$, one can calculate its participation ratio (defined in Eq. (2.30)). However, participation ratio cannot differentiate a localized state in the bulk from an edge state. Therefore, we have to define a quantity called the skin distance $d_s(|b\rangle)$, which captures the averaged position of an eigenstate $|b\rangle$. To define skin distance, we first review the definition of node distance $d(i,j)$ between node $i$ and node $j$ in the graph theory [203]: it is defined as the number of edges in a shortest path (also called a graph geodesic) connecting them. After that, we define the skin distance $d_s(i)$ of node $i$ in the network as the minimal distance between node $i$ and all the boundary nodes:

$$d_s(i) = \min_j d(i,j)|_{j\,\in\,\text{Set of boundary nodes}}. \tag{A.1}$$

Taking the network in Fig. A.1 as an example, we can define skin distances of nodes going from 1 to the network thickness, i.e. 9 in this case. Skin distance $d_s = 1$ corresponds to any node on the boundary of the network while the highest value of $d_s$, here $d_s = 9$, corresponds to the nodes at the center of the network. Then, we can define the skin distance of an eigenstate $|b\rangle$ as

$$d_s(|b\rangle) = \frac{\sum_i d_s(i)|b_i|^2}{\sum_i |b_i|^2}, \tag{A.2}$$

where $b_i$ is the amplitude of $|b\rangle$ at the port $i$. A state with a small (resp. large) skin distance will be located in the vicinity of the boundary (resp. in the deep bulk).

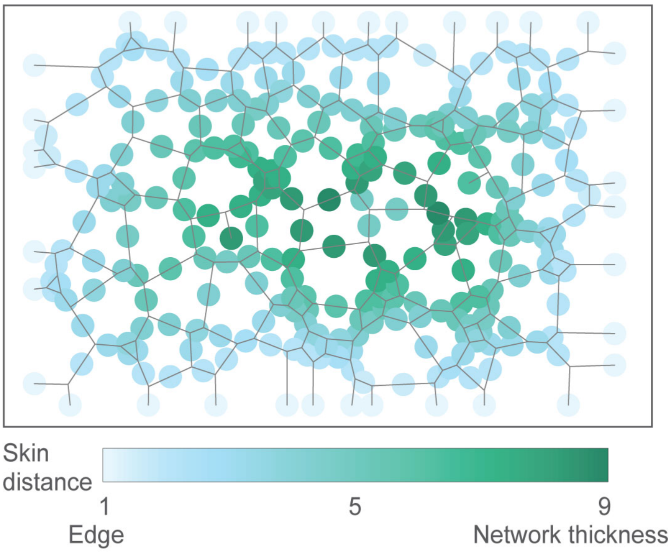
Skin distance
1
5
9
Edge
Network thickness

Figure A.1: **Definition of the skin distance.** We define the skin distance of a node in the network by the minimal graph distance between the node and all the boundary nodes.

# B Distinction between frequency and phase-delay (Floquet) band structures

In this part, we illustrate the distinction between frequency band structure and phase-delay band structure in a scattering network. The phase-delay (Floquet) band structure is formed at a single frequency, which implies that the network links should be scaled in length to vary the value of $\varphi$. In the frequency band structure, the dispersion of both the phase links and the scattering nodes plays a major role, since the length of the links are kept constant, but the phase evolves as frequency is varied. Both points of view are valid, however only one of them (the phase-delay band structure) is able to distinguish between Chern and anomalous chiral edge states, and explain differences in robustness when distributed disorder is imparted. Therefore, adopting the Floquet point of view leads to a more appropriate description of the physics, by revealing the existence of the anomalous phase [19, 112, 123, 148].

Let us consider two non-reciprocal networks consisting of circulators. The dispersive scattering matrices of the circulators are modeled by coupled mode theory described by Eq. (2.21). The circulators of these two networks are chosen with slightly distinct reflection coefficients $|R|$ at $f = f_0$, and their resulting frequency band structures are shown in Fig. B.1 for $|R_{f=f_0}| = 0.24$ (left), $|R_{f=f_0}| = 0.51$ (right). A direct calculation of the Chern numbers for each frequency band, in agreement with the computation of chiral edge states in the projected frequency spectrum for a strip geometry with top and bottom edges (panels c and d of Fig. B.1), indicates that the wave topology is supposed to be equivalent in these two networks. Indeed, the frequency point of view cannot distinguish between a Chern and an anomalous insulator: Chern numbers just count the number of edge states leaving and entering the bands in this frequency picture, whereas at different frequency the phase-delay spectra can be of Chern or anomalous types.

To show the hidden physical difference between these two networks, strong phase or structural disorder should be imparted. We evidence this by fixing the frequency in one of the frequency gaps hosting a chiral edge state and performing the edge transmissions for finite networks (Fig. B.2). When the amorphism becomes high enough ($\alpha = 8$), only the edge state in the case $|R_{f=f_0}| = 0.24$ is preserved, while the chiral edge state for $|R_{f=f_0}| = 0.51$ is destroyed and the network is insulating. This unveils that these two networks actually correspond to two distinct topological phases from the Floquet point of view, which are not resolved by their frequency spectrum, but only by their phase-delay spectrum (Fig. B.3). Indeed, the case $|R_{f=f_0}| = 0.51$ corresponds to a phase-delay Chern regime while $|R_{f=f_0}| = 0.24$ corresponds to a phase-delay anomalous regime, although both correspond to a frequency Chern phase.

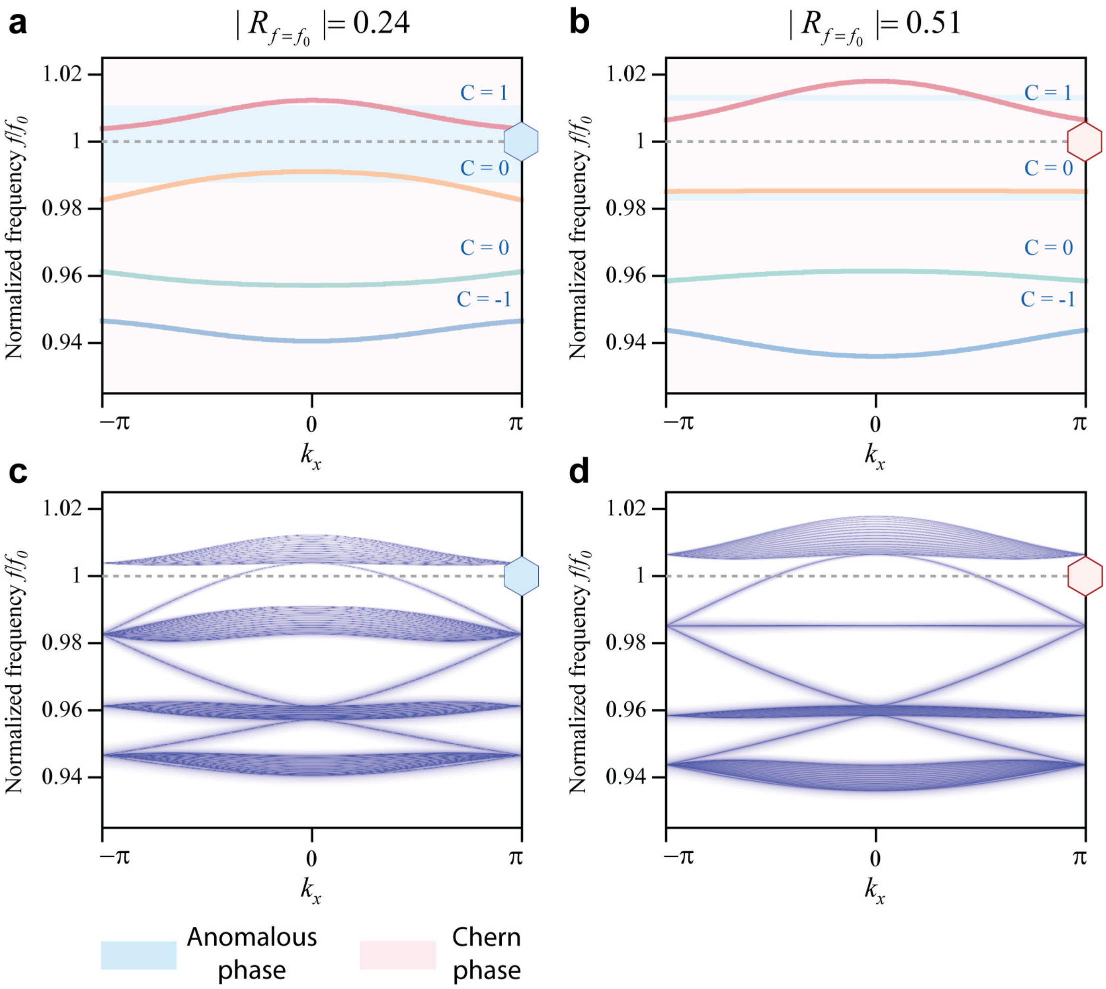

Figure B.1: **Frequency band structures of our networks in the clean limit. a, b,** Bulk frequency band structures for two different reflection coefficients $|R| = 0.24$ (a) and $|R| = 0.51$ (b) that characterize the circulators at frequency $f_0$. We calculate the corresponding Chern number $C$ for each bulk band. Two cases have the same Chern number for any band. We mark the region to blue or red as when we look at the phase delay band structure. **c, d,** Ribbon band structures for $|R| = 0.24$ (c) and $|R| = 0.51$ (d)

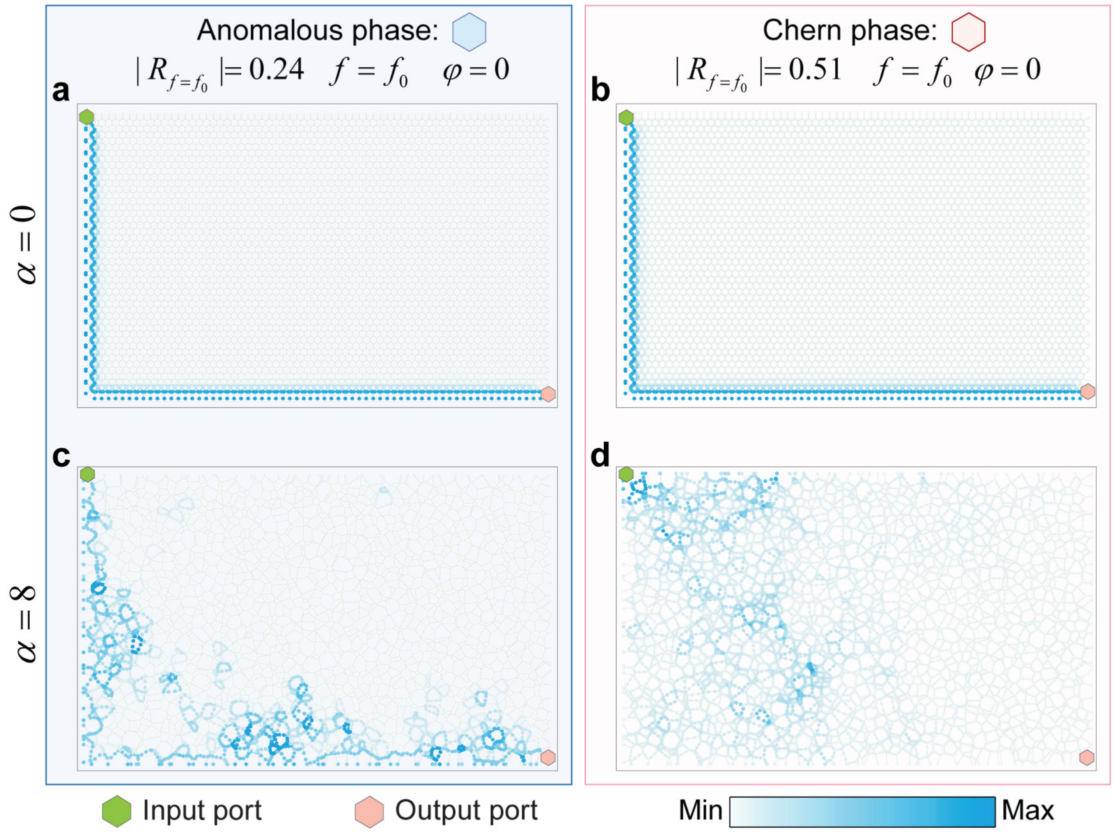

Figure B.2: **Field maps of wave transmissions in the clean limit** ($\alpha = 0$) **and fully amorphous regime** ($\alpha = 8$) **for** $|R| = 0.24$ **and** $|R| = 0.51$ **at** $f = f_0$**.** We can distinguish two networks in the same frequency Chern bands by introducing strong amorphous disorder. Only network built by $|R_{f=f_0}| = 0.24$ survives with a unidirectional edge state, attributed to its anomalous topological phase.

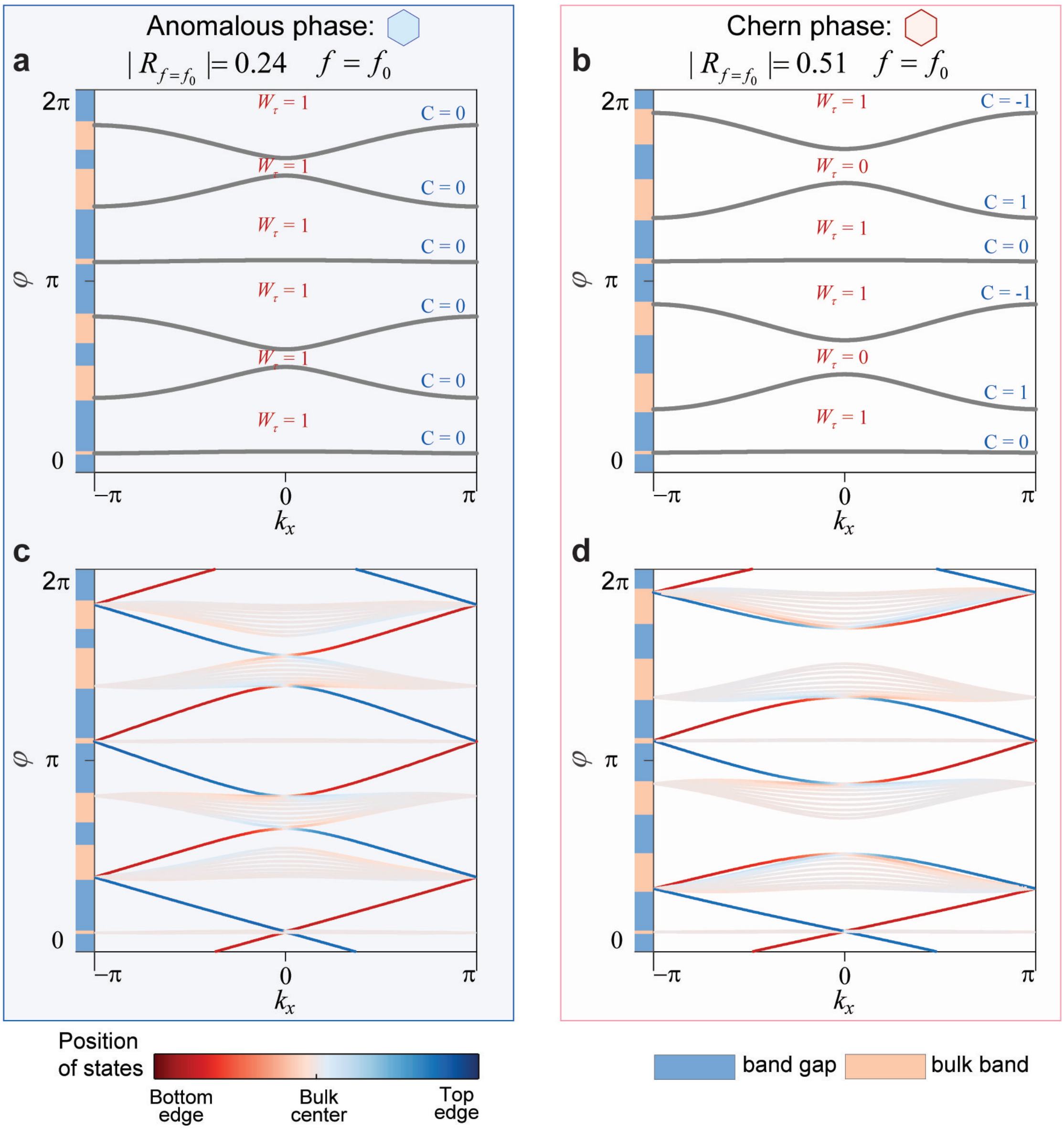

Figure B.3: **Phase-delay spectra for** $|R| = 0.24$ **and** $|R| = 0.51$ **at** $f = f_0$**. a, b,** Bulk phase-delay band structures for two different reflection coefficients $|R| = 0.24$ (a) and $|R| = 0.51$ (b) at frequency $f_0$. We calculate the corresponding Chern number $C$ for each bulk band and gap invariant $W_{gap}$ for each gap. Two cases have the same Chern number for any band. We mark the region to blue or red as when we look at the phase delay band structure. **c, d,** Ribbon phase-delay band structures for $|R| = 0.24$ (c) and $|R| = 0.51$ (d).

# C Unitarity of $S_{probe}$ upon invertible $C_{net} - S_{net}$

Here, we prove the unitarity of the external network scattering matrix $S_{probe}$ defined in Eq. (2.38) when the matrix $C_{net} - S_{net}$ is invertible, as claimed in Sec. 2.3.1. We recall that $S$ is a $(N + N_0) \times (N + N_0)$ unitary matrix, and $C$ is a $N \times N$ unitary matrix. For simplicity, let us call $C_{net}$ as $C$ , $S_{ext}$ as $S_1$, $S_{out}$ as $S_2$, $S_{in}$ as $S_3$, and $S_{net}$ as $S_4$. Therefore, we represent $S$ in the form of block matrix as $S = \begin{bmatrix} S_1 & S_2 \\ S_3 & S_4 \end{bmatrix}$, where $S_1$ and $S_4$ are $N_0 \times N_0$ and $N \times N$ square matrices, respectively.

**Claim:** If $C - S_4$ is invertible, the $N_0 \times N_0$ square matrix $S_{probe} = S_1 + S_2(C - S_4)^{-1} S_3$ is unitary.

**Proof:** From the unitarity of $S$: $S^\dagger S = \mathbb{I}$ ($\mathbb{I}$ is the identity matrix), we get

$$\begin{cases} S_1^\dagger S_1 + S_3^\dagger S_3 = \mathbb{I} \\ S_2^\dagger S_2 + S_4^\dagger S_4 = \mathbb{I} \\ S_1^\dagger S_2 + S_3^\dagger S_4 = 0 \\ S_2^\dagger S_1 + S_4^\dagger S_3 = 0 \end{cases} \tag{C.1}$$

The spirit of the proof is to replace $S_1$ and $S_2$ matrices by $S_3$, $S_4$ and $C$ matrices. When gathering the terms of $S_{probe}^\dagger S_{probe}$, we hope that they finally cancel each other to eventually yield $\mathbb{I}$.

$$
\begin{aligned}
S^\dagger_{probe} S_{probe} &= \left[S_1^\dagger + S_3^\dagger (C^\dagger - S_4^\dagger)^{-1} S_2^\dagger\right] \left[S_1 + S_2 (C - S_4)^{-1} S_3\right] \\
&= S_1^\dagger S_1 + S_1^\dagger S_2 (C - S_4)^{-1} S_3 + S_3^\dagger (C^\dagger - S_4^\dagger)^{-1} S_2^\dagger S_1 \\
&+ S_3^\dagger (C^\dagger - S_4^\dagger)^{-1} S_2^\dagger S_2 (C - S_4)^{-1} S_3 \\
&= \mathbb{1} - S_3^\dagger S_3 - S_3^\dagger S_4 (C - S_4)^{-1} S_3 - S_3^\dagger (C^\dagger - S_4^\dagger)^{-1} S_4^\dagger S_3 \\
&+ S_3^\dagger (C^\dagger - S_4^\dagger)^{-1} (\mathbb{1} - S_4^\dagger S_4)(C - S_4)^{-1} S_3 \\
&= \mathbb{1} - S_3^\dagger \big[\mathbb{1} + S_4 (C - S_4)^{-1} + (C^\dagger - S_4^\dagger)^{-1} S_4^\dagger \\
&- (C^\dagger - S_4^\dagger)^{-1} (\mathbb{1} - S_4^\dagger S_4)(C - S_4)^{-1}\big] S_3 \\
&= \mathbb{1} - S_3^\dagger \big[\mathbb{1} + S_4 (C - S_4)^{-1} + (C^\dagger - S_4^\dagger)^{-1} S_4^\dagger \\
&+ (C^\dagger - S_4^\dagger)^{-1} S_4^\dagger S_4 (C - S4)^{-1} - (C^\dagger - S_4^\dagger)^{-1} (C - S_4)^{-1}\big] S_3 \\
&= \mathbb{1} - S_3^\dagger \Big\{\big[\mathbb{1} + (C^\dagger - S_4^\dagger)^{-1} S_4^\dagger\big]\big[\mathbb{1} + S_4 (C - S_4)^{-1}\big] \\
&- (C^\dagger - S_4^\dagger)^{-1} (C - S_4)^{-1}\Big\} S_3 \\
&= \mathbb{1} - S_3^\dagger \Big\{\big[(C^\dagger - S_4^\dagger)^{-1} C^\dagger\big]\big[C (C - S_4)^{-1}\big] \\
&- (C^\dagger - S_4^\dagger)^{-1} (C - S_4)^{-1}\Big\} S_3 \\
&= \mathbb{1} \\
&\mathit{Q.E.D.}
\end{aligned}
\tag{C.2}
$$

# D Recovery of one $S' \in U(3)$ from 3 by 3 non-negative matrix $E_S$

In the Sec. 6.3.1, we replace a large unitary matrix $S \in U(M)$ to a much smaller one, $S' \in U(3)$. As discussed in Sec. 6.3.1, we first blocklize $S$ into Eq. (6.1), then utilize Landauer-Büttiker formalism and averaged reflections, and finally obtain a non-negative 3×3 matrix $E_S$. This part bridges the gap between $E_S$ and a unitary $3 \times 3$ matrix $S'$.

As the key step of transformation from $S \in U(M)$ to $S' \in U(3)$ in the block-scattering transformations (Sec. 6.3.1), we now elucidate the approach of recovering one corresponding unitary matrix $S'$ from non-negative matrix $E_S$, by keeping the information of nonreciprocity and reflection. As indicated by the recovery of quark-mixing matrix from the experimental data [196, 197], the prerequisite of the $U(3)$ matrix recovery is a double stochastic matrix $A_{DS}$, defined as

$$A_{DS}(i,j) \geq 0, \sum_{i=1}^{3} A_{DS}(i,j) = 1, \sum_{j=1}^{3} A_{DS}(i,j) = 1, \tag{D.1}$$

which forms Birkhoff's polytope. The matrix $A_U$ with $A_U(i,j) := \left|S'(i,j)\right|^2$, defined as the energy part of a unitary matrix $S'$, belongs to the set of double stochastic matrices $\{A_{DS}\}$. As a result, our recovery contains two steps. Firstly, with $E_S$ in Eq. (6.5), we obtain the corresponding $A_{DS}$. Secondly, with the recovery method from CKM parameterization [197], we transform $A_{DS}$ into a desired unitary matrix $S'$.

For the first step, as there are three variables $A_1, A_2$, and $A_3$ in $E_S$ and six equations from double stochastic matrices, we form underdetermined system of equations

$$M\vec{A} = \vec{R}. \tag{D.2}$$

where

$$M = \begin{bmatrix} 1 & 0 & NR_{13}^2 \\ NR_{21}^2 & 1 & 0 \\ 0 & NR_{32}^2 & 1 \\ NR_{21}^2 & 0 & 1 \\ 1 & NR_{32}^2 & 0 \\ 0 & 1 & NR_{13}^2 \end{bmatrix}, \tag{D.3}$$

$$\vec{A} = \begin{bmatrix} A_1^2 \\ A_2^2 \\ A_3^2 \end{bmatrix}, \vec{R} = \begin{bmatrix} 1-R_1^2 \\ 1-R_2^2 \\ 1-R_3^2 \\ 1-R_1^2 \\ 1-R_2^2 \\ 1-R_3^2 \end{bmatrix}. \tag{D.4}$$

To minimize the differences $\min_{\vec{A}} \|M\vec{A} - \vec{R}\|$, we adopt the ordinary least square solution

$$\vec{A}_a = (M^\dagger M)^{-1} M^\dagger \vec{R}. \tag{D.5}$$

With $\vec{A}_a$, we define the energy part of new matrix $E_S|_{\vec{A}=\vec{A}_a}$ as $A_E$

$$A_E(i,j) := |E_S|_{\vec{A}=\vec{A}_a}(i,j)|^2. \tag{D.6}$$

Due to the underdetermined property, $A_E$ in most instances is not a double stochastic matrix, but much close to $A_{DS}$. Therefore, we do perturbations on $A_{ES}$ by a perturbation matrix $\epsilon$, which satisfies $A_E - \epsilon \in \{A_{DS}\}$. To keep the information of nonreciprocity and reflection, perturbation matrix $\epsilon$ should be small enough. As a result, we reshape the goal into a simple optimization problem:

$$\min_{\epsilon} \|\epsilon\|_2 \tag{D.7}$$

$$s.t. \quad A_E - \epsilon \in \{A_{DS}\}. \tag{D.8}$$

With the solved $\epsilon_a$, we reach one $A_{DS}$ corresponding to $E_S$.

In the second step, since CKM matrix $S_{CKM}$ is parameterized by

$$\begin{bmatrix} c_{12} & c_{13}s_{12} & s_{12}s_{13} \\ c_{23}s_{12} & -c_{12}c_{13}c_{23} - e^{i\delta}s_{13}s_{23} & -c_{12}c_{23}c_{13} + e^{i\delta}c_{13}c_{23} \\ s_{12}s_{23} & c_{23}s_{13}e^{i\delta} - c_{12}c_{13}s_{23} & -c_{13}c_{23}e^{i\delta} - c_{12}s_{13}s_{23} \end{bmatrix}, \tag{D.9}$$

where $c_{ij} = \cos\theta_{ij}, s_{ij} = \sin\theta_{ij}$, three angle $\theta_{12}, \theta_{13}, \theta_{23}$ along with one phase $\delta$ are parameters to be determined by $A_{DS}$. For simplicity, we define $a := \sqrt{A_{DS}(1,1)}, b := \sqrt{A_{DS}(1,2)}, c :=$

$\sqrt{A_{DS}(2,1)}$, and $d := \sqrt{A_{DS}(2,2)}$.

After that, the four parameters are recovered by [197]

$$\cos\theta_{12} = a \tag{D.10}$$

$$\cos\theta_{13} = \frac{b}{\sqrt{1-a^2}} \tag{D.11}$$

$$\cos\theta_{23} = \frac{c}{\sqrt{1-a^2}} \tag{D.12}$$

and

$$\cos\delta = \frac{-(1-a^2)^2(1-d^2)}{2abc\sqrt{1-a^2-b^2}\sqrt{1-a^2-c^2}} + \frac{(1-a^2)(b^2+c^2) - b^2c^2(1+a^2)}{2abc\sqrt{1-a^2-b^2}\sqrt{1-a^2-c^2}}. \tag{D.13}$$

In a few cases, $\cos\delta > 1 / < -1$, we can choose $\delta = 0/\pi$ solution. In practical, the averaged perturbation of $\|\epsilon\|_2$ is less than 0.05.

# Bibliography

1. Kosterlitz, J. M. & Thouless, D. J. Ordering, metastability and phase transitions in two-dimensional systems. *Journal of Physics C: Solid State Physics* **6,** 1181. https://dx.doi.org/10.1088/0022-3719/6/7/010 (Apr. 1973).
2. Klitzing, K. v., Dorda, G. & Pepper, M. New Method for High-Accuracy Determination of the Fine-Structure Constant Based on Quantized Hall Resistance. *Physical Review Letters* **45.** Publisher: American Physical Society, 494–497. https://link.aps.org/doi/10.1103/PhysRevLett.45.494 (Aug. 11, 1980).
3. Stormer, H. L., Tsui, D. C. & Gossard, A. C. The fractional quantum Hall effect. *Reviews of Modern Physics* **71.** Publisher: American Physical Society, S298–S305. https://link.aps.org/doi/10.1103/RevModPhys.71.S298 (Mar. 1, 1999).
4. Hasan, M. Z. & Kane, C. L. *Colloquium* : Topological insulators. *Reviews of Modern Physics* **82,** 3045–3067. https://link.aps.org/doi/10.1103/RevModPhys.82.3045 (Nov. 8, 2010).
5. Moore, J. E. The birth of topological insulators. *Nature* **464.** Number: 7286 Publisher: Nature Publishing Group, 194–198. https://www.nature.com/articles/nature08916 (Mar. 2010).
6. Lu, L., Joannopoulos, J. D. & Soljačić, M. Topological photonics. *Nature Photonics* **8,** 821–829. http://www.nature.com/articles/nphoton.2014.248 (Nov. 2014).
7. Ozawa, T. *et al.* Topological photonics. *Reviews of Modern Physics* **91,** 015006. https://link.aps.org/doi/10.1103/RevModPhys.91.015006 (Mar. 25, 2019).
8. Thouless, D. J., Kohmoto, M., Nightingale, M. P. & den Nijs, M. Quantized Hall Conductance in a Two-Dimensional Periodic Potential. *Physical Review Letters* **49,** 405–408. https://link.aps.org/doi/10.1103/PhysRevLett.49.405 (Aug. 9, 1982).
9. Laughlin, R. B. Quantized Hall conductivity in two dimensions. *Physical Review B* **23,** 5632–5633. https://link.aps.org/doi/10.1103/PhysRevB.23.5632 (May 15, 1981).
10. Haldane, F. D. M. & Raghu, S. Possible Realization of Directional Optical Waveguides in Photonic Crystals with Broken Time-Reversal Symmetry. *Physical Review Letters* **100,** 013904. https://link.aps.org/doi/10.1103/PhysRevLett.100.013904 (Jan. 10, 2008).

11. Halperin, B. I. Quantized Hall conductance, current-carrying edge states, and the existence of extended states in a two-dimensional disordered potential. *Physical Review B* **25,** 2185–2190. https://link.aps.org/doi/10.1103/PhysRevB.25.2185 (Feb. 15, 1982).

12. Raghu, S. & Haldane, F. D. M. Analogs of quantum-Hall-effect edge states in photonic crystals. *Physical Review A* **78,** 033834. https://link.aps.org/doi/10.1103/PhysRevA.78.033834 (Sept. 23, 2008).

13. Wang, Z., Chong, Y., Joannopoulos, J. D. & Soljačić, M. Observation of unidirectional backscattering-immune topological electromagnetic states. *Nature* **461,** 772–775. http://www.nature.com/articles/nature08293 (Oct. 2009).

14. Hafezi, M., Demler, E. A., Lukin, M. D. & Taylor, J. M. Robust optical delay lines with topological protection. *Nature Physics* **7,** 907–912. http://www.nature.com/articles/nphys2063 (Nov. 2011).

15. Hafezi, M., Mittal, S., Fan, J., Migdall, A. & Taylor, J. M. Imaging topological edge states in silicon photonics. *Nature Photonics* **7,** 1001–1005. http://www.nature.com/articles/nphoton.2013.274 (Dec. 2013).

16. Hafezi, M. Measuring Topological Invariants in Photonic Systems. *Physical Review Letters* **112,** 210405. https://link.aps.org/doi/10.1103/PhysRevLett.112.210405 (May 29, 2014).

17. Bahari, B. *et al.* Nonreciprocal lasing in topological cavities of arbitrary geometries. *Science* **358,** 636–640. https://www.sciencemag.org/lookup/doi/10.1126/science.aao4551 (Nov. 3, 2017).

18. Liu, G.-G. *et al.* Topological Chern vectors in three-dimensional photonic crystals. *Nature* **609,** 925–930. https://www.nature.com/articles/s41586-022-05077-2 (Sept. 29, 2022).

19. Zhang, Z., Delplace, P. & Fleury, R. Superior robustness of anomalous non-reciprocal topological edge states. *Nature* **598,** 293–297. https://www.nature.com/articles/s41586-021-03868-7 (Oct. 14, 2021).

20. Zhang, Z., Delplace, P. & Fleury, R. Anomalous topological waves in strongly amorphous scattering networks. *Science Advances* **9,** eadg3186. https://www.science.org/doi/10.1126/sciadv.adg3186 (Mar. 22, 2023).

21. Qin, H., Zhang, Z., Chen, Q. & Fleury, R. *Anomalous Floquet Topological Disclination States* Apr. 6, 2023. arXiv: 2304.03206[cond-mat,physics:physics]. http://arxiv.org/abs/2304.03206.

22. Chen, Q. *et al. Anomalous and Chern topological waves in hyperbolic networks* Oct. 5, 2023. https://www.researchsquare.com/article/rs-3286219/v1.

23. Ding, Y. *et al.* Experimental Demonstration of Acoustic Chern Insulators. *Physical Review Letters* **122,** 014302. https://link.aps.org/doi/10.1103/PhysRevLett.122.014302 (Jan. 9, 2019).

24. Süsstrunk, R. & Huber, S. D. Observation of phononic helical edge states in a mechanical topological insulator. *Science* **349,** 47–50. https://www.sciencemag.org/lookup/doi/10.1126/science.aab0239 (July 3, 2015).
25. Peri, V. *et al.* Experimental characterization of fragile topology in an acoustic metamaterial. *Science* **367,** 797–800. https://www.sciencemag.org/lookup/doi/10.1126/science.aaz7654 (Feb. 14, 2020).
26. Zangeneh-Nejad, F. & Fleury, R. Disorder-Induced Signal Filtering with Topological Metamaterials. *Advanced Materials* **32,** 2001034. https://onlinelibrary.wiley.com/doi/abs/10.1002/adma.202001034 (July 2020).
27. Perrot, M., Delplace, P. & Venaille, A. Topological transition in stratified fluids. *Nature Physics* **15,** 781–784. http://www.nature.com/articles/s41567-019-0561-1 (Aug. 2019).
28. Delplace, P., Marston, J. B. & Venaille, A. Topological origin of equatorial waves. *Science* **358,** 1075–1077. https://www.science.org/doi/10.1126/science.aan8819 (Nov. 24, 2017).
29. Delplace, P. & Venaille, A. *From the geometry of Foucault pendulum to the topology of planetary waves* June 8, 2020. arXiv: 2006.08488[astro-ph,physics:cond-mat,physics:physics]. http://arxiv.org/abs/2006.08488.
30. Altland, A., Kamenev, A. & Tian, C. Anderson Localization from the Replica Formalism. *Physical Review Letters* **95,** 206601. https://link.aps.org/doi/10.1103/PhysRevLett.95.206601 (Nov. 7, 2005).
31. Kitaev, A. *Periodic table for topological insulators and superconductors* in *AIP Conference Proceedings* (2009), 22–30. arXiv: 0901.2686[cond-mat,physics:hep-th,physics:math-ph]. http://arxiv.org/abs/0901.2686.
32. Kane, C. L. & Mele, E. J. Quantum Spin Hall Effect in Graphene. *Physical Review Letters* **95,** 226801. https://link.aps.org/doi/10.1103/PhysRevLett.95.226801 (Nov. 23, 2005).
33. Chiu, C.-K., Teo, J. C. Y., Schnyder, A. P. & Ryu, S. Classification of topological quantum matter with symmetries. *Reviews of Modern Physics* **88,** 035005. https://link.aps.org/doi/10.1103/RevModPhys.88.035005 (Aug. 31, 2016).
34. Fu, L. Topological Crystalline Insulators. *Physical Review Letters* **106.** Publisher: American Physical Society, 106802. https://link.aps.org/doi/10.1103/PhysRevLett.106.106802 (Mar. 8, 2011).
35. Wu, L.-H. & Hu, X. Scheme for Achieving a Topological Photonic Crystal by Using Dielectric Material. *Physical Review Letters* **114,** 223901. https://link.aps.org/doi/10.1103/PhysRevLett.114.223901 (June 3, 2015).
36. Khanikaev, A. B., Fleury, R., Mousavi, S. H. & Alù, A. Topologically robust sound propagation in an angular-momentum-biased graphene-like resonator lattice. *Nature Communications* **6,** 8260. https://www.nature.com/articles/ncomms9260 (Oct. 6, 2015).
37. Cha, J., Kim, K. W. & Daraio, C. Experimental realization of on-chip topological nanoelectromechanical metamaterials. *Nature* **564,** 229–233. http://www.nature.com/articles/s41586-018-0764-0 (Dec. 2018).

38. Fruchart, M. Complex classes of periodically driven topological lattice systems. *Physical Review B* **93,** 115429. https://link.aps.org/doi/10.1103/PhysRevB.93.115429 (Mar. 21, 2016).
39. Roy, R. & Harper, F. Periodic table for Floquet topological insulators. *Physical Review B* **96.** Publisher: American Physical Society, 155118. https://link.aps.org/doi/10.1103/PhysRevB.96.155118 (Oct. 13, 2017).
40. Rudner, M. S. & Lindner, N. H. *The Floquet Engineer's Handbook* arXiv.org. https://arxiv.org/abs/2003.08252v2.
41. Niu, Q., Thouless, D. J. & Wu, Y.-S. Quantized Hall conductance as a topological invariant. *Physical Review B* **31,** 3372–3377. https://link.aps.org/doi/10.1103/PhysRevB.31.3372 (Mar. 15, 1985).
42. Haldane, F. D. M. Model for a Quantum Hall Effect without Landau Levels: Condensed-Matter Realization of the "Parity Anomaly". *Physical Review Letters* **61,** 2015–2018. https://link.aps.org/doi/10.1103/PhysRevLett.61.2015 (Oct. 31, 1988).
43. Banerjee, D., Souslov, A., Abanov, A. G. & Vitelli, V. Odd viscosity in chiral active fluids. *Nature Communications* **8,** 1573. http://www.nature.com/articles/s41467-017-01378-7 (Dec. 2017).
44. Souslov, A., van Zuiden, B. C., Bartolo, D. & Vitelli, V. Topological sound in active-liquid metamaterials. *Nature Physics* **13,** 1091–1094. http://www.nature.com/articles/nphys4193 (Nov. 2017).
45. Mitchell, N. P., Nash, L. M., Hexner, D., Turner, A. M. & Irvine, W. T. M. Amorphous topological insulators constructed from random point sets. *Nature Physics* **14,** 380–385. http://www.nature.com/articles/s41567-017-0024-5 (Apr. 2018).
46. Hofmann, T., Helbig, T., Lee, C. H., Greiter, M. & Thomale, R. Chiral Voltage Propagation and Calibration in a Topolectrical Chern Circuit. *Physical Review Letters* **122,** 247702. https://link.aps.org/doi/10.1103/PhysRevLett.122.247702 (June 21, 2019).
47. Nuckolls, K. P. *et al.* Strongly correlated Chern insulators in magic-angle twisted bilayer graphene. *Nature* **588,** 610–615. http://www.nature.com/articles/s41586-020-3028-8 (Dec. 24, 2020).
48. Liu, G.-G. *et al.* Observation of an unpaired photonic Dirac point. *Nature Communications* **11,** 1873. http://www.nature.com/articles/s41467-020-15801-z (Dec. 2020).
49. Kong, J. A. *ELECTROMAGNETIC WAVE THEORY* ISBN: 0-471-52214-7 (Wiley-Interscience, Oct. 1, 1990).
50. McGinley, M. & Cooper, N. R. Fragility of time-reversal symmetry protected topological phases. *Nature Physics* **16,** 1181–1183. http://www.nature.com/articles/s41567-020-0956-z (Dec. 2020).
51. Nassar, H. *et al.* Nonreciprocity in acoustic and elastic materials. *Nature Reviews Materials.* http://www.nature.com/articles/s41578-020-0206-0 (July 6, 2020).

52. Tokura, Y., Yasuda, K. & Tsukazaki, A. Magnetic topological insulators. *Nature Reviews Physics* **1.** Number: 2 Publisher: Nature Publishing Group, 126–143. https://www.nature.com/articles/s42254-018-0011-5 (Feb. 2019).

53. Xue, H., Yang, Y. & Zhang, B. Topological acoustics. *Nature Reviews Materials* **7.** Number: 12 Publisher: Nature Publishing Group, 974–990. https://www.nature.com/articles/s41578-022-00465-6 (Dec. 2022).

54. Huckestein, B. Scaling theory of the integer quantum Hall effect. *Reviews of Modern Physics* **67.** Publisher: American Physical Society, 357–396. https://link.aps.org/doi/10.1103/RevModPhys.67.357 (Apr. 1, 1995).

55. Bellissard, J., van Elst, A. & Schulz-Baldes, H. The Non-Commutative Geometry of the Quantum Hall Effect. *Journal of Mathematical Physics* **35,** 5373–5451. arXiv: cond-mat/9411052. http://arxiv.org/abs/cond-mat/9411052 (Oct. 1, 1994).

56. Prodan, E. & Schulz-Baldes, H. Non-commutative odd Chern numbers and topological phases of disordered chiral systems. *Journal of Functional Analysis* **271,** 1150–1176. https://www.sciencedirect.com/science/article/pii/S0022123616301380 (Sept. 1, 2016).

57. Bourne, C. & Prodan, E. Non-commutative Chern numbers for generic aperiodic discrete systems. *Journal of Physics A: Mathematical and Theoretical* **51,** 235202. https://iopscience.iop.org/article/10.1088/1751-8121/aac093 (June 8, 2018).

58. Anderson, P. W. Absence of Diffusion in Certain Random Lattices. *Physical Review* **109,** 1492–1505. https://link.aps.org/doi/10.1103/PhysRev.109.1492 (Mar. 1, 1958).

59. Weidemann, S., Kremer, M., Longhi, S. & Szameit, A. Coexistence of dynamical delocalization and spectral localization through stochastic dissipation. *Nature Photonics* **15.** Publisher: Nature Publishing Group, 576–581. https://www.nature.com/articles/s41566-021-00823-w (Aug. 2021).

60. Rotter, S. & Gigan, S. Light fields in complex media: Mesoscopic scattering meets wave control. *Reviews of Modern Physics* **89,** 015005. https://link.aps.org/doi/10.1103/RevModPhys.89.015005 (Mar. 2, 2017).

61. Vynck, K. *et al. Light in correlated disordered media* June 25, 2021. arXiv: 2106.13892[cond-mat,physics:physics]. http://arxiv.org/abs/2106.13892.

62. Groth, C. W., Wimmer, M., Akhmerov, A. R., Tworzydło, J. & Beenakker, C. W. J. Theory of the topological Anderson insulator. *Physical Review Letters* **103,** 196805. arXiv: 0908.0881[cond-mat]. http://arxiv.org/abs/0908.0881 (Nov. 6, 2009).

63. Jiang, H., Wang, L., Sun, Q.-f. & Xie, X. C. Numerical study of the topological Anderson insulator in HgTe/CdTe quantum wells. *Physical Review B* **80.** Publisher: American Physical Society, 165316. https://link.aps.org/doi/10.1103/PhysRevB.80.165316 (Oct. 14, 2009).

64. Prodan, E. Disordered Topological Insulators: A Non-Commutative Geometry Perspective. *Journal of Physics A: Mathematical and Theoretical* **44,** 113001. arXiv: 1010.0595[cond-mat,physics:math-ph]. http://arxiv.org/abs/1010.0595 (Mar. 18, 2011).

65. Song, J., Liu, H., Jiang, H., Sun, Q.-f. & Xie, X. C. Dependence of topological Anderson insulator on the type of disorder. *Physical Review B* **85.** Publisher: American Physical Society, 195125. https://link.aps.org/doi/10.1103/PhysRevB.85.195125 (May 11, 2012).
66. Liu, G.-G. *et al.* Topological Anderson Insulator in Disordered Photonic Crystals. *Physical Review Letters* **125,** 133603. https://link.aps.org/doi/10.1103/PhysRevLett.125.133603 (Sept. 24, 2020).
67. Laughlin, R. B. Levitation of Extended-State Bands in a Strong Magnetic Field. *Physical Review Letters* **52,** 2304–2304. https://link.aps.org/doi/10.1103/PhysRevLett.52.2304 (June 18, 1984).
68. Levine, H., Libby, S. B. & Pruisken, A. M. M. Electron Delocalization by a Magnetic Field in Two Dimensions. *Physical Review Letters* **51,** 1915–1918. https://link.aps.org/doi/10.1103/PhysRevLett.51.1915 (Nov. 14, 1983).
69. Melcer, R. A. *et al.* Heat conductance of the quantum Hall bulk. *Nature* **625.** Number: 7995 Publisher: Nature Publishing Group, 489–493. https://www.nature.com/articles/s41586-023-06858-z (Jan. 2024).
70. Mott, N. The mobility edge since 1967. *Journal of Physics C: Solid State Physics* **20,** 3075. https://dx.doi.org/10.1088/0022-3719/20/21/008 (July 1987).
71. Liu, H., Fulga, I. C. & Asbóth, J. K. Anomalous levitation and annihilation in Floquet topological insulators. *Physical Review Research* **2,** 022048. https://link.aps.org/doi/10.1103/PhysRevResearch.2.022048 (June 4, 2020).
72. Trugman, S. A. Localization, percolation, and the quantum Hall effect. *Physical Review B* **27,** 7539–7546. https://link.aps.org/doi/10.1103/PhysRevB.27.7539 (June 15, 1983).
73. Pruisken, A. On localization in the theory of the quantized hall effect: A two-dimensional realization of the -vacuum. *Nuclear Physics B* **235,** 277–298. https://linkinghub.elsevier.com/retrieve/pii/0550321384901019 (June 1984).
74. Ostrovsky, P. M., Gornyi, I. V. & Mirlin, A. D. Electron transport in disordered graphene. *Physical Review B* **74,** 235443. https://link.aps.org/doi/10.1103/PhysRevB.74.235443 (Dec. 28, 2006).
75. Schuessler, A., Ostrovsky, P. M., Gornyi, I. V. & Mirlin, A. D. Analytic theory of ballistic transport in disordered graphene. *Physical Review B* **79.** Publisher: American Physical Society, 075405. https://link.aps.org/doi/10.1103/PhysRevB.79.075405 (Feb. 3, 2009).
76. Zhu, Q., Wu, P., Bhatt, R. N. & Wan, X. Localization-length exponent in two models of quantum Hall plateau transitions. *Physical Review B* **99.** Publisher: American Physical Society, 024205. https://link.aps.org/doi/10.1103/PhysRevB.99.024205 (Jan. 29, 2019).
77. Zirnbauer, M. R. Toward a theory of the integer quantum Hall transition: Continuum limit of the Chalker–Coddington model. *Journal of Mathematical Physics* **38,** 2007–2036. https://pubs.aip.org/jmp/article/38/4/2007/229520/Toward-a-theory-of-the-integer-quantum-Hall (Apr. 1, 1997).

78. Sbierski, B., Dresselhaus, E. J., Moore, J. E. & Gruzberg, I. A. Criticality of Two-Dimensional Disordered Dirac Fermions in the Unitary Class and Universality of the Integer Quantum Hall Transition. *Physical Review Letters* **126.** Publisher: American Physical Society, 076801. https://link.aps.org/doi/10.1103/PhysRevLett.126.076801 (Feb. 18, 2021).

79. Ludwig, A. W. W., Fisher, M. P. A., Shankar, R. & Grinstein, G. Integer quantum Hall transition: An alternative approach and exact results. *Physical Review B* **50,** 7526–7552. https://link.aps.org/doi/10.1103/PhysRevB.50.7526 (Sept. 15, 1994).

80. Zhang, Y.-Y., Chu, R.-L., Zhang, F.-C. & Shen, S.-Q. Localization and mobility gap in the topological Anderson insulator. *Physical Review B* **85.** Publisher: American Physical Society, 035107. https://link.aps.org/doi/10.1103/PhysRevB.85.035107 (Jan. 12, 2012).

81. Puschmann, M., Cain, P., Schreiber, M. & Vojta, T. Integer quantum Hall transition on a tight-binding lattice. *Physical Review B* **99.** Publisher: American Physical Society, 121301. https://link.aps.org/doi/10.1103/PhysRevB.99.121301 (Mar. 19, 2019).

82. Corbae, P., Hannukainen, J. D., Marsal, Q., Muñoz-Segovia, D. & Grushin, A. G. Amorphous topological matter: Theory and experiment. *Europhysics Letters* **142,** 16001. https://iopscience.iop.org/article/10.1209/0295-5075/acc2e2 (Apr. 1, 2023).

83. Bera, S., Dieplinger, J. & Nayak, N. P. *Quantum Hall criticality in an amorphous Chern insulator* Jan. 22, 2024. arXiv: 2401.11855[cond-mat]. http://arxiv.org/abs/2401.11855.

84. Chalker, J. T. & Coddington, P. D. Percolation, quantum tunnelling and the integer Hall effect. *Journal of Physics C: Solid State Physics* **21,** 2665–2679. https://iopscience.iop.org/article/10.1088/0022-3719/21/14/008 (May 20, 1988).

85. Fertig, H. A. & Halperin, B. I. Transmission coefficient of an electron through a saddle-point potential in a magnetic field. *Physical Review B* **36,** 7969–7976. https://link.aps.org/doi/10.1103/PhysRevB.36.7969 (Nov. 15, 1987).

86. Klesse, R. & Metzler, M. Universal Multifractality in Quantum Hall Systems with Long-Range Disorder Potential. *Europhysics Letters (EPL)* **32,** 229–234. https://iopscience.iop.org/article/10.1209/0295-5075/32/3/007 (Oct. 20, 1995).

87. Ho, C.-M. & Chalker, J. T. Models for the integer quantum Hall effect: The network model, the Dirac equation, and a tight-binding Hamiltonian. *Physical Review B* **54,** 8708–8713. https://link.aps.org/doi/10.1103/PhysRevB.54.8708 (Sept. 15, 1996).

88. Klesse, R. & Metzler, M. Spectral Compressibility at the Metal-Insulator Transition of the Quantum Hall Effect. *Physical Review Letters* **79,** 721–724. https://link.aps.org/doi/10.1103/PhysRevLett.79.721 (July 28, 1997).

89. Shapiro, B. Renormalization-Group Transformation for the Anderson Transition. *Physical Review Letters* **48,** 823–825. https://link.aps.org/doi/10.1103/PhysRevLett.48.823 (Mar. 22, 1982).

90. Huckestein, B. Scaling and Universality in the Integer Quantum Hall Effect. *Europhysics Letters* **20,** 451. https://dx.doi.org/10.1209/0295-5075/20/5/012 (Nov. 1992).

91. Galstyan, A. G. & Raikh, M. E. Localization and conductance fluctuations in the integer quantum Hall effect: Real-space renormalization-group approach. *Physical Review B* **56,** 1422–1429. https://link.aps.org/doi/10.1103/PhysRevB.56.1422 (July 15, 1997).

92. Janssen, M., Merkt, R. & Weymer, A. S-matrix network models for coherent waves in random media: construction and renormalization. *Annalen der Physik* **510,** 353–362. http://arxiv.org/abs/cond-mat/9810148 (Nov. 1998).

93. Metzler, M. The Influence of Percolation in the generalized Chalker-Coddington Model. *Journal of the Physical Society of Japan* **68,** 144–150. arXiv: cond-mat/9809285. http://arxiv.org/abs/cond-mat/9809285 (Jan. 15, 1999).

94. Cain, P., E. Raikh, M. & A. Römer, R. Real-Space Renormalization Group Approach to the Quantum Hall Transition. *Journal of the Physical Society of Japan* **72,** 135–136. http://journals.jps.jp/doi/10.1143/JPSJS.72SA.135 (Suppl.A Jan. 3, 2003).

95. Kramer, B., Ohtsuki, T. & Kettemann, S. Random network models and quantum phase transitions in two dimensions. *Physics Reports* **417,** 211–342. https://www.sciencedirect.com/science/article/pii/S0370157305002851 (Oct. 1, 2005).

96. Li, W., Csáthy, G. A., Tsui, D. C., Pfeiffer, L. N. & West, K. W. Scaling and Universality of Integer Quantum Hall Plateau-to-Plateau Transitions. *Physical Review Letters* **94,** 206807. https://link.aps.org/doi/10.1103/PhysRevLett.94.206807 (May 26, 2005).

97. Slevin, K. & Ohtsuki, T. Critical exponent for the quantum Hall transition. *Physical Review B* **80,** 041304. https://link.aps.org/doi/10.1103/PhysRevB.80.041304 (July 9, 2009).

98. Amado, M., Malyshev, A. V., Sedrakyan, A. & Domínguez-Adame, F. Numerical Study of the Localization Length Critical Index in a Network Model of Plateau-Plateau Transitions in the Quantum Hall Effect. *Physical Review Letters* **107,** 066402. https://link.aps.org/doi/10.1103/PhysRevLett.107.066402 (Aug. 3, 2011).

99. Obuse, H., Subramaniam, A. R., Furusaki, A., Gruzberg, I. A. & Ludwig, A. W. W. Boundary Multifractality at the Integer Quantum Hall Plateau Transition: Implications for the Critical Theory. *Physical Review Letters* **101.** Publisher: American Physical Society, 116802. https://link.aps.org/doi/10.1103/PhysRevLett.101.116802 (Sept. 8, 2008).

100. Obuse, H., Ryu, S., Furusaki, A. & Mudry, C. Spin-directed network model for the surface states of weak three-dimensional Z 2 topological insulators. *Physical Review B* **89,** 155315. https://link.aps.org/doi/10.1103/PhysRevB.89.155315 (Apr. 21, 2014).

101. Merkt, R., Janssen, M. & Huckestein, B. Network model for a two-dimensional disordered electron system with spin-orbit scattering. *Physical Review B* **58,** 4394–4405. https://link.aps.org/doi/10.1103/PhysRevB.58.4394 (Aug. 15, 1998).

102. Onoda, M., Avishai, Y. & Nagaosa, N. Localization in a Quantum Spin Hall System. *Physical Review Letters* **98.** Publisher: American Physical Society, 076802. https://link.aps.org/doi/10.1103/PhysRevLett.98.076802 (Feb. 12, 2007).

103. Obuse, H., Furusaki, A., Ryu, S. & Mudry, C. Two-dimensional spin-filtered chiral network model for the Z 2 quantum spin-Hall effect. *Physical Review B* **76,** 075301. https://link.aps.org/doi/10.1103/PhysRevB.76.075301 (Aug. 1, 2007).

104. Liu, S., Ohtsuki, T. & Shindou, R. Effect of Disorder in a Three-Dimensional Layered Chern Insulator. *Physical Review Letters* **116,** 066401. https://link.aps.org/doi/10.1103/PhysRevLett.116.066401 (Feb. 10, 2016).

105. Son, J. H. & Raghu, S. 3D Network Model for Strong Topological Insulator Transitions. *Physical Review B* **104,** 125142. arXiv: 2008.03315[cond-mat]. http://arxiv.org/abs/2008.03315 (Sept. 27, 2021).

106. Luo, X., Xiao, Z., Kawabata, K., Ohtsuki, T. & Shindou, R. Unifying the Anderson transitions in Hermitian and non-Hermitian systems. *Physical Review Research* **4,** L022035. https://link.aps.org/doi/10.1103/PhysRevResearch.4.L022035 (May 11, 2022).

107. Xiao, Z., Kawabata, K., Luo, X., Ohtsuki, T. & Shindou, R. Anisotropic Topological Anderson Transitions in Chiral Symmetry Classes. *Physical Review Letters* **131,** 056301. https://link.aps.org/doi/10.1103/PhysRevLett.131.056301 (Aug. 1, 2023).

108. Wang, F.-J. *et al. Anderson Critical Metal Phase in Trivial States Protected by $C_{2z}T$ Symmetry on Average* June 7, 2023. arXiv: 2306.04683[cond-mat]. http://arxiv.org/abs/2306.04683.

109. Gruzberg, I. A., Klümper, A., Nuding, W. & Sedrakyan, A. Geometrically disordered network models, quenched quantum gravity, and critical behavior at quantum Hall plateau transitions. *Physical Review B* **95,** 125414. https://link.aps.org/doi/10.1103/PhysRevB.95.125414 (Mar. 10, 2017).

110. Klümper, A., Nuding, W. & Sedrakyan, A. Random network models with variable disorder of geometry. *Physical Review B* **100.** Publisher: American Physical Society, 140201. https://link.aps.org/doi/10.1103/PhysRevB.100.140201 (Oct. 2, 2019).

111. Rudner, M. S. & Lindner, N. H. Band structure engineering and non-equilibrium dynamics in Floquet topological insulators. *Nature Reviews Physics* **2,** 229–244. http://www.nature.com/articles/s42254-020-0170-z (May 2020).

112. Delplace, P., Fruchart, M. & Tauber, C. Phase rotation symmetry and the topology of oriented scattering networks. *Physical Review B* **95,** 205413. http://link.aps.org/doi/10.1103/PhysRevB.95.205413 (May 10, 2017).

113. Oka, T. & Aoki, H. Photovoltaic Hall effect in graphene. *Physical Review B* **79.** Publisher: American Physical Society, 081406. https://link.aps.org/doi/10.1103/PhysRevB.79.081406 (Feb. 23, 2009).

114. Kitagawa, T., Oka, T., Brataas, A., Fu, L. & Demler, E. Transport properties of nonequilibrium systems under the application of light: Photoinduced quantum Hall insulators without Landau levels. *Physical Review B* **84.** Publisher: American Physical Society, 235108. https://link.aps.org/doi/10.1103/PhysRevB.84.235108 (Dec. 1, 2011).

115. Lindner, N. H., Refael, G. & Galitski, V. Floquet topological insulator in semiconductor quantum wells. *Nature Physics* **7,** 490–495. http://www.nature.com/articles/nphys1926 (June 2011).

116. Yao, W., MacDonald, A. H. & Niu, Q. Optical Control of Topological Quantum Transport in Semiconductors. *Physical Review Letters* **99.** Publisher: American Physical Society, 047401. https://link.aps.org/doi/10.1103/PhysRevLett.99.047401 (July 24, 2007).

117. Wang, Y. H., Steinberg, H., Jarillo-Herrero, P. & Gedik, N. Observation of Floquet-Bloch States on the Surface of a Topological Insulator. *Science* **342.** Publisher: American Association for the Advancement of Science, 453–457. https://www.science.org/doi/10.1126/science.1239834 (Oct. 25, 2013).

118. Jotzu, G. *et al.* Experimental realization of the topological Haldane model with ultracold fermions. *Nature* **515,** 237–240. http://www.nature.com/articles/nature13915 (Nov. 13, 2014).

119. McIver, J. W. *et al.* Light-induced anomalous Hall effect in graphene. *Nature Physics* **16,** 38–41. https://www.nature.com/articles/s41567-019-0698-y (Jan. 2020).

120. Karzig, T., Bardyn, C.-E., Lindner, N. H. & Refael, G. Topological Polaritons. *Physical Review X* **5,** 031001. https://link.aps.org/doi/10.1103/PhysRevX.5.031001 (July 1, 2015).

121. Fang, K., Yu, Z. & Fan, S. Realizing effective magnetic field for photons by controlling the phase of dynamic modulation. *Nature Photonics* **6,** 782–787. http://www.nature.com/articles/nphoton.2012.236 (Nov. 2012).

122. Kitagawa, T., Berg, E., Rudner, M. & Demler, E. Topological characterization of periodically driven quantum systems. *Physical Review B* **82,** 235114. https://link.aps.org/doi/10.1103/PhysRevB.82.235114 (Dec. 10, 2010).

123. Rudner, M. S., Lindner, N. H., Berg, E. & Levin, M. Anomalous Edge States and the Bulk-Edge Correspondence for Periodically Driven Two-Dimensional Systems. *Physical Review X* **3,** 031005. https://link.aps.org/doi/10.1103/PhysRevX.3.031005 (July 23, 2013).

124. Nathan, F. & Rudner, M. S. Topological singularities and the general classification of Floquet–Bloch systems. *New Journal of Physics* **17.** Publisher: IOP Publishing, 125014. https://dx.doi.org/10.1088/1367-2630/17/12/125014 (Dec. 2015).

125. Carpentier, D., Delplace, P., Fruchart, M. & Gawędzki, K. Topological Index for Periodically Driven Time-Reversal Invariant 2D Systems. *Physical Review Letters* **114,** 106806. https://link.aps.org/doi/10.1103/PhysRevLett.114.106806 (Mar. 10, 2015).

126. Roy, R. & Harper, F. Floquet topological phases with symmetry in all dimensions. *Physical Review B* **95.** Publisher: American Physical Society, 195128. https://link.aps.org/doi/10.1103/PhysRevB.95.195128 (May 12, 2017).

127. Yao, S., Yan, Z. & Wang, Z. Topological invariants of Floquet systems: General formulation, special properties, and Floquet topological defects. *Physical Review B* **96.** Publisher: American Physical Society, 195303. https://link.aps.org/doi/10.1103/PhysRevB.96.195303 (Nov. 10, 2017).

128. Gómez-León, A. & Platero, G. Floquet-Bloch Theory and Topology in Periodically Driven Lattices. *Physical Review Letters* **110,** 200403. https://link.aps.org/doi/10.1103/PhysRevLett.110.200403 (May 14, 2013).

129. Asbóth, J. K., Tarasinski, B. & Delplace, P. Chiral symmetry and bulk-boundary correspondence in periodically driven one-dimensional systems. *Physical Review B* **90.** Publisher: American Physical Society, 125143. https://link.aps.org/doi/10.1103/PhysRevB.90.125143 (Sept. 24, 2014).

130. Graf, G. M. & Tauber, C. Bulk–Edge Correspondence for Two-Dimensional Floquet Topological Insulators. *Annales Henri Poincaré* **19,** 709–741. http://link.springer.com/10.1007/s00023-018-0657-7 (Mar. 2018).

131. Tauber, C. Effective vacua for Floquet topological phases: A numerical perspective on the switch-function formalism. *Physical Review B* **97,** 195312. https://link.aps.org/doi/10.1103/PhysRevB.97.195312 (May 24, 2018).

132. Shapiro, J. & Tauber, C. Strongly Disordered Floquet Topological Systems. *Annales Henri Poincaré* **20,** 1837–1875. arXiv: 1807.03251[cond-mat,physics:math-ph]. http://arxiv.org/abs/1807.03251 (June 2019).

133. Moessner, R. & Sondhi, S. L. Equilibration and order in quantum Floquet matter. *Nature Physics* **13,** 424–428. https://www.nature.com/articles/nphys4106 (May 2017).

134. Hauke, P. *et al.* Non-Abelian Gauge Fields and Topological Insulators in Shaken Optical Lattices. *Physical Review Letters* **109.** Publisher: American Physical Society, 145301. https://link.aps.org/doi/10.1103/PhysRevLett.109.145301 (Oct. 5, 2012).

135. Cooper, N. R., Dalibard, J. & Spielman, I. B. Topological bands for ultracold atoms. *Reviews of Modern Physics* **91,** 015005. https://link.aps.org/doi/10.1103/RevModPhys.91.015005 (Mar. 25, 2019).

136. Wintersperger, K. Realization of an anomalous Floquet topological system with ultracold atoms. *Nature Physics* **16,** 8 (2020).

137. Zhang, J.-Y. *et al.* Tuning Anomalous Floquet Topological Bands with Ultracold Atoms. *Physical Review Letters* **130.** Publisher: American Physical Society, 043201. https://link.aps.org/doi/10.1103/PhysRevLett.130.043201 (Jan. 24, 2023).

138. Sokhen, R. E. *et al. Discrete step walks reveal unconventional anomalous topology in synthetic photonic lattices* Nov. 17, 2023. arXiv: 2311.10619[cond-mat,physics:physics]. http://arxiv.org/abs/2311.10619.

139. Kitagawa, T., Rudner, M. S., Berg, E. & Demler, E. Exploring topological phases with quantum walks. *Physical Review A* **82,** 033429. https://link.aps.org/doi/10.1103/PhysRevA.82.033429 (Sept. 24, 2010).

140. Kitagawa, T. *et al.* Observation of topologically protected bound states in photonic quantum walks. *Nature Communications* **3,** 882. http://www.nature.com/articles/ncomms1872 (Jan. 2012).

141. Adiyatullin, A. F. *et al. Multi-topological Floquet metals in a photonic lattice* Number: arXiv:2203.01056. Mar. 2, 2022. arXiv: 2203.01056[physics]. http://arxiv.org/abs/2203.01056.

142. Upreti, L. K. *et al.* Floquet Winding Metals. *arXiv:1907.09914 [cond-mat, physics:physics].* arXiv: 1907.09914. http://arxiv.org/abs/1907.09914 (July 23, 2019).

143. Weidemann, S. *et al.* Topological funneling of light. *Science* **368,** 311–314. https://www.sciencemag.org/lookup/doi/10.1126/science.aaz8727 (Apr. 17, 2020).

144. Weidemann, S., Kremer, M., Longhi, S. & Szameit, A. Topological triple phase transition in non-Hermitian Floquet quasicrystals. *Nature* **601.** Number: 7893 Publisher: Nature Publishing Group, 354–359. https://www.nature.com/articles/s41586-021-04253-0 (Jan. 2022).

145. Groh, T. *et al.* Robustness of topologically protected edge states in quantum walk experiments with neutral atoms. *Physical Review A* **94,** 013620. https://link.aps.org/doi/10.1103/PhysRevA.94.013620 (July 29, 2016).

146. Asboth, J. K. & Edge, J. M. Edge-state-enhanced transport in a two-dimensional quantum walk. *Physical Review A* **91.** Publisher: American Physical Society, 022324. https://link.aps.org/doi/10.1103/PhysRevA.91.022324 (Feb. 19, 2015).

147. Rechtsman, M. C. *et al.* Photonic Floquet topological insulators. *Nature* **496,** 196–200. http://www.nature.com/articles/nature12066 (Apr. 2013).

148. Pasek, M. & Chong, Y. D. Network models of photonic Floquet topological insulators. *Physical Review B* **89,** 075113. https://link.aps.org/doi/10.1103/PhysRevB.89.075113 (Feb. 13, 2014).

149. Delplace, P. Topological chiral modes in random scattering networks. *SciPost Physics* **8,** 081. arXiv: 1905.11194[cond-mat]. http://arxiv.org/abs/1905.11194 (May 29, 2020).

150. Plotnik, Y. *et al.* Observation of unconventional edge states in 'photonic graphene'. *Nature Materials* **13.** Number: 1 Publisher: Nature Publishing Group, 57–62. https://www.nature.com/articles/nmat3783 (Jan. 2014).

151. Mukherjee, S. *et al.* Experimental observation of anomalous topological edge modes in a slowly driven photonic lattice. *Nature Communications* **8,** 13918. http://www.nature.com/articles/ncomms13918 (Apr. 2017).

152. Stützer, S. *et al.* Photonic topological Anderson insulators. *Nature* **560,** 461–465. http://www.nature.com/articles/s41586-018-0418-2 (Aug. 2018).

153. Yang, Z., Lustig, E., Lumer, Y. & Segev, M. Photonic Floquet topological insulators in a fractal lattice. *Light: Science & Applications* **9,** 128. http://www.nature.com/articles/s41377-020-00354-z (Dec. 2020).

154. Pyrialakos, G. G. *et al.* Bimorphic Floquet topological insulators. *Nature Materials* **21.** Number: 6 Publisher: Nature Publishing Group, 634–639. https://www.nature.com/articles/s41563-022-01238-w (June 2022).

155. Biesenthal, T. *et al.* Fractal photonic topological insulators. *Science* **376,** 1114–1119. https://www.science.org/doi/10.1126/science.abm2842 (June 3, 2022).

156. Liang, G. Q. & Chong, Y. D. Optical Resonator Analog of a Two-Dimensional Topological Insulator. *Physical Review Letters* **110,** 203904. https://link.aps.org/doi/10.1103/PhysRevLett.110.203904 (May 14, 2013).

157. Gao, F. *et al.* Probing topological protection using a designer surface plasmon structure. *Nature Communications* **7,** 11619. http://www.nature.com/articles/ncomms11619 (Sept. 2016).

158. Peng, Y.-G. *et al.* Experimental demonstration of anomalous Floquet topological insulator for sound. *Nature Communications* **7,** 13368. http://www.nature.com/articles/ncomms13368 (Dec. 2016).

159. Afzal, S. & Van, V. Topological phases and the bulk-edge correspondence in 2D photonic microring resonator lattices. *Optics Express* **26,** 14567. https://www.osapublishing.org/abstract.cfm?URI=oe-26-11-14567 (May 28, 2018).

160. Afzal, S., Zimmerling, T. J., Ren, Y., Perron, D. & Van, V. Realization of Anomalous Floquet Insulators in Strongly Coupled Nanophotonic Lattices. *Physical Review Letters* **124,** 253601. https://link.aps.org/doi/10.1103/PhysRevLett.124.253601 (June 24, 2020).

161. Bellec, M., Michel, C., Zhang, H., Tzortzakis, S. & Delplace, P. Non-diffracting states in one-dimensional Floquet photonic topological insulators. *EPL (Europhysics Letters)* **119,** 14003. https://iopscience.iop.org/article/10.1209/0295-5075/119/14003 (July 1, 2017).

162. Fritzsche, A. *et al.* Parity–time-symmetric photonic topological insulator. *Nature Materials.* Publisher: Nature Publishing Group, 1–6. https://www.nature.com/articles/s41563-023-01773-0 (Jan. 9, 2024).

163. Titum, P., Berg, E., Rudner, M. S., Refael, G. & Lindner, N. H. Anomalous Floquet-Anderson Insulator as a Nonadiabatic Quantized Charge Pump. *Physical Review X* **6,** 021013. https://link.aps.org/doi/10.1103/PhysRevX.6.021013 (May 6, 2016).

164. Roy, S. & Sreejith, G. J. Disordered Chern insulator with a two-step Floquet drive. *Physical Review B* **94.** Publisher: American Physical Society, 214203. https://link.aps.org/doi/10.1103/PhysRevB.94.214203 (Dec. 6, 2016).

165. Titum, P., Lindner, N. H., Rechtsman, M. C. & Refael, G. Disorder-Induced Floquet Topological Insulators. *Physical Review Letters* **114,** 056801. https://link.aps.org/doi/10.1103/PhysRevLett.114.056801 (Feb. 4, 2015).

166. Nathan, F., Rudner, M. S., Lindner, N. H., Berg, E. & Refael, G. Quantized Magnetization Density in Periodically Driven Systems. *Physical Review Letters* **119,** 186801. https://link.aps.org/doi/10.1103/PhysRevLett.119.186801 (Oct. 31, 2017).

167. Kundu, A., Rudner, M., Berg, E. & Lindner, N. H. Quantized large-bias current in the anomalous Floquet-Anderson insulator. *Physical Review B* **101.** Publisher: American Physical Society, 041403. https://link.aps.org/doi/10.1103/PhysRevB.101.041403 (Jan. 8, 2020).

168. Nathan, F., Abanin, D., Berg, E., Lindner, N. H. & Rudner, M. S. Anomalous Floquet insulators. *Physical Review B* **99,** 195133. https://link.aps.org/doi/10.1103/PhysRevB.99.195133 (May 20, 2019).

169. Kim, K. W., Bagrets, D., Micklitz, T. & Altland, A. Quantum Hall criticality in Floquet topological insulators. *Physical Review B* **101,** 165401. https://link.aps.org/doi/10.1103/PhysRevB.101.165401 (Apr. 1, 2020).

170. Kim, K. W., Bagrets, D., Micklitz, T. & Altland, A. Floquet Simulators for Topological Surface States in Isolation. *Physical Review X* **13.** Publisher: American Physical Society, 011003. https://link.aps.org/doi/10.1103/PhysRevX.13.011003 (Jan. 10, 2023).

171. Du, L., Schnase, P. D., Barr, A. D., Barr, A. R. & Fiete, G. A. Floquet topological transitions in extended Kane-Mele models with disorder. *Physical Review B* **98.** Publisher: American Physical Society, 054203. https://link.aps.org/doi/10.1103/PhysRevB.98.054203 (Aug. 13, 2018).

172. Janssen, M., Metzler, M. & Zirnbauer, M. R. Point-contact conductances at the quantum Hall transition. *Physical Review B* **59,** 15836–15853. https://link.aps.org/doi/10.1103/PhysRevB.59.15836 (June 15, 1999).

173. Hu, W. *et al.* Measurement of a Topological Edge Invariant in a Microwave Network. *Physical Review X* **5,** 011012. https://link.aps.org/doi/10.1103/PhysRevX.5.011012 (Feb. 6, 2015).

174. Potter, A. C., Chalker, J. T. & Gurarie, V. Quantum Hall Network Models as Floquet Topological Insulators. *Physical Review Letters* **125,** 086601. https://link.aps.org/doi/10.1103/PhysRevLett.125.086601 (Aug. 20, 2020).

175. Harris, N. C. *et al.* Quantum transport simulations in a programmable nanophotonic processor. *Nature Photonics* **11.** Number: 7 Publisher: Nature Publishing Group, 447–452. https://www.nature.com/articles/nphoton.2017.95 (July 2017).

176. Pai, S. *et al.* Parallel Programming of an Arbitrary Feedforward Photonic Network. *IEEE Journal of Selected Topics in Quantum Electronics* **26,** 1–13. https://ieeexplore.ieee.org/document/9103211/ (Sept. 2020).

177. Dai, T. *et al.* Topologically protected quantum entanglement emitters. *Nature Photonics* **16,** 248–257. https://www.nature.com/articles/s41566-021-00944-2 (Mar. 2022).

178. Dai, T. *et al.* Non-Hermitian topological phase transitions controlled by nonlinearity. *Nature Physics* **20.** Number: 1 Publisher: Nature Publishing Group, 101–108. https://www.nature.com/articles/s41567-023-02244-8 (Jan. 2024).

179. Bogaerts, W. *et al.* Programmable photonic circuits. *Nature* **586,** 207–216. http://www.nature.com/articles/s41586-020-2764-0 (Oct. 8, 2020).

180. Wang, X. S. *et al.* Graph model for multiple scattering in lithium niobate on insulator integrated photonic networks. *Optics Express* **31.** Publisher: Optica Publishing Group, 42255–42270. https://opg.optica.org/oe/abstract.cfm?uri=oe-31-25-42255 (Dec. 4, 2023).

181. On, M. B. *et al.* Programmable integrated photonics for topological Hamiltonians. *Nature Communications* **15.** Number: 1 Publisher: Nature Publishing Group, 629. https://www.nature.com/articles/s41467-024-44939-3 (Jan. 20, 2024).

182. Stanley, H. E. Scaling, universality, and renormalization: Three pillars of modern critical phenomena. *Reviews of Modern Physics* **71.** Publisher: American Physical Society, S358–S366. https://link.aps.org/doi/10.1103/RevModPhys.71.S358 (Mar. 1, 1999).

183. Tao, R. & Wu, Y.-S. Gauge invariance and fractional quantum Hall effect. *Physical Review B* **30,** 1097–1098. https://link.aps.org/doi/10.1103/PhysRevB.30.1097 (July 15, 1984).

184. Avron, J. E. & Seiler, R. Quantization of the Hall Conductance for General, Multiparticle Schrödinger Hamiltonians. *Physical Review Letters* **54,** 259–262. https://link.aps.org/doi/10.1103/PhysRevLett.54.259 (Jan. 28, 1985).

185. Lannebère, S., Fernandes, D. E., Morgado, T. A. & Silveirinha, M. G. Nonreciprocal and non-Hermitian material response inspired by semiconductor transistors. *Physical Review Letters* **128,** 013902. arXiv: 2201.02118[physics]. http://arxiv.org/abs/2201.02118 (Jan. 6, 2022).

186. Buddhiraju, S., Song, A., Papadakis, G. T. & Fan, S. Nonreciprocal Metamaterial Obeying Time-Reversal Symmetry. *Physical Review Letters* **124,** 257403. https://link.aps.org/doi/10.1103/PhysRevLett.124.257403 (June 24, 2020).

187. Asadchy, V., Mirmoosa, M. S., Díaz-Rubio, A., Fan, S. & Tretyakov, S. A. Tutorial on Electromagnetic Nonreciprocity and Its Origins. *Proceedings of the IEEE* **108,** 1684–1727. arXiv: 2001.04848[physics]. http://arxiv.org/abs/2001.04848 (Oct. 2020).

188. Sakurai, J. J. & Napolitano, J. J. *Modern Quantum Mechanics* 2nd Edition. ISBN: 0-8053-8291-7 (Pearson, July 4, 2010).

189. Tai, C.-t. *Dyadic Green Functions in Electromagnetic Theory* (IEEE Press, 1994).

190. Kord, A., Sounas, D. L. & Alu, A. Microwave Nonreciprocity. *Proceedings of the IEEE* **108,** 1728–1758. https://ieeexplore.ieee.org/document/9143399/ (Oct. 2020).

191. Fleury, R., Sounas, D. L., Sieck, C. F., Haberman, M. R. & Alu, A. Sound Isolation and Giant Linear Nonreciprocity in a Compact Acoustic Circulator. *Science* **343,** 516–519. https://www.sciencemag.org/lookup/doi/10.1126/science.1246957 (Jan. 31, 2014).

192. Zhang, Z., Yang, S., Chen, Y., Qu, S. & Hu, J. Fast Analysis of Parallel-Plate Cylindrical Luneberg Lens Antennas Through Dyadic Green's Functions. *IEEE Transactions on Microwave Theory and Techniques* **66,** 4327–4337. https://ieeexplore.ieee.org/document/8428453/ (Oct. 2018).

193. Pozar, David. M. *Microwave Engineering* 2nd edn (Wiley, 1998).

194. Murnaghan, F. D. The Orthogonal and Symplectic Groups. *Communications of the Dublin Institute for Advanced Studies.* https://dair.dias.ie/id/eprint/27/ (1958).

195. Reck, M., Zeilinger, A., Bernstein, H. J. & Bertani, P. Experimental realization of any discrete unitary operator. *Physical Review Letters* **73,** 58–61. https://link.aps.org/doi/10.1103/PhysRevLett.73.58 (July 4, 1994).

196. Chau, L.-L. & Keung, W.-Y. Comments on the Parametrization of the Kobayashi-Maskawa Matrix. *Physical Review Letters* **53,** 1802–1805. https://link.aps.org/doi/10.1103/PhysRevLett.53.1802 (Nov. 5, 1984).

197. Diţă, P. Separation of unistochastic matrices from the double stochastic ones: Recovery of a 3×3 unitary matrix from experimental data. *Journal of Mathematical Physics* **47,** 083510. https://doi.org/10.1063/1.2229424 (Aug. 17, 2006).

198. Jarlskog, C. Commutator of the Quark Mass Matrices in the Standard Electroweak Model and a Measure of Maximal CP Nonconservation. *Physical Review Letters* **55,** 1039–1042. https://link.aps.org/doi/10.1103/PhysRevLett.55.1039 (Sept. 2, 1985).

199. Dita, P. On the parametrisation of unitary matrices by the moduli of their elements. *Communications in Mathematical Physics* **159,** 581–591. http://link.springer.com/10.1007/BF02099985 (Jan. 1994).

200. Dita, P. *Factorization of Unitary Matrices* Mar. 6, 2001. arXiv: math-ph/0103005. http://arxiv.org/abs/math-ph/0103005.

201. Wang, Z. & Fan, S. Magneto-optical defects in two-dimensional photonic crystals. *Applied Physics B* **81,** 369–375. http://link.springer.com/10.1007/s00340-005-1846-x (July 2005).

202. Wang, Z. & Fan, S. Optical circulators in two-dimensional magneto-optical photonic crystals.

203. Diestel, R. *Graph theory* 5th ed. ISBN: 0072-5285. https://doi.org/10.1007/978-3-662-53622-3 (Springer Berlin, Heidelberg, 2017).

204. Berthier, L. & Biroli, G. Theoretical perspective on the glass transition and amorphous materials. *Reviews of Modern Physics* **83,** 587–645. https://link.aps.org/doi/10.1103/RevModPhys.83.587 (June 20, 2011).

205. Marsal, Q., Varjas, D. & Grushin, A. G. Topological Weaire–Thorpe models of amorphous matter. *Proceedings of the National Academy of Sciences* **117,** 30260–30265. https://pnas.org/doi/full/10.1073/pnas.2007384117 (Dec. 2020).

206. Grushin, A. G. & Repellin, C. Amorphous and Polycrystalline Routes toward a Chiral Spin Liquid. *Physical Review Letters* **130,** 186702. https://link.aps.org/doi/10.1103/PhysRevLett.130.186702 (May 2, 2023).

207. Cassella, G., d'Ornellas, P., Hodson, T., Natori, W. M. H. & Knolle, J. An exact chiral amorphous spin liquid. *Nature Communications* **14.** Number: 1 Publisher: Nature Publishing Group, 6663. https://www.nature.com/articles/s41467-023-42105-9 (Oct. 20, 2023).

208. Edelsbrunner, H. *Algorithms in combinatorial geometry* https://books.google.com/books?hl=en&lr=&id=mxugg47mzK4C&oi=fnd&pg=PR15&dq=Algorithms+in+Combinatorial+Geometry&ots=J8406KUbFx&sig=Myvf_pWM6VaSeg9jfNW43W_PqHs (Springer Science & Business Media, 1987).

209. Domínguez-Castro, G. A. & Paredes, R. The Aubry–André model as a hobbyhorse for understanding the localization phenomenon. *European Journal of Physics* **40,** 045403. https://iopscience.iop.org/article/10.1088/1361-6404/ab1670 (July 1, 2019).

210. Fabre, A., Bouhiron, J.-B., Satoor, T., Lopes, R. & Nascimbene, S. Laughlin's Topological Charge Pump in an Atomic Hall Cylinder. *Physical Review Letters* **128,** 173202. https://link.aps.org/doi/10.1103/PhysRevLett.128.173202 (Apr. 25, 2022).

211. Bardyn, C.-E., Filippone, M. & Giamarchi, T. Bulk pumping in two-dimensional topological phases. *Physical Review B* **99,** 035150. https://link.aps.org/doi/10.1103/PhysRevB.99.035150 (Jan. 25, 2019).

212. Chen, A. *et al.* Hyperbolic matter in electrical circuits with tunable complex phases. *Nature Communications* **14,** 622. https://www.nature.com/articles/s41467-023-36359-6 (Feb. 4, 2023).

213. Chen, L., Liu, Q., Lin, X., Zhang, X. & Jiang, X. Disorder dependence of helical edge states in HgTe/CdTe quantum wells. *New Journal of Physics* **14.** Publisher: IOP Publishing, 043028. https://dx.doi.org/10.1088/1367-2630/14/4/043028 (Apr. 2012).

214. Essin, A. M. & Moore, J. E. Topological insulators beyond the Brillouin zone via Chern parity. *Physical Review B* **76.** Publisher: American Physical Society, 165307. https://link.aps.org/doi/10.1103/PhysRevB.76.165307 (Oct. 10, 2007).

215. Lin, L., Ke, Y., Zhang, L. & Lee, C. Calculations of the Chern number: Equivalence of real-space and twisted-boundary-condition formulas. *Physical Review B* **108,** 174204. https://link.aps.org/doi/10.1103/PhysRevB.108.174204 (Nov. 27, 2023).

216. Lin, L., Ke, Y. & Lee, C. Topological invariants for interacting systems: From twisted boundary conditions to center-of-mass momentum. *Physical Review B* **107.** Publisher: American Physical Society, 125161. https://link.aps.org/doi/10.1103/PhysRevB.107.125161 (Mar. 30, 2023).

217. Prodan, E. Non-commutative tools for topological insulators. *New Journal of Physics* **12,** 065003. https://iopscience.iop.org/article/10.1088/1367-2630/12/6/065003 (June 17, 2010).

218. Loring, T. A. & Hastings, M. B. Disordered topological insulators via C*-algebras. *Europhysics Letters* **92,** 67004. https://dx.doi.org/10.1209/0295-5075/92/67004 (Jan. 2011).

219. Mansha, S. & Chong, Y. D. Robust edge states in amorphous gyromagnetic photonic lattices. *Physical Review B* **96,** 121405. https://link.aps.org/doi/10.1103/PhysRevB.96.121405 (Sept. 15, 2017).

220. Wang, X. S., Brataas, A. & Troncoso, R. E. Bosonic Bott Index and Disorder-Induced Topological Transitions of Magnons. *Physical Review Letters* **125.** Publisher: American Physical Society, 217202. https://link.aps.org/doi/10.1103/PhysRevLett.125.217202 (Nov. 18, 2020).

221. Kitaev, A. Anyons in an exactly solved model and beyond. *Annals of Physics* **321,** 2–111. https://linkinghub.elsevier.com/retrieve/pii/S0003491605002381 (Jan. 2006).

222. Verbaarschot, J. J. M., Weidenmüller, H. A. & Zirnbauer, M. R. Grassmann integration in stochastic quantum physics: The case of compound-nucleus scattering. *Physics Reports* **129,** 367–438. https://www.sciencedirect.com/science/article/pii/0370157385900705 (Dec. 1, 1985).

223. Meidan, D., Micklitz, T. & Brouwer, P. W. Topological classification of adiabatic processes. *Physical Review B* **84,** 195410. https://link.aps.org/doi/10.1103/PhysRevB.84.195410 (Nov. 2, 2011).

224. Fulga, I. C., Hassler, F. & Akhmerov, A. R. Scattering theory of topological insulators and superconductors. *Physical Review B* **85.** Publisher: American Physical Society, 165409. https://link.aps.org/doi/10.1103/PhysRevB.85.165409 (Apr. 5, 2012).

225. Büttiker, M. Four-Terminal Phase-Coherent Conductance. *Physical Review Letters* **57,** 1761–1764. https://link.aps.org/doi/10.1103/PhysRevLett.57.1761 (Oct. 6, 1986).

226. Sheng, L., Sheng, D. N., Ting, C. S. & Haldane, F. D. M. Nondissipative Spin Hall Effect via Quantized Edge Transport. *Physical Review Letters* **95,** 136602. https://link.aps.org/doi/10.1103/PhysRevLett.95.136602 (Sept. 19, 2005).

227. Jalabert, R. Mesoscopic transport and quantum chaos. *Scholarpedia* **11,** 30946. http://www.scholarpedia.org/article/Mesoscopic_transport_and_quantum_chaos (2016).

228. Beenakker, C. W. J. Random-matrix theory of quantum transport. *Reviews of Modern Physics* **69,** 731–808. https://link.aps.org/doi/10.1103/RevModPhys.69.731 (July 1, 1997).

229. Yang, Y. *et al.* Realization of a three-dimensional photonic topological insulator. *Nature* **565.** Number: 7741 Publisher: Nature Publishing Group, 622–626. https://www.nature.com/articles/s41586-018-0829-0 (Jan. 2019).

230. Chen, Q. *et al.* Discovery of a maximally charged Weyl point. *Nature Communications* **13,** 7359. https://www.nature.com/articles/s41467-022-34978-z (Nov. 30, 2022).

231. Yan, Q. *et al.* Experimental discovery of nodal chains. *Nature Physics* **14,** 461–464. https://www.nature.com/articles/s41567-017-0041-4 (May 2018).

232. Yang, B. *et al.* Ideal Weyl points and helicoid surface states in artificial photonic crystal structures. *Science* **359,** 1013–1016. https://www.science.org/doi/10.1126/science.aaq1221 (Mar. 2, 2018).

233. Hatsugai, Y., Ishibashi, K. & Morita, Y. Sum Rule of Hall Conductance in a Random Quantum Phase Transition. *Physical Review Letters* **83.** Publisher: American Physical Society, 2246–2249. https://link.aps.org/doi/10.1103/PhysRevLett.83.2246 (Sept. 13, 1999).

234. Liu, H., You, J.-S., Ryu, S. & Fulga, I. C. Supermetal-insulator transition in a non-Hermitian network model. *Physical Review B* **104.** Publisher: American Physical Society, 155412. https://link.aps.org/doi/10.1103/PhysRevB.104.155412 (Oct. 7, 2021).

235. Schwartz, T., Bartal, G., Fishman, S. & Segev, M. Transport and Anderson localization in disordered two-dimensional photonic lattices. *Nature* **446,** 52–55. http://www.nature.com/articles/nature05623 (Mar. 2007).

236. Yu, S., Qiu, C.-W., Chong, Y., Torquato, S. & Park, N. Engineered disorder in photonics. *Nature Reviews Materials* **6,** 226–243. http://www.nature.com/articles/s41578-020-00263-y (Mar. 2021).

237. Yamilov, A. *et al.* Anderson localization of electromagnetic waves in three dimensions. *Nature Physics.* Publisher: Nature Publishing Group, 1–6. https://www.nature.com/articles/s41567-023-02091-7 (June 15, 2023).

238. Anderson, P. W., Thouless, D. J., Abrahams, E. & Fisher, D. S. New method for a scaling theory of localization. *Physical Review B* **22,** 3519–3526. https://link.aps.org/doi/10.1103/PhysRevB.22.3519 (Oct. 15, 1980).

239. MacKinnon, A. & Kramer, B. MacKinnon and Kramer Respond. *Physical Review Letters* **49,** 695–695. https://link.aps.org/doi/10.1103/PhysRevLett.49.695 (Aug. 30, 1982).

240. Munshi, S. & Yang, R. Self-adjoint elements in the pseudo-unitary group U(p,p). *Linear Algebra and its Applications* **560,** 100–113. https://www.sciencedirect.com/science/article/pii/S0024379518304750 (Jan. 1, 2019).

241. Slevin, K. & Ohtsuki, T. Critical exponent for the Anderson transition in the three-dimensional orthogonal universality class. *New Journal of Physics* **16,** 015012. https://iopscience.iop.org/article/10.1088/1367-2630/16/1/015012 (Jan. 10, 2014).

242. MacKinnon, A. & Kramer, B. One-Parameter Scaling of Localization Length and Conductance in Disordered Systems. *Physical Review Letters* **47,** 1546–1549. https://link.aps.org/doi/10.1103/PhysRevLett.47.1546 (Nov. 23, 1981).

243. Brouwer, P. W. Scattering approach to parametric pumping. *Physical Review B* **58,** R10135–R10138. https://link.aps.org/doi/10.1103/PhysRevB.58.R10135 (Oct. 15, 1998).

244. Fulga, I. C., Hassler, F., Akhmerov, A. R. & Beenakker, C. W. J. Scattering formula for the topological quantum number of a disordered multi-mode wire. *Physical Review B* **83,** 155429. arXiv: 1101.1749[cond-mat]. http://arxiv.org/abs/1101.1749 (Apr. 18, 2011).

245. Fulga, I. C. & Maksymenko, M. Scattering matrix invariants of Floquet topological insulators. *Physical Review B* **93.** Publisher: American Physical Society, 075405. https://link.aps.org/doi/10.1103/PhysRevB.93.075405 (Feb. 2, 2016).

246. Franca, S., Hassler, F. & Fulga, I. C. Topological reflection matrix. *Physical Review B* **105,** 155121. https://link.aps.org/doi/10.1103/PhysRevB.105.155121 (Apr. 13, 2022).

247. Braeunlich, G., Graf, G. M. & Ortelli, G. Equivalence of topological and scattering approaches to quantum pumping. *Communications in Mathematical Physics* **295,** 243–259. arXiv: 0902.4638[cond-mat,physics:math-ph]. http://arxiv.org/abs/0902.4638 (Apr. 2010).

248. Pierrat, R. *et al.* Invariance property of wave scattering through disordered media. *Proceedings of the National Academy of Sciences* **111,** 17765–17770. https://pnas.org/doi/full/10.1073/pnas.1417725111 (Dec. 16, 2014).

249. Makris, K. G., Brandstötter, A., Ambichl, P., Musslimani, Z. H. & Rotter, S. Wave propagation through disordered media without backscattering and intensity variations. *Light: Science & Applications* **6,** e17035–e17035. http://www.nature.com/articles/lsa201735 (Sept. 2017).

250. Orazbayev, B., Malléjac, M., Bachelard, N., Rotter, S. & Fleury, R. *Wave momentum shaping for moving objects in heterogeneous and dynamic media* Dec. 4, 2023. arXiv: 2401.00853[physics]. http://arxiv.org/abs/2401.00853.

251. Brouwer, P. W., Frahm, K. M. & Beenakker, C. W. J. Quantum Mechanical Time-Delay Matrix in Chaotic Scattering. *Physical Review Letters* **78,** 4737–4740. https://link.aps.org/doi/10.1103/PhysRevLett.78.4737 (June 23, 1997).

252. Maczewsky, L. J., Zeuner, J. M., Nolte, S. & Szameit, A. Observation of photonic anomalous Floquet topological insulators. *Nature Communications* **8,** 13756. http://www.nature.com/articles/ncomms13756 (Apr. 2017).

253. Fruchart, M., Hanai, R., Littlewood, P. B. & Vitelli, V. Non-reciprocal phase transitions. *Nature* **592,** 363–369. http://www.nature.com/articles/s41586-021-03375-9 (Apr. 15, 2021).

254. Fleury, R., Khanikaev, A. B. & Alù, A. Floquet topological insulators for sound. *Nature Communications* **7,** 11744. https://www.nature.com/articles/ncomms11744 (June 17, 2016).

255. Khanikaev, A. B. & Shvets, G. Two-dimensional topological photonics. *Nature Photonics* **11,** 763–773. http://www.nature.com/articles/s41566-017-0048-5 (Dec. 2017).

256. Zeng, Y. *et al.* Electrically pumped topological laser with valley edge modes. *Nature* **578,** 246–250. http://www.nature.com/articles/s41586-020-1981-x (Feb. 13, 2020).

257. Zangeneh-Nejad, F., Sounas, D. L., Alù, A. & Fleury, R. Analogue computing with metamaterials. *Nature Reviews Materials.* http://www.nature.com/articles/s41578-020-00243-2 (Oct. 19, 2020).

258. Darabi, A., Ni, X., Leamy, M. & Alù, A. Reconfigurable Floquet elastodynamic topological insulator based on synthetic angular momentum bias. *Science Advances* **6,** eaba8656. https://advances.sciencemag.org/lookup/doi/10.1126/sciadv.aba8656 (July 2020).

259. Chen, G. *et al.* Tunable correlated Chern insulator and ferromagnetism in a moiré superlattice. *Nature* **579,** 56–61. http://www.nature.com/articles/s41586-020-2049-7 (Mar. 2020).

260. Kane, C. L. & Mele, E. J. Z 2 Topological Order and the Quantum Spin Hall Effect. *Physical Review Letters* **95,** 146802. https://link.aps.org/doi/10.1103/PhysRevLett.95.146802 (Sept. 28, 2005).

261. Treacy, M. M. J. & Borisenko, K. B. The Local Structure of Amorphous Silicon. *Science* **335,** 950–953. https://www.science.org/doi/10.1126/science.1214780 (Feb. 24, 2012).

262. Hong, S. *et al.* Ultralow-dielectric-constant amorphous boron nitride. *Nature* **582,** 511–514. http://www.nature.com/articles/s41586-020-2375-9 (June 25, 2020).

263. Eggleton, B. J., Luther-Davies, B. & Richardson, K. Chalcogenide photonics. *Nature Photonics* **5,** 141–148. http://www.nature.com/articles/nphoton.2011.309 (Mar. 2011).

264. Ryu, S. Classification of topological insulators and superconductors, 22.

265. Ando, Y. Topological Insulator Materials. *Journal of the Physical Society of Japan* **82,** 102001. http://journals.jps.jp/doi/10.7566/JPSJ.82.102001 (Oct. 15, 2013).

266. Pöyhönen, K., Sahlberg, I., Westström, A. & Ojanen, T. Amorphous topological superconductivity in a Shiba glass. *Nature Communications* **9,** 2103. http://www.nature.com/articles/s41467-018-04532-x (Dec. 2018).

267. Zhou, P. *et al.* Photonic amorphous topological insulator. *Light: Science & Applications* **9,** 133. http://www.nature.com/articles/s41377-020-00368-7 (Dec. 2020).

268. Kim, S., Agarwala, A. & Chowdhury, D. *Fractionalization and topology in amorphous electronic solids* May 23, 2022. arXiv: 2205.11523[cond-mat]. http://arxiv.org/abs/2205.11523.

269. Agarwala, A. & Shenoy, V. B. Topological Insulators in Amorphous Systems. *Physical Review Letters* **118,** 236402. http://link.aps.org/doi/10.1103/PhysRevLett.118.236402 (June 8, 2017).

270. Marsal, Q., Varjas, D. & Grushin, A. G. *Obstructed insulators and flat bands in topological phase-change materials* Apr. 29, 2022. arXiv: 2204.14177[cond-mat]. http://arxiv.org/abs/2204.14177.

271. Wang, J.-H., Yang, Y.-B., Dai, N. & Xu, Y. Structural-Disorder-Induced Second-Order Topological Insulators in Three Dimensions. *Physical Review Letters* **126,** 206404. https://link.aps.org/doi/10.1103/PhysRevLett.126.206404 (May 20, 2021).

272. Wang, C., Cheng, T., Liu, Z., Liu, F. & Huang, H. Structural Amorphization-Induced Topological Order. *Physical Review Letters* **128,** 056401. https://link.aps.org/doi/10.1103/PhysRevLett.128.056401 (Feb. 2, 2022).

273. Liang, G. *et al.* Robust, efficient, micrometre-scale phase modulators at visible wavelengths. *Nature Photonics* **15,** 908–913. https://www.nature.com/articles/s41566-021-00891-y (Dec. 2021).

274. Padilla, P., Muñoz-Acevedo, A., Sierra-Castañer, M. & Sierra-Pérez, M. Electronically Reconfigurable Transmitarray at Ku Band for Microwave Applications. *IEEE Transactions on Antennas and Propagation* **58,** 2571–2579. http://ieeexplore.ieee.org/document/5466046/ (Aug. 2010).

275. Wilson, K. G. The renormalization group: Critical phenomena and the Kondo problem. *Reviews of Modern Physics* **47.** Publisher: American Physical Society, 773–840. https://link.aps.org/doi/10.1103/RevModPhys.47.773 (Oct. 1, 1975).

276. Fisher, M. E. Renormalization group theory: Its basis and formulation in statistical physics. *Reviews of Modern Physics* **70.** Publisher: American Physical Society, 653–681. https://link.aps.org/doi/10.1103/RevModPhys.70.653 (Apr. 1, 1998).

277. Cardy, J. *Scaling and Renormalization in Statistical Physics* (Cambridge University Press, 1996).

278. Efrati, E., Wang, Z., Kolan, A. & Kadanoff, L. P. Real-space renormalization in statistical mechanics. *Reviews of Modern Physics* **86.** Publisher: American Physical Society, 647–667. https://link.aps.org/doi/10.1103/RevModPhys.86.647 (May 16, 2014).

279. Arovas, D. P., Janssen, M. & Shapiro, B. Real-space renormalization of the Chalker-Coddington model. *Physical Review B* **56.** Publisher: American Physical Society, 4751–4759. https://link.aps.org/doi/10.1103/PhysRevB.56.4751 (Aug. 15, 1997).

280. Schomerus, H. Renormalization approach to the analysis and design of Hermitian and non-Hermitian interfaces. *Physical Review Research* **5,** 043224. arXiv: 2208.14626[cond-mat, physics:physics, physics:quant-ph]. http://arxiv.org/abs/2208.14626 (Dec. 11, 2023).

281. Gu, Z.-C. & Wen, X.-G. Tensor-entanglement-filtering renormalization approach and symmetry-protected topological order. *Physical Review B* **80,** 155131. https://link.aps.org/doi/10.1103/PhysRevB.80.155131 (Oct. 26, 2009).

282. Chen, X., Gu, Z.-C. & Wen, X.-G. Local unitary transformation, long-range quantum entanglement, wave function renormalization, and topological order. *Physical Review B* **82,** 155138. https://link.aps.org/doi/10.1103/PhysRevB.82.155138 (Oct. 26, 2010).

283. Morimoto, T., Furusaki, A. & Mudry, C. Anderson localization and the topology of classifying spaces. *Physical Review B* **91,** 235111. https://link.aps.org/doi/10.1103/PhysRevB.91.235111 (June 8, 2015).

284. Chen, W. Scaling theory of topological phase transitions. *Journal of Physics: Condensed Matter* **28,** 055601. https://iopscience.iop.org/article/10.1088/0953-8984/28/5/055601 (Feb. 10, 2016).

285. Mong, R. S. K., Bardarson, J. H. & Moore, J. E. Quantum Transport and Two-Parameter Scaling at the Surface of a Weak Topological Insulator. *Physical Review Letters* **108,** 076804. https://link.aps.org/doi/10.1103/PhysRevLett.108.076804 (Feb. 15, 2012).

286. Fulga, I. C., Van Heck, B., Edge, J. M. & Akhmerov, A. R. Statistical topological insulators. *Physical Review B* **89,** 155424. https://link.aps.org/doi/10.1103/PhysRevB.89.155424 (Apr. 21, 2014).

287. Rohden, M., Sorge, A., Timme, M. & Witthaut, D. Self-Organized Synchronization in Decentralized Power Grids. *Physical Review Letters* **109.** Publisher: American Physical Society, 064101. https://link.aps.org/doi/10.1103/PhysRevLett.109.064101 (Aug. 9, 2012).

288. Hul, O. *et al.* Experimental simulation of quantum graphs by microwave networks. *Physical Review E* **69,** 056205. https://link.aps.org/doi/10.1103/PhysRevE.69.056205 (May 11, 2004).

289. Xiang, Z.-L., Zhang, M., Jiang, L. & Rabl, P. Intracity Quantum Communication via Thermal Microwave Networks. *Physical Review X* **7,** 011035. https://link.aps.org/doi/10.1103/PhysRevX.7.011035 (Mar. 27, 2017).

290. Guo, C. & Fan, S. Reciprocity Constraints on Reflection. *Physical Review Letters* **128,** 256101. https://link.aps.org/doi/10.1103/PhysRevLett.128.256101 (June 21, 2022).

291. Franca, S., Könye, V., Hassler, F., van den Brink, J. & Fulga, C. Non-Hermitian Physics without Gain or Loss: The Skin Effect of Reflected Waves. *Physical Review Letters* **129.** Publisher: American Physical Society, 086601. https://link.aps.org/doi/10.1103/PhysRevLett.129.086601 (Aug. 17, 2022).

292. Fisher, M. E. The renormalization group in the theory of critical behavior. *Reviews of Modern Physics* **46,** 597–616. https://link.aps.org/doi/10.1103/RevModPhys.46.597 (Oct. 1, 1974).

293. Benzi, R. & Petronzio, R. Finite-Size Real-Space Renormalization Group. *Europhysics Letters (EPL)* **9,** 17–22. https://iopscience.iop.org/article/10.1209/0295-5075/9/1/004 (May 1, 1989).

294. Parisi, G. *On the replica approach to glasses* Jan. 10, 1997. arXiv: cond-mat/9701068. http://arxiv.org/abs/cond-mat/9701068.

295. Parisi, G. *The physical Meaning of Replica Symmetry Breaking* May 18, 2002. arXiv: cond-mat/0205387. http://arxiv.org/abs/cond-mat/0205387.

296. Castellana, M. *The Renormalization Group for Disordered Systems* July 25, 2013. arXiv: 1307.6891[cond-mat]. http://arxiv.org/abs/1307.6891.

297. Angelini, M. C. & Biroli, G. Real space renormalization group theory of disordered models of glasses. *Proceedings of the National Academy of Sciences* **114.** Publisher: Proceedings of the National Academy of Sciences, 3328–3333. https://www.pnas.org/doi/full/10.1073/pnas.1613126114 (Mar. 28, 2017).

298. Slevin, K. & Ohtsuki, T. Corrections to Scaling at the Anderson Transition. *Physical Review Letters* **82,** 382–385. https://link.aps.org/doi/10.1103/PhysRevLett.82.382 (Jan. 11, 1999).

299. Ovchinnikov, D. *et al.* Topological current divider in a Chern insulator junction. *Nature Communications* **13.** Number: 1 Publisher: Nature Publishing Group, 5967. https://www.nature.com/articles/s41467-022-33645-7 (Oct. 10, 2022).

300. Cai, J. *et al.* Electric control of a canted-antiferromagnetic Chern insulator. *Nature Communications* **13.** Publisher: Nature Publishing Group, 1668. https://www.nature.com/articles/s41467-022-29259-8 (Mar. 29, 2022).

301. Zhao, Y.-F. *et al.* Creation of chiral interface channels for quantized transport in magnetic topological insulator multilayer heterostructures. *Nature Communications* **14.** Number: 1 Publisher: Nature Publishing Group, 770. https://www.nature.com/articles/s41467-023-36488-y (Feb. 11, 2023).

302. Wang, J., Sciarrino, F., Laing, A. & Thompson, M. G. Integrated photonic quantum technologies. *Nature Photonics* **14.** Publisher: Nature Publishing Group, 273–284. https://www.nature.com/articles/s41566-019-0532-1 (May 2020).

303. Elshaari, A. W., Pernice, W., Srinivasan, K., Benson, O. & Zwiller, V. Hybrid integrated quantum photonic circuits. *Nature Photonics* **14.** Publisher: Nature Publishing Group, 285–298. https://www.nature.com/articles/s41566-020-0609-x (May 2020).

304. Wang, Y. *et al.* Topological protection of two-photon quantum correlation on a photonic chip. *Optica* **6.** Publisher: Optica Publishing Group, 955–960. https://opg.optica.org/optica/abstract.cfm?uri=optica-6-8-955 (Aug. 20, 2019).

305. Zheng, Y. *et al.* Multichip multidimensional quantum networks with entanglement retrievability. *Science* **381.** Publisher: American Association for the Advancement of Science, 221–226. https://www.science.org/doi/10.1126/science.adg9210 (July 14, 2023).

306. Rechtsman, M. C. *et al.* Topological protection of photonic path entanglement. *Optica* **3.** Publisher: Optica Publishing Group, 925–930. https://opg.optica.org/optica/abstract.cfm?uri=optica-3-9-925 (Sept. 20, 2016).

307. Mittal, S., Orre, V. V., Leykam, D., Chong, Y. D. & Hafezi, M. Photonic Anomalous Quantum Hall Effect. *Physical Review Letters* **123,** 043201. https://link.aps.org/doi/10.1103/PhysRevLett.123.043201 (July 23, 2019).

308. Xiao, L. *et al.* Observation of topological edge states in parity–time-symmetric quantum walks. *Nature Physics* **13.** Number: 11 Publisher: Nature Publishing Group, 1117–1123. https://www.nature.com/articles/nphys4204 (Nov. 2017).

309. Price, H. *et al.* Roadmap on topological photonics. *Journal of Physics: Photonics* **4,** 032501. https://iopscience.iop.org/article/10.1088/2515-7647/ac4ee4 (July 1, 2022).

310. Chen, Z. & Segev, M. Highlighting photonics: looking into the next decade. *eLight* **1,** 2. https://elight.springeropen.com/articles/10.1186/s43593-021-00002-y (June 8, 2021).

311. Klesse, R. & Metzler, M. Modeling Disordered Quantum Systems with Dynamical Networks. *International Journal of Modern Physics C* **10,** 577–606. arXiv: cond-mat/9902100. http://arxiv.org/abs/cond-mat/9902100 (June 1999).

312. Perseguers, S., Lewenstein, M., Acín, A. & Cirac, J. I. Quantum random networks. *Nature Physics* **6.** Number: 7 Publisher: Nature Publishing Group, 539–543. https://www.nature.com/articles/nphys1665 (July 2010).

313. Wang, H., Zhou, L. & Chong, Y. D. Floquet Weyl phases in a three-dimensional network model. *Physical Review B* **93.** Publisher: American Physical Society, 144114. https://link.aps.org/doi/10.1103/PhysRevB.93.144114 (Apr. 14, 2016).

314. Wang, Y., Price, H. M., Zhang, B. & Chong, Y. D. Circuit implementation of a four-dimensional topological insulator. *Nature Communications* **11,** 2356. https://www.nature.com/articles/s41467-020-15940-3 (May 12, 2020).

315. Lee, C. H., Wang, Y., Chen, Y. & Zhang, X. Electromagnetic response of quantum Hall systems in dimensions five and six and beyond. *Physical Review B* **98.** Publisher: American Physical Society, 094434. https://link.aps.org/doi/10.1103/PhysRevB.98.094434 (Sept. 28, 2018).

316. Abrahams, E., Anderson, P. W., Licciardello, D. C. & Ramakrishnan, T. V. Scaling Theory of Localization: Absence of Quantum Diffusion in Two Dimensions. *Physical Review Letters* **42,** 673–676. https://link.aps.org/doi/10.1103/PhysRevLett.42.673 (Mar. 5, 1979).

317. Ozawa, T. & Carusotto, I. Synthetic Dimensions with Magnetic Fields and Local Interactions in Photonic Lattices. *Physical Review Letters* **118.** Publisher: American Physical Society, 013601. https://link.aps.org/doi/10.1103/PhysRevLett.118.013601 (Jan. 3, 2017).

318. Maczewsky, L. J. *et al.* Synthesizing multi-dimensional excitation dynamics and localization transition in one-dimensional lattices. *Nature Photonics* **14,** 76–81. http://www.nature.com/articles/s41566-019-0562-8 (Feb. 2020).

319. Xiao, M., Chen, W.-J., He, W.-Y. & Chan, C. T. Synthetic gauge flux and Weyl points in acoustic systems. *Nature Physics* **11,** 920–924. http://www.nature.com/articles/nphys3458 (Nov. 2015).

320. Upreti, L. K. *et al.* Topological Swing of Bloch Oscillations in Quantum Walks. *Physical Review Letters* **125,** 186804. https://link.aps.org/doi/10.1103/PhysRevLett.125.186804 (Oct. 30, 2020).

321. Dutt, A. *et al.* A single photonic cavity with two independent physical synthetic dimensions. *Science* **367,** 59–64. https://www.science.org/doi/10.1126/science.aaz3071 (Jan. 3, 2020).

322. Artime, O. *et al.* Robustness and resilience of complex networks. *Nature Reviews Physics.* Publisher: Nature Publishing Group, 1–18. https://www.nature.com/articles/s42254-023-00676-y (Jan. 8, 2024).

323. Watts, D. J. & Strogatz, S. H. Collective dynamics of ‘small-world’ networks. **393** (1998).

324. Barthélémy, M. & Amaral, L. A. N. Small-World Networks: Evidence for a Crossover Picture. *Physical Review Letters* **82.** Publisher: American Physical Society, 3180–3183. https://link.aps.org/doi/10.1103/PhysRevLett.82.3180 (Apr. 12, 1999).

325. Efimkin, D. K. & MacDonald, A. H. Helical network model for twisted bilayer graphene. *Physical Review B* **98,** 035404. https://link.aps.org/doi/10.1103/PhysRevB.98.035404 (July 2, 2018).

326. De Beule, C., Dominguez, F. & Recher, P. Aharonov-Bohm Oscillations in Minimally Twisted Bilayer Graphene. *Physical Review Letters* **125,** 096402. https://link.aps.org/doi/10.1103/PhysRevLett.125.096402 (Aug. 25, 2020).

327. De Beule, C., Dominguez, F. & Recher, P. Network model and four-terminal transport in minimally twisted bilayer graphene. *Physical Review B* **104.** Publisher: American Physical Society, 195410. https://link.aps.org/doi/10.1103/PhysRevB.104.195410 (Nov. 8, 2021).

328. De Beule, C., Phong, V. T. & Mele, E. J. *Network model for periodically strained graphene* Sept. 6, 2022. arXiv: 2209.02554[cond-mat]. http://arxiv.org/abs/2209.02554.

329. De Beule, C., Phong, V. T. & Mele, E. J. Network model for periodically strained graphene. *Physical Review B* **107,** 045405. https://link.aps.org/doi/10.1103/PhysRevB.107.045405 (Jan. 5, 2023).

330. Apffel, B., Wildeman, S., Eddi, A. & Fort, E. Experimental Implementation of Wave Propagation in Disordered Time-Varying Media. *Physical Review Letters* **128,** 094503. https://link.aps.org/doi/10.1103/PhysRevLett.128.094503 (Mar. 4, 2022).

331. Carminati, R., Chen, H., Pierrat, R. & Shapiro, B. Universal Statistics of Waves in a Random Time-Varying Medium. *Physical Review Letters* **127,** 094101. https://link.aps.org/doi/10.1103/PhysRevLett.127.094101 (Aug. 27, 2021).

# Zhe Zhang

Gender: Male; Date of Birth: 7/13/1996; Phone: 0041782643150;
Address: Rue de Bassenges 2, Ecublens, CH-1024. E-mail: zhe.zhang@epfl.ch

## Education

*École Polytechnique Fédérale de Lausanne (EPFL)*, Switzerland **09. 2019- Present**
-Doctoral School of Photonics, Doctoral Assistant, Advisor: Prof. Romain Fleury
*University of Electronic Science and Technology of China* **09. 2012- 07. 2019**
- Master and Bachelor of Engineering in Electromagnetic Field and Microwave Technology;
- GPA: 3.93/4, Ranking: 1/128;

## Publications & Talks

### Publications (Journals):

[1] Zhe Zhang, Pierre Delplace, and Romain Fleury, "Superior robustness of anomalous non-reciprocal topological edge states," ***Nature*** 598.7880 (2021): 293-297.
[2] Zhe Zhang, Pierre Delplace, and Romain Fleury, "Anomalous topological waves in strongly amorphous scattering networks," ***Science Advances*** (2023).
[3] Zhe Zhang, Yifei Guan, Junda Wang, Benjamin Apffel, Aleksi Bossart, Haoye Qin, Oleg Yazyev, and Romain Fleury, "Renormalization group of topological scattering networks," arXiv:2404.15866.
[4] Qiaolu Chen$^{\dagger}$, Zhe Zhang$^{\dagger}$, Haoye Qin, Aleksi Bossart, Yihao Yang, Hongsheng Chen, Romain Fleury, "Anomalous and Chern topological waves in hyperbolic networks", ***Nature Communications*** 15.1 (2024): 2293.
[5] Zhe Zhang, *et al*, "Non-Hermitian topological transport in the spectrum continuum", ***in preparation***.
[6] Zhe Zhang, *et al*, "On the connection between frequency band structure and Floquet band structure in scattering networks", ***in preparation***.
[7] Haoye Qin, Zhe Zhang, Qiaolu Chen, and Romain Fleury, "Disclination states in nonreciprocal topological networks," ***Physical Review Research*** 6, no. 1 (2024): 013031.
[8] Haoye Qin, Zhe Zhang, Qiaolu Chen, Zhechen Zhang, and Romain Fleury, "Anomalous-Chern steering of topological nonreciprocal guided waves," ***Advanced Materials, In press***.
[9] Haoye Qin, Zhe Zhang, Qiaolu Chen, Zhechen Zhang, and Romain Fleury, "Skyrmion Bound States in the Continuum for 3D light trapping in arbitrarily large volumes," ***Under Review***.
[10] Zhe Zhang, Shiwen Yang, Yikai Chen, Shiwei Qu, and Jun Hu, "Fast analysis of parallel-plate cylindrical Luneberg lens antennas through dyadic Green's functions," ***IEEE Trans. Microw. Theory Tech.***, vol. 66, no. 10, pp. 4327-4337, Oct. 2018.
[11] Zhishu Qu, Shiwei Qu, Zhe Zhang, and Shiwen Yang, "A wide-angle scanning lens fed by antenna array," ***IEEE Trans. Antennas Propag.***, 68, no. 5 (2020): 3635-3643.
[12] Zhe Zhang, Shiwen Yang, Yuansong Zeng, Shiwei Qu, and Jun Hu, "Design optimization of an extremely flat-beam cylindrical Luneberg lens antenna," ***IEEE Access.***, 7 (2019), 156675-156685.

### Conference Talks:

[1] Zhe Zhang, Pierre Delplace, and Romain Fleury, "Amorphous topological scattering networks," *Photonics & Electromagnetics Research Symposium (**PIERS**), Prague* (2023) [**Invited**]
[2] Zhe Zhang, Pierre Delplace, and Romain Fleury, "Amorphous topological scattering networks," ***META**, Paris* (2023) [**Invited**]

[3] Zhe Zhang, Pierre Delplace, and Romain Fleury, “Exceptional robustness and anomalous topology in non-reciprocal scattering networks,” ***Metamaterial**, Crete* (2023).

[4] Zhe Zhang, Pierre Delplace, and Romain Fleury, “Anomalous Topology in Strongly Amorphous Networks,” *Conference on Lasers and Electro-Optics/Europe– European Quantum Electronics Virtual Conferences (**CLEO/Europe-EQEC**), Munich* (2023).

[5] Zhe Zhang, Pierre Delplace, and Romain Fleury, “Anomalous amorphous topological networks,” ***Metamaterials**, Siena* (2022).

[6] Zhe Zhang, Pierre Delplace, and Romain Fleury, “Exceptional transport robustness in anomalous topological scattering network: theory and experiment,” *Photonics & Electromagnetics Research Symposium (**PIERS**), Hangzhou* (2021).

## Honors and Awards

| | |
|---|---|
| EPS-QEOD Travel Grant Student Awards | *CLEO Europe and Europe Physics Society* 2023 |
| Best Student Paper Award (1st prize) | *PhotonIcs and ElectRomagnetic Symposium* 2021 |
| Outstanding Thesis | *Sichuan Provincial Department of Education* |
| Outstanding Graduate Student | *Sichuan Provincial Department of Education* |
| National Scholarship | *Ministry of Education of the People's Republic of China* |

## Skills

Matlab, LaTeX, Ansys HFSS, COMSOL Multiphysic, ADS, Origin, Adobe Illustrator, Photoshop, Blender.

## Teaching Experiences

TA of Electromagnetics I : Transmission lines and waves, 2021-2022

## Peer Review

*Physical Review Letters, Physical Review Research, IEEE Trans AP*, *New journal of physics*, *Electronic Letter*, *et al*